Automated, Scalable Robotic NDT Inspections of Unknown Free Form Parts

PhD Thesis

Alastair Poole

Centre of Ultrasonic Engineering

Electronic and Electrical Engineering

University of Strathclyde, Glasgow

September 28, 2023

This thesis is the result of the author's original research. It has been composed by the author and has not been previously submitted for examination which has led to the award of a degree.

Acknowledgements

I would like to express my deepest gratitude to my industrial supervisor Mark Sutcliffe for his steadfast support, without whose astute and innovative guidance I would not have been able to complete this project. I am immensely grateful also to my academic supervisor Gareth Pierce whose futurist commentary coupled to his analytic interrogation of the foundations of any concept accorded explicability to this thesis, and insight to its continuations. Thanks also to Carmelo Mineo for his kind advice, selflessly proffering work hours to talk and to inform. I am also grateful to the whole team within TWI, in particular Ian Nicholson, Nathan Hartley and Dave Carswell, whose own innovations and camaraderie were conducive to personal development and the development of novel (yet useful) concepts. I would like to extend thanks to my family for making every effort to listen, to question, and to remain positive through years of dry musings. Finally but by no means least, thanks to Mich Scott and Peter Poole, who saw a spark, fed it kindling, and sought to place it on a candlestick.

"The world at present is full of angry self-centred groups, each incapable of viewing human life as a whole, each willing to destroy civilization rather than yield an inch."

- Bertrand Russell, In Praise of Idleness.

Abstract

Manufacturing techniques have evolved around requirements of the consumer in the context of competition, with quality assurance central to the 20th century paradigm of consumer spending on high value goods, the mainstay of Non-Destructive Testing (NDT) during this period. Prioritisation of end-use reliability lead to a plethora of techniques such as subtractive manufacturing in which material and energy waste were given attention proportional to their marginal costs at the time. Mass-produced goods in this value bracket were often guaranteed to have homogeneity and so automating their inspection with repeatable, accurate, yet dull robotic platforms provided a natural extension and boon to inspections. In recent years, increasing direct and external costs in energy production and end-of-life waste have exhibited themselves as an increasing focus in government and industry on reducing greenhouse emissions through novel manufacturing methods and closing product life-cycles by way of remanufacturing. Lightweight moulded composites and pre-used parts present a break from the repeatable product archetype that robotic NDT is traditionally suited to, requiring

adaptable inspection processes to scan hosts of parts with minor but geometry-deforming defects.

Currently, path planning for NDT inspections require either digital representations to create and simulate inspection routines, or for a lengthy operator driven jogging procedure that can present bottlenecks to a scanning process. Repeatably manufactured parts in prior production processes were either provided with a digital model as an accurate template for manufacturing, or were sufficiently similar that a jogged path could be applied to every part produced. Digital path planning on moulded and remanufactured parts is not possible in the same way, requiring extensive metrological inspection prior to planning, with jogged planning completely unfeasible. Separately, the demand for online path planning for mobile robotic arm platforms has seen large growth recent years, driven by a desire for remote scanning in hazardous environments and to increase the inspection through-put of green technology such as wind turbines. In these conditions, a digital representation of the part is not necessarily available or can entail a lengthy digital-world to real-world calibration procedure for path planning to commence. Post inspection, while industrial robotic arms can generally reconstruct NDT data to sub-mm accuracy, a mobile base with poor or no odometric data can entail the use of high-cost, fixed volume metrological equipment to reconstruct data to the same accuracy in order to enable an operator to properly validate, repair, or sentence the part.

By taking the novel perspective of minimising the number of mathematical perspectives necessary for each sub-problem, this thesis investigates the minimal quantity of data necessary to profile and inspect an unknown free-form part autonomously and independently of additional equipment, and in the subsequent data reconstruction when multiple scans are taken. Of particular interest is the dry-dock scanning of RNLI Severn class lifeboat hulls, the targeted industrial use case scenario. The output is a novel autonomous path planning system using low-cost RGB/D cameras, laser line sensors and force/torque control that reduces the path planning and deployment time from up to a month down to several minutes. This thesis further provides a novel approach to data stitching with visual reference markers, demonstrating an optimal accuracy in the order of mm. The result is an easy to use process utilising Python software that requires no prior information from a human operator. The process workflow from part placement to part reconstruction is represented in Fig: 1. It is capable of quickly generating and then deploying scan paths for fixed or mobile robotic-arm platforms, and of accurate reconstructing of parts in the latter case.

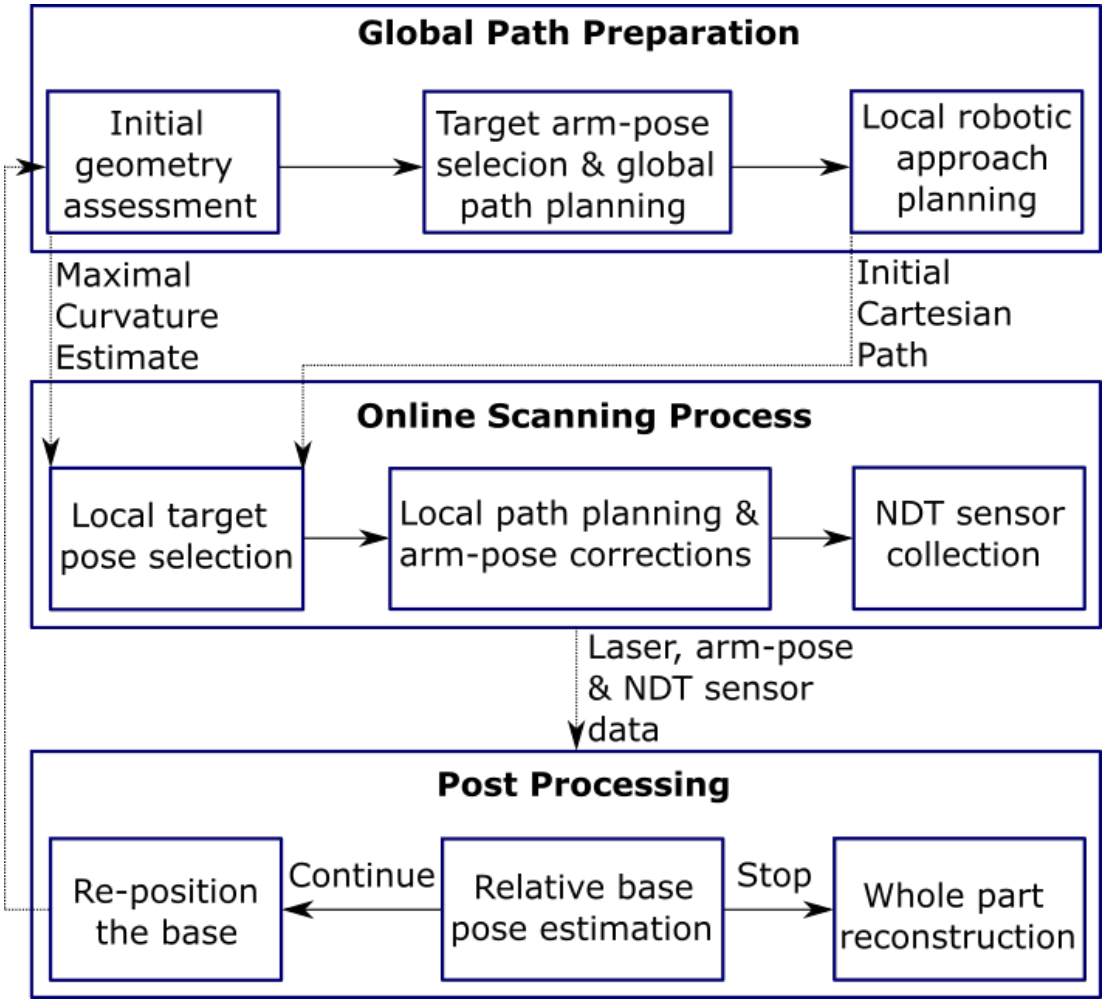

Figure 1: A graphical representation of the plan and scan workflow presented by this thesis. Two options for path planning are presented, either relying on an operator estimating global curvatures (Chapter: 3), or using a commercial colour + depth stereo camera (Chapter: 4).

Contents

List of Figures

List of Tables

Acronyms and Abbreviations

UT	Ultrasonic Testing
NDT	Non Destructive Testing
AUT	Automatic Ultrasonic Testing
ROS	Robot Operating System
RTDE	Real Time Data Exchange
WBIS	Wind Blade Inspection System
RGB/D camera	Red-Green-Blue-Depth camera
ACUT	Air Coupled Ultrasonic Testing
PAUT	Phased Array Ultrasonic Testing
CWP	Conformable Wedge Probe
CT	Computed Tomography
TT	Tap Testing
Cobots	Collabrative Robots
CFRP	Carbn Fibre Reinforced Polymers
DR	Digital Representation

RNLI	Royal National Lifeboat Institution
VO	Visual Odometry
SIFT	Scale Invariant Feature Transform
SURF	Speeded Up Robust Features
CAD	Computer Aided Design
SfM	Structure from Motion
ICP	Iterative Closest Point
QR code	Quick Response code
AR	Augmented Reality
CPP	Coverage Path Planning
TSP	Travelling Sales Person
RL	Reinforced Learning
CV	Computer Vision
SSIM	Structural Similarity Index
ddl	dynamic link library
PI controller	Position Integral controller
PID controller	Position Integral Derivative controller
SVD	Singular Value Decomposition
MLE	Maximum Likelihod Estimator

Chapter 1

Introduction

1.1 Automatic Ultrasonic Testing

Ultrasonic Testing (UT) is a Non-Destructive Testing (NDT) method whereby a high frequency sound wave is transmitted through a material and the resulting signal's waveform received by a corresponding probe and any irregular echoes or shadows in the detected signal are used to interpret the presence of defects. Several other NDT methods exist, each with their own strengths and weaknesses that are dependant on the material of the part being inspected, its geometry, or the environment where the scan is taking place. The first NDT method applied on an industrial scale was visual inspections, seeing legislation mandating its use in boiler inspections as far back as 1864 [1]. However this approach could only detect surface level defects, the value of regimes that could determine the

location of defects beneath the surface led to a subsequent rapid adoption of novel technology within the NDT field. Soon after in the 1860's, a prototypical magnetic inspection technique was developed for the inspection of gun barrels [2]. Soon after it was discovered that x-rays provided high quality cross-sectional images of bones, it was adopted as an NDT technique. X-ray testing quickly became the preferred method for quality verification of industrial parts, since the results were detailed and were produced as a single image, providing a record of the results and the position of the scan for later interpretation.

While use of sonic testing dates back to the ancient practice of blacksmiths tapping finished products to instinctively listen for the resonant sound of defects, it was not until the 1920's that methods of applying high frequency UT waves were considered. Research led by Paul Langevin into subsurface sonic ranging to detect U-boats during the first world war used piezoelectric crystals for their electro-mechanical properties, creating a prototype method of pulse-echo testing [3]. However the early equipment necessary for applied industrial UT inspection was bulky and required a highly skilled operator to operate, simultaneously observing an oscilloscope while applying the UT transducer to the surface. The large quantity of data produced coupled to application by hand meant results could not be logged for further interpretation and were not traceable to a specific position on parts, as well as introducing sources of human error as the operator was forced to pour intense focus on both tasks. Due to the complications

of traceability, and simultaneous interpretation and application, UT as an inspection technique from the 1930s to 1940s saw specific and limited applications. Despite these drawbacks, interest in UT gathered as it could see planar defects and non-metallic inclusions in hot rolled sheet metals where X-ray inspections could not, a fact that led to significant research led advancements during the Second World War by Britain, the US and Germany simultaneously [4]. Beginning in the late 1940's and early 1950's, a rapid advancement in commercial UT was spurred on by the technological boom in compact, easy to deploy UT equipment invented to supplement the war effort. Building on these developments, on-site UT inspections became a post-war possibility. By the 1950s, the first portable devices that could be operator applied were developed, leading to the invention in that decade of the first transportable Automated UT (AUT) platform designed for inspections within pipe mills called the RTD Rotoscan, seen in Fig: 1.1.

Innovating on the small hand-held transducer design, this device incorporated one or more transducers linked to a paper chart recording UT data in real time. These were mounted along the circumference of a rotating mechanical platform that logged the transducer position, linking UT and position data streams to solve data traceability issues during pipe scans. By the 1980s its advanced design was further improved with the second generation seeing use in on-site offshore inspections. An explosion in interest in reliable data logging and positioning led to significant developments in mechanically applied UT. By the late 1970s, a pro-

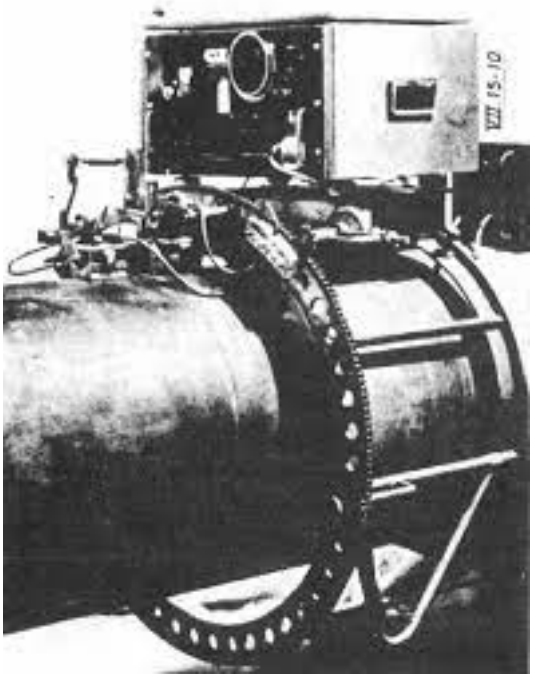

Figure 1.1: An original 1959 RTD Rotoscan. While the bulky equipment made it impractical for on-site deployments, its successors building upon its efficient frame saw use in various on-site situations.

totypical UT deployed mechanical arm for medical applications was invented in the form of the Combison 202 Kretz, an operator moving the arm into position to record UT data seen in Fig: 1.2. The three degrees of freedom enabled accurate position and orientation recordings of UT data collected over the patient's abdomens.

Advances in the field of industrial robotic arms saw experimental deployments of ultrasonic tools applied by them begin in earnest in the 1980s. Fixed base robotic arms, while not practical for on-site deployments, could reduce the strain on human operators since the arm could apply the probe and collect position-linked data. Whereas the RTD Rotoscan could record data along a single ro-

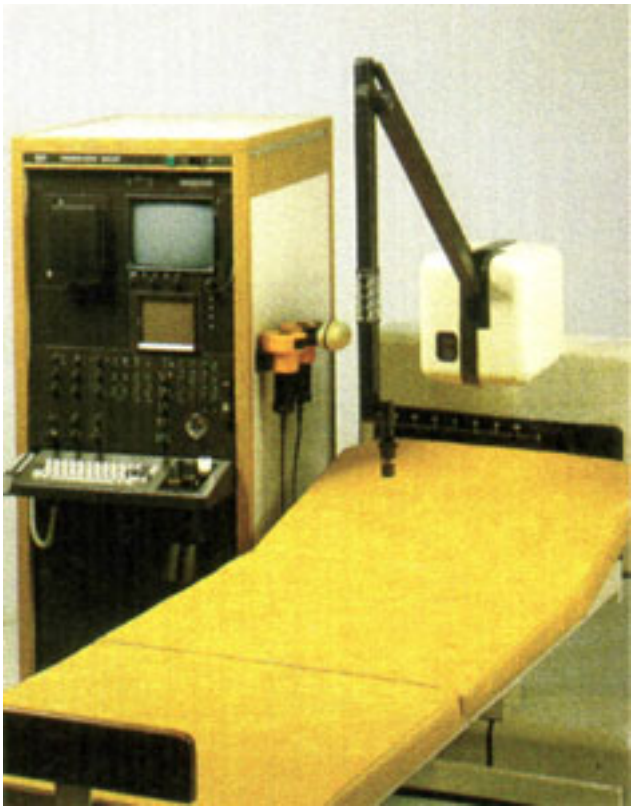

Figure 1.2: The Combison 202 Kretz device would enable recordings of UT data linked to both the position and pose of the device while an operator guided it along portions of a patient's body.

tational axis, fully articulated 6-axis robotic arms could both apply the sensor using complex programmed paths and record data across an entire part's volume, coupling NDT data to the tool's position and orientation where it was taken.

Meanwhile, the need for on-site inspections remained. Crawler technology enabled the mounting of NDT sensors to the carriages of remotely controlled vehicles traversing difficult to access geometries. By 1975, remote X-ray scanning of pipe butt-welds were being completed [5]. The advantages of robotic arms over crawlers were still stark, since complex geometries could not be fully accessed or

scanned by wide-base crawler platforms. As early as the mid to late 1990's, hybrid robotic arm/crawler platforms were being developed to test dangerous and hard to reach pipe welds within energy and ship building sectors [6, 7], benefiting from the mobility of the crawler and access-ability of the arm. Innovative hybrid applications demonstrated that this approach could reduce the down-time of plants where they were applied, but still relied on regular and known geometries for proper path execution. Due to the technological and processing limitations of the time, hybrid mobile platforms saw less interest and developments than either fixed base industrial arms or mobile crawlers/drones respectively.

Due to their controller's scale, their mass, and the platform's inherent safety limitations, fixed cells are required by industrial robotic arms - a factor that is both a boon and a drawback. Novel technology, algorithms and software can be applied safely within the controlled cell conditions, leading to significant developments in their application over the past four decades. In scanning mass produced parts, their accuracy in data reconstructions, sensing within complex materials, and sensor deployments to the surface of known parts has dominated industrial focus.

1.2 Industrial Robotic Arm Applied NDT

Widespread robotic inspection cell deployments began in the 2000's. Dual and single robotic systems were either mounted with water squirter-jet systems, the

UT device coupled to the surface through laminar flow streams directed from the tool's nozzle, or mounted with UT sensors that were coupled via a static water-bath immersing the part. An example of a dual robotic cell is show in Fig: 1.3. Though industrial robots have large, immobile fixed-based control stacks requiring cell deployments, the volume of these cells may be expanded with linear or rotary axes that either the robots are mounted to or are external to the robot.

Figure 1.3: Dual robotic cell within TWI undergoing through transmission of a wing part mounted to a rotary table.

To deploy the sensor to the surface as a human operator would by hand, industrial robots require scan paths to be generated and then executed on their controllers. The first path programming method involved a human operator incrementally jogging the robot through its teach-pendant to points along the

scan path that were saved for later execution, reducing the time to deployment when scanning identical parts from a running-cost to an overhead-cost. Later on, commercially available software that would plan paths over a digital geometric representation of the component within a virtual copy of the robotic cell opened up progress towards the repeatable and accurate inspection of parts of increasing complexity. Since then, methods to accurately digitally copy the robotic cell's contents for path planning and deployment within a virtual environment has become a focus of robotic-arm deployed NDT, harnessing offline path planning in tandem with intelligent systems to update digital representations to better reflect realistic industrial conditions where parts cannot be easily placed in identical poses and are not manufactured with millimetre accuracy. The outcome of this focus is a reduced time-to-deploy for repeatable and near-identical parts within laboratory settings accounting for part-placement error, though still relying on accurate digital geometric representations of the parts to generate paths.

Core to current general robotic arm developments are the focus on increasing both ease-of-use by downstream operators and the range of possible areas for deployment, accelerating the adoption of robotic arms in industrial settings by lowering the economic barriers of high-cost training and deployment. A new wave of industrial robotic deployments is being driven by a mixture of open source and proprietary path planning software such as the Robot Operating System (ROS) [8] that incorporate cutting edge algorithms as modules to facilitate easy integration,

or the Real Time Data Exchange (RTDE) package by universal robots allowing full external control from Python [9].

1.3 Mobile Robotic Arm Applied NDT

Extensive use of fixed base robotic arms within NDT has naturally shaped cutting edge path planning and deployment strategies, a by-product of which is that both path planning and robotic solutions are highly specialised when designed for unstructured, non-laboratory like conditions.

Robotic arms are seen as accurate and repeatable as set out by ISO 9283:1998 [10], but only capable of scanning parts that are known and can comfortably fit within their work-volume. Meanwhile, crawlers and drones are inherently inaccurate due to exogenous factors such as wheel-slippage or wind, but extremely scalable in their scanning volume, and capable of traversing complex scan-paths under extreme conditions. While the specific NDT sensor dimensions limit the geometries that can be inspected, tools mounted on crawlers tend to be under-carriage mounted rendering them unfeasible for highly curved geometries such as T-welds. Meanwhile, robotic arms though with a higher chance of collision with the part due to their kinematic structure, are limited only by the tool's dimensions and terrain preventing access to the scanning poses.

In tandem to the developments in robotic-arm software's ease of use, specialisation of industrial-grade robotics has lead to a variety of models on the market in

terms of size and weight. Collaborative-robotics (Cobots), first developed in the late 1990's, are designed for working alongside human operators with stringent safety requirements compared to their larger industrial fixed-based antecedents. The development of Cobots from industrial robot platforms also mirrored advances in UT technology, having smaller footprints and lower masses that over the past decade has led to a high powered if niche market building them into mobile platforms. Utilising an established off the shelf Cobot and mobile base solutions has reduced the need for custom builds and increased the attractiveness of hybrid solutions for various industries. Cobot-hybrids are of interest for NDT research and industrial solutions, particularly in on-site deployments alongside human operators: where traditional industrial robotic arms are too dangerous to deploy, and custom hybrid solutions too niche to consider for applications at scale.

1.4 Flexible Robotic NDT: Academic and Industrial Developments

Cutting edge semi - autonomous robotic arm inspections rely upon prior information provided by the operator, either of pre-planned paths for part profiling, or a reference database of expected geometric models. Research in this field has progressed rapidly, relying on visual and even Ultrasonic real-time feedback,

optimising the operator's time significantly. However, wide spread adoption of autonomous procedures in hazardous or on-site environments, or in scanning deformed surfaces are hampered by current process' reliance on well known and well structured parts and environment that may be easily modelled by a simple digital geometric representation. Enabling behaviour to scan full, unknown surfaces with explicable algorithms would mirror the developments in modern robotics, providing a host of benefits. Robotic scans would no longer be limited to known models, further empowering robotic-arm NDT to service a wider range of traditionally problematic industries where parts can have no accurate digital geometric representations and whose surfaces cannot be fitted to simple geometric primitives. Developing approaches to autonomise robotic-arm scanning without relying on prior information would also reduce the economic cost of highly skilled operators by optimising their time away from manual scans and robotic path planning, and towards data interpretation and part validation. In servicing green industries whose production processes are not lent to producing accurate digital geometric representations such as additive manufacturing and remanufacturing, a reduction in costs at the quality assurance stage would increase their competitiveness with carbon-intensive traditional manufacturing techniques.

Further to inspection flexibility, a resurgence in focus on mobile robotic arm platforms is being spearheaded by various energy industries who are seeking innovative ways to reduce the risk to human operators inspecting components within

hazardous environments, equipped now with high-accuracy Cobot arms. Several products combining robotic arms with mobile bases are in development or are already in consumer markets. Recently released wheel base systems are targeted towards laboratory environments with prior part information. Products such as Olympus' Wind Blade Inspection System (WBIS) [11] can inspect parts of varying scale, the only limiting factor being the height of the part. The E-blade by ENDITY [12] fully automates wind turbine blade inspections with a similar system, using an industrial robotic arm instead of a Cobot.

Mobile robotic arm developments have also attracted a burgeoning interest in on-site applications. Oil and gas research in particular has long sought after hybrid robotic base and arm platforms, initially to access and scan pipe weld geometries to both assist human operators and reduce operation down-times necessary to allow technicians access to hard to reach regions. Recent progressions in research have led to the development of several platforms that, instead of aiding operators, actively replace them in dangerous environments. Companies such as PETRONAS and Taurob either offer or are utilising commercial hybrid inspection systems for offshore inspections [13, 14]. Similarly, research produced by institutes and competitions such as ORCA and the ARGOS project have shown industrial and academic desire for full autonomisation of inspection tasks in human-centric on-site environments. The winner of the ARGOS challenge can be seen in Fig: 1.4.

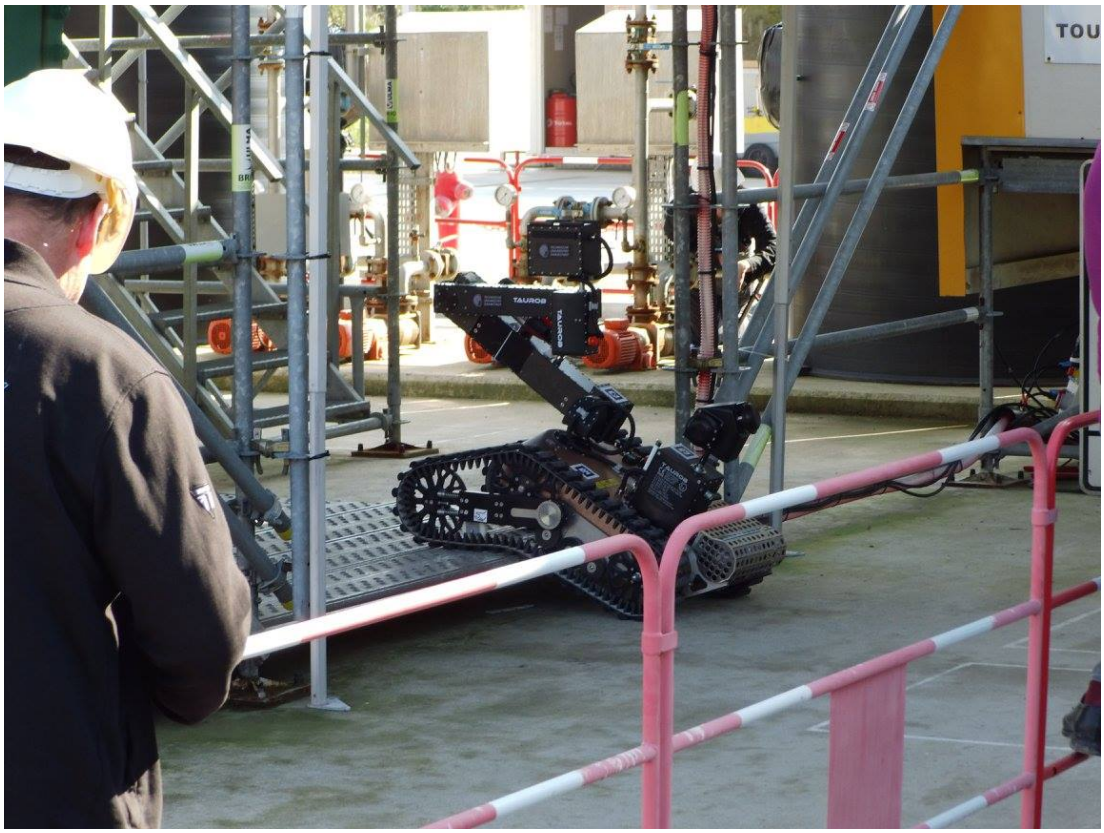

Figure 1.4: The winner of the 2017 ARGOS challenge by the Argonaut team. The platform is capable of autonomous visual inspections and condition monitoring within the human-centric architecture of an offshore oil and gas station.

Industrial hybrid robotic arm NDT solutions with wheel or leg-based mobile bases have mainly focused on non-contact visual inspection techniques whose paths have greater freedom in planning and are less prone to collisions. A camera is mounted to the arm that then observes pressurised vessels, gauges, and other components a human operator would normally inspect in order to ascertain operational safety on-site. Cutting edge contact solutions such as Eddy Current (EC) sensors are also being investigated, though not in the context of full autonomisation, requiring external control to inspect parts. While visual inspections can

detect probable surface level defects with EC providing greater clarity for metallic structures, UT is preferable for identifying defects at depth. With an increasing focus on autonomy in this field in particular, real time path planning is becoming a focal point of research in this sector. While the platforms have met the technological challenge, the underlying path planning algorithms have not matured as fast.

Developments aimed towards the energy sectors also have positive external utility to multiple sectors. Mirroring developments within the oil and gas sectors, an avenue of research into robotised inspection within aerospace is the use of light weight robots that can be manually fixed upon various positions along either pipe or wing segments, an example of which is shown in Fig: 1.5. A pre-planned path is then loaded, or a quick manual jogging pattern is completed that is then executed by the robotic arm.

These robotic platforms, similar to their mobile cousins, are developed to reach the technical challenges of inspections within difficult to reach locations. However, the path planning has not developed the same flexibility and autonomy as the platforms themselves, following in the footsteps of manual jogging or requiring strict digital geometric representations. Similarly, with drone inspections in aerospace, a reliance on offline path planning or online operator control limits the application or speed of drone based visual inspections within environments such as hangers.

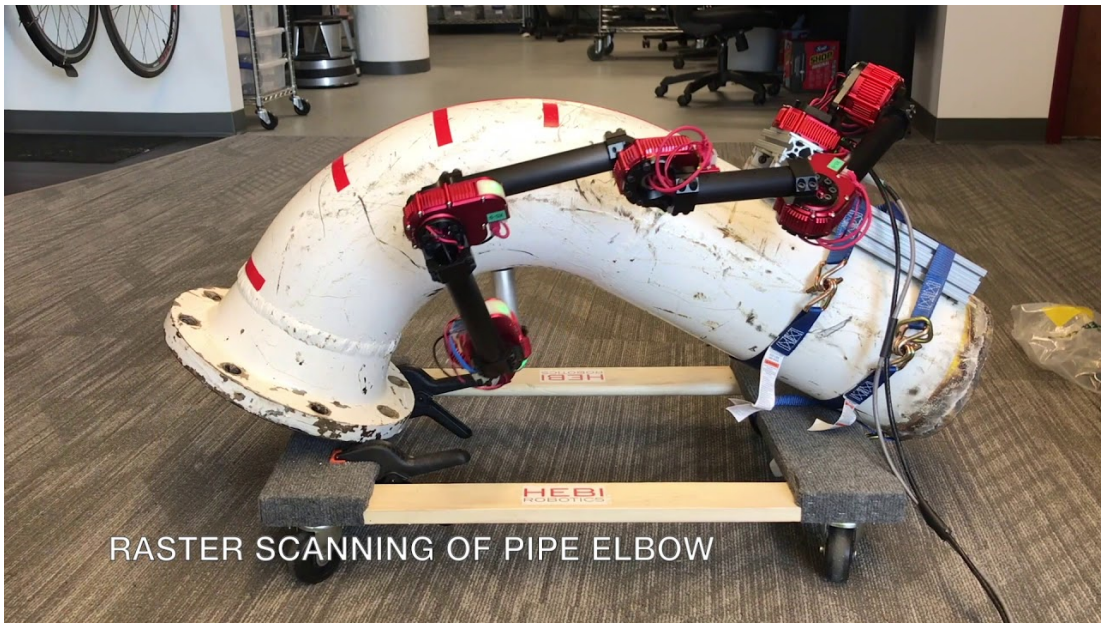

Figure 1.5: A cutting edge proof of concept solution by Hebi robotics, demonstrating complex curved pipe section inspection by an ultrasonic sensor. The robot is jogged over the surface, a prior model fitted and a raster scan path generated for full coverage.

A particular use of real time correction in robotic path planning comes from infrastructure inspection routines. In 2013 an EU funded project, ROBO-SPECT was instigated to investigate autonomous scanning of tunnels for cracks. The result is a system that integrates visual inspection that finds probable cracks, a laser system for refining the crack geometry, and an ultrasonic sensor for sub surface concrete inspection. Delivered in 2016, the result is an effective platform and routine that includes ultrasonic inspection. However, as before the contact based path planning requires knowledge of the tunnel's geometry, fitting the point cloud data to a polynomial spline for subsequent UT inspection. Introduction of online correction algorithms for such inspections would remove the need for

expensive laser scanners and enable the profiling of irregular geometries in the context of infrastructure inspection routines.

Mobile robotic arms have reached several industries, their scalability in inspection volume and leaner form singling them out as a leading light of future developments in robotised NDT.

1.5 Motivation for Research

Improvements in light-weighting robotic platform design and online programming capability have led to the introduction of commercial and research platforms targeting arenas requiring flexible scanning approaches, as set out above. The ease of use and deployment of these platforms furthers the direction of robotic arm NDT: towards collaborative settings, with scalable-volume delivery, and away from a reliance on prior digital geometric representations. However the path planning methods developed still largely rely on human operators to input some form of prior knowledge in order to deploy, limiting their use in situations where information is lacking such as in mould manufacturing or remanufacturing.

Mould manufacturing of composites is key to the aeronautic sector, replacing metallic components of greater mass. Unlike traditional subtractive metallic manufacturing some moulding techniques may result in non-critical defects, the part deviating from the design digital-twin in a way that does not harm overall structural integrity. Flexible path planning algorithms would be able to scan

these components, without requiring lengthy pre-scanning procedures to produce reliable digital geometric representations of a part.

In closing the product life-cycle, remanufacturing of parts is a key enabler of reducing global greenhouse emissions. Within the remanufacturing process, visual inspections are used as an economic viability test of remanufacturing versus manufacturing a new part. While sub-surface NDT inspections would provide greater certainty of viability, the uptake of UT or X-ray based inspections has been slow. Several large-value research projects have investigated the possibility of robotising aspects of the remanufacturing process. Despite this, robotised sub-surface inspections of remanufactured parts are not as focused upon. Primarily: legacy parts, parts that have warped in use, and parts for which intellectual property issues have prevented the sharing of digital representations in turn result in a challenge for robotic NDT in scanning these parts. Jogged paths or part reconstructions are historically necessary to begin scanning parts such as these, often with a large time cost or need for repeatable pre-scan paths with wide aperture sensors such as cameras. Flexible online path planning would reduce the economic cost of remanufacturing by reducing time-to-deploy of robotised scans, make the inspection process scalable in terms of parts geometries that can be inspected while providing high quality data for ascertaining remanufacturing viability.

In combination, fast and flexible online path planning for inspection routines

would increase the economic viability of certain products that would reduce carbon emissions, and would be applicable to various sectors where there is potential for growth in autonomous on-site inspections such as transport and civil engineering sectors. It is also desirable to enable such path planning regimes with low cost sensors, since equipment may be damaged or broken in potential on-site deployments.

Taking the novel approach of describing the work space with a minimalist mathematical framework, this work also concurrently provides the minimal set of sensors required for each task. Taking into account imperfect data from low-cost sensors, the algorithms developed within this thesis seek to be robust in the presence of dynamic workspaces, while also ensuring safety of the part and robot in developed autonomous scanning processes.

1.6 Research Aims and Hypothesis

To complement the current and ongoing research into hybrid platforms aimed for on-site deployment, this thesis aims to explore the representations of the work, global, and part spaces to qualify the following hypotheses.

Seeking the minimal number of representations to describe the work-space can enable development of autonomous algorithmic solutions to robotic scanning of unknown surfaces with minimal or no prior information. Novel combinations of

cost-effective sensors and respective software deployments, selected to suit their complementary perspectives can be used to produce these solutions.

This thesis investigates the little-researched topic of autonomy and full automation with no prior information in robotised NDT path planning. The fundamental objective of this thesis is to provide novelty while assuring industrial relevance. An industrial use-case highlighted as the target of this thesis is as follows.

Manual scans of a boat hull within a dry-dock can take up to a week of continuous scanning, with severe strain placed on the operator. Dry docks present the dual challenges of having humans work in close proximity to the platform, and of being significantly less ordered than a laboratory environment. Moreover, several boat hulls lack a digital geometric representation to plan scan trajectories or for later data alignment to accurately localise defects. This work seeks to develop novel algorithms in order to iteratively scan an unknown boat hull within a laboratory environment mocked up to represent a dry-dock, and reconstructing the data as a digital representation of the hull.

1.7 Research Methodology

The task of autonomous full surface profiling and reconstruction with a mobile robotic arm is partitioned by reviewing the mathematical representations of the

work space. Each part is then investigated by introducing novel approaches, or by developing previous algorithms tailored to suit an industrial environment, while also providing generality in order to be able to solve other key academic and industrial problems at the forefront of robotic NDT.

1.8 Contributions to Knowledge

The specific contributions to knowledge produced by this thesis are as follows.

1. This thesis has demonstrated a novel algorithmic solution to full surface profiling of a part. This solution also shows the robot tool's frame of reference is the only necessary perspective for full surface discovery, while requiring a world-frame to define a stopping condition. The tool's frame of reference is also shown to be equivalent to the surface's tangent plane. This is shown on a variety of industrial use-case parts with both a linear UT transducer and short-range Laser distance sensors.

2. The additional perspective of an extrinsic low cost commercial RGB + depth camera can ensure optimal, rasterised traversal of the surface and also allow for collision detection and avoidance, enabling the robot to avoid obstacles, a task not possible with just the tool's frame of reference and data. The embedded camera frame also provides autonomisation of part detection and path planning with multi-scale parts when provided with

minimal prior information.

3. In combining scans taken iteratively over large structures with limited work-volume robotic arms, extrinsic embedded frames of reference are capable of aligning NDT data in situations where relative pose estimates are not available. This thesis has further shown that 3D data in the form of RGB + depth (RGB/D) camera collected point clouds can provide higher accuracy visual marker based reconstructions than traditional RGB visual artefact alignment methods. This thesis experimentally determines the optimal conditions for maximising data stitching accuracy with an Intel Realsense D415 RGB/D camera.

These contributions to knowledge are published within several journals and conference proceedings.

1. 'A novel complete-surface-finding-algorithm for online surface scanning with limited view sensors', Sensors, 2021. A. Poole, M. Sutcliffe, S.G. Pierce, A. Gachagan.

2. 'Autonomous, Digital-Twin Free Path Planning and Deployment for Robotic NDT: Introducing LPAS: Locate, Plan, Approach, Scan Using Low Cost Vision Sensors', Appl. Sci. 2022. A. Poole, M. Sutcliffe, S.G. Pierce, A. Gachagan.

3. 'Autonomous Robotic Sensing for Simultaneous Geometric and Volumetric Inspection of Free-Form Parts', Journal of Intelligent Robotic Systems, 2022. C. Mineo, D. Cerniglia, A. Poole.

4. 'Autonomous, scalable, mobile robotic-arm NDT: stitching digital twins with visual artefacts', BINDT: NDT Conference Proceedings, 2022. A. Poole, M. Sutcliffe, S.G. Pierce, A. Gachagan.

5. 'Force and sound data fusion for enhanced tap testing scanning of composites', IEEE Access, 2023. A. Poole, N. Hartley.

Bibliography

[1] Gena Johnson. Ultrasonic flaw detectors ... and beyond: a history of the discovery of the tools of nondestructive technology. 52(4):22+, Apr 2013. ISSN 03609936. URL `https://link.gale.com/apps/doc/A328422064/AONE?u=googlescholar&sid=bookmark-AONE&xid=da1345b8`. Article.

[2] David Lovejoy. *The history and basis of the magnetic particle testing method*, pages 1–12. Springer Netherlands, Dordrecht, 1993. ISBN 978-94-011-1536-0. doi: 10.1007/978-94-011-1536-0_1. URL `https://doi.org/10.1007/978-94-011-1536-0_1`.

[3] Jacques Lewiner. Paul langevin and the birth of ultrasonics. *Japanese Jour-*

nal of Applied Physics, 30(S1):5, jan 1991. doi: 10.7567/JJAPS.30S1.5. URL https://dx.doi.org/10.7567/JJAPS.30S1.5.

[4] Volker Deutsch. History of ndt-instrumentation. In *In-proceedings of the 15th WCNDT*, Rome, Oct 2000.

[5] Shuncong Zhong and Walter Nsengiyumva. *Introduction to Nondestructive Testing and Evaluation of Fiber-Reinforced Composites*, pages 61–95. Springer Nature Singapore, Singapore, 2022. ISBN 978-981-19-0848-4. doi: 10.1007/978-981-19-0848-4_2. URL https://doi.org/10.1007/978-981-19-0848-4_2.

[6] London South Bank University. Remote robotic ndt, Jan 2001. Grant from the Community Research and Development Information Service (CORDIS), grant ID: BRPR960254.

[7] A. Khalid, B. Bridge, Tariq Sattar, Sumin Chen, and Mia Rakocevic. *Non-Destructive Testing: An Eastern-Western European Perspective*, chapter The Centre for Automated and Robotic NDT at South Bank University (UK): Development of Novel Climbing Robot Technology for Non-Destructive Testing in Hazardous Environments, pages 304–320. British Institute for Non-Destructive Testing (BINDT), 01 1998.

[8] Stanford Artificial Intelligence Laboratory et al. Robotic operating system. URL https://www.ros.org.

[9] Universal Robots. Real time data exchange. URL `https://github.com/UniversalRobots/RTDE_Python_Client_Library`.

[10] ISO 9283:1998(en). Manipulating industrial robots — performance criteria and related test methods. Standard, International Organization for Standardization, Geneva, CH, Apr 1998.

[11] Olympus: Evident. Automated inspection systems, 2022. URL `https://www.olympus-ims.com/en/in-line/`.

[12] ENDITY Solutions Limited. A new era in ultrasonic wind blade inspection: e-blade by endity, 2022. URL `https://www.ndt.net/?id=27370`.

[13] Anybotics. Anymal robots inspecting petronas' offshore platform, 2021. URL `https://www.anybotics.com/anymal-robots-inspecting-petronas-offshore-platform/`.

[14] Taurob. Taurob inspector, 2020. URL `https://taurob.com/taurob-inspector/`.

Chapter 2

Review of Previous Works

2.1 Ultrasonic Testing

The primary focus of this thesis is to develop methods of deploying Ultrasonic Testing (UT) with robotic platforms. This section covers the basic principles of UT, to contextualise the robotic research which is the focus.

2.1.1 Longitudinal Wave Fronts

Conventional UT leverages the electro-mechanical properties of materials of Piezo-crystals such as quartz, that expand when an electrical current is passed through it [1]. The expansion generates a pressure (sound) wave in the neighbouring medium. Conversely, when placed under pressure a piezo-electric material generates a voltage, allowing interpretation of a received sound wave. Acting as

transducers, the UT devices allow emitters to receive a signal (Pulse-Echo) or for a signal to be passed through a medium (Through Transmission).

Sound waves expand spherically, acting as sources for secondary waves when a material boundary is reached, where a boundary is defined as a change in acoustic impedance in the medium [2]. Energy conservation causes some of the wave to be reflected back from the boundary, and some to be transferred through it. The fraction of the initial energy E_0 that is transferred through the boundary E_T is measured by the acoustic impedance of materials 1 and 2 in Fig: 2.1, Z_1 and Z_2 respectively, given as;

$$\frac{E_\mathrm{T}}{E_0} = 4\frac{Z_1 Z_2}{(Z_1 + Z_2)^2}. \tag{2.1}$$

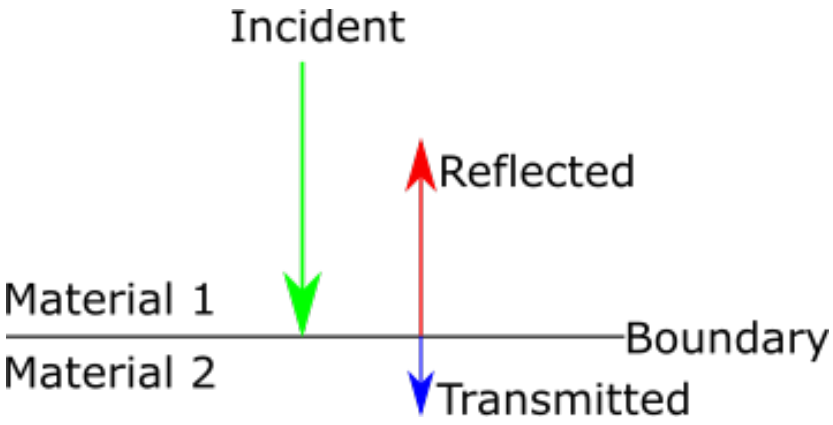

Figure 2.1: Illustration of energy transmission through media. The arrow size represent the proportion of the initial energy incident at the boundary.

The shortest time path for acoustic waves to travel from the source to each boundary point and back is taken [3] due to the wave's sphere-like (with modifica-

tions to materials with boundaries or in anistropic media) expansion. Spherical-like expansion equivalently means a wave takes the shortest time path from transducer to any other point. The velocity of sound's material dependency lead to spatially non-linear routes when there is a change in acoustic impedance such as when a boundary between materials is met, resulting in Snell's law applied to sound [4].

Irregular boundaries from the solid material to another with a lower impedance such as air [5] are caused by defects within the material, allowing their identification from UT imaging. Reflections from discontinuities with low energy absorption given by Eq: 2.1 are received by a transceiver in pulse-echo testing, or prevent transmission to the receiver in the case of through-transmission. This thesis considers area scanning with the pulse-echo technique. In this case the optimal echo response is gained when the back-wall is observed verifying the wave has passed through the material without impedance by a defect, optimally acquired when the probe is aligned to the surface's normal vector. Further, non-isotropic materials such as composites can propagate UT waves at variable speeds depending on the angle of incidence [6] complicating defect localisation when the probe is non-normal to the surface.

In realistic scenarios, UT sources are not point generators and so do not produce perfectly spherical waves initially. The UT wave-front is modelled as function with given speed c. The propagation equation within a medium of uni-

form wave-speed and without attenuation, generated by wave-source (expansions and contractions of the piezo piece) S is modelled by the pump-modified wave equation;

$$\nabla^2\phi - \frac{1}{c^2}\frac{\partial^2\phi}{\partial t^2} = S(\omega, x). \tag{2.2a}$$

Solutions to this equation are in the form of Greens functions G [7], integral solutions to linear partial differential equations. Greens functions propagating the wave-front from the transducer's face x at a given time t to another $\hat{x}, \hat{t}$;

$$\phi\left(\hat{x}, \hat{t}\right) = \int\int G(\hat{x} - x, \hat{t} - t)S(x, t)dxdt. \tag{2.2b}$$

In three dimensions, the generalised solutions are ideally placed within the complex frequency domain ω;

$$G(x, \omega) = \frac{1}{4\pi|x|}e^{-i\omega|x|/c}, \tag{2.2c}$$

Attenuation of a realistic waveform due to absorption, scattering, refraction, or diffraction has a non-trivial effect on the amplitude of a real wave-front [8], with beam divergence considered in Eq: 2.2c. The realistic wave-front's total amplitude A is modified with a complex wave-number induced in the Green's function Eq: 2.2c, resulting in exponential decay from the initial amplitude A_0, reliant on

distance d from the transducer, and experimentally determined constant α;

$$A(d,\omega) \sim A_0 \frac{e^{-\alpha d\omega}}{d}. \tag{2.2d}$$

An implication of Eq: 2.2d is that high frequency wave fronts decay at a higher exponential rate than lower frequencies, resulting in lower signal to noise ratios. A probe's frequency is chosen then for both the specific attenuation constant of the material inspected, and the imaging accuracy required with an enhancement of one leading to a trade off with the other. Probes cannot be applied directly to parts, and require a liquid medium to generate wave fronts within. Air has a very high attenuation rate which, except for very low frequency probes such as used in Air Coupled Ultrasonic Testing (ACUT), requires a coupling media such as water or gel between the probe and the part. ACUT probes typically operate within KHz frequency ranges, whereas the most common and accurate water or gel applied probes are in the order of MHz frequency ranges, providing greater defect location accuracy. Additionally, while it does not require a coupling medium that could be a hindrence to autonomous on-site inspections, ACUT is further limited to thin materials due to its low penetrative range [9].

Since wave-speed within an isotropic medium is constant for sound, the relationship between wavelength and frequency is crucial in scanning resolution. Lower frequencies, though their amplitude is carried further through the media,

have a reduced resolution due to their longer wavelengths that can be key when defects are masked by other boundaries such as the surface.

The best transducer frequency is dependant on the application due to the physical laws governing UT propagation. The choice of accurate near-surface imaging or imaging at depth has to be made for each application. Subsequent applications of differing frequency probes may be necessary for highly critical components. Requirement of an application medium for UT has led to the development of various transmission methods, from highly controlled laboratory-suited media, to techniques that require less control but place more requirements on the robotic coupling that are useful for on-site inspections. These are explored in the next section, providing context for the choice of probe used in this thesis.

2.1.2 Robot Deployed UT: Coupling methods

Standard coupling methods applied by human operators such as ultrasonic gel are transferable to robotic deployments, though several coupling methods are not reciprocally deployed. Methods such as using jets of water with high stand off distances from the surface require high precision deployment to ensure surface-normal alignment. This section introduces robot-specific coupling methods, while the platforms are covered later.

Immersion testing, one of the earliest coupling methods applied with robotic platforms, submerges the part within water to guarantee that the transducer al-

ways has sufficient coupling to the part, as shown in Fig: 2.2. In collecting UT data, the key drawback is wave-scatter within the water-medium. Since UT expands spherically, curved and complex components can be misaligned when the UT-probe to part stand off is large, requiring high accuracy and near-contact deployment. From the robotic perspective, while this guarantees constant coupling, water degradation to transducers and robots can cause a host of issues. The application of highly specialised tools to repeatable scanning procedures is necessary. Flexible deployment of robotised NDT must utilise more complex coupling methods, in order to assure the alignment of the probe to the surface's normal to within acceptable ranges.

Figure 2.2: Immersion testing of a component. By submerging the component, the UT sensor, as long as it is appropriately placed and oriented, will be able to test the part.

Commonly within industry, robotic systems are equipped with water jet-Phased Array UT (jet-PAUT) equipment. Water pumped through a machined tool (or where parts of varying geometries are inspected, 3D-printed) housing the UT transceiver acts as a couplant with the surface. Laminar flow is induced by a honeycomb structure, minimising turbulence so that UT waves may propagate in approximately straight lines, minimising noise [10]. Jet-PAUT systems require a host of conditions to be met for successful and safe deployment. Bacterial filtering of the water reservoirs and electrical device protection are paramount to ensure health and safety. The pipes required to convey water to the tool introduces complications such entanglement. These conditions render this deployment method only suitable for static-cell deployment. In addition, while some industrial robots such as the Quantec range manufactured by KUKA are waterproof with a rating of IP 65 [11], other platforms require different UT application and coupling methods to ensure their safety.

Contact probes offer an alternative, containing a two or three-layer coupling structure. Roller probes are commonly used due to their versatility in component testing. The outer layer rotates around a central pivot, with a water coupling medium between the transducer and flexible outer layer. The outer-probe is commonly coupled with a thin layer of lubrication so as to guarantee signal transfer to the part. While this does introduce some safety concerns regarding wetting the robot the quantity of lubrication required is significantly reduced, reducing

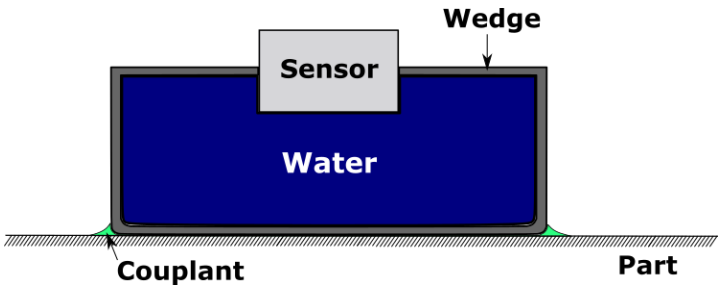

Figure 2.3: Cross-section of a Conformable Wedge Probe, with a layer of water sheathed within a wedge that has a well-matched speed of sound. There is a mixture of solid and couplant contact between the probe and part, however the additional scattering due to differing contact-offset is negligible when a force is applied.

risk caused by proximity to unprotected/unrated electronic equipment.

Alternatively, the Conformable Wedge Probe (CWP) is similarly designed. However, instead of a rolling outer layer the wedge is mostly planar, sliding over the surface. Allowed to flex when in contact with the part, this probe allows greater coverage of curved components as the outer couplant layer conforms to the surface. A schematic of the probe in contact with a part is shown in Fig:2.3.

While there are 3 coupling mediums from transducer to the surface, the wedge's refraction index is matched well to the water layer, reducing the number of effective mediums to two. Since the more viscous water-soluble UT couplant can be used, risk of water-damage is reduced and may be deployed by a wider array of platforms with lower waterproof ratings. The main disadvantage of the wedge probe is, an operator is required to apply couplant to the exterior of parts before it can be applied, instead of the simultaneous and automated appliance with a jet-PAUT, or the guaranteed appliance in immersion testing. Since this is

a minimal cost in operator effort and reduces the risk to electronic components, it is acceptable in comparison when considering flexible deployment with a range of non water-proof robotic platforms.

Investigating the flexible and safe deployment of UT methods, the CWP approach is the most suitable for onsite testing since it does not require reservoirs for coupling and can be deployed within onsite environments with potentially low IP-rated equipment for other tasks in the nearby vicinity. Pulse echo testing is chosen over through-transmission as the imaging method, removing the necessity for cooperative-robot positioning in on-site and cluttered environments where accurate robot-robot relative position calibration would be inaccurate, if the positioning either side of the structures of interest were possible at all. While CWP deployed UT is chosen, alternate NDT imaging methods are available and are more suited to given tasks.

2.1.3 Other Robot Deployed NDT Sensors

UT is applicable to a wide range of materials with ongoing development investigating novel imaging techniques within non-isotropic materials, small near-surface defects. Alternatives with greater accuracy, specialisation to specific defects, and with fewer restrictions on deployment method and medium are available.

Thermal imaging images sub-surface defects within composite components by heating the part to then measure the black-body radiation of the surface [12, 13],

without additional coupling media. The wide sensor aperture of the thermal camera is capable of a larger stand off than UT. While this is an attractive technology, it is also in its infancy with ongoing research into its effective data interpretation and deployment [14, 15]. While suited to near-surface defects, its penetrative depth is hindered by thermal absorption and transmission rates.

Radiography is another alternative, allowing the user to see a range of defects with high repeatability [16]. However this method is a health risk to human operators preventing its use in human-robot collaborative and on-site environments. The requirement for a source-detector dual-robot set up further complicates deployments as the reconstruction accuracy of Computed Tomography (CT) scans is numerically incapable of detailed reconstructions without tens of microns of precision. While future deployments may be able to correct robotic error [17], the risk to human safety still precludes it from on-site deployments.

Microwave testing (Microwave Imaging - MI), with underlying physics and transmission techniques similar to UT, is a favoured technique for dielectric composites such as CFRP since it is both low risk and responsive to the ply-layups without the significant wave-speed variations of ultrasound depending on incidence angle [18]. In enabling pulse-echo MI through these media, a coating of material with a low electromagnetic wave-speed such as metal is required to reflect the microwave signal, similar to the function of an air interface in back-wall UT inspections. While scanning metal-backed structures such as bound pipes

or with cooperative robots, this is highly effective, it is not suited for on-site single-robot inspection techniques.

2.1.4 Tap Testing

While Ultrasound uses pressure wave frequencies significantly higher than the audible range, Tap testing (TT) is traditionally an audible sonic method that has evolved from its early usage in NDT. Modern applications involve an instrumented tapping force applied to a surface, with skilled operators detecting changes in a material's thickness through the resultant sound or impact-force contact duration, identifying defects as aberrations in the expected signal of either contact force or resulting sound [19]. UT is favoured when applied to isotropic materials or where the material properties allow a low signal-to-noise ratio. However in materials such as concrete or thick composites, isotropy of the material is such that measurements become unreliable due to signal dispersal. Near-surface defects can also be difficult to detect with UT when the defect responses are masked by front wall reflections or are in the near-field of the transducer. Tap testing is sought out in application to these areas due to its relatively high probability of detection of defects within complex composites using the sonic response, and sensitivity to surface level defects with its force response. There are significant disadvantages of TT compared to UT, force and sound based methods primarily require and recognise local surface resonance with the instrumented tap, reduc-

ing defect detection accuracy as non-local resonant nodes are induced and by requiring a larger defect size than UT in order to be identified.

Its application while popular in certain areas is less prevalent in robotic deployments, however its couplant-free contact transmission and low power demands make it a plausible candidate technology for on-site inspections of composites, similarly to how it was applied to remote UAV inspection of concrete elsewhere [20]. It is also considered for on-site inspections in Chapter: 6 for its penetrative depth for composites in comparison with traditional UT. UT is primarily considered over TT in this thesis since it is not limited by surface elasticity as TT [21].

2.2 Robotised UT Area Scanning

Area scanning of materials is common practice in many industries that require or seek to acquire high quality product assurances. Critical components will undergo a scan of their surface, to ensure no defects are embedded either during manufacturing or in service.

Repetitive, lengthy scanning processes of large parts with relatively small UT sensors can create the conditions for human error and restricts the skilled operators working time and focus primarily to deployment. Starting in the late 1980's, robotic arm deployment has become the prevalent answer [22]. Their advantages are a high repeatability in line with ISO 9283 [23], with many industrial robots

also capable of sub-mm accuracy. From then, their use has become widespread. In robotic arm deployment, the work-flow of robotic UT deployment can generally be expressed as the flow-chart in Fig:2.4.

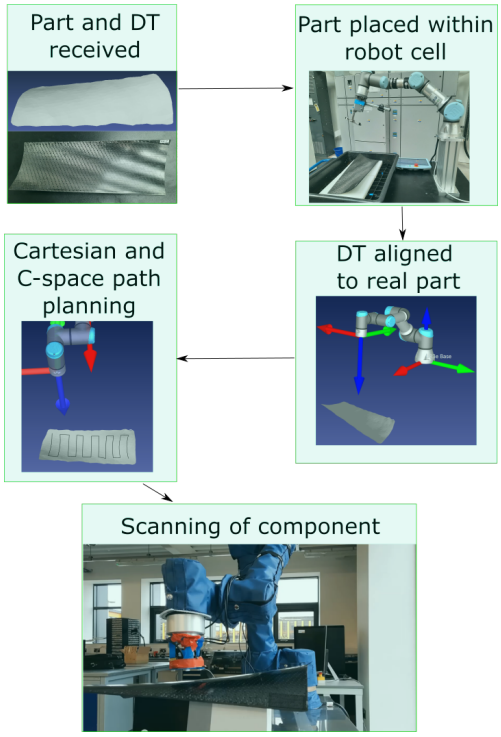

Figure 2.4: Robotic-cell scanning process. The majority of time cost is in the digital twin/real-part alignment procedure. Tool calibration can also present significant time delays.

This thesis is written within an industrial setting that has seen a twin-KUKA KR16 robot jet-PAUT system developed in 2014 [24]. Enabling through transmission and pulse-echo jet-PAUT testing, a custom toolbox was developed to plan paths over digital geometric representations of parts, pair them with a robotic simulation, and then deploy them via the teach pendant. Several large-scale robotic systems have been added to this setting's inventory in the years since,

Figure 2.5: TWI's table and track assisted cooperating KUKA KR120 work-cell. The table in the foreground is capable of full revolutions, with the integrated track mounts extending the effective working range of the KUKAs to the entire cell.

including a multi-axis robotic cell incorporating a multi-link rotary table and two track-based KR120 robots seen in Fig: 2.5. The advantage of this set-up is that the inspection volume has increased from $3000mm \times 1000mm \times 1000mm$ to a $1000mm \times 4000mm \times 4000mm$, in addition to the 3 additional degrees of robotic freedom.

Re-use of scan paths and custom built rigs within near-laboratory conditions are a significant advantage considering repetitive scans of parts with little variation. Reciprocally static UT deployments, specifically development of immersion and jet-PAUT deployment methods have accelerated in the past few decades. Static-arm deployments relying on a simple master-follower architecture are the chief components of industrial UT with jet-PAUT imaging [25, 26, 27]. Progres-

sion towards larger work-cell deployments, such as linear-track mounted robots allow greater work-volumes, and multiple scale scans with the same or similar accuracy. Cooperative robotic cells have become ubiquitous since their introduction, and a full list near impossible. Due to this, both the context and primary focus of this thesis is placed on this setting's systems.

2.2.1 Collaborative Robots

The research laboratory contains two UR3e's and one UR10e collaborative-robots (Cobots) from Universal Robots. With work-volumes of $500mm$ and $1300mm$ respectively, the current robotic scanning work-flow restricts the parts they are able to scan significantly. As non-waterproof platforms only certified to IP 54 [28], no robot from the UR range cannot mount the jet-PAUT system, and require extreme restrictions when applying immersion testing. However, their built in safety features make up for the lost ability to deploy certain UT coupling methods. While universal robot platforms are not water resistant, they are not fixed in place, allowing them to be either static or placed on a mobile base. Accuracy of the increased work-volume of the KUKA cell places it well for highly repeatable large-volume scanning. However, in terms of on-site deployments and scans of parts of varying dimensions, the scalable working envelope of the UR platform presents greater potential.

Whereas traditional industrial robots seek to maximise the metrics of repeata-

bility and payload, collaborative robotic arms include accurate embedded force torque sensors that enable their deployment alongside human operators with minimal risk. Similarly to industrial robotic control methods, the UR platforms can be programmed with both a teach-pendant script and external control.

2.2.2 Alternate Robotic Platforms

Specialised tasks within limited or hazardous environments, such as wind-turbine blade or internal pipe scanning require robots such as crawlers or UAVs to access their geometries.

Crawler vehicles and UAVs are commonly applied to specific geometries in order to fulfill specialised tasks such as bridge scanning [29], tank assessments [30] and other large-structure scanning [31]. The choice in deployment is between dexterous, accurate motion with robotic arms, and the practically unlimited work-spaces of mobile platforms unencumbered by heavy robotic arm controller cabinets. While solutions combining the two have been sought since the late 1990's [32], current robotic arm path planning methods covered in Section: 2.4.6 severely limit the application of mobile robotic arms, the large majority of which is application to area-scanning of well known environments.

2.2.3 Robotics in NDT: Special Considerations

Specific to NDT, robotic platforms need to meet a stringent set of criteria in order to both meet the standards required of NDT, and ensure the safety of human operators and parts.

1. In the case of through-transmission or pulse-echo inspections, alignment of the ultrasonic tool to the part's normal vector is critical to ensure accurate identification of defects [33]. For conformable wedge probes, the alignment issue is critical, since misalignment produces an air/wedge boundary, preventing the wave's transmission to the part, in addition to the surface/wedge reflection producing undesirable double reflections that mask signals within the interior of the part.

2. Robotic platforms need to meet or exceed the defect-placement accuracy of a human operator. Replacing parts, or sections of parts such as train chassis that are defective require accurate knowledge of the defect's placement. This condition is relaxed in sectors such as remanufacturing and mould manufacturing. In the former, the part may be deemed more expensive to fix than to be bought new and would simply be thrown out once a threshold for defect size or quantity is reached. In the latter, once a considerable defect such as delamination is detected, the entire part is rendered redundant by virtue of the structure of the material. Importantly, the path-accuracy for

UT is only necessary for certain applications such as through transmission, but the defect-mapping accuracy is critical to NDT's position in informing the (re)manufacturing process.

3. The scanning path taken by the robot needs to ensure total coverage of the part or section of the part considered. For pre-planned paths of complex paths, a misalignment of the part and generated path can lead to missed sections of the surface resulting in an incomplete scan. For more flexible routines, an autonomous path planning module would require either a generated path to ensure complete coverage, or define completeness of a part's coverage.

4. The robotic platform cannot collide with the part, or any human operators in the work-cell. Particularly for parts such as Carbon-Fibre-Reinforced-Polymers (CFRP) components, low energy surface impact damage has a critical effect on structural integrity [34]. In the past, this has been guaranteed through a multi-step process;

   (a) Accurate positioning of the part relative to the robot so the part's digital twin is closely aligned to the actual part's pose,

   (b) simulated path planning to ensure the robot and part do not collide,

   (c) alignment of the robot near the initial robotic configuration.

   For jet-PAUT, the potential for wire and hose entanglement complicate

the path planning further, requiring additional iterations of this process for expert operators to path plan. While some error can be expected in Step: 4a, corrections from a trial-scan can be provided from UT feedback data [35] further satisfying Condition: 2. For more flexible robotic operations seeking automatic and autonomous control, software controls are required to facilitate safe deployment to replace operator intervention.

Meeting the goals of this thesis require satisfying these conditions to ensure the systems can be deployed within the industrial setting and meet the standards of ISO 16810:2012 [36]. The standards for robotic ultrasonic testing are under review in ISO/DIS 24647 and are not available at the time of writing this thesis. Despite this, the author has composed this list as a minimal and non-exhaustive set of requirements for robotised UT as a guide for later discussions.

2.3 NDT 4.0

Combining autonomy, prior knowledge, and advanced algorithmic control and inference of NDT inspection systems, NDT 4.0 prioritises a Digital-Representation (DR) perspective in long term structural health assessments [37]. DRs in this context cover multiple digitised perspectives including Cartesian geometric models of the work-space and part, statistical models of the part's long term health, and representative models of the robot's joint-space.

The NDT 4.0 model applied to robotics has seen an increase in autonomy with increased computing power. Flexible robotic platforms are explored in Section: 2.5.2. For mass and repeatably manufactured products, geometric Digital Representation (DR) model creation from NDT data is intensely investigated. While for the industries mentioned in Section: 2.3.1, obtaining a DR from pre-existing non-digitised or variable geometry structures requires flexibility coupled to the NDT 4.0 principles of automation and data exploitation and inference from multiple work-space perspectives, which is also explored in Section: 2.4.

This thesis focuses on the generation of DTs through multiple geometric perspectives in order to complement industry 4.0. The platform and deployment methods are considered for on-site scanning of unknown surfaces, and are not limited to manufacturing environments. The algorithms produced can be applied to large, unstructured, or otherwise unknown environments in order to construct accurate DTs of critical parts or structures within the environment.

2.3.1 Target Industries

Both high-volume industries that traditionally employ NDT such as aerospace, and newcomers to NDT such as remanufacturing are seeking to move in favour of the Industry 4.0 target.

Within remanufacturing the prevalence of legacy parts and third-party remanufacturers without access to digital twins has often required reverse engineering

of components to satisfy demand for components. While remanufacturing is highlighted as one of the key growth sectors in order to reduce the carbon footprint of specific domestic and industrial goods sectors [38], the high costs of limited labour render the process uneconomical for many industries [39]. The remanufacturing sector is highlighted as a chief beneficiary of future robotisation in order to increase competition with traditional manufacturing processes [40].

Viability determined by autonomous robotised visual inspection is faced by the challenges of traditionally requiring accurate structural and geometric DTs [41]. While research in the wider literature targets reverse engineering of legacy parts [42], these focus primarily on visual data and not robotisation of contact inspection processes. While UT is not traditionally a part of the remanufacturing process, the data provided from sub-surface measurements have a positive impact on the expected life-cycle of remanufactured products [43]. To enable robotic inspections, reverse engineering to produce a geometric DR is necessary and is at the forefront of robotic NDT 4.0 as discussed in Section: 2.3.

In the case of industries such as automotive or aerospace manufacturing that contain high-volumes, the search for higher productivity is driving the move towards Industry 4.0.

Mould manufacturing is used to produce modern light-weight parts within the aerospace sector, which may with some manufacturing processes result in non-critically damage such as warping [44]. Though these parts do not match their

digital-twins, they are considered acceptable for industrial applications. Flexible robotic path planning procedures are necessary to scan the non-consistent surface variations these manufacturing artefacts produce.

The focal industry of this thesis and the one that provides the supplementary industrial use-case are consumers of boats. The Royal National Lifeboat Institute (RNLI) is a long-term partner of TWI, requiring on-site scanning of dry-docked boats. Currently, a single inspection can take an operator 36 hours of manual-scanning resulting in fatigue. The geometric DTs of hulls are currently unavailable, with noisy LIDAR readings providing the best solution. The aim of this thesis is in part to provide an autonomous robotic solution that is capable of scanning these structures with no digital twin. An example comparing the scale of the front of the hull with a UR10e robot is shown in Fig: 2.6.

2.4 Work-Space Representations

The workflow represented in Fig: 2.4 takes the Cartesian perspective for path planning in creating raster-paths. Then once the geometric DR is aligned with the real-part in the work-space, the robotic joint-coordinate (configuration/C-space) representation is derived. Historic use of DTs has allowed the selection of two necessary work-space representation, however they are not sufficient when the DR data available is noisy or incomplete. Additional extrinsic perspectives are already in use to enable flexibility, as explored further in Section: 2.4.3,

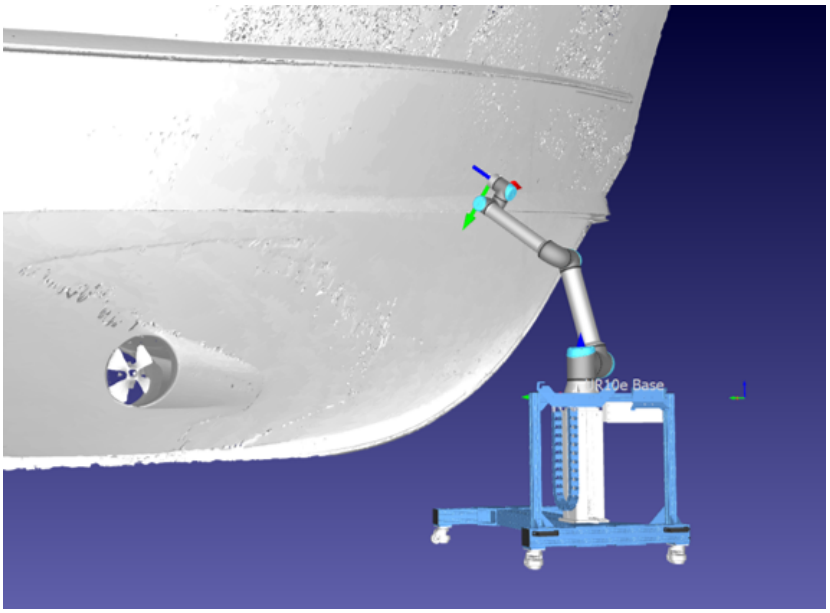

Figure 2.6: RoboDK simulation of a trolley-mounted UR10e next to an RNLI hull. The robot will require several iterative scans to cover the entire boat, with no digital twin currently available of the hull. The shown model was collected with a LIDAR camera, unable to meet the requisite accuracy for an on-site contact UT scan and with significant holes that can be seen speckling the surface.

and in calibration of frames of reference in Section: 2.4.2. This section reviews different perspectives of the work-space, their current use in traditional cell-based NDT and wider robotics, ultimately culminating with their combined use in the forefront of flexible NDT inspections.

2.4.1 Cartesian Space

Assuming a world-frame origin and an orientation, oriented positions within Cartesian space are represented by matrix elements of the non-commutative Special Euclidean-3 Lie Group $\mathbb{SE}(3)$ [45]. The $\mathbb{SE}(3)$ group is a composition of the Special Orthogonal Lie group $SO(3)$ of rotations, and translation Lie Group $\mathbb{R}^3$.

Each element M can be represented with a 3×3 rotation matrix R and 3×1 translation vector t;

$$M = \begin{bmatrix} R & t \\ 0 & 1 \end{bmatrix}. \tag{2.3}$$

$\mathbb{SE}(3)$ is additionally equipped with a metric;

$$d(M_1, M_2) = |\log\left(R_1^T R_2\right)| + |t_1 - t_2|_2, \tag{2.4}$$

where $|\cdot|_2$ is the standard Euclidean-2 metric, combining the metric of Special Orthogonal 3 matrices ($SO(3)$) [46] and the standard distance metric. More importantly, $\mathbb{SE}(3)$ is also represented as a Lie-algebra $\mathfrak{se}(3)$ structure of finite elements. For each element $g \in \mathfrak{se}(3)$, the exponential is expressed as;

$$\exp(g) = \sum_{n=0}^{\infty} \frac{1}{n!} g^n. \tag{2.5}$$

This representation is particularly useful in tool calibrations. In solving the problem $AX = XB$ where $A, B, X \in \mathbb{SE}(3)$, the solution by [47] utilises the Lie-algebra components of the known A, B to solve sequentially for X first in rotation then translation elements, also minimising the covariance assuming uniformly noisy data.

For rotations, the exponential is used to express using the Rodrigues rotation formula [48]. A rotation R given by the exponential of the rotation vector $g \in$

$\mathfrak{so}(3)$;

$$R = \exp(g) = I + \sin(\theta)[h] + (1 - \cos(\theta))[h]^2, \tag{2.6a}$$

where I is the 3×3 identity, $\theta = |g|$ and $h = g/\theta$. The $[h]$ operator is;

$$[h] = \begin{bmatrix} 0 & -h_z & h_y \\ h_z & 0 & -h_x \\ -h_y & h_x & 0 \end{bmatrix}. \tag{2.6b}$$

The inversion of Eq: 2.6a;

$$\theta = \cos^{-1}\left(\frac{\text{trace}(R) - 1}{2}\right). \tag{2.6c}$$

The angle of rotation requires only one trigonometric inversion, the other operations are addition and one division by 2. Retrieval of the full rotation vector is;

$$g = \frac{1}{2\sin(\theta)} \begin{bmatrix} R_{21} - R_{12} \\ R_{02} - R_{20} \\ R_{10} - R_{01} \end{bmatrix}. \tag{2.6d}$$

Although there are several alternate ways of expressing $\mathbb{SE}(3)$, the Lie algebraic is chosen as it is common in robotics discourse, utilised as the non-essential-singularity free Jacobian of the end effector [49], in solving hand-eye calibration as above, and as the coordinate system of the Universal Robotics series [50]. For

system integration across software packages and platforms, it is both one of the most commonly used, and the easiest to convert between matrix and vector notations. As the differential lie algebra of the group, features such as gradient descent are well understood and utilised [51].

Several robotics manufacturers have chosen the Euler-rotation representation instead, to make the rotations easier to understand. Euler-angles represent rotations as around a choice of three of x, y, z axes, with at least two unique axes. Euler angles, also known as 'roll', 'pitch', 'yaw' are traditionally used throughout manufacturing, due to their easy use by humans. However, they suffer a host of issues such as the gimbal lock (non-essential singularities), and difficulty in angle composition [52].

Quaternions are an effective representation providing descriptions of rotations as the lie algebra. The choice of all-round representation becomes one of convenience, and $\mathfrak{se}(3)$ is chosen.

2.4.2 Projective Space Representation and Machine Vision

Cameras lenses project the space in front of the lens given by a frustum displayed in Fig:2.7 to a plane, $P : V \in \mathbb{R}^3 \longrightarrow \Pi \in \mathbb{R}^2$.

Locating an object for scanning within a sequence of 2D frames can enable relative pose estimation, part localisation, or digital twin constructions using well investigated techniques from the topic of Machine Vision. Machine Vision pro-

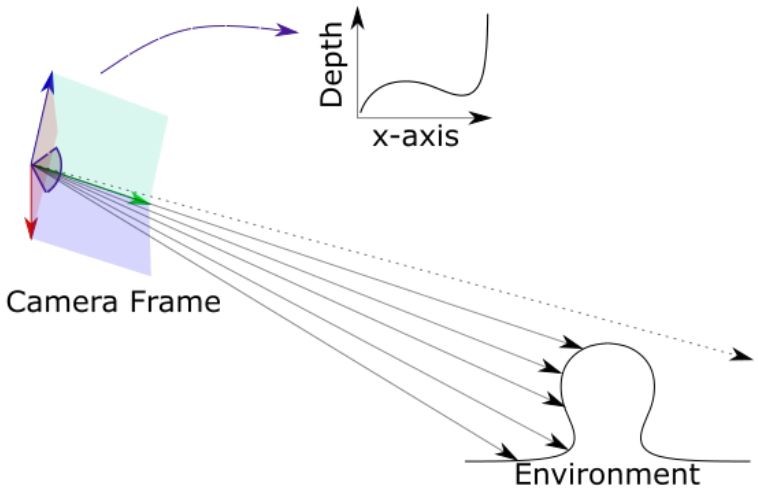

Figure 2.7: Camera, within its own frame of reference, viewing a part. When available the depth value of each pixel whose view is seen as rays, is used with the pixel's position to calculate the 3D position of points on the surface. The frustum's total view is determined by the range of the spherical arc at the focal point, placed at the origin of the frame of reference.

grams and software such as OpenCV [53] are well used and finely optimised, used primarily to extract patterns from a single or multiple 2D projected images. Single image machine vision applications seek to extract a known geometric primitive from an image, such as lines, corners or circles. Hough transforms seek geometric objects such as lines or circles, applying a transformation of the 2D image space to one that better displays the patterns sought, polling the resultant space to find the best fit candidates given prior likelihood bounds. Machine Vision techniques applied to visual data streamed over time is primarily aimed at finding common points within subsequent images for either relative pose estimation or environmental mapping, a set of techniques known as Visual Odometry (VO). Applied

to pose estimation and mapping with sequences of images, Hough transforms are useful in providing environmental information from a sequence of 2D frames, provided the environment is feature rich, commonly applied to autonomous driving [54]. Alternatively, gradient methods convert images to gray-scale maps from which the first or second order pixel intensity gradient is calculated and used to detect boundaries or corners. This is particularly useful in corner detection [55], selecting complex object boundaries [56, 57], and camera calibration routines [58]. Differential edge based detection is applicable to surfaces of greater range and unknown geometry, but may require results of lower accuracy for image segmentation as morphological operations are needed to ensure boundary closure.

While traditional applications aim to estimate the relative pose of the platform between images, when the pose is known with relative accuracy, the environment can be mapped. Optical flow techniques are enabled by high frequency (relative to motion speed) monocular camera capture methods, assuming that the image intensity is a locally conserved quantity between frames and from this determining the relative velocity of the camera with the environment. Low sampling frequency or dropped frames reduces motion estimation accuracy, feature based methods becoming preferable since they require less image-image overlap [59]. Similarly to optical flow, the Scale Invariant Feature Transform (SIFT) or Speeded Up Robust Features (SURF) algorithms locate and map features through a differential intensity metric, though computed for each pixel within a three dimensional

state-space manifold whose dimensions are the x and y pixel coordinates coupled to an additional Gaussian smoothing parameter. Visual artefacts recognised and matched between multiple frames paired with the camera poses are used to triangulate the artefact's absolute 3D position. Applications of VO within robotised NDT include part reconstruction and environmental mapping.

An early study into monocular VO applied within NDT showed severe limiting factors such as reflectivity [60], since accurate maps of defects could not necessarily be drawn breaching Condition: 2. Further work targeted at remanufacturing demonstrated that a non-reflective part with significant visual artefacts could be reconstructed with a standard deviation of up to $2.77mm$ [61]. While this generates accurate and fully-robotised reconstructions, the proof of concept still suffers from the issues inherent with reflective parts. Further, the necessary image-image overlap is up to 80%, requiring vast quantities of information coupled to a high tool-calibration threshold.

In specific applications, visual methods have succeeded in online corrections to path planning challenges. While the reconstructed multi-planar projection perspective is useful in reconstructing non-reflective parts of high artefact density, the application to reflective or visually uniform surfaces is severely limited to pre-known path placement. Further, key to all of these methods is the need for operator intervention, planning initial collision-free paths covering the surface for the camera to enable surface reconstruction, or during the scan in guiding the

preferred rasterisation strategy over the reconstructed part.

2.4.3 Embedded Spaces

Complete-coverage trajectories over complex components are studied in full profiling procedures, spray painting parts, and machining of parts to a high grade. The complexity, interaction, and scale of both the component and sensor informs the optimised application and path over the surface.

In some wide-aperture/small part scanning tasks such as visual inspections, the number of poses required for full coverage is relatively small, enabling optimisation of information-gain metrics from a set of discrete positions. Coverage optimisation can be selected for static photogrammetric rigs [62], robotically-deployed [63], or drone-based [64] to optimise the information gain from each position to minimise the required scan-time and required reconstruction-data quantity.

Surface and tool interaction for limited aperture sensors require a simplified space to maximise computational efficiency. Particularly for sub-surface NDT sensors that require a high-tolerance for surface-tool alignment and have apertures in the order of centimetres, discrete pose optimisation is not practical. An answer is to introduce functional approximations of the surfaces (for example polynomial approximations or Fourier transforms) in order to reduce the number of variables, from discrete poses to differentiable functional vector spaces representing the surface as embedded spaces.

Embedded surfaces within $\mathbb{R}^3$ are described by an atlas of continuous and differentiable functions $F_i : \mathbb{R}^2 \longrightarrow \mathbb{R}^3$. Parts such as moulded CFRP parts are often produced with splined representations in Computer Aided Design (CAD) software [65], allowing such a representation. Welded, printed, or machined parts cannot necessarily be represented by a single map, and are at best given by a set of piece-wise functions.

The success of many embedded surface planning regimes relies on first and second order derivatives of the surface. Given a functional map $F : \mathbb{R}^2 \longrightarrow \mathbb{R}^3$, the first fundamental form I is defined as the correlation of derivatives along the cardinal differential directions of $F(u, v)$;

$$I = \begin{bmatrix} \partial_u F \cdot \partial_v F & \partial_u F \cdot \partial_v F \\ \partial_v F \cdot \partial_u F & \partial_v F \cdot \partial_v F \end{bmatrix}. \tag{2.7}$$

The map acts on the tangent space of F, $T_{u,v}F$ lowering the dimensionality of spatial calculations from three to two. Curve length on the surface of F is given;

For each location, the parameterisations of F can be chosen so that I is diagonal. Orthonormalising the directions $\partial_{u/v}F$ using the Gram-Schmidt orthonormalisation process [66] and subsequent rotation identifies the local tangent plane to the tool's reference frame. The Tool's frame of reference is commonly used in robotic jogging tasks in order to traverse flat surfaces not aligned to the cardinal Cartesian space coordinate directions. Non-differentiable points along the em-

bedded surface may not allow partial derivatives to be computed, however as is shown in Chapter: 3 realistic tool-flange perspectives acting as surface-smoothing agents allows us to ignore these.

In scanning surfaces, ensuring the scan intervals are evenly spaced along the surface is important, which the first fundamental form provides. It defines a differential scale, and can be integrated to find the length of curves $F(c_u(t), c_v(t))$ bound to the surface;

$$L(c)[T] = \int_0^T \sqrt{\begin{bmatrix} \frac{dc_u}{dt} \\ \\ \frac{dc_v}{dt} \end{bmatrix} I \begin{bmatrix} \frac{dc_u}{dt} \\ \\ \frac{dc_v}{dt} \end{bmatrix}} dt. \tag{2.8}$$

However, this perspective ignores the ambient space used to define completeness of surface-maps and how far a curve has travelled within it, also known as arc-length. This can be found by measuring the curvature of the part when there is no prior knowledge, allowing down-sampling of the space while ensuring preservation of detail. The curvature described by the second fundamental form is necessary to define cartographic completeness and is explored in Chapter: 3 as requisite knowledge for an autonomous surface-mapping algorithm.

2.4.4 Extrinsic Frames of Reference

In addition to the tool, other frames of reference may be embedded within Cartesian space. They are useful in position-agnostic calibration procedures, allowing

the operator to reference the tool or world-frame through multi-pose procedures that are invariant under transformations within the work-space. One dimensional artefacts are utilised for spiking procedures for 1D sensors such as laser-distance sensors. 2D artefacts such as chess-boards are utilised to calibrate the 6D camera-tool matrix. World-frame calibrations also rely on additional coordinate systems free from the robot's. The three-point calibration method for robot-to-part alignment uses this perspective to enable the operator to specify a tangent plane on the digital-twin and the part for virtual alignment [67]. Robotic frames of reference may also be aligned to a work-piece based on visual markers with known geometries [68].

Visual map building algorithms that enable robotic perception use many zero-dimensional reference points to either estimate their own relative positioning through ego-motion estimation programs [69], or to build world maps through Structure from Motion (SfM) algorithms using their own known relative motion or a given depth scale coupled to an image-to-image feature matching algorithm [70, 71]. Incorporating prior information such as known geometric shapes and scales enables features of interest to be interpreted as extrinsic frames of reference. Prior information and a well controlled environment coupled to a wide aperture has made 2D visual inspections the most investigated method of in-hangar inspections of aircraft with automated drone systems [72]. Correlating single or multiple features, such as circles or lines found using Hough transforms

[73], to known 3D counterparts can reduce the number of artefacts necessary for full relative positioning by incorporating prior information, used in methods explored further in Chapter: 4. Additional 2D sensor perspectives can also improve relative positioning accuracy.

Structured light cameras and stereoscopic systems utilise two or more well calibrated cameras to determine distance of objects by correlating the 2D projection of 3D space onto the lens(es) of the cameras [74, 75]. Collections of zero-dimensional artefacts in 3D space are correlated through feature recognition between image frames in order to generate relative motion estimates of the robotic platform between images. Where the points may be affected by noise, estimated transformations are refined through processes such as Iterative-Closest-Point (ICP) gradient-based methods [76]. Primarily in these methods, the global alignment perspective that features noise is complemented by local optimisation processes.

Within noisy or dynamic environments, or in scanning visually isotropic parts seen in Section: 2.3.1, there are insufficient visual artefacts to form a passive extrinsic frame of reference in order to reconstruct the robot's relative pose between scans. Within robotic manufacturing processes, artificial visual artefacts such as Quick Response (QR) codes have been used extensively to align the digitised representation of the robot to the work-space. Autonomous localisation is complemented with artificial markers in industrial and warehouse environments,

removing the significant visual symmetries of these environments. Unique reference markers also provide task-information symbolically represented [68], and route-guides to optimise robotic navigation [77], enabling the robot to have a richer perception of its environment than that which is available with just visual data. Aspects of human-collaborative Augmented-Reality (AR) assisted NDT apply artificial reference markers in visually isotropic environments for this reason [78].

Extrinsic frames of reference, particularly visually derived frames are applied throughout the literature in calibration and localisation procedures, with data interpretation and localisation relative to artificial frames already benefiting human-assisted NDT. Whereas previous sections looked at localised points given within a specific robotic world-frame, extrinsic frames allow data to be re-localised if the relative pose of the robot and environment is changed. For NDT 4.0 this is particularly important, assisting in the long term health monitoring of goods through accurate data positioning with respect to an easily digitally recognised frame. While the Cartesian representations so far explored real-time spatial interpretations, the extrinsic frames from the environment and artificial markers relate DTs to their real-world counterparts. Representations of the workspace are not all Cartesian, and robotic spaces describing the equivalent compact Cartesian space are a completely different topology to the $\mathbb{SE}(3)$ group. The next section will explore the space of robotic motion, its relationship with Cartesian

space, and the limitations of the kinematic map between both spaces.

2.4.5 Configuration Space

Rotational six-axis (6R) jointed robots are used within this thesis, though a number of other joint types and numbered robots exist. The tool's pose is manipulated by rotating their joints. Joint positions are related to the robot's end effector through forward-kinematic equations $P = F(\theta)$ by the Denavit-Hartenberg parameters [79]. The $\mathbb{SE}(3)$ transformation between links $i-1$ and i is;

$$L_i^{i-1} = Z_i\left(\theta, d\right) X_i\left(\alpha, r\right), \tag{2.9a}$$

where d are the link lengths along the axis of the joint and r the lengths perpendicular, and α describing the angle of the joint's end point relative to its axis as rotations in the x-axis, and finally θ is the joint position. The flange's pose is then;

$$F(\theta) = \Pi_{i=1}^{6} L_i^{i-1}. \tag{2.9b}$$

The Configuration space of the robot is given by $\mathbb{T}^6$ the six-torus of rotational axis positions. Allowed joint positions on different platforms describe the branches of the torus and coverage over it. The KUKA KR6 agilus as an example has axis ranges of $[\pm 170°, -190°\ 45°, -120°\ 156°, \pm 185°, \pm 120°, \pm 350°]$, that does not allow motion over the complete torus, with only axis six enabling near-double

coverage of its 360° circular motion space.

While this is restrictive for complex motions, the solution space to the KR6 is limited preventing onerous calculations for C-space paths, ideal for repeatable and limited-environment applications. More complex and varied tasks may require more freedom to execute full Cartesian paths within the work-space. The Universal-Robots series has joint limits of $\pm 360°$, allowing $\mathbb{T}^6$ to be traversed twice, admitting greater flexibility in executing complex or long-distance Cartesian paths. However, its admissible solution C-space is vast and can be complex for direct C-space planning tasks.

The forward-kinematics solution is injective, but not surjective. For a 6-link robot, the inverse kinematic solution F^{-1} admits up to 8 configuration solutions for each Cartesian position in the work-space [80]. The $\pm 2\pi$ allowed axis angle positions admit up to two further additions to the principle-branch cut taken in inverting the trigonometric functions. The result is $512 = 8^3$ potential inverse kinematic solutions for each position. Solving for each inverse kinematic solution at each position then choosing which is best given the current position can be seen as less efficient than taking an approximation to the configuration for a given Cartesian position.

2.4.6 Jacobian Planning and Singularities

A Taylor expansion of the forward-kinematics returns;

$$F(\theta + \delta\theta) = F(\theta) + \sum_i \frac{\partial F}{\partial \theta_i}|_\theta \delta\theta_i, \tag{2.10}$$

the Jacobian relates a small change in the tool position to a small change in the Configuration position;

$$J^{-1}\delta x = \delta\theta. \tag{2.11}$$

Path planning becomes a calculation of the Jacobian and not the full inverse kinematics, and is commonly used for online path planning methods [81]. While the Jacobian can be used for online path planning, it is also informative of the relationship between Cartesian and C-space. Generalised Jacobians for closed and open loop manipulators whose governing equations are described by;

$$F_1(x) + F_2(\theta) = 0 \tag{2.12}$$

are given by;

$$J_1\delta x + J_2\delta\theta = 0. \tag{2.13}$$

Function F_1 corresponds to Cartesian restrictions on the motion of the robot, associated to parallel and constrained robots. This differential relationship was first described by [82]. When $\det(J_1) = 0$, a type-1 singularity occurs, the plat-

form gains a degree of freedom and motion becomes unconstrained. Type II singularities, when $\det(J_2) = 0$ conversely reduce the dimensionality of potential motions of the manipulator. When a Jacobian-based motion planner encounters a singularity, the inverse-Jacobian solution becomes numerically unstable, the magnitude of the right hand side of Eq: 2.11 tends to infinity as the minimum eigenvalue of the Jacobian tends to zero.

Static cell deployments in Section: 2.2 traditionally check for singularities along paths, potentially resulting in a re-arrangement of the positioning of the part. Flexible procedures requiring online corrections may suffer adverse effects, as the exact C-space position of singularities is unknown. Proximity to singularities can be attained by the function;

$$C_1(\theta) = \det(J)^2, \tag{2.14}$$

where for serial manipulators $J = J_2$.

Limited motion due to singularities is such an issue in industrial robotics, there it is a source of extensive and thorough investigation throughout robotic literature. One has relied on the analytic Jacobi formula [83] for the determinant's derivative [84];

$$\frac{\partial}{\partial\theta_i} C_1(\theta) = \text{trace}\left(\text{Adj}(M)\frac{\partial M}{\partial\theta_i}\right), \tag{2.15}$$

to find singularities with gradient descent processes. Online methods tradition-

ally rely on Jacobian or velocity-correction vectors preventing infinite joint speeds when singularities are reached, perturbing the end effector's motion in order to avoid them [85, 86]. For NDT, avoidance of singular poses is incompatible with Condition: 3, as the entire surface would not be covered. Within NDT, current robotic path planning methods rely on operator intuition about the placement of singularities. While paths are determined by the shape of the embedded surface in Cartesian space, the ability of the robot to enact them is limited by the co-ordinate relationship between Cartesian and C-spaces. In enabling flexible and autonomous procedures without a high repeatability for which path planning is not an overhead but instead a running cost, the C-space perspective is necessary in determining the position of the path in order to prevent loss of robotic motion in-scan.

Path Planning in Static Cell NDT

Traditional static-cell NDT coverage path planning is concerned with well defined geometries within a well controlled environment. Path planning for area inspections falls under the category of Coverage Path Planning (CPP) or Travelling Salesman Problems (TSP), a well investigated topic in 2D environments for applications of mapping and cleaning.

Traditional DR assisted NDT deployment methods utilise commercial software developed for coverage path planning, often also applied to machining and

painting due to their shared goal of complete optimal-time coverage. Software packages available include fast suite [87]. In some situations where path planning software is available, the lengthy process of jogging the robot to points along its path is also seen as viable [88]. Recent output fuses the two approaches, since area scans can in some cases require only limited traversal, with the policy (area to scan) set by an operator [89]. Novel NDT based area scanning utilised reference edge planning is [90], specifying non-linear bases for covering the part, a perspective taken into modern autonomous path planning explored in Section: 2.5.2.

Additional functional perspectives further generalise the concept of linear intersection, where surfaces are functionally approximated with basis functions $f : \mathbb{R}^2 \longrightarrow \mathbb{R}^3$. Linear combinations of the $\mathbb{R}^2$ parameter basis are used to construct surface paths [91, 92]. Introduced by [93] Morse function decomposition sub-divides Cartesian space into cells that are then independently rasterised by linear basis combinations. While they have enabled efficient online coverage path planning in unknown environments with obstacles [94], cellular decompositions are primarily applicable to accurate wide aperture sensors used for pre-profiling and are sub-optimal when points along the target surface are not seen or their pose misidentified. Topological decompositions similarily split the surface into sets of mutually compatible sub-surfaces [95] of similar curvature that are capable of individual rasterisation.

Through different functional approximations to surfaces, rasterisations are possible by; 1). associating the surface to a set of paths that are linear with some basis functions or paths, 2). then finding a full traversal by using this 2D basis.

Alternative coverage methods from other industries primarily rely on discrete pose optimisations [96], selecting an optimal sub-set of poses that cover the path , then constructing a path between all of them. The minimal sensor aperture of a UT tool cannot efficiently take advantage of these methods, as the initial pose-set generated by discrete methods would need to consider tools of cm-size. Because of the aperture limitations, NDT methods utilise a basis-spline approach, re-sampling along two bases functions instead of relying on saturated direct sampling of a mesh.

Traditional approaches to path planning like these suffer when the surface representation is noisy or incomplete. Topological decompositions require the surface curvature to be accurately represented by the DT, otherwise unnecessary partitions and extraneous surface path segments are created. Traditional splining or reference edge planning would produce extraneous paths due to the additional area caused by noise. Most importantly for data collection, even with the extraneous paths, without online corrections the surface normal wouldn't be aligned to the probe. These reasons provide context as to why accurate part profiling and DR alignment is the current prominent area of investigation for robotic autonomy in NDT when applied to the areas mentioned in Section: 2.5.2.

2.5 Robotic Autonomy in NDT

In many of the high-growth target industries of this thesis, DTs are ill-defined during the production stage or are not available at all, requiring novel approaches to NDT scanning, inspiring growth in NDT 4.0 targeted algorithms and approaches.

2.5.1 Robotic Autonomy and Risk

Several architectures of autonomous robotic systems exist throughout the literature. A key review [97] advocates for structured control architectures, building reactive components upon objective aims, responding to uncertain environments to achieve goals. Core to the argument is that successful autonomous robotic systems must not be constrained by rigid policy decisions, instead having the autonomy and sensing capacity to complete them as data changes.

Recently, [98] highlighted the ongoing focus on human-in-the-loop control architectures adopted by a wide range of industries seeking autonomous robotic designs. Autonomous modules assist and complement a human operator- policy decisions taken by the human are then supplemented with flexible autonomous robotic processes for planning and optimisation. The specific modules enabling autonomy or semi-autonomy vary from algorithmic to Bayesian/Reinforced Learning (RL), and onto Q-learning neural networks.

Advanced autonomy in future applications will allow robotic architectures to assess risk in task operation with varying autonomy, feeding back to low-level

operation policy [99]. While this is an advantage in hazardous environments where reactivity is a sub-component of risk minimisation, this thesis looks at on-site environments, where time to deployment is not a risk factor.

2.5.2 Advanced Robotic NDT

Path planning for robotic arm NDT is currently implemented semi-autonomously. Reflexivity to changing situations when enacting a task are kept to a minimum, and DTs as prior information incorporated during all NDT data collection and interpretation steps.

Inspection in 2D is a significantly easier problem than in higher dimensions. Complete coverage path planning for suction or magnetically coupled platforms such as wheeled crawlers is aided as the surface's map is naturally flattened by its method of motion. 2D complete coverage is a well-researched topic, a variety of algorithms available for both structured and completely unknown environments [100], with many of the same algorithms successfully applied in well-known, static 3D contexts [101]. The cutting edge framework for autonomous 3D-motion capable platforms is for prior knowledge to be fitted to the current situation, then extrapolated from. This is apparent considering semi-autonomous drone scanning procedures such as [102], where machine vision fits a wind-turbine rotor to current observations allowing localisation of the robot and of any seen defects. Advanced approaches enabling autonomy in unknown environments still rely on

learned data such as in Bayesian mapping [103].

Low in-process information availability is affordable for these small, relatively risk-free vehicles. Non-holonomic vehicles exist along a 2D embedded space, minimising collision probability unless the terrain is non-smooth and the velocity of the vehicle large. Meanwhile, drones are capable of traversing 3D paths while scanning 2D objects, only risking collisions when the path traverses a confined space or the deployment method is contact-based.

Robotic arms present a significantly greater challenge, capable of 3D motion yet each link presenting a collision possibility. Visual inspections minimise the collision likelihood, as a large stand-off is acceptable. Autonomous path determination [104] and optimisation [105, 106] for visual inspection has been investigated due to the reduced risk in deployment. However, visual inspection is only part of the picture; sub-surface defects can still present significant viability issues to industries such as remanufacturing [107], reducing the expected lifespan of products significantly. Contact NDT is more desirable, but present greater risk of collisions due to the reduced stand-off. It is due to this that there is a focus on gaining accurate knowledge of the part and its position relative to the robot in the literature. The autonomy level of current robotic-arm contact-sensing NDT deployment is limited by the need to ensure the minimisation of risk.

Autonomous mobile robotic platforms have specialised for given tasks, with most platforms consisting of a chassis mounted sensor, allowing constant cou-

pling to gently curved surfaces. Interest has gained in manipulators mounted on mobile platforms to increase the effective deployment-space of the sensor. The combination of mobility and dexterity has recently engaged the oil and gas sector. From visual inspections with arms mounted on non-holonomic chassis [108], and more recently an advanced Boston-Dynamics Spot robot-dog [109]. These have all displayed the capability of modern collaborative robotics when applied to autonomous NDT challenges. So far these platforms have engaged in either low collision risk visual inspections, single-position scans with little low-level autonomy, or are enabled by accurate DTs with little investigation into either autonomous contact UT area scans with human-set high level policies or alternative risk minimisation models.

2.5.3 Prior Information in Enabling Robotic-Arm Semi-Autonomy

Flexibility in robotic-arm path planning modules for area scans initially began with pre-set paths used to accurately profile parts within the work-cell [110, 61] so that free form surfaces of uniform complexity and of multiple scales could be scanned without being seen previously. Autonomous next best view systems allowed dynamic sensing to reconstruct models of varying complexity [111]. Applied to 3D data, a proof of concept process for path planning on noiseless point cloud data was introduced by [112]. A later depth based approach applied im-

age processing capabilities to fulfil the need for minimal noise when scanning geometries of which there is prior knowledge [113]. While introducing a level of autonomy to scanning processes, these all involve accuracy enhancements in prior profiling tasks and not during the execution of NDT scans. Due to the required processing of large quantities of UT data, several investigations into enhancing scans when the DR is not accurately calibrated have focused on offline alignment optimisation with an a pre-scan procedure [33] for jet-PAUT deployments and in reconstruction post-scan [114] in simulated immersion tests.

The most flexible models for in-scan UT collection gave dynamic autonomy to path planning given the policy of full-surface scanning through either fine adjustments [115] or extrapolating the normal vector offset from the received ultrasonic energy profile [116]. Modelling the surface with parametric functions, an example shown in Fig: 2.8, these approaches required; the part to be globally represented by a set of differentiable basis functions, initial data of a manually inputted reference edge, and the part to be submerged. The first requirement severely limits the parts able to be scanned, as machined components presenting ridges or holes, and manufactured parts of varying curvatures cannot necessarily be easily globally splined with a single basis set. The final requirement hinders both the geometry and flexibility of the system as the robot must be protected from water damage. The targeted autonomy in deployment is only possible with the supplementary information of a reference curve, and with severe restrictions

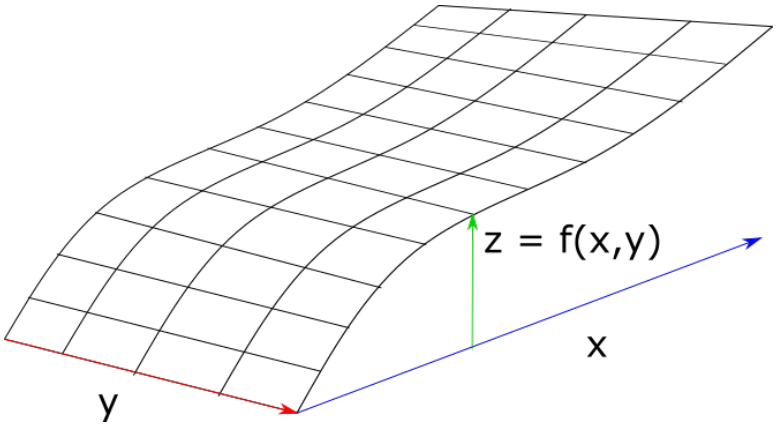

Figure 2.8: Parametric surface required by the program in [115, 116] to scan the entire surface with semi-autonomy. While for a large section of surfaces, this can be completed, discontinuities can prevent full surface profiling as each basis spline in x is extrapolated over increments of y.

on the deployment method.

Computer vision as a mature technology can provide the requisite accuracy, given ideal lighting and either prior knowledge of the part or significant visual anisotropy. Meanwhile, imperfect UT delivery methods increased the necessity for risk-avoidance to be placed in the model-discovery phase emphasising the utility of computer vision. The use of and lessons in NDT-applied computer vision can be seen in weld seam tracking.

Due to the well-structured and defined geometry of the weld-seam, this problem has been approached from several angles. Visual [117, 118, 119], and depth [120, 121] information has enabled algorithmic autonomous situation-assessments for on-site scanning. Applying the known model of the weld geometry to the current information, a weld-seam can be tracked and scanned with adjustments in-situ. Applied AI processes also utilise prior information, requiring large quan-

tities of well labeled data [122] entailing that they are tailored to specific and limited tasks and environments. Most of the above approaches rely on primitive-shape fitting algorithms, assuming the regularity of the surfaces and weld lines in order to provide accurate paths. However [121] takes the discrete perspective, demonstrating an effective tracking method without relying on given continuity, differentiability, and known-geometry pre-conditions.

Structural scanning for civic and commercial architecture has also adopted a degree of autonomy. The most advanced robotic contact scanning platform integrates vision, force, and prior global knowledge to scan tunnels with an integrated robotic arm [123]. This method is of great significance as the architecture allows for safe and full autonomy at the situational level. While it does incorporate prior knowledge of the structure, it is capable of parametrised path planning with local adaptations. While the scale of the platform and delivery method prevents fast delivery of results using minimal sensor data, it provides a prototypical system for robotically deployed UT inspection capabilities. Reliance on parametric world models is not a disadvantage for the specific purpose, it is not an applicable system for robotic area scanning. The point to point trajectories are optimised by [124], optimality does not extend to the base frame of the robot. Since it does not conduct large area scans, it does not need full Cartesian control, by-passing kinematic effects such as singularities. Area scanning in this sector was significantly advanced also by the earlier work of [125], whose methods of applying a mobile 7

DoF platform to imprecise paths enabled the semi-autonomous scanning of critical structures, when a general road-map is known. Relying on either force control or magnetic adhesion for position corrections of a planar dry-coupled Eddy Current probe, the method showed it was at least as good at maintaining contact with the surface as a human operator. As in [126], corrections to a pre-defined path allowed defects to be accurately localised. However these approaches are not suitable for contact coupled, non-planar, deformable probes with couplant since neither the UT signal through this medium nor pure force-moment can provide accurate normal-vector estimations. Prior information of the trajectory is also required for these approaches, and a DR required for defect localisation on the part. Finally, in none of these studies is the effect of surface curvature on data acquisition or required path corrections discussed. A similar approach is applied in Chapter: 3, where a more general system of path planning and delivery is deployed allowing application to a wider selection of geometries and materials within on-site environments while also considering curvature limitations.

2.6 Summary

Significant advances in autonomy for situational adaptation in NDT are present in the literature, specifically for tasks focused on particular geometries. Incorporating prior models is the mainstay of these approaches, with the main gain in autonomy being in situational assessment given rigid policies given by human

programmers. The closest to full situational autonomy requires prior information to instead be built into computer vision and surface modelling. Online adaptations to area scanning applications are not well-researched, the most advanced technique requiring a restrictive UT coupling method to provide accurate online data. Despite this, the market for robotic autonomy in NDT has never been greater. The increased focus on specific and upcoming manufacturing methods, mentioned in Section: 2.3.1, presents an opportunity for autonomous robotic-arm deployed UT scanning. While medium-level policy setting is well explored for non-holonomic and drone based delivery systems, autonomy is restricted by the perspective of narrow task setting. Robotic arm NDT has attained some level of autonomy in visual scanning and part profiling before scans, but is limited by the perspective of maximising the available geometric information of the part before a scan may commence as opposed to during a scan. Further, few investigations have sought optimisation along with adaptation, instead focusing on maximising the information available at every step and digital twin enhancement.

To attain the Industry 4.0 standard of autonomy in NDT, flexible in-scan contact delivery methodologies are necessary to ensure robust, scalable, and safe deployment platforms and algorithms. Meanwhile, the deployments must meet the standards of current fixed-cell NDT methods described in Section: 2.2.3 in order to directly compare to traditional methods of cell-based NDT. Accuracy and safety must be guaranteed, as well as production of DT's for future track-

ing and assessment of potential defects. In partially achieving these goals, this thesis has sought to take advantage of advancements in modern computing and robotics in order to enable online autonomy and optimality in policies set by a human in the loop. This thesis investigates the topic of autonomy through different representations of the robot's work-space, their relationships, and how complementary perspectives can enable autonomous and optimal free-form area in-process scanning. While this work seeks a set of generalisable solutions to these issues, there are several limitations to and much potential for improving the proposed algorithms, provided in Chapter: 8.

Bibliography

[1] Amir Manbachi and Richard S C Cobbold. Development and application of piezoelectric materials for ultrasound generation and detection. *Ultrasound*, 19(4):187–196, 2011. doi: 10.1258/ult.2011.011027. URL `https://doi.org/10.1258/ult.2011.011027`.

[2] *Fundamentals of acoustics / Lawrence E. Kinsler ... [et al.].* Wiley, New York, 4th ed. edition, 2000. ISBN 0471847895.

[3] R.P. Feynman, R.B. Leighton, M. Sands, and EM Hafner. *The Feynman Lectures on Physics; Vol. I*, volume 33. AAPT, 1965.

[4] Max Born, Emil Wolf, A. B. Bhatia, P. C. Clemmow, D. Gabor, A. R.

Stokes, A. M. Taylor, P. A. Wayman, and W. L. Wilcock. *Basic properties of the electromagnetic field*, page 1–74. Cambridge University Press, 7 edition, 1999. doi: 10.1017/CBO9781139644181.010.

[5] B.S. Wong. 11 - non-destructive evaluation (nde) of composites: detecting delamination defects using mechanical impedance, ultrasonic and infrared thermographic techniques. In Vistasp M. Karbhari, editor, *Non-Destructive Evaluation (NDE) of Polymer Matrix Composites*, Woodhead Publishing Series in Composites Science and Engineering, pages 279–308e. Woodhead Publishing, 2013. ISBN 978-0-85709-344-8. doi: https://doi.org/10.1533/9780857093554.2.279. URL `https://www.sciencedirect.com/science/article/pii/B9780857093448500117`.

[6] R.A. Kline. Wave propagation in fiber reinforced composites for oblique incidence. *Journal of Composite Materials*, 22(3):287–303, 1988. doi: 10.1177/002199838802200306. URL `https://doi.org/10.1177/002199838802200306`.

[7] M.D. Verweij, B.E. Treeby, K.W.A. Dongen, van, and L. Demi. *Simulation of ultrasound fields*, pages 465–499. Elsevier, Netherlands, 2014. ISBN 978-0-444-53633-4. doi: 10.1016/B978-0-444-53632-7.00221-5.

[8] *Ultrasound Waves*, chapter 19, pages 303–316. John Wiley Sons, Ltd, 2002. ISBN 9780471221159. doi: https://doi.org/10.1002/

0471221155.ch19. URL https://onlinelibrary.wiley.com/doi/abs/10.1002/0471221155.ch19.

[9] Air-coupled ultrasonic nde: experiments in the frequency range 750khz–2mhz. *NDT E International*, 35(7):417–426, 2002. ISSN 0963-8695. doi: https://doi.org/10.1016/S0963-8695(02)00012-9. URL https://www.sciencedirect.com/science/article/pii/S0963869502000129.

[10] M.Á.N. Elices Z. Correas and E. Cuevas-Aguado. Ttu phased array: Quality and productivity. 6th International Symposium on NDT in Aerospace, 2015.

[11] KUKA Robotics GmbH. Industrial robots: High payloads.

[12] Rubén Usamentiaga, Pablo Venegas, Jon Guerediaga, Laura Vega, Julio Molleda, and Francisco G. Bulnes. Infrared thermography for temperature measurement and non-destructive testing. *Sensors*, 14(7):12305–12348, 2014. ISSN 1424-8220. doi: 10.3390/s140712305. URL https://www.mdpi.com/1424-8220/14/7/12305.

[13] Jiacheng Wei, Fei Wang, Junyan Liu, Yang Wang, and Lin He. A laser arrays scan thermography (lasst) for the rapid inspection of cfrp composite with subsurface defects. *Composite Structures*, 226:111201, 2019. ISSN 0263-8223. doi: https://doi.org/10.1016/j.compstruct.2019.111201. URL https://www.sciencedirect.com/science/article/pii/S0263822319319786.

[14] Piotr Hellstein and Mariusz Szwedo. 3d thermography in non-destructive testing of composite structures. *Measurement Science and Technology*, 27 (12):124006, oct 2016. doi: 10.1088/0957-0233/27/12/124006. URL `https://doi.org/10.1088/0957-0233/27/12/124006`.

[15] Francesco Ciampa, Pooya Mahmoodi, Fulvio Pinto, and Michele Meo. Recent advances in active infrared thermography for non-destructive testing of aerospace components. *Sensors*, 18(2), 2018. ISSN 1424-8220. doi: 10.3390/s18020609. URL `https://www.mdpi.com/1424-8220/18/2/609`.

[16] Sandeep Kumar Dwivedi, Manish Vishwakarma, and Prof.Akhilesh Soni. Advances and researches on non destructive testing: A review. *Materials Today: Proceedings*, 5(2, Part 1):3690–3698, 2018. ISSN 2214-7853. doi: https://doi.org/10.1016/j.matpr.2017.11.620. URL `https://www.sciencedirect.com/science/article/pii/S2214785317328936`. 7th International Conference of Materials Processing and Characterization, March 17-19, 2017.

[17] T. Pengpen and M. Soleimani. Motion-compensated cone beam computed tomography using a conjugate gradient least-squares algorithm and electrical impedance tomography imaging motion data. *Philosophical Transactions of the Royal Society A: Mathematical, Physical and Engineering Sci-*

ences, 373(2043):20140390, 2015. doi: 10.1098/rsta.2014.0390. URL `https://royalsocietypublishing.org/doi/abs/10.1098/rsta.2014.0390`.

[18] Teng Wei Siang, Muhammad Firdaus Akbar, Ghassan Nihad Jawad, Tan Shin Yee, and Mohd Ilyas Sobirin Mohd Sazali. A past, present, and prospective review on microwave nondestructive evaluation of composite coatings. *Coatings*, 11(8), 2021. ISSN 2079-6412. doi: 10.3390/coatings11080913. URL `https://www.mdpi.com/2079-6412/11/8/913`.

[19] Peter Cawley. A high frequency coin-tap method of non-destructive testing. *Mechanical Systems and Signal Processing*, 5(1):1–11, 1991. ISSN 0888-3270. doi: https://doi.org/10.1016/0888-3270(91)90011-S. URL `https://www.sciencedirect.com/science/article/pii/088832709190011S`.

[20] F. Moreu, E. Ayorinde, J. Mason, C. Farrar, and D. Mascarenas. Remote railroad bridge structural tap testing using aerial robots. *International Journal of Intelligent Robotics and Applications*, 2(1):67–80, Mar 2018. ISSN 2366-598X. doi: 10.1007/s41315-017-0041-7. URL `https://doi.org/10.1007/s41315-017-0041-7`.

[21] John Nash. Tap testing vs. thermography. *e-Journal of Non Destructive Testing*, 2017.

[22] J W Long and R S Peckover. Inspection techniques: Robotic NDT system.

Physics Bulletin, 37(6):250–250, jun 1986. doi: 10.1088/0031-9112/37/6/019. URL https://doi.org/10.1088/0031-9112/37/6/019.

[23] ISO 9283:1998(en). Manipulating industrial robots — Performance criteria and related test methods. Standard, International Organization for Standardization, Geneva, CH, 1998.

[24] B Wright I Cooper C Mineo, S G Pierce and P I Nicholson. Paut inspection of complex shaped composite materials through 6 dofs robotic manipulators. *Insight: The Journal of the British Institute of Non-Destructive Testing*, 57(3):161–166, March 2015. ISSN 1354-2575. doi: 10.1784/insi.2014.57.3.161. URL https://doi.org/10.1784/insi.2014.57.3.161.

[25] Matthias Schwabe, Dr. Albrecht Maurer, Dr. Roman Koch, 50354 Hürth, and Industriegebiet Süd. Ultrasonic testing machines with robot mechanics – a new approach to cfrp component testing. 2010.

[26] Albrecht Dr.-Phys. Maurer, W. DeOdorico, Roland Huber, and Thierry Laffont. 18th world conference on nondestructive testing, 16-20 april 2012, durban, south africa aerospace composite testing solutions using industrial robots. 2022.

[27] Zongxing Lu, Chunguang Xu, Xinyu Zhao, Lan Zhang, Hongbo Wang, and Qinxue Pan. Ultrasonic transmission testing of twin-robots coordinated

control. In *2013 IEEE International Conference on Mechatronics and Automation*, pages 1256–1260, 2013. doi: 10.1109/ICMA.2013.6618094.

[28] Universal Robots. Precise quality inspection, testing and measuring with robotic arms. URL `https://www.universal-robots.com/applications/quality-inspection/`.

[29] Ebi Maher Ali Asmari, Andrew Marrero. Autonomous navigation and geotagging for concrete bridge deck inspections with the rabit robotic platform. ASNT Annual Conference 2017, Oct 2017.

[30] Marco Antonio Simos Teixeira, Higor Barbosa Santos, Andre Schneider De Oliveira, Lucia Valeria Ramos De Arruda, and Flavio Neves. Environment identification and path planning for autonomous ndt inspection of spherical storage tanks. In *2016 XIII Latin American Robotics Symposium and IV Brazilian Robotics Symposium (LARS/SBR)*, pages 193–198, 2016. doi: 10.1109/LARS-SBR.2016.39.

[31] Love P. Kalra, Weimin Shen, and Jason Gu. A wall climbing robotic system for non destructive inspection of above ground tanks. In *2006 Canadian Conference on Electrical and Computer Engineering*, pages 402–405, 2006. doi: 10.1109/CCECE.2006.277523.

[32] London South Bank University. Remote robotic ndt, Jan 2001. Grant from

the Community Research and Development Information Service (CORDIS), grant ID: BRPR960254.

[33] Jonathan Riise, Carmelo Mineo, S. Gareth Pierce, P. Ian Nicholson, and Ian Cooper. Adapting robot paths for automated ndt of complex structures using ultrasonic alignment. *AIP Conference Proceedings*, 2102(1):040006, 2019. doi: 10.1063/1.5099756. URL `https://aip.scitation.org/doi/abs/10.1063/1.5099756`.

[34] C. Soutis. Carbon fiber reinforced plastics in aircraft construction. *Materials Science and Engineering: A*, 412(1):171–176, 2005. ISSN 0921-5093. doi: https://doi.org/10.1016/j.msea.2005.08.064. URL `https://www.sciencedirect.com/science/article/pii/S0921509305009780`. International Conference on Recent Advances in Composite Materials.

[35] Adapting robot paths for automated ndt of complex structures using ultrasonic alignment. *AIP Conference Proceedings*, 2102(1), May 2019. ISSN 1551-7616. doi: 10.1063/1.5099756. URL `https://doi.org/10.1063/1.5099756`.

[36] ISO 16810:2012(E). Non-destructive testing — Ultrasonic testing — General principles. Standard, International Organization for Standardization, Geneva, CH, March 2012.

[37] Johannes Vrana. Industrial internet of things, digital twins, and cyber-

physical loops for nde 4.0. *Handbook of Nondestructive Evaluation 4.0*, pages 1–34, 2021.

[38] Evelien Dils. Etc/wmge report 10/2021: Contribution of remanufacturing to circular economy. Technical report, European Environment Information and Observation Network, Dec 2021. `https://www.eionet.europa.eu/etcs/etc-wmge/products/etc-wmge-reports/contribution-of-remanufacturing-to-circular-economy`.

[39] Seigo Robinson Harry Symington Jane Tewson Kim Jansson Shyaam Ramkumar David Peck David Parker, Kate Riley. Remanufacturing market study. Technical report, European Remanufacturing Network, Nov 2015. `https://www.remanufacturing.eu/assets/pdfs/remanufacturing-market-study.pdf`.

[40] Mairi Kerin and Duc Truong Pham. Smart remanufacturing: a review and research framework. *Journal of Manufacturing Technology Management*, 31(6):1205–1235, Jan 2020. ISSN 1741-038X. doi: 10.1108/JMTM-06-2019-0205. URL `https://doi.org/10.1108/JMTM-06-2019-0205`.

[41] Jan-Philipp Kaiser, Simon Lang, Marco Wurster, and Gisela Lanza. A concept for autonomous quality control for core inspection in remanufacturing. *Procedia CIRP*, 105:374–379, 2022. ISSN 2212-8271. doi: https://

doi.org/10.1016/j.procir.2022.02.062. URL https://www.sciencedirect.com/science/article/pii/S2212827122000622. The 29th CIRP Conference on Life Cycle Engineering, April 4 – 6, 2022, Leuven, Belgium.

[42] Keith Wei Liang Nguyen. *Towards automated damage detection for in-situ remanufacturing.* PhD thesis, Nanyang Technological University, Jan 2020.

[43] A. K. Koul and R. Castillo. Assessment of service induced microstructural damage and its rejuvenation in turbine blades. *Metallurgical Transactions A*, 19(8):2049–2066, Aug 1988. ISSN 1543-1940. doi: 10.1007/BF02645208. URL https://doi.org/10.1007/BF02645208.

[44] M Zakaria, Y Aminanda, S A Rashidi, and M A Mat Sah. Spring-back of thick uni-directional carbon fibre reinforced composite laminate for aircraft structure application. *Journal of Physics: Conference Series*, 1005:012003, apr 2018. doi: 10.1088/1742-6596/1005/1/012003. URL https://doi.org/10.1088/1742-6596/1005/1/012003.

[45] V.G. Ivancevic and T.T. Ivancevic. *Applied Differential Geometry: A Modern Introduction.* World Scientific, 2007. ISBN 9789812706140. URL https://books.google.co.uk/books?id=z-9oDQAAQBAJ.

[46] Maher Moakher. Means and averaging in the group of rotations. *SIAM journal on matrix analysis and applications*, 24(1):1–16, 2002.

[47] F.C. Park and B.J. Martin. Robot sensor calibration: solving ax=xb on the euclidean group. *IEEE Transactions on Robotics and Automation*, 10 (5):717–721, 1994. doi: 10.1109/70.326576.

[48] R M Brannon. Axis and angle of rotation. In *Rotation, Reflection, and Frame Changes*, 2053-2563, pages 5–1 to 5–28. IOP Publishing, 2018. ISBN 978-0-7503-1454-1. doi: 10.1088/978-0-7503-1454-1ch5. URL `https://dx.doi.org/10.1088/978-0-7503-1454-1ch5`.

[49] Li Z. Sastry S.S. Murray, R.M. *A Mathematical Introduction to Robotic Manipulation*. CRC Press, 1st edition, 1994. doi: https://doi.org/10.1201/9781315136370.

[50] Explanation on robot orientation. `https://www.universal-robots.com/articles/ur/application-installation/explanation-on-robot-orientation/`, . Accessed: 2022-08-12.

[51] Camillo Taylor and David Kriegman. Minimization on the lie group so(3) and related manifolds. Technical report, Yale University, April 1994.

[52] David Hoag. Apollo guidance and navigation considerations of apollo imu gimbal lock. Technical report, NASA, April 1963.

[53] G. Bradski. The OpenCV Library. *Dr. Dobb's Journal of Software Tools*, 2000.

[54] Allam Shehata Hassanein, Sherien Mohammad, Mohamed Sameer, and Mohammad Ehab Ragab. A survey on hough transform, theory, techniques and applications. 2015. doi: 10.48550/ARXIV.1502.02160. URL `https://arxiv.org/abs/1502.02160`.

[55] C. Harris and M. Stephens. A combined corner and edge detector. In *Proc. AVC*, pages 23.1–23.6, 1988. doi:10.5244/C.2.23.

[56] John Canny. A computational approach to edge detection. *IEEE Transactions on Pattern Analysis and Machine Intelligence*, PAMI-8(6):679–698, 1986. doi: 10.1109/TPAMI.1986.4767851.

[57] Irwin Sobel and Gary Feldman. An isotropic 3x3 image gradient operator, 08 2015.

[58] Yu Liu, Shuping Liu, Yang Cao, and Zengfu Wang. A practical algorithm for automatic chessboard corner detection. In *2014 IEEE International Conference on Image Processing (ICIP)*, pages 3449–3453, 2014. doi: 10.1109/ICIP.2014.7025701.

[59] S. S. Beauchemin and J. L. Barron. The computation of optical flow. *ACM Comput. Surv.*, 27(3):433–466, sep 1995. ISSN 0360-0300. doi: 10.1145/212094.212141. URL `https://doi.org/10.1145/212094.212141`.

[60] Gordon Dobie, Rahul Summan, Charles MacLeod, and S. Gareth Pierce.

Visual odometry and image mosaicing for nde. *NDT E International*, 57: 17–25, 2013. ISSN 0963-8695. doi: https://doi.org/10.1016/j.ndteint.2013.03.002. URL https://www.sciencedirect.com/science/article/pii/S0963869513000443.

[61] Aamir Khan, Carmelo Mineo, Gordon Dobie, Charles Macleod, and Gareth Pierce. Vision guided robotic inspection for parts in manufacturing and remanufacturing industry. *Journal of Remanufacturing*, 11(1):49–70, Apr 2021. ISSN 2210-4690. doi: 10.1007/s13243-020-00091-x. URL https://doi.org/10.1007/s13243-020-00091-x.

[62] Stuart Robson, Lindsay MacDonald, Stephen Kyle, Jan Boehm, and Mark Shortis. Optimised multi-camera systems for dimensional control in factory environments. *Proceedings of the Institution of Mechanical Engineers, Part B: Journal of Engineering Manufacture*, 232(10):1707–1718, 2018. doi: 10.1177/0954405416654936. URL https://doi.org/10.1177/0954405416654936.

[63] E. Dunn and G. Olague. Pareto optimal camera placement for automated visual inspection. In *2005 IEEE/RSJ International Conference on Intelligent Robots and Systems*, pages 3821–3826, 2005. doi: 10.1109/IROS.2005.1544990.

[64] Yufeng Sun and Ou Ma. Automating aircraft scanning for inspection or 3d

model creation with a uav and optimal path planning. *Drones*, 6(4), 2022. ISSN 2504-446X. doi: 10.3390/drones6040087. URL https://www.mdpi.com/2504-446X/6/4/87.

[65] Wolfgang Böhm, Gerald Farin, and Jürgen Kahmann. A survey of curve and surface methods in cagd. *Computer Aided Geometric Design*, 1(1): 1–60, 1984. ISSN 0167-8396. doi: https://doi.org/10.1016/0167-8396(84)90003-7. URL https://www.sciencedirect.com/science/article/pii/0167839684900037.

[66] W. Cheney and D. Kincaid. *Linear Algebra: Theory and Applications*. Jones & Bartlett Learning Inte. Jones & Bartlett Learning, 2012. ISBN 9781449613525. URL https://books.google.co.uk/books?id=S0imN2tl1qwC.

[67] Canzhi Guo, Chunguang Xu, Dingguo Xiao, Juan Hao, and Hanming Zhang. Trajectory planning method for improving alignment accuracy of probes for dual-robot air-coupled ultrasonic testing system. *International Journal of Advanced Robotic Systems*, 16(2):1729881419842713, 2019. doi: 10.1177/1729881419842713. URL https://doi.org/10.1177/1729881419842713.

[68] Rasmus S. Andersen, Jens S. Damgaard, Ole Madsen, and Thomas B. Moes-

lund. Fast calibration of industrial mobile robots to workstations using qr codes. In *IEEE ISR 2013*, pages 1–6, 2013. doi: 10.1109/ISR.2013.6695636.

[69] Naila Habib Khan and Awais Adnan. Ego-motion estimation concepts, algorithms and challenges: an overview. *Multimedia Tools and Applications*, 76(15):16581–16603, Aug 2017. ISSN 1573-7721. doi: 10.1007/s11042-016-3939-4. URL `https://doi.org/10.1007/s11042-016-3939-4`.

[70] Chandler J.H. Micheletti, N. and S.N. Lane. 2015.

[71] Monika Bansal, Munish Kumar, and Manish Kumar. 2d object recognition: a comparative analysis of sift, surf and orb feature descriptors. *Multimedia Tools and Applications*, 80(12):18839–18857, May 2021. ISSN 1573-7721. doi: 10.1007/s11042-021-10646-0. URL `https://doi.org/10.1007/s11042-021-10646-0`.

[72] Yuri D.V. Yasuda, Fabio A.M. Cappabianco, Luiz Eduardo G. Martins, and Jorge A.B. Gripp. Aircraft visual inspection: A systematic literature review. *Computers in Industry*, 141:103695, 2022. ISSN 0166-3615. doi: https://doi.org/10.1016/j.compind.2022.103695. URL `https://www.sciencedirect.com/science/article/pii/S0166361522000926`.

[73] R. Strzodka, I. Ihrke, and M. Magnor. A graphics hardware implementation of the generalized hough transform for fast object recognition, scale, and

3d pose detection. In *12th International Conference on Image Analysis and Processing, 2003.Proceedings.*, pages 188–193, 2003. doi: 10.1109/ICIAP.2003.1234048.

[74] Ali Hosseininaveh Ahmadabadian, Stuart Robson, Jan Boehm, Mark Shortis, Konrad Wenzel, and Dieter Fritsch. A comparison of dense matching algorithms for scaled surface reconstruction using stereo camera rigs. *ISPRS Journal of Photogrammetry and Remote Sensing*, 78:157–167, 2013. ISSN 0924-2716. doi: https://doi.org/10.1016/j.isprsjprs.2013.01.015. URL `https://www.sciencedirect.com/science/article/pii/S0924271613000452`.

[75] Jason Geng. Structured-light 3d surface imaging: a tutorial. *Adv. Opt. Photon.*, 3(2):128–160, Jun 2011. doi: 10.1364/AOP.3.000128. URL `http://opg.optica.org/aop/abstract.cfm?URI=aop-3-2-128`.

[76] K. S. Arun, T. S. Huang, and S. D. Blostein. Least-squares fitting of two 3-d point sets. *IEEE Transactions on Pattern Analysis and Machine Intelligence*, PAMI-9(5):698–700, 1987. doi: 10.1109/TPAMI.1987.4767965.

[77] Huijuan Zhang, Chengning Zhang, Wei Yang, and Chin-Yin Chen. Localization and navigation using qr code for mobile robot in indoor environment. In *2015 IEEE International Conference on Robotics and Biomimetics (ROBIO)*, pages 2501–2506, 2015. doi: 10.1109/ROBIO.2015.7419715.

[78] Martin Schickert, Christian Koch, and Frank Bonitz. Augmented-reality-visualisierung von abbildungsergebnissen an betonbauteilen – implementierung und ausblick. In *4. Fachseminar des FA MTHz, Mikrowellen- und Terahertz-Prüftechnik in der Praxis*, 2019.

[79] J. Denavit and R. S. Hartenberg. A Kinematic Notation for Lower-Pair Mechanisms Based on Matrices. *Journal of Applied Mechanics*, 22(2):215–221, 06 2021. ISSN 0021-8936. doi: 10.1115/1.4011045. URL `https://doi.org/10.1115/1.4011045`.

[80] Nie Liqing and Huang Qingjiu. Inverse kinematics for 6-dof manipulator by the method of sequential retrieval. In *Proceedings of the 1st International Conference on Mechanical Engineering and Material Science (MEMS 2012)*, pages 600–603. Atlantis Press, 2012/12. ISBN 978-90-78677-59-8. doi: https://doi.org/10.2991/mems.2012.157. URL `https://doi.org/10.2991/mems.2012.157`.

[81] Avantsa V.S.S. Somasundar and G. Yedukondalu. Robotic path planning and simulation by jacobian inverse for industrial applications. *Procedia Computer Science*, 133:338–347, 2018. ISSN 1877-0509. doi: https://doi.org/10.1016/j.procs.2018.07.042. URL `https://www.sciencedirect.com/science/article/pii/S1877050918309876`. International Conference on Robotics and Smart Manufacturing (RoSMa2018).

[82] C. Gosselin and J. Angeles. Singularity analysis of closed-loop kinematic chains. *IEEE Transactions on Robotics and Automation*, 6(3):281–290, 1990. doi: 10.1109/70.56660.

[83] J.R. Magnus and H. Neudecker. *Matrix Differential Calculus with Applications in Statistics and Econometrics*. PROBABILISTICS AND STATISTICS. Wiley, 1999. ISBN 9780471986331. URL `https://books.google.co.uk/books?id=0CXXdKKiIpQC`.

[84] Ahmad Almarkhi. and Anthony Maciejewski. Singularity analysis for redundant manipulators of arbitrary kinematic structure. In *Proceedings of the 16th International Conference on Informatics in Control, Automation and Robotics - Volume 2: ICINCO,*, pages 42–49. INSTICC, SciTePress, 2019. ISBN 978-989-758-380-3. doi: 10.5220/0007833100420049.

[85] Changwu Qiu, Qixin Cao, and Shouhong Miao. An on-line task modification method for singularity avoidance of robot manipulators. *Robotica*, 27(4): 539–546, 2009. doi: 10.1017/S026357470800492X.

[86] Helin Wang, Ziqiang Zhou, Xianyou Zhong, and Qijun Chen. Singular configuration analysis and singularity avoidance with application in an intelligent robotic manipulator. *Sensors*, 22(3), 2022. ISSN 1424-8220. doi: 10.3390/s22031239. URL `https://www.mdpi.com/1424-8220/22/3/1239`.

[87] Non destructive testing (ndt). `https://www.fastsuite.com/`

`solutions-products/technology-based-offline-programming/ndt`, . Accessed: 2022-08-12.

[88] Dieter Ungerer Wolfgang Haase and Friedrich Mohr. Automated non-destructive examination of complex shapes. 2014.

[89] Miguel Angel Funes-Lora, Edgar Alfredo Portilla-Flores, Eduardo Vega-Alvarado, Raúl Rivera Blas, Emmanuel Alejandro Merchán Cruz, and Manuel Faraón Carbajal Romero. A novel mesh following technique based on a non-approximant surface reconstruction for industrial robotic path generation. *IEEE Access*, 7:22807–22817, 2019. doi: 10.1109/ACCESS.2019.2897079.

[90] Maxim Morozov, Stephen Pierce, Carmelo Mineo, Pascual Ian Nicholson, and Ian Cooper. Computer-aided tool path generation for robotic non-destructive inspection. In *52nd Annual Conference of the British Institute of Non-Destructive Testing 2013*. British Institute of Non-Destructive Testing, Telford (UK), 2013. ISBN 9781629939933. URL `https://strathprints.strath.ac.uk/54911/`.

[91] Carmelo Mineo, Douglas Herbert, M Morozov, SG Pierce, PI Nicholson, and Ian Cooper. Robotic non-destructive inspection. In *51st Annual Conference of the British Institute of Non-Destructive Testing*, pages 345–352, 2012.

[92] Sungchul Jee and Taehoon Koo. Tool-path generation for nurbs surface

machining. In *Proceedings of the 2003 American Control Conference, 2003.*, volume 3, pages 2614–2619 vol.3, 2003. doi: 10.1109/ACC.2003.1243471.

[93] Ercan U. Acar, Howie Choset, Alfred A. Rizzi, Prasad N. Atkar, and Douglas Hull. Morse decompositions for coverage tasks. *The International Journal of Robotics Research*, 21(4):331–344, 2002. doi: 10.1177/027836402320556359. URL https://doi.org/10.1177/027836402320556359.

[94] Enric Galceran, Ricard Campos, Narcís Palomeras, David Ribas, Marc Carreras, and Pere Ridao. Coverage path planning with real-time replanning and surface reconstruction for inspection of three-dimensional underwater structures using autonomous underwater vehicles. *Journal of Field Robotics*, 32(7):952–983, 2015. doi: https://doi.org/10.1002/rob.21554. URL https://onlinelibrary.wiley.com/doi/abs/10.1002/rob.21554.

[95] Pierre-Olivier Dubois Michel Brassard Loic Seguin Charbonneau, Julien Walter and David St-Jacques. Automated path generation for robotic ut inspection of cfrp components. 2020.

[96] Randa Almadhoun, Tarek Taha, Lakmal Seneviratne, Jorge Dias, and Guowei Cai. A survey on inspecting structures using robotic systems. *International Journal of Advanced Robotic Systems*, 13(6):1729881416663664,

2016. doi: 10.1177/1729881416663664. URL https://doi.org/10.1177/1729881416663664.

[97] R.G. Simmons. Structured control for autonomous robots. *IEEE Transactions on Robotics and Automation*, 10(1):34–43, 1994. doi: 10.1109/70.285583.

[98] Cuebong Wong, Erfu Yang, Xiu-Tian Yan, and Dongbing Gu. Autonomous robots for harsh environments: a holistic overview of current solutions and ongoing challenges. *Systems Science & Control Engineering*, 6(1):213–219, 2018. doi: 10.1080/21642583.2018.1477634. URL https://doi.org/10.1080/21642583.2018.1477634.

[99] Lawrence A. Bush and Andrew Wang. Autonomous robot control via autonomy levels. 2017.

[100] AMNA KHAN, IRAM NOREEN, and ZULFIQAR HABIB. On complete coverage path planning algorithms for non-holonomic mobile robots: Survey and challenges. *Journal of Information Science and Engineering*, 33(1): 101–121, Jan 2017. ISSN 1016-2364. doi: 10.6688/JISE.2017.33.1.7.

[101] Tauã M. Cabreira, Lisane B. Brisolara, and Paulo R. Ferreira Jr. Survey on coverage path planning with unmanned aerial vehicles. *Drones*, 3(1), 2019. ISSN 2504-446X. doi: 10.3390/drones3010004. URL https://www.mdpi.com/2504-446X/3/1/4.

[102] Martin Stokkeland, Kristian Klausen, and Tor A. Johansen. Autonomous visual navigation of unmanned aerial vehicle for wind turbine inspection. In *2015 International Conference on Unmanned Aircraft Systems (ICUAS)*, pages 998–1007, 2015. doi: 10.1109/ICUAS.2015.7152389.

[103] Morteza Tabatabaeipour, Oksana Trushkevych, Gordon Dobie, Rachel S. Edwards, Ross McMillan, Charles Macleod, Richard O'Leary, Steve Dixon, Anthony Gachagan, and Stephen G. Pierce. Application of ultrasonic guided waves to robotic occupancy grid mapping. *Mechanical Systems and Signal Processing*, 163:108151, 2022. ISSN 0888-3270. doi: https://doi.org/10.1016/j.ymssp.2021.108151. URL `https://www.sciencedirect.com/science/article/pii/S0888327021005318`.

[104] Emile Glorieux, Pasquale Franciosa, and Dariusz Ceglarek. Coverage path planning with targetted viewpoint sampling for robotic free-form surface inspection. *Robotics and Computer-Integrated Manufacturing*, 61: 101843, 2020. ISSN 0736-5845. doi: https://doi.org/10.1016/j.rcim.2019.101843. URL `https://www.sciencedirect.com/science/article/pii/S0736584518305246`.

[105] Zvezdan Lončarević, Andrej Gams, Simon Reberšek, Bojan Nemec, Jure Škrabar, Jure Skvarč, and Aleš Ude. Specifying and optimizing robotic motion for visual quality inspection. *Robotics and Computer-Integrated*

Manufacturing, 72:102200, 2021. ISSN 0736-5845. doi: https://doi.org/10.1016/j.rcim.2021.102200. URL `https://www.sciencedirect.com/science/article/pii/S0736584521000831`.

[106] Boris Bogaerts, Seppe Sels, Steve Vanlanduit, and Rudi Penne. A gradient-based inspection path optimization approach. *IEEE Robotics and Automation Letters*, 3(3):2646–2653, 2018. doi: 10.1109/LRA.2018.2827161.

[107] Sara J. Ridley. Improving the efficiency of the remanufacture of complex mechanical assemblies with robust inspection of core units. In Mitsutaka Matsumoto, Yasushi Umeda, Keijiro Masui, and Shinichi Fukushige, editors, *Design for Innovative Value Towards a Sustainable Society*, pages 547–551, Dordrecht, 2012. Springer Netherlands. ISBN 978-94-007-3010-6.

[108] Matthias Bengel, Kai Pfeiffer, Birgit Graf, Alexander Bubeck, and Alexander Verl. Mobile robots for offshore inspection and manipulation. In *2009 IEEE/RSJ International Conference on Intelligent Robots and Systems*, pages 3317–3322, 2009. doi: 10.1109/IROS.2009.5353885.

[109] Journal of Petroleum Technology. Meet spot, the quadruped robot for offshore inspections. `https://jpt.spe.org/meet-spot-quadruped-robot-offshore-inspections`, Feb 2020. Accessed: 31/08/2022.

[110] Carmelo Mineo, Charles MacLeod, Maxim Morozov, S. Gareth Pierce,

Rahul Summan, Tony Rodden, Danial Kahani, Jonathan Powell, Paul McCubbin, Coreen McCubbin, Gavin Munro, Scott Paton, and David Watson. Flexible integration of robotics, ultrasonics and metrology for the inspection of aerospace components. *AIP Conference Proceedings*, 1806(1):020026, 2017. doi: 10.1063/1.4974567. URL `https://aip.scitation.org/doi/abs/10.1063/1.4974567`.

[111] Carmelo Mineo, Donatella Cerniglia, Vito Ricotta, and Bernhard Reitinger. Autonomous 3d geometry reconstruction through robot-manipulated optical sensors. *The International Journal of Advanced Manufacturing Technology*, 116(5):1895–1911, Sep 2021. ISSN 1433-3015. doi: 10.1007/s00170-021-07432-5. URL `https://doi.org/10.1007/s00170-021-07432-5`.

[112] Zhen Zhang, Hualiang Zhang, Xiaolong Yu, Yongsheng Deng, and Zheng Chen. Robotic trajectory planning for non-destructive testing based on surface 3d point cloud data. *Journal of Physics: Conference Series*, 1965 (1):012148, jul 2021. doi: 10.1088/1742-6596/1965/1/012148. URL `https://doi.org/10.1088/1742-6596/1965/1/012148`.

[113] Jianjun Zhao, Zhong Zhang, Minghui Zhang, and Xiaozhong Du. Scanning path planning of ultrasonic testing robot based on deep image processing. *Russian Journal of Nondestructive Testing*, 58(3):167–175, Mar 2022. ISSN

1608-3385. doi: 10.1134/S1061830922030020. URL https://doi.org/10.1134/S1061830922030020.

[114] Hanming Zhang, Chunguang Xu, and Dingguo Xiao. Offline correction of tool path deviations for robot-assisted ultrasonic nondestructive testing. *Proceedings of the Institution of Mechanical Engineers, Part C: Journal of Mechanical Engineering Science*, 233(8):2879–2893, 2019. doi: 10.1177/0954406218792581. URL https://doi.org/10.1177/0954406218792581.

[115] D. Guo, Guojun Jiang, Yue Wu, and J. Cheng. Automatic ultrasonic testing for components with complex surfaces. *DEStech Transactions on Engineering and Technology Research*, 2017.

[116] Yang Zhang, Kai Chen, Peng Guo, Fan Li, Jiang Zhu, and Li-Min Zhu. Profile tracking for multi-axis ultrasonic inspection of model-unknown free-form surfaces based on energy concentration. *Measurement*, 172:108867, 2021. ISSN 0263-2241. doi: https://doi.org/10.1016/j.measurement.2020.108867. URL https://www.sciencedirect.com/science/article/pii/S0263224120313579.

[117] A. Nasser Moradi, B. Mashalah Abasi Dezfulli, and C. Seyed Enayatollah Alavi. Development a vision based seam tracking system for none destructive testing machines.

[118] Jinle Zeng, Baohua Chang, Dong Du, Yuxiang Hong, Yirong Zou, and

Shuhe Chang. A visual weld edge recognition method based on light and shadow feature construction using directional lighting. *Journal of Manufacturing Processes*, 24:19–30, 2016. ISSN 1526-6125. doi: https://doi.org/10.1016/j.jmapro.2016.07.002. URL `https://www.sciencedirect.com/science/article/pii/S1526612516300834`.

[119] Yanling Xu, Gu Fang, Na Lv, Shanben Chen, and Ju Jia Zou. Computer vision technology for seam tracking in robotic gtaw and gmaw. *Robotics and Computer-Integrated Manufacturing*, 32:25–36, 2015. ISSN 0736-5845. doi: https://doi.org/10.1016/j.rcim.2014.09.002. URL `https://www.sciencedirect.com/science/article/pii/S0736584514000775`.

[120] Zhaoxuan Dong, Jianchang Huang, Shiqi Yin, and Yuenong Fei. A weld line detection method based on 3d point cloud for automatic NDT. *IOP Conference Series: Earth and Environmental Science*, 440(2):022003, feb 2020. doi: 10.1088/1755-1315/440/2/022003. URL `https://doi.org/10.1088/1755-1315/440/2/022003`.

[121] Liguo Zhang, Qixiang Ye, Wei Yang, and Jianbin Jiao. Weld line detection and tracking via spatial-temporal cascaded hidden markov models and cross structured light. *IEEE Transactions on Instrumentation and Measurement*, 63(4):742–753, 2014. doi: 10.1109/TIM.2013.2283139.

[122] Jie Li, Shanshan Jin, Cunjin Wang, Jiameng Xue, and Xingsong Wang.

Weld line recognition and path planning with spherical tank inspection robots. *Journal of Field Robotics*, 39(2):131–152, 2022. doi: https://doi.org/10.1002/rob.22042. URL `https://onlinelibrary.wiley.com/doi/abs/10.1002/rob.22042`.

[123] Elisabeth Menendez, Juan G. Victores, Roberto Montero, Santiago Martínez, and Carlos Balaguer. Tunnel structural inspection and assessment using an autonomous robotic system. *Automation in Construction*, 87:117–126, 2018. ISSN 0926-5805. doi: https://doi.org/10.1016/j.autcon.2017.12.001. URL `https://www.sciencedirect.com/science/article/pii/S0926580516303806`.

[124] J.J. Kuffner and S.M. LaValle. Rrt-connect: An efficient approach to single-query path planning. In *Proceedings 2000 ICRA. Millennium Conference. IEEE International Conference on Robotics and Automation. Symposia Proceedings (Cat. No.00CH37065)*, volume 2, pages 995–1001 vol.2, 2000. doi: 10.1109/ROBOT.2000.844730.

[125] Tariq P. Sattar and Alina-Alexandra Brenner. Robotic system for inspection of test objects with unknown geometry using ndt methods. *Industrial Robot: An International Journal*, 36(4):340–343, Jan 2009. ISSN 0143-991X. doi: 10.1108/01439910910957093. URL `https://doi.org/10.1108/01439910910957093`.

[126] Xiao Zhen, You Yong, Xu Chun Guang, Xiao Ding Guo, Liu Fang Fang, and Li Xin Liang. Profile tracking with ultrasonic alignment for automatic non-destructive testing of complex structures. *Robotics and Computer-Integrated Manufacturing*, 49:134–142, 2018. ISSN 0736-5845. doi: https://doi.org/10.1016/j.rcim.2017.06.007. URL `https://www.sciencedirect.com/science/article/pii/S0736584516301284`.

Chapter 3

Autonomous Full Surface Mapping Through the Tool's Frame of Reference

Key to robotic NDT of freeform surfaces is defining full-surface coverage from an algorithmic perspective. This is a well-defined and answered problem in the context of well-known surfaces. OLP for full surface coverage is offered by a host of companies, allowing the operator to select a face that is then automatically rastered. The rasterisation offered consists of path segments bridged by transition paths that may require step-overs in the case of surface-probe coupled sensors. In the context of unknown or poorly represented surfaces, full surface coverage is an ill-defined problem. To fully scan a surface with no prior information for

NDT applications in an efficient way, it is necessary to;

1. Traverse the whole surface without losing contact and without losing extraneous search patterns using high data-volume sensors such as UT,

2. define a traversal stopping condition to prevent an infinite traversal loop.

This chapter sets out the heuristic basis that the author has used to answer this question in Section: 3.2, the required information for traversal and stopping conditions in three dimensions utilising well known results in Differential Geometry in Section: 3.3, and experimental results in Section: 3.5.2. Enabling autonomous full surface discovery, work-flows for current and proposed full-surface scanning methodologies are shown in Fig: 3.1.

The following sections introduce the impetus and previous research completed in the area of unknown surface profiling in Section: 3.1. A candidate heuristic method is explored in Section: 3.2 followed by its heuristic expansion and application to embedded surfaces in Section: 3.3 through perspectives from differential geometry. Finally, software validation, early experimentation with UT sensors and finally a laser-based deployment method are presented in Sections: 3.5.1, 3.5.3, and 3.5.4 respectively.

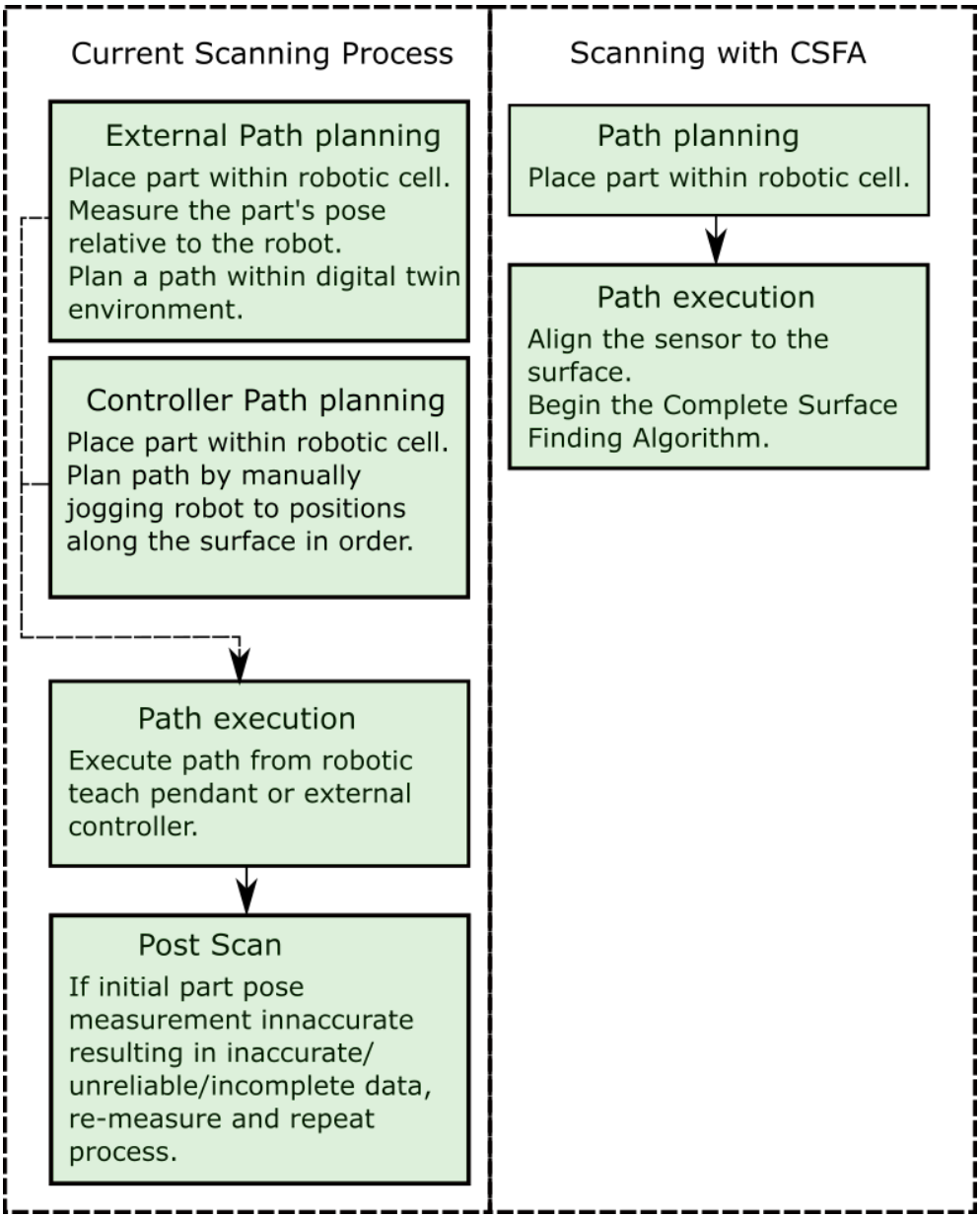

Figure 3.1: The one-step process enabled by the presented algorithm removes the necessity of accurate digital-twins and world-frame calibration, or lengthy robotic jogging procedures.

3.1 Autonomous and Automatic Inspection Processes

Covered in Section: 1, industries such as moulded-part manufacturing involve parts that do not match the original digital twin due to non-critical deformations that are caused in production. In other industries such as remanufacturing, a digital twin of the part may not be available. In remote inspection work, the variety of parts necessary to scan and the degradation due to wear and tear entail large costs to any digital-twinned platform inspection process. A flexible, model free process of complete scanning for unknown surfaces would be highly beneficial to these industries.

Robotic NDT has recently been able to define a 2-scan process to satisfy these requirements. The first scan reconstructs the part, followed by path planning over its digital reconstruction. This then enables a subsequent scan with NDT equipment, fully covering the known surface that is within reach of the robot. Methods of reconstructing part surfaces in the initial scan have been widely researched with respect to both Photogrammetry and in the field of machining.

In the field of Photogrammetry, automated robotised methods for free-form surface profiling have developed significantly. Processes involving 3D or 2D cameras have evolved from requiring user-inputted positions [1] to fully automated 3D model reconstruction techniques. Automated photogrammetry has been applied

to a wide range of scales, from fine-detail model reconstruction using robotic arms [2, 3] to large-scale reconstruction using autonomous robots with wide-aperture sensors [4]. A recent example of photogrammetry enabling a 2-pass scan within NDT utilising Structure-from-Motion (SfM) [5].

These methods have relied on multiple volumetric inspections of a complex object using wide field-of-view sensors such as traditional RGB or RGB + Depth (RGB/D) cameras. This work has considered surface profiling in the case of limited-range sensors, such as line-scanners or ultrasonic devices that have a field of view many magnitudes smaller than the inspected surfaces. In the case of laser scanners, a volumetric pre-scan is not safe for human operators working nearby. Volumetric scanning of curved objects cannot guarantee surface discovery in the case of water-coupled ultrasound devices without lengthy re-scanning processes due to beam divergence and scattering.

Within the field of machining, validation of machining quality or accurate part profiling when there is no available CAD model has been implemented using Co-ordinate Measuring Machines (CMMs). CMMs utilising limited field-of-view sensors for full-surface profiling have also been thoroughly investigated [6]. Their use has relied on spline-surface approximations to predict surface positions [7, 8, 9], or planar raster-tangent path planning [10]. These methods all require saturation of user-sampled positions, user input to define surface tangents, or rely on tangents defined by a gantry constrained rasterization pattern. The spline-surface

approximation method has been successfully applied to ultrasonic-sensor surface discovery [11]. This method requires that the surface can be defined by a global spline, as opposed to an atlas of piece-wise smooth splines. This is a disadvantage when inspecting objects with discontinuities such as holes, as these cannot be captured by a single global b-spline representation. Surfaces with a global b-spline representation defined by a single function are also known as doubly ruled surfaces.

CMM specific machinery and software have shown its efficacy in Eddy-Current (EC) inspection planning previously [12]. While shown to be highly effective for the high-accuracy requirements of EC systems [13], the guided pre-scan still entails a two-step strategy to enable high-accuracy NDT sensor trajectories that are less necessary for deployment methods such as UT that do not suffer from small variations in surface-probe stand off in the order of millimetres.

The lessened requirement for surface-tool stand off accuracy and consistency for UT profiling allows online methods to take advantage of dynamic corrections that contain small errors in positioning at each step, while preventing accumulating errors in alignment. To enable full surface discovery, a search process and memory structure to discover and store potential surface points for later traversal are required.

3.2 Flood-Fill Algorithms

A candidate heuristic process are Flood Fill Algorithms (FFAs) [14] that propagate through maps or networks in order to discover all positions within a connected surface or graph. The pseudo-code for the FFAs abstraction is presented in Algorithm 1 and accompanied by graphical representation in application to the 2D image domain in Figure: 3.2.

Algorithm 1: Flood Fill Algorithm Heuristic.

Data: Image, graph, or other connected structure in which 'clear' and 'boundary' nodes are defined. Starting node (pixel). Either the graph must be finite or the node-set bounded by boundary nodes must be finite.
Data: Collection of 'clear' nodes path-wise connected to the starting node.

```
begin
    Begin at Pixel P_1;
    Open-List = {P_1};
    Points-Found = {};
    while |Open-List| > 0 do
        P_a = Open-List.back();
        Points-Found.insert(P_a);
        Open-List.delete(P_a);
        for direction ∈ {'UP','DOWN','LEFT','RIGHT'} do
            P_b = P_a + direction;
            if P_b is new point AND not boundary point then
                Open-List.insert(P_b);
            end
        end
    end
end
```

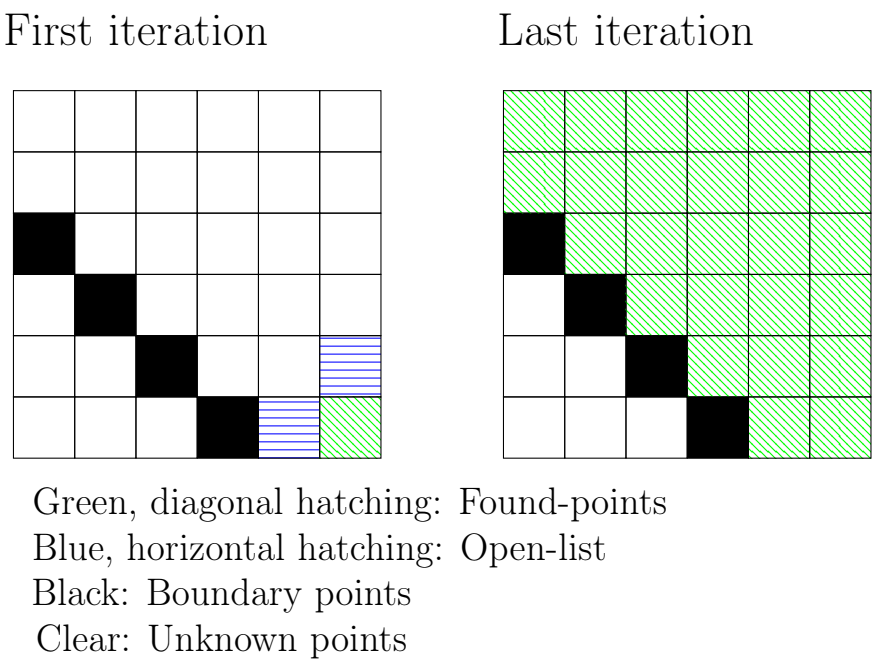

Figure 3.2: Colour Flood-Fill on the plane.

This work has generalised planar FFA heuristics to three-dimensional surface traversal, inventing the Complete-Surface Finding Algorithm (CSFA). Whereas FFAs require a pre-known data structure, the novel CSFA requires only curvature information about the target surface to ensure complete coverage when applied to sensors of arbitrary dimensions and sensitivity.

Simple stack-based FFA and scanline heuristics are of particular interest in the simulation section. Scanline implementations choose a preferred direction of motion for search until a boundary position is reached. When a boundary position is discovered, the less-preferable step is then taken until a free path is found in the preferred direction of motion. The resultant path is a traditional rasterization pattern, which is widely utilised within NDT path planning operations.

FFAs have been applied in various contexts, due to their simplicity and versatility. In the context of image processing, FFAs have seen ongoing widespread use in commercial products as a time-efficient method for filling a bounded region with a given colour [15]. The principle of the bucket-fill programme has been inverted to aid segmentation algorithms in 2D and 3D contexts from a user-inputted mask [16, 17, 18]. In recent years FFAs have aided machine-learning programmes in object recognition through automatic mask generation [19]. Mixed mapping and network theoretic implementations have been implemented to guide image reconstruction. First, FFAs were shown to be as effective as quality guided algorithms [20], and subsequently used to enhance nearest neighbour node quality optimisation methods in various fields [21, 22, 23].

Further, FFA variants have been extensively implemented in robotic path planning and control. Discretised potential field variants such as modified CFill and Flood-Field Methods (FFMs) have been shown to have greater time efficiency in comparison to Potential Field Methods (PFMs) [24, 25]. FFAs have gained interest in the context of optimal path planning for 2D platforms [26, 27], that has demonstrated flexibility through effective integration with optimal motion planners such as the A* algorithm [28]. These concepts have evolved in application to optimal motion planning in 3D space for UAVs with an exhaustive search pattern [29]. Further FFA integration and heuristic mirroring has shown to enhance traditional path planning algorithms [30, 31].

The above Flood-Fill methods have been implemented on data either with a pre-defined link structure or with a full exploration in each potential direction. For unknown surface profiling constrained by costly rearrangement procedures and a limited field of view, these procedures are either non-applicable or significantly sub-optimal.

3.3 Full Surface Description

Surfaces in 3D and surfaces of interest are not always directly parameterised by the plane, as mentioned in Section:1.

Despite potential global disassociation from the plane, perspectives from differential geometry are applied in Section: 3.3.1 to the local tool frame of reference to lift the basic planar FFA processes to $\mathbb{R}^3$ and apply them to an embedded surface. Since the traversal method is not directly implemented on the cardinal basis of $\mathbb{R}^3$ but on local continuous variations with the normal, additional guarantees are required to ensure that distinct points on the surface are not within the same spatial-position as is the case in 2D pixelisation. In Section: 3.3.2, the surface's second order expansions, equivalent to the tool frame's observed rate of change of the surface, are used to apply 3D segmentation to the embedded 2D problem. The combination is a traversal method that benefits from the local isomorphism to the plane, but are able to cope with topologically complex objects that cannot be globally and continuously unwrapped or projected to the plane, while also

describing parameterised surfaces without explicit foreknowledge necessary.

3.3.1 Traversal

Embedded surfaces $S \in \mathbb{R}^3$ that are described by a function $F : \mathbb{R}^2 \longrightarrow S$ or set of piecewise- functions that are differentiable are equipped with a tangent plane $T_{P^j}M$, given by the partial derivatives; $\partial_u F$ and $\partial_v F$ at a point $P^j = F(u^j, v^j)$. A position $F\left(u^0 + \delta u, v^0 + \delta v\right)$ in the infinitesimal region around $F\left(u^0, v^0\right)$ can be given by the extension in either tangent direction;

$$F\left(u^0 + \delta u, v^0 + \delta v\right) = F\left(u^0, v^0\right) + \delta u \partial_u F\left(u^0, v^0\right) + \delta v \partial_v F\left(u^0, v^0\right). \quad (3.1)$$

For surfaces that can be seen as embedded Riemannien manifolds, the tangent plane is isometric to $\mathbb{R}^2$ across the entire part [32], however tangent planes can be derived on any surface at a position that has a locally differentiable structure.

Assuming the surface is locally differentiable in the region of the sensor, new positions P_k^j can be approximated by taking the current position P^j and tangent directions in the local tangent plane $\partial_{k=u,v}F \in T_{P^j}M$. Traversal in any of the four directions $\pm\partial_{k=u,v}F$ by a distance d hypothecates four new positions $P_{\pm k}^j = P^j \pm \partial_k F$ along the surface, in analogue to the FFA heuristic's 'left', 'right', 'forward', and 'back' processes.

A sensor arrangement is required to measure the real surface position P^j and

tangent plane $T_{P^j}M$. For a collection of at least three positions on the surface $\{q_i\}_{i=1}^{N\geq 3}$, three coplanar but not colinear positions are chosen; q_1, q_2, q_3, and the vectors $v_1 = q_2 - q_1$ and $v_2 = q_3 - q_1$ found. The surface normal vector n_S is extracted using the flange's current z-axis vector n_F;

$$n_S = -\text{sign}(n_F \cdot v_1 \times v_2)\frac{v_1 \times v_2}{|v_1 \times v_2|}. \tag{3.2}$$

From a saturation of sensor measurements within a given aperture window, measurements at the fringe of the aperture window approximate the tangent plane for each of the four cardinal directions instead.

The surface normal describes the plane that is approximately tangent to the surface, the cardinal differential directions from Eq: 3.1 extracted simply as shown in Fig: 3.3.

An ultrasonic probe is sought to both scan the material and obtain the necessary data to find the surface normal. By applying a linear phased array sensor within an immersion bath set-up, the single element Synthetic Aperture Focusing Technique (SAFT) was used as the most appropriate method to approximate the local surface profile [33]. Measuring the time of flight of each element firing then receiving a signal, the approximate surface distance is calculated. Returned signal depths are inaccurate in the case of dipping reflectors, as the reflection is not necessarily beneath the element. By describing the surface's potential po-

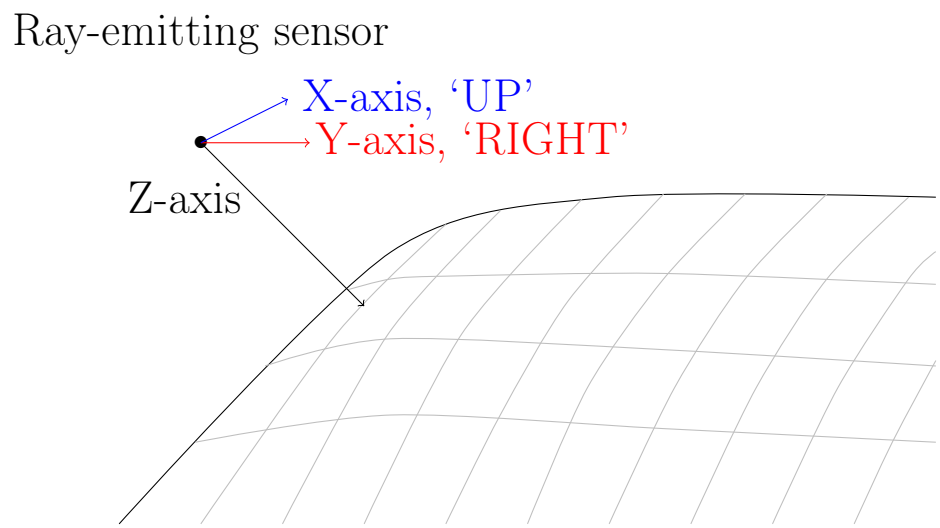

Figure 3.3: Extracting the cardinal directions in 3D as an analogue to the directions in traditional FFAs by using the tool's z-direction aligned to the surface normal. Grey lines represent iso-lines on the surface.

sition relative to each element as a set of spheres, whose radii are equal to the time-of-flight calculated distance measurement, the line fitted assuming surface to probe distance is within the probe's z direction purely results in points along the line closer to the probe's elements than the discovered minimal distance. By migrating the line's position, it intersects each sphere only once reflecting that the minimal probe to surface distance is already measured. The necessary shift to properly find the surface's tangent using the dipping reflector algorithm [34] is shown in Fig: 3.4

Seismic migration surface profiling results for a sinusoidal curved block are shown in Fig:3.5.

In order to prevent infinite recursion caused by adding already traversed positions to the 'To-Check' stack in Alg: 1, traditional FFAs segment space into

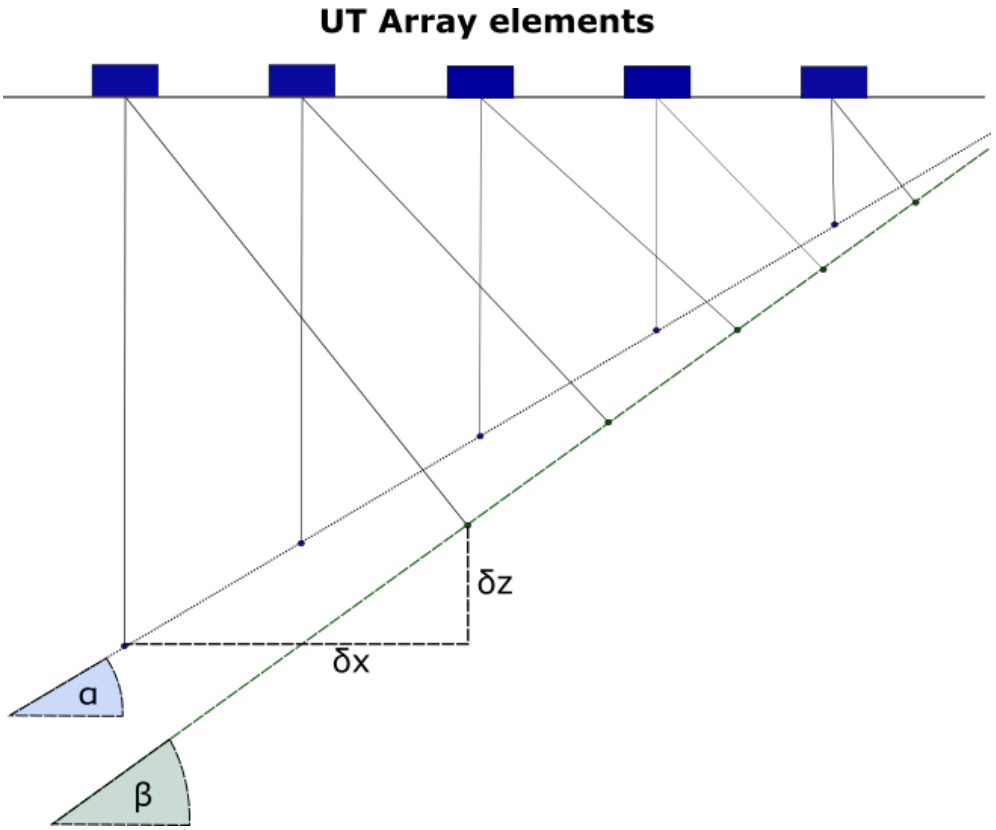

Figure 3.4: Seismic Migration of a wave when profiling a dipping reflector. The inferred surface (black dotted line) is incorrect, and must be perturbed by an x and z offset to the correct reflector position (green dotted line).

discretised pixels. It is necessary to segment $\mathbb{R}^3$ similarly so that infinite recursion does not happen. However, it is also necessary that each newly hypothesised position is not within the same spatial segment as the current position. Segmenting space so that these two requirements are met prevent infinite recursion and enable full surface traversal respectively.

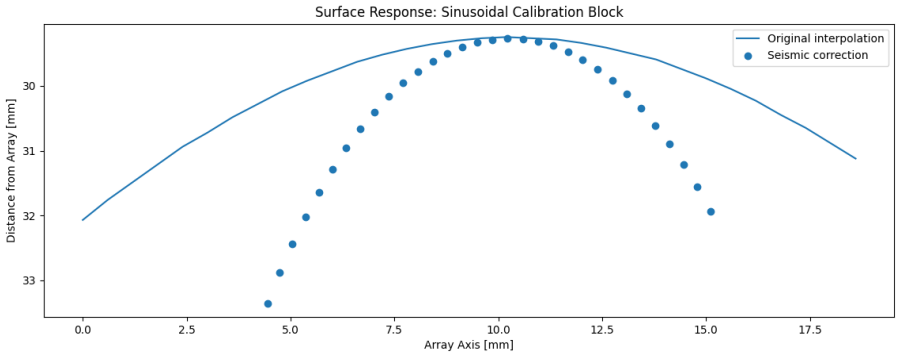

Figure 3.5: Seismic migration on the surface of a curved block corrects the inferred surface positions from single-element SAFT, projecting them to actual closest positions.

3.3.2 Segmentation: Traversal and Completeness

Analogue to 2D pixelisation in three dimensions, Voxelisation partitions the space into boxed segments. For both the the 2D and 3D FFA cases the traversal length is considered a unit, as is the length of the pixel's side since the tangent directions are consistent.

Traversing surfaces within 3D, the tangent directions may vary depending on the orientation of the local tangent plane. Additionally the current position may not be at the centre of the current voxel but near a boundary. In order for the step from one position to another to also traverse to a new voxel, the voxel widths must be limited. Additionally, the cumulative effects of surface curvature need to be considered so that in the case of surface inflection, different positions on the surface can be defined in different voxels.

For a flat surface, the largest single linear step within the voxel is along the

diagonal, restricting the voxel's width bound w given the traversal step distance λ as $w \leq \lambda/\sqrt{3}$.

The approximation of the surface as flat deteriorates from the local frame of reference at a rate that is dependant on the curvature. Between steps m and $m+1$ tangent vectors in the direction of motion $\hat{v}_m, \hat{v}_{m+1}$ deviate towards the normal vector $\hat{n}_m$ and away from the tangent plane by a value $\delta\hat{v}_m$;

$$\delta\hat{v}_m = \partial_{\hat{v}_m}\hat{v}_m \cdot \hat{n}_m. \tag{3.3}$$

The deviation also describing the error in approximating the local surface with a tangent plane is decomposed in terms of cardinal tangent directions defined in 3.1 by the second fundamental form $\mathbb{II}$ [35]. Assuming the surface is locally twice differentiable, $\mathbb{II}$ is framed by the tensor product of cardinal differential directions $\partial_u F = F_u$, $\partial_v F = F_v$;

$$\mathbb{II} = LF_u \otimes F_u + 2MF_u \otimes F_v + NF_v \otimes F_v, \tag{3.4a}$$

where;

$$L = -F_u \cdot \partial_u \hat{n}, \tag{3.4b}$$

$$M = -\frac{1}{2}\left(F_v \cdot \partial_u \hat{n} + F_u \cdot \partial_v \hat{n}\right), \tag{3.4c}$$

and,

$$N = -F_v \cdot \partial_v \hat{n}. \tag{3.4d}$$

Deviation of the tangent vector towards the normal stated in Eq: 3.5 is;

$$\kappa \delta \hat{v}_m = \mathbb{III} \hat{v}_m. \tag{3.5}$$

The inflection of a tangent direction away from the tangent plane is bounded by the maximal eigenvalue of $\mathbb{III}$ over the surface κ_{max};

$$\hat{v}_m \cdot \hat{n}_{m+1} \leq \kappa_{max}. \tag{3.6}$$

Treating the value λ as the arc-length along the hypothesised surface, the non-normalised defect of the projected tangent plane direction vector at $m+1$ against the current tangent resulting from a small expansion is;

$$\hat{v}_{m+1} = \hat{v}_m + \lambda \delta \hat{v}_m. \tag{3.7}$$

Integrating this value to raise it from tangent to position defect, the second order surface expansion of arc-length λ around P_m is given;

$$P_{m+1} = P_m + \lambda \hat{v}_m + \frac{\lambda^2}{2} \delta \hat{v}_m + O(\lambda^3). \tag{3.8}$$

The positional difference is;

$$|P_{m+1} - P_m| = \lambda|\hat{v}_m + \frac{\kappa_{max}}{2}\lambda\delta\hat{v}_m|. \tag{3.9}$$

A lower bound for the smallest step in 3D space for distinct points along the surface needs to be found to prevent voxel-map collisions.

Since $\delta\hat{v}_m \cdot \hat{v}_m \approx 0$, this can be approximately expanded as;

$$|P_{m+1} - P_m|^2 = \lambda^2||\hat{v}_m|^2 + |\frac{\kappa_{max}}{2}\lambda\delta\hat{v}_m|^2| \geq \lambda^2||\hat{v}_m|^2 - |\frac{\kappa_{max}}{2}\lambda\delta\hat{v}_m|^2|. \tag{3.10}$$

The negative term coming from the desire for a lower bound on the error due to inflection caused by curvature.

Since $\hat{v}_m$ and $\delta\hat{v}_m$ are unit vectors the real traversal length is bounded;

$$\hat{\lambda} \leq \lambda\sqrt{1 - (\kappa_{max}\lambda/2)^2}, \tag{3.11a}$$

and the voxel-widths are limited to the size of the box whose maximum interior step distance is $\hat{\lambda}$;

$$w \leq \frac{\lambda\sqrt{1 - (\kappa_{max}\lambda/2)^2}}{\sqrt{3}}. \tag{3.11b}$$

The voxelisation that allows full surface traversal requires the curvature information in order to ensure points within the part considered distinct fall within different voxels. Where planar FFA algorithms begin with a known structure

and regular discretisation pattern, the CSFA splits the volume with the prior knowledge of maximal surface curvature.

An alternate method to voxelisation are hash-tables, assigning each coordinate a coordinate via a hash function. Hash tables are not limited to subdivisions of powers of 2, as Octrees are, potentially requiring saturations of positions within an Octree. Octrees may either place itself within a leaf of another node or subdivide a node, whereas a hash table requires a flexible memory structure to enable re-hashing of elements in order to expand, contract, or refine the space [36]. Voxels within an Octree environment were chosen over hash-tables for space discretization, primarily due to their ensured lack of hashing collisions. The primary advantage of hash-tables is the flexibility of choosing the size and discretisation of the space. This is potentially an issue for octree implementations since each smallest leaf width dx in terms of the full space width x must be $dx = x/2^n$ for an integer n, or the compulsory space width x_c assigned such that $x_c = 2^n dx$. For large spaces x and small leaf widths dx, $n = \lceil \log_2(x/dx) \rceil$ that may result in $2x >> x_c > x$ for small values of $\log_2(x/dx) - n$. The strength of Octrees however are the flexible leaf structure that does not require population of all leafs or nodes reducing the memory overheads required compared to fully populated hash-tables of the same volume and accuracy. The scalable data structure additionally and relatively low memory overheads, requiring just $600KB$ to partition an $2m \times 2m \times 2m$ volume into $1mm^3$ chunks for example, allow the method to be

directly and quickly applied to static robotic work-volumes and mobile platforms.

3.3.3 Parts of interest

Parts in a variety of industries are commonly designed using splining functions due to the ease of which their shapes may be optimised continuously with respect to production properties [37, 38, 39, 40]. Spline modelled parts approximating the surface with a set of at least twice differentiable functions, admit a tangent plane and a second fundamental form. Machined parts, or parts produced without a spline function basis set do not meet these requirements. For sharp ridges or holes, the surface is continuous but not differentiable. However, in deployment the surface is smoothed by the radius of the laser measurements from the tool's centre point. An example of this on the Weierstrass function is shown in Fig: 3.6. The function is a famous historical example of a function that is continuous but not differentiable anywhere, meaning a tangent at any position is impossible to find. The smoothing as a result of taking multiple readings to approximate the tangent plane results in a continuous and differentiable approximation of the function. Boundary positions cannot be smoothed in this way, this being the condition to not produce further hypothesised search points. For even strictly non-differentiable surfaces, the algorithm is applicable on the condition that the curvature is not so great so that the surface leaves the line of sight and range of the applied sensors between steps. Large discontinuities such as with a stepped

calibration block may be smoothed with a set of sensors placed further apart and with greater range, however this reduces the overall accuracy of the estimates tangent plane. However, the laser data may be used in post processing to reconstruct a digital twin without relying on the estimated surface normal's value so this would only effect traversal to which it is a boon.

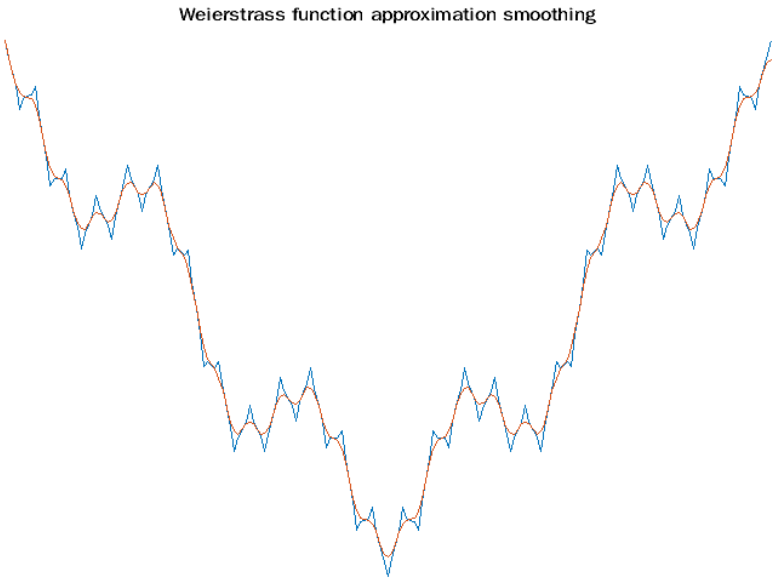

Figure 3.6: Weierstrass function in blue, and in orange the smoothed approximation obtained through a 5-point averaging method. Despite being non-differentiable at a number of points in this version (and at no points in the full infinite series expansion), from the perspective of a collection of sensors with a non-zero distance between them, the function appears smooth.

3.4 Autonomous Surface Discovery

Each part of the algorithm is laid out in the previous sections with the complete algorithm presented in Alg: 2. Using the first and second order differential approximations to surfaces, the result is an algorithm capable of complete discovery of unknown second order differentiable surfaces. The sensors under consideration cannot measure the surface normal with a zero dimensional point-like measurement, a factor that enables the practical deployment to cover non-differentiable surfaces such as corners, provided sensor measurements are still possible.

Algorithm 2: Pseudo-code for the novel CSFA.

Data: Maximum expected curvature κ, step-size d, and maximum Cartesian reach ΔX

Result: Discrete object surface positions and normal orientation vectors coupled to Ultrasonic data.

```
begin
    Octree = GenerateWorkSpace(κ, d, ΔX);
    // Generates a geometric description of the workspace.;
    Operator moves sensor to surface;
    GetData() →surface position and normal vector P_1, N_1;
    Open-List = {P_1};
    Points-Found = {};
    // Initialise lists describing where we have been and where we need to
     search.;
    while |Open-List| > 0 do
        P_a = Open-List.back();
        Open-List.delete(P_a);
        // Check that the next selected scanning position is within reach;
        if 0 < |J_a^Ω = InverseKin(P_a)| then
            Move to J_a = min_motion J_a^Ω;
            GetData() → P_a, N_a, data;
            if !data.empty() then
                Sensor.z_direction → N_a;
                GetUTdata();
                Octree.insert(P_a);
                GramSchmidt(N_a) →
                 {'UP','DOWN','LEFT','RIGHT'};
                // Orthonormalise the tangent plane to assign an
                 orientation within the world frame, assigning
                 positive/negative x and y cardinal directions to
                 'UP','DOWN',....;
                for direction ∈ {'UP','DOWN','LEFT','RIGHT'} do
                    P_b = P_a + direction;
                    if P_b ∉ Octree then
                        Open-List.insert(P_b);
                        Adding a new position to check. Octree checks
                         ensure closure of the process over a finite surface.;
                    end
                end
            end
        end
    end
end
```

In practice, despite only local sensor measurements being necessary to fulfil the algorithm a robotic platform is necessary for actual deployment. Within Section: 3.4.1 the path planning elements specifically related to the UR10e robotic arm platform are detailed. Surfaces are selected in the following Section: 3.5 due to their unique and specific properties that prove that the algorithm can be applied to a wide range of surfaces of interest. Initial validation of the algorithm presented in Alg: 2 is shown in simulation in Section: 3.5.1, followed by experimental validation. While the simulation validation is completed with an idealised deployment model with a sensor capable of normal measurement from an infinitesimal surface point, realistic sensor deployments require overcoming several hurdles. Application of UT sensors for surface normal measurement is explored in the context of immersion testing in Section: 3.5.3. This is followed by Section: 3.5.4 in which three low cost laser distance sensors are used instead for surface normal approximation. Finally a proof of concept for simultaneous laser-enabled surface discovery and Conformable Wedge Probe applied UT scanning is provided.

3.4.1 Robotic Control

Singularities and reachability of the robot may impact the profiling process, since for unknown parts the required robotic configurations cannot be seen in advance. These issues are incurred by a break in the correspondence between Cartesian

space and the robot's fundamental coordinates as introduced in Section: 1, the possible joint-positions and link structure. In overcoming the spatial limitations of the robotic manipulator, oriented target-points were converted to configuration space coordinates. As a proof of concept investigation for the deployment of the novel CSFA, test pieces were chosen to test the algorithm's ability to ensure full coverage on curved and complex surfaces while minimising the risk of collision. Collision avoidance in the test cases were achieved by placing a motion-length limit. To maintain full coverage in the case of required back-tracking, any motion above this joint-space limit would cause the robot to move safely through a known point above the part. In the case of a convex part, point-to-point motion was considered admissible within one step if the subsequent point did not require motion in the current point's normal direction of more than the sensor-surface stand off. Since the algorithm requires an initial position to be defined along the surface, an initial configuration is given at the start. The path-planner then proceeded to choose the next in Cartesian space, and selected the candidate robotic configuration with the smallest joint-motion. If the selected point induced a configuration motion larger than the allowed threshold, the point was pushed back into the Open-List and another chosen until a suitable point was found or only large-motions were possible. In the latter case, the point with the smallest joint-wise motion was chosen. The robot was then sent joint-wise position command motions, avoiding kinematic singularities and ensuring the reachability of target

points.

3.5 Simulation and Experimental Validation

A variety of shapes were chosen for both software and experimental validation, owing to their respective properties described in Table: 3.1.

Iteration through inferred surface positions provides an initial pose for the subsequent sub-processes, and is the only portion of the algorithm that relies on previous iterations. The surface normal measurement and proceeding surface discovery phase is independent of the previous discovery step. If the normal measurement and surface position inference methods can be proved to be successful on a surface with a particular property, then the memory dependent portion of the algorithm is implicitly satisfied. By the independence of discovery steps, demonstration on shapes with specific properties also provides proof of the process on surfaces combining the respective test-shape features.

In realistic scenarios, surfaces such as boat hulls or wing sections are both convex in sections and concave in others. Bolt holes, port holes and windows are described by continuous boundaries that are not connected to the edges of the surface. Surfaces such as hulls have mixed and continuously changing curvature. The next part of this chapter involves testing each of these properties in either software of experimental situations.

Shape	**Quality of Interest**	**Reason for Inclusion**	**Inspection Image(s)**
Sphere and Bowl	Positive curvature surface, from both concave and convex perspectives.	Demonstrate the algorithm on convex and concave surfaces.	3.10,3.11, 3.12, and 3.13.
Holed Surfaces	Presence of multiple disconnected, continuous boundaries that prevent traversal along a principle tangent direction while the surface re-continues in that direction.	Show that the algorithm can handle real scenarios where the number of possible directions of motion are reduced due to surface discontinuities (e.g. portholes).	3.8, and 3.9.
Doubly Curved Surface	Non-constant curvature that varies across the surface.	Demonstrate the algorithm is not limited to constant magnitude or signed surfaces.	3.19.
Wing Section	Realistic digital twin of a component that is commonly inspected.	Show the algorithm is capable of providing full and efficient coverage of a realistic surface in an offline environment.	3.7.

Table 3.1: Shapes investigated, their key properties, and references to their specific demonstrations are listed. The result is an algorithm that is able to handle surfaces combining the listed features.

3.5.1 Simulation Results

Applied in C++ using the Octree package [41], the CSFA is shown to be able to traverse structures of varying complexity within an offline environment.

Tests on shapes with key non-linear aspects have demonstrated the method's total coverage of generalised locally differentiable surfaces. The shapes chosen have been selected on the basis of surface irregularities that present challenges to full scanning. Surfaces with cut-outs that are not captured by a global surface spline representation demonstrated the advantage of the algorithm in handling

machined parts, or in piece-wise spline produced parts. These are not handled by the nearest available algorithm. Additionally, curved and doubly-curved surfaces were chosen to validate the suitability of the linearisation approximation method. In this section, surfaces chosen demonstrate complete coverage of locally smooth parts and parts with cut-outs. By demonstrating on positive, negative and zero curvature surfaces individually, the iterative and non-recursive algorithm has been validated for all locally smooth and holed surfaces. The software validation process is implemented in C++, utilising Simon Perrault's Octree structure [41]. Robotic simulations have been generated using RoboDK software with the Universal-Robotics UR10e as a demonstrative platform, with mesh simulations presented in MeshLab.

In post-processing, the CSFA has demonstrated the generation of raster-motions on an aerofoil component with varying step-sizes, displayed in Figure 3.7. This simulation represents a realistic scan upon a digital twin of an aeroplane's wing-section, with a discrete scanning increment of both $3mm$ and $10mm$ displaying consistency in rasterisation with both incremental scales. Due to the relative flatness of the surface a raster pattern was achieved. For more curved surfaces, over-sampling of the space is observed.

The stack based memory of 'positions to check' allowed effective full-surface discovery in the presence of irregular geometries. The method is demonstrated to avoid surface-holes, later re-scanning areas previously uncaptured in early-scan

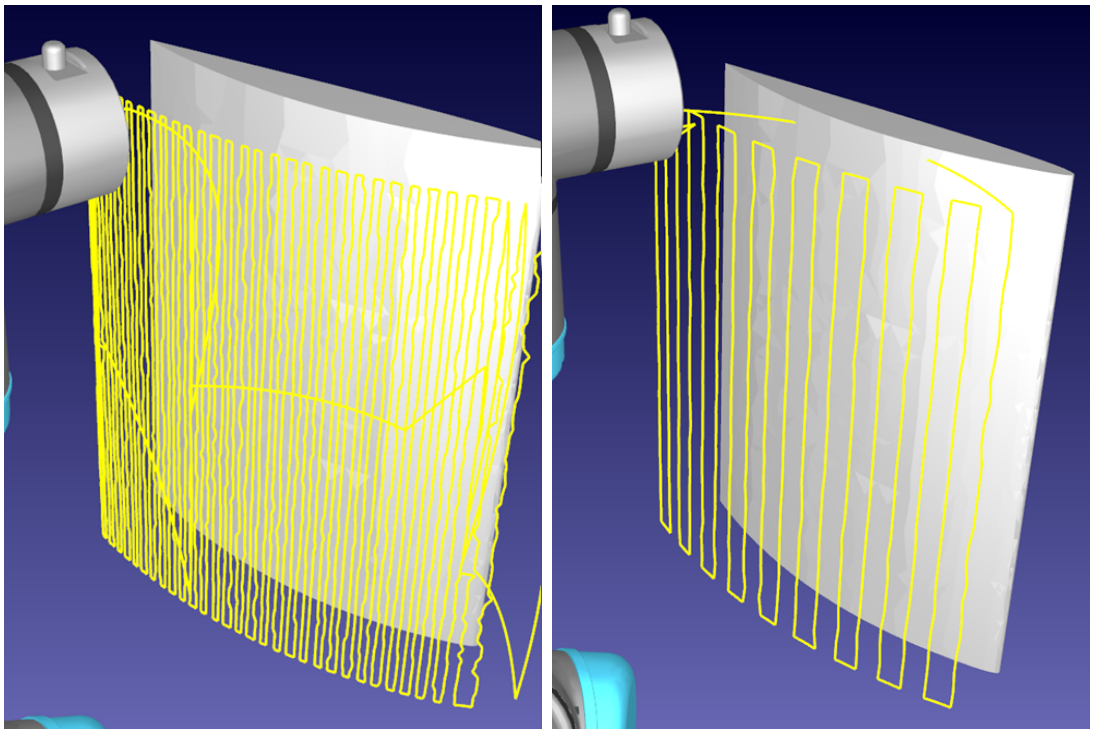

(a) (b)

Figure 3.7: Demonstration of rasterizing a curved aerofoil component. The robotic path is traced in yellow, demonstrating the raster-like path obtained. (**a**) Sampling distance: 3 mm. (**b**) Sampling distance: 10 mm.

stages, displayed in Fig: 3.8. Fig: 3.8 demonstrates that the CSFA is adept at covering complex surfaces without traversing holed regions while still capturing the whole surface without the planar limits of the plate as input.

Repeatedly holed surfaces present multiple points of return, demonstrated in Figure 3.9.

The surface linearisation approximation made by the CSFA in order to discover discrete neighbouring positions is demonstrated to be effective on surfaces of positive and negative curvature, as in the sphere and bowl. Robustness to local curvature variations is displayed in Figure 3.10.

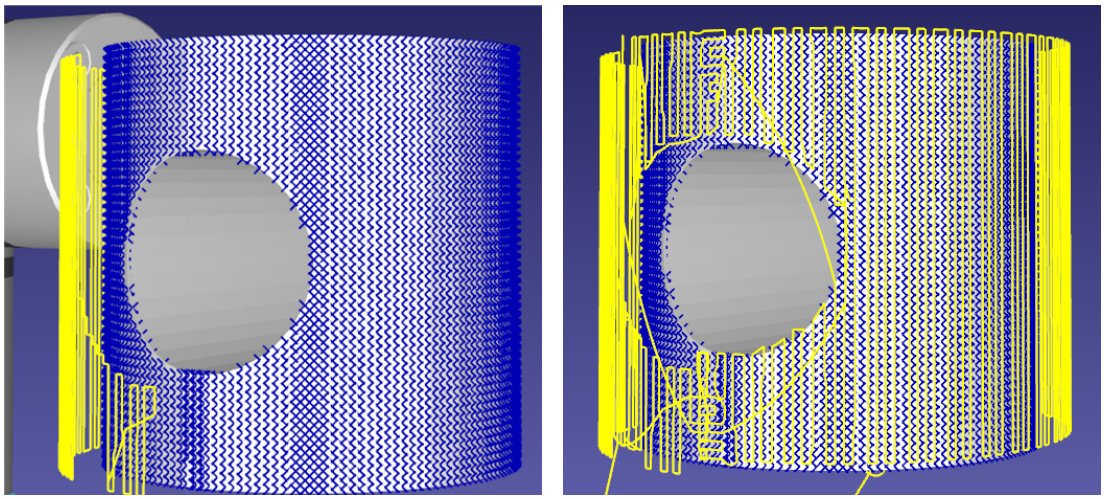

(a) (b)

Figure 3.8: The scan initially misses sections of the pipe due to the shape's cross-sectional hole.The missed points are picked up at the end of the scan as there is memory of surface-positions to check. Points found are marked in blue, the robotic path traced in yellow. (**a**) Initial scan-pass, the robot's flange seen to the left. (**b**) End-of-scan.

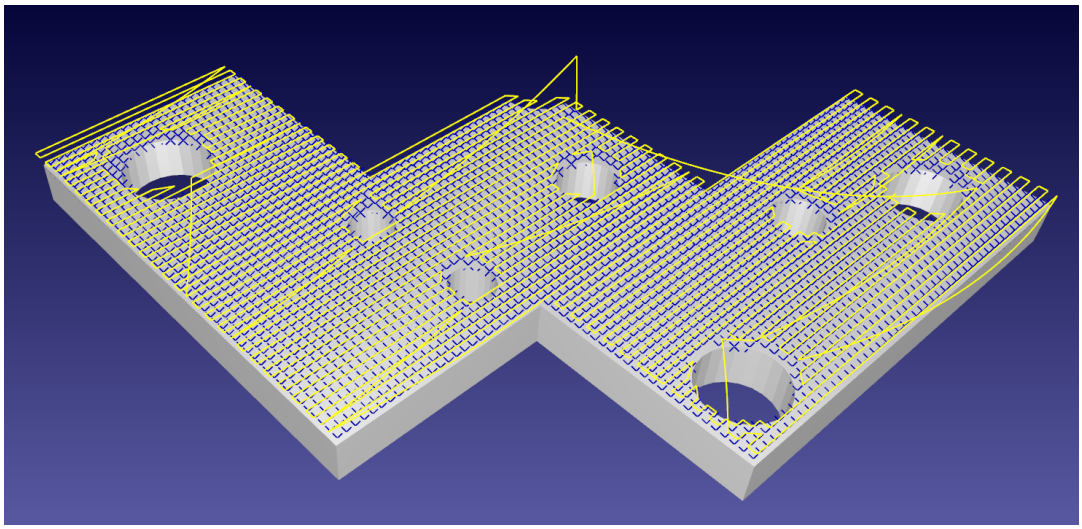

Figure 3.9: A complex flat plate holed with differently sized voids. The robotic path in yellow backtracks to allow for full surface discovery, shown by blue crosses, in the presence of surface-discontinuities.

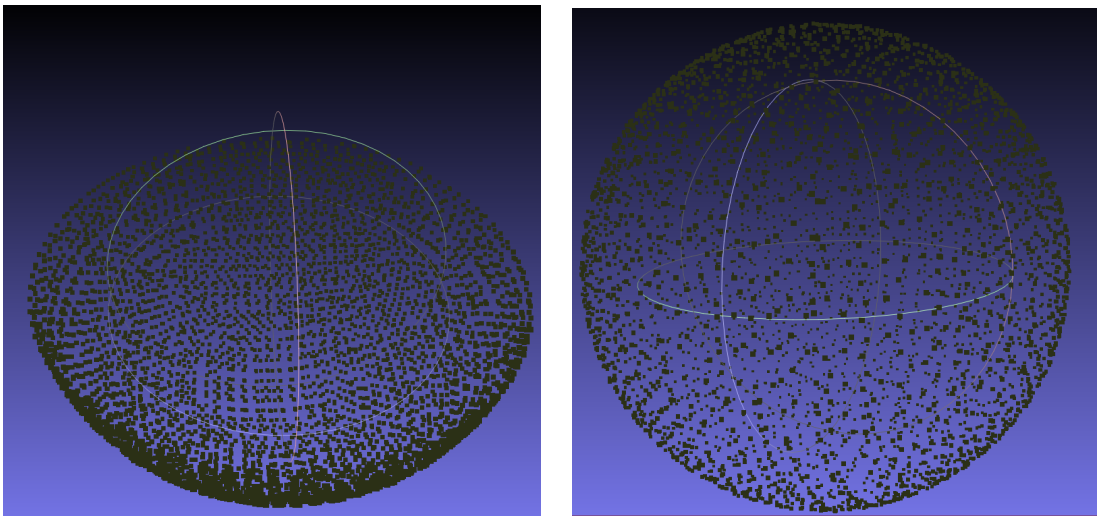

(a) (b)

Figure 3.10: Points discovered while simulating a scan on a bowl and sphere of radius 150 mm with a sampling distance of 3 mm. (**a**) Concave shape sampling. (**b**) Sphere sampling.

The irregular rasterization patterns may be seen in Figure 3.11. Unlike for surfaces of only one direction of curvature such as in Fig: 3.7 or Fig: 3.8, rasterization for double-curvature surfaces is irregular. This incurs inefficient motions compared to traditional spiral-rasterization patterns.

A horizontal rasterization pattern of subsequent circles resembling traditional spiralized patterns may be imposed by using a preferred direction vector; however, they can result in large re-arrangement procedures seen in Fig: 3.12.

Curvature considerations are also demonstrably necessary for full surface coverage of components. Without over-sampling the space based on known surface curvature, full coverage is not guaranteed since taking a step will not necessarily take the algorithm to a new Octree-leaf. In turn, the algorithm stops prematurely

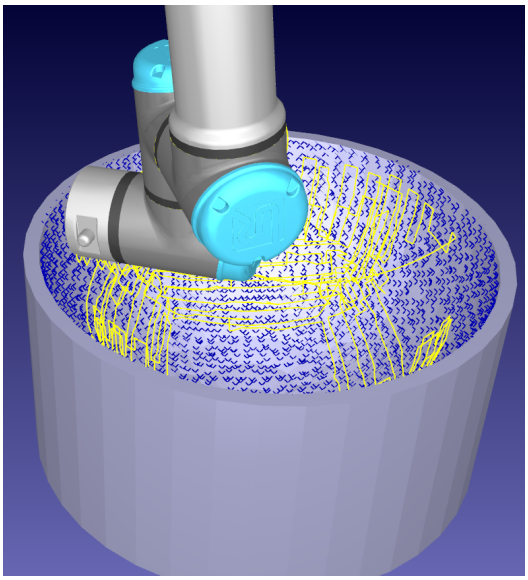

Figure 3.11: Sampling on a concave shape. The robotic path, that can form irregular patterns without a preferred direction, is shown in yellow. Discovered points on the bowl are shown as blue crosses.

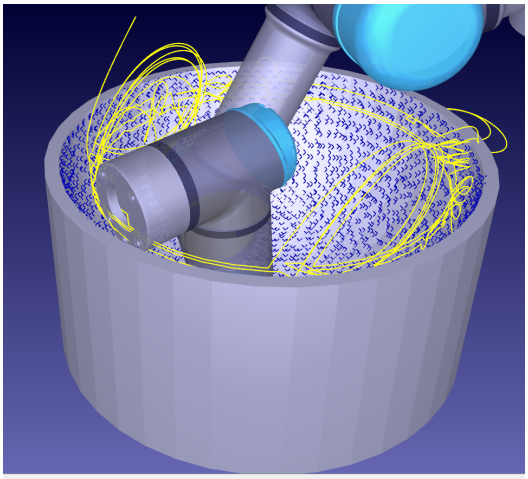

Figure 3.12: Sub optimal horizontal rasterization of a concave surface. Yellow trace lines demonstrate costly re-arrangement procedures to discover all the points shown in blue.

as it aliases the points before and after the step within the Octree map. The effect of this is displayed in Figure 3.13.

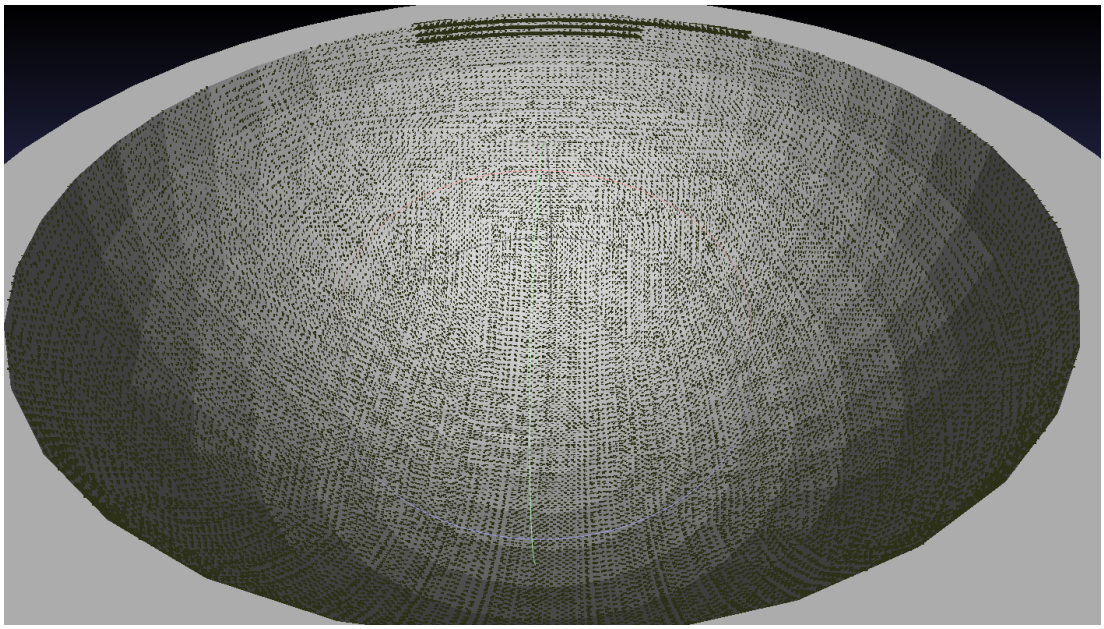

Figure 3.13: Points in bold display the extent of discovery with no over-sampling regime. Sampling rate: 1 mm, radius of bowl: 150 mm.

3.5.2 Experimental Results

Operated on a UR10e platform, experimental results were gathered using both a Matlab and a C++ toolbox. For collecting the UT data, a TCP/IP connection through Matlab was set-up with both a PeakNDT LTPA pulser/receiver, communicating with the UR10e through RoboDK, a robotics simulation and interface software package.

For the tri-laser tests, an external arduino relayed the laser signal through to an external C++ programme, also communicating with the robotic platform through a TCP/IP connection.

In the deployment stage, two key test pieces were identified to validate the algorithm's practicality in deployment. These were a surface of doubled-curvature

and a surface with a cut-out. The doubly curved surface has been chosen to show that with the correct step size, sensors with small ranges may complete the search process, and that the approximation found for the surface normal is a suitable one. Moreover, since the important quantity in Octree sampling to guarantee completeness is the ratio of curvature to step size, the doubly curved surface shows that the heuristic presented is applicable to surfaces of all curvatures, given a step size that does not hinder sensor-surface coupling. The part with a section cut out further validates the approach when the surface is not globally represented by a global b-spline, as is necessary within the nearest algorithm.

It is important to note that the hardware chosen for completing the scanning process is the limiting factor, as smaller sensors are necessary to complete scans on objects that have extreme curvatures.

3.5.3 Immersion UT Probe

Initially, an immersion UT sensor was deployed to cover the surface completely. By using the single-element SAFT method, the surface's boundary is approximated. A linear 64 element 5MHz UT sensor was used to collect data and path plan in real time. Due to the necessity of using the tangent plane, two sets of data in perpendicular orientations were collected for each position, with each set of data processed to approximate the best fit spline for the surface and the four cardinal tangent directions extracted.

With the overall set-up seen in Fig: 3.14, the iterative process was tested on an immersed and curved CFRP component seen in Fig: 3.15.

Figure 3.14: Immersion bath set-up of a 5MHz linear PA sensor mounted to an UR10e robotic platform. Flange height and orientation as well as speed limits were in place to prevent submersion or leakage onto the robotic controller.

The key drawback of the immersion probe method was the unreliable surface response from the probe, resulting in erroneous positions identified at the edges of each part, highlighted in Fig: 3.16. Further, to protect the robotic platform a set of safety measures had to be taken to ensure the flange did not go beneath the water-line. This severely limited the geometries that could be scanned, resulting in sub-optimal results and a limitation to the parts. The coupling method added further issues that prevent either scalability in the case of immersion scanning,

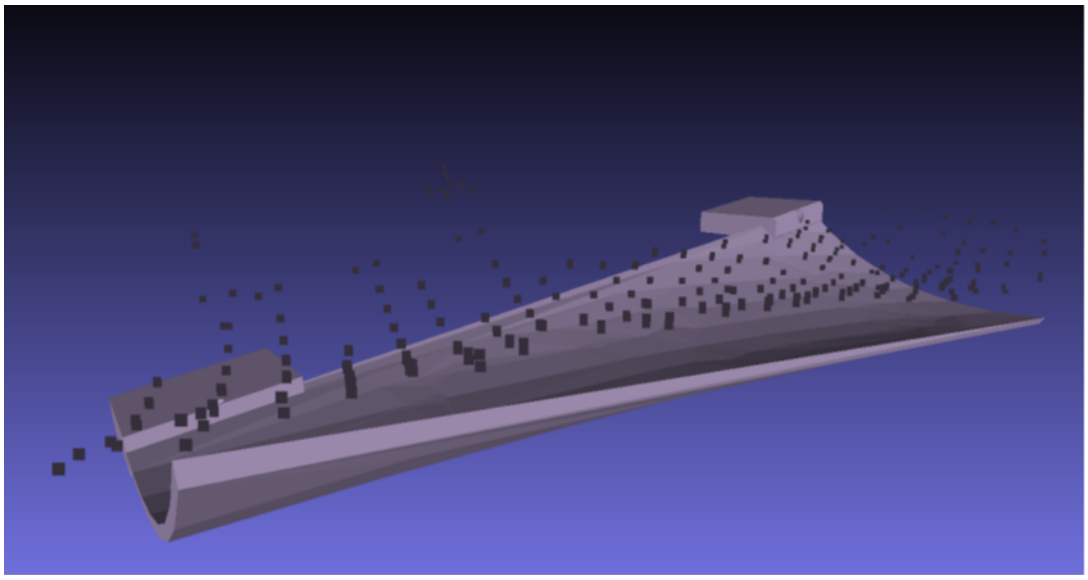

Figure 3.15: Immersion testing of the CSFA with a curved CFRP component. Complete traversal was hindered by the curvature and necessary height and orientation limitations ensuring the safety of the probe and robot.

or on-site deployment in the case of jet-PAUT.

The images in this section have been compared against provided CAD models within a MeshLab environment, since algorithmic alignment was impossible with the fringe artefact positions present.

An alternate coupling method for surface scanning was sought to prevent the limitations of water-based coupling to the surface. Conformable Wedge Probes (CWPs) were employed later in Chapter: 4 to scan parts. Due to the limitations of the variable gating necessary for CWP deployment in accurate surface profile retrieval, the process of tangent plane extraction required additional sensing capabilities. The next section describes how three low-cost laser distance sensors were used to provide high-accuracy tangent plane and position estimates.

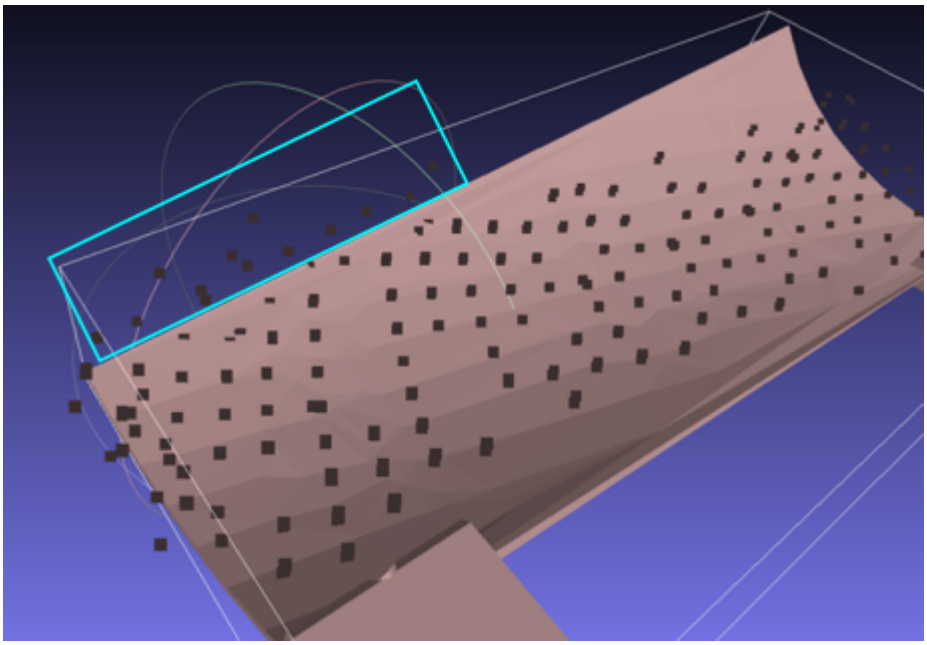

Figure 3.16: CSFA applied to a curved part within an immersion tub. Reflections from edge positions along the part created phantom signals, examples highlighted in blue, when the probe was not directly over the part, extending the scan and reducing the resultant point cloud's resemblance to the real part.

3.5.4 Tri-Laser

The three hG-C 1030 Panasonic lasers used within the following experiments had an accuracy in the order of $10\mu m$, several times smaller than the robotic repeatability of $0.05mm$ [42]. The laser's class II rating enables deployment alongside human operators, enabling easy deployment to on-site inspections.

The laser's viewing range was 30 mm $\pm$ 5 mm, limiting the feasible step size over highly curved surfaces, as height variations of over 5 mm over the step would remove the possibility of further surface discovery. The laser's repeatability did not affect motion planning, as the robot's own repeatability is in the range of 100 μm. The lasers were held within a 3D-printed cradle displayed in Fig: 3.17.

Connecting through a COM port and Ethernet-enabled TCP/IP connection, respectively, position data and commands were received and sent to the robot from a laptop. The CSFA, data interpretation, and inverse kinematics solutions were coded in C++. The external laptop had an Intel Core i5 processor with the program built and run from a Visual Studio programming environment.

Figure 3.17: The tri-laser holder, attached to the UR10e flange. The design with rotational symmetry around axis 6 of the robot minimised the footprint of the tool.

To represent a non globally smooth b-splineable surface, laminate plates were placed into a planar pattern with a cut out displayed in Figure: 3.18a alongside

the point-cloud of collected data displayed in Fig: 3.18b. Full discovery of the target surface demonstrates the applicability of the CSFA in cases where a direct path along the surface to every point is not possible. The recollection of hypothesised points to visit allows traversal around corners, completely scanning regions with no direct path to one another.

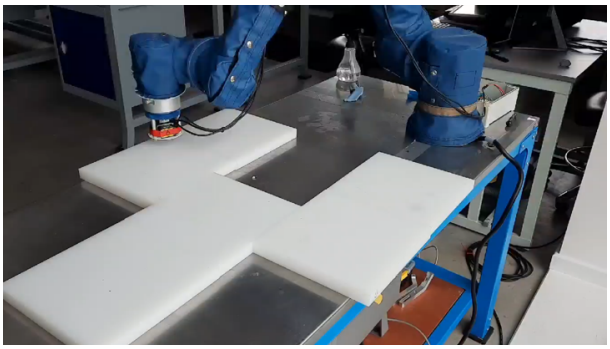

(a)

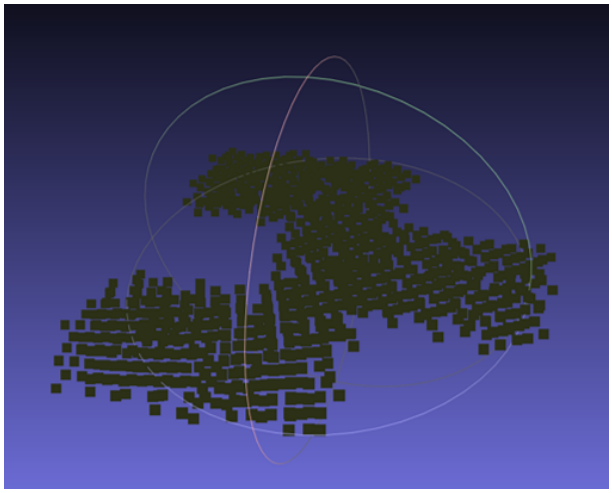

(b)

Figure 3.18: Automatic online profiling and scanning of an object with non-smooth shape. After a new point is found, the UT probe is applied to collect data. (**a**) Non-smooth shape created from arranged plates. (**b**) Resultant point cloud collected by the tri-laser and projected to the World-Frame using the live Joint-position of the robot.

A curved mock-aerofoil segment provided additional experimental data dis-

playing application to a use-case commonly seen within NDT in Fig: 3.19. The total time taken for this use-case was 7 min 30 s for 30mm spaced collection points. Providing a real-world use-case for NDT, the full surface discovery of a doubly-curved surface with no-prior path planning provides the proof of concept for single-pass profiling of a complex surface and validation for the linearised surface approximation, while the part is relatively small compared to the robot's reach, the strength of this example is in the surface's extreme curvature. This use-case validates the application to surfaces commonly seen as complex within NDT.

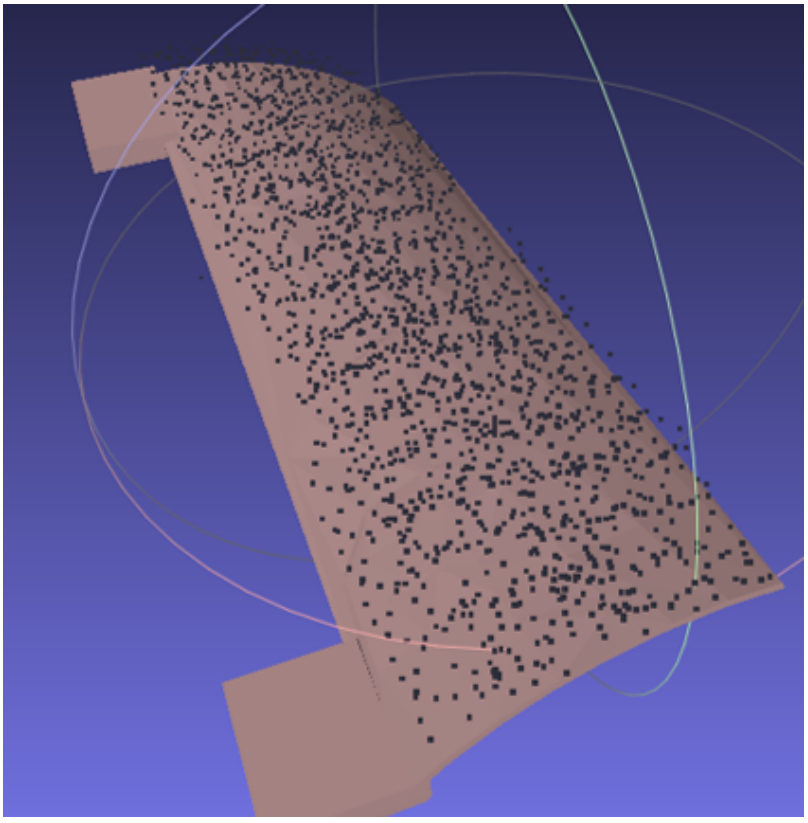

Figure 3.19: Point Cloud of a complex doubly-curved surface profiled in real time, aligned to the CAD model in post-processing.

Finally, a proof of concept for simultaneous non-contact surface profiling with the tri-laser platform combined with Conformable-Wedge-Probe scanning was developed. Each step involves two sub-steps; the tri-laser discovers the surface, displayed in Fig: 3.20a, the tool reversed and the Conformable Wedge Probe applied to the discovered position, displayed in Figure: 3.20b.

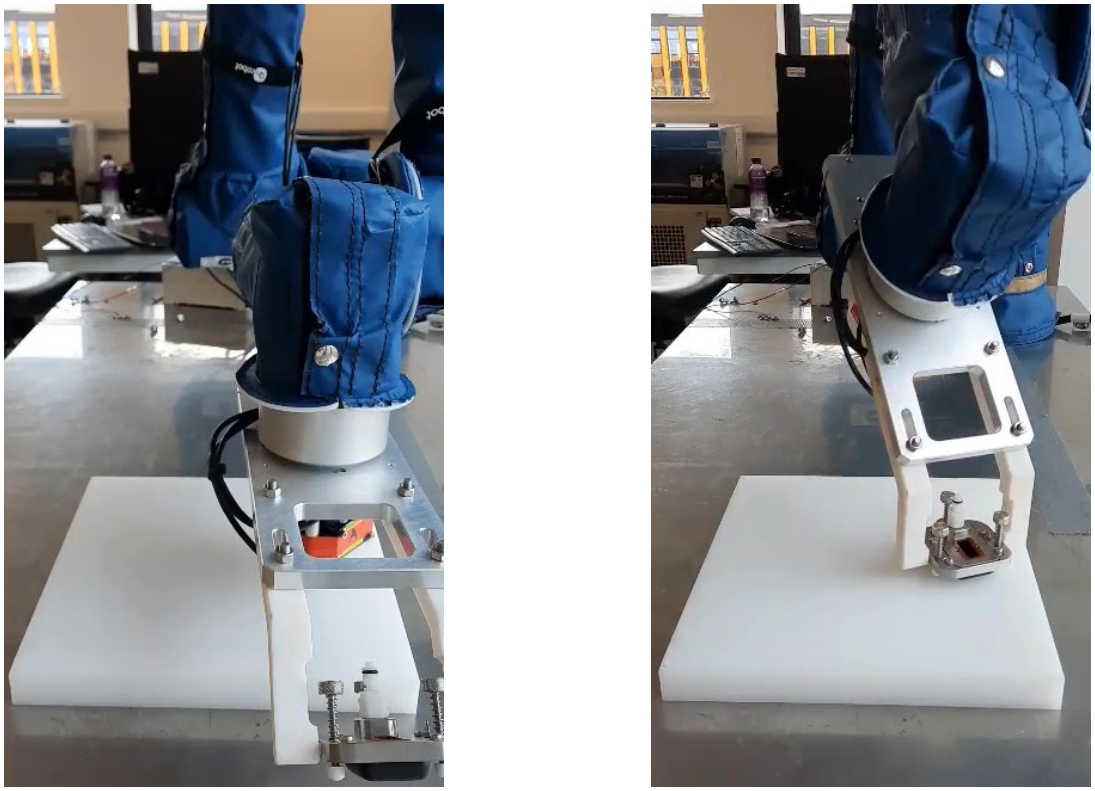

(a) (b)

Figure 3.20: Automatic online single-pass profiling of a surface. (**a**) Initial non-contact surface discovery and profiling with the tri-laser. (**b**) Subsequent application of the Conformable-Wedge coupled UT device.

In deployment, sensor ranges provided the most significant challenge. Since the tool's base had a diameter of $50mm$, the curvature of parts observed within that region had to not exceed the viewing range of the laser-sensors in order to

ensure the tool and part did not collide.

The main source of risk to deployment was an incorrect laser-tool calibration. During early testing, the sensor's beam had an orientation offset caused by printing errors that with larger step-sizes often risking collisions with the part. For the experimental validation phase, the tool was re-printed to correct the laser-flange alignment issue, then one laser was calibrated using the standard four-point spiking method used in robotic tool calibration procedures [43]. Since there was rotational symmetry of the tool around the z-axis, the other two laser's positions were inferred from rotating the initial laser calibration value. To find the accuracy of the calibrated system, data was collected along a smooth planar polymer surface, the data fitted to a plane and the error taken as deviation from the plane. The standard deviation of the absolute error was $0.81mm$, however the mean signed error was $O\left(10^{-16}\text{ mm}\right)$. This implies that while the laser data represented an offset from the surface with $> 100\mu m$ deviation, this was caused by the 3D printer's tolerance, displacing each laser from the idealised rotated position around the flange resulting in an offset that led to deviations from the plane's surface, a factor that can be solved with machining of the tool. Given the lasers range of $30mm \pm 5mm$, this error did not represent a large risk of collision since even at up to 3 standard deviations of error at the laser's minimum operating distance, the position estimate would only be 10% out of alignment.

Further, while demonstrations were limited by the lack of a collision avoidance

process, these experiments have proven the algorithm's capability in autonomous scanning processes, and applicability to robotic NDT. The main challenge facing industrial deployment of robotic NDT where parts have no accurate digital representation is the flexibility of the robotic platforms in use, and their ability to define complete surface coverage. The author has demonstrated the ability of this algorithm to overcome this issue in realistic contexts through autonomous limited-aperture sensor traversal.

3.6 Conclusion and Discussion

In post-processing, the CSFA has been shown to output a raster-path along arbitrarily locally differentiable surfaces. For doubly-curved surfaces, the rasterization pattern becomes irregular and there is an over-sampling of points. However, the method ensures total coverage of the part which is preferable in NDT to sparse sampling. The potential applications of the algorithm are not limited to automatic rasterization procedures. The Octree memory method would allow fully automated discovery and scanning of structures with any robotic platform, such as mobile robots traversing a large structure. Further, the traversal method can be applied with any limited-aperture sensor, enabling a generalised surface-movement strategy when sensor data is limited. Finally, the discrete-point approach allows the method to capture surfaces that cannot be globally splined. The limitation in the case of significant surface discontinuities such as part-edges is that the process will not necessarily find the other side of the part, the limit to full surface discovery being then the sensor's range and aperture size relative to the discontinuity. In practical deployments the sensor range also limited the sensor's step size due to the surface curvature so as to continue full surface discovery. Practical experiments applied to complex cut-out surfaces and realistic doubly curved aerofoil mock-ups show the real-world application with limited-range laser sensors. Proof of concept for wedge-probe coupled UT applications provide the NDT specific aims of this chapter of removing the need to path plan

for full-surface scanning.

For complex surfaces such as aerofoils or machined plates with cut-outs, the algorithm demonstrated is safe for deployment. For more complex shapes such as external pipe-scans, limited knowledge of the environment is necessary to prevent collisions. Future work will deploy the algorithm using low-cost environmental sensors to prevent collisions and path planning such as Rapidly exploring Random Trees (RRT) algorithms to scan complex components.

Future work considering collision prevention is key to the robotic-arm deployment method. While the presented approach is suitable for drone or crawler based deployment due to their relatively small profiles, robotic arm complexity presents a significant challenge when naïvely scanning complex objects.

The simulated extraction of raster-patterns takes advantage of the programme's ability to check positions without adding them to the visited bucket. A direction preference therefore allows the process to fill positions within the given raster line, and then recursively check positions which have already been visited, without the need to visit them. The output is the visited stack presenting as a rasterisation pattern similar to most path planning software. However, in practice the curvature of the part may require the robot to exhaustively visit positions within the to-visit stack since the hypothesised position may align to a point which has been visited. The offline version allows this point to be ignored, while the online version must visit this point to ensure it has been visited. Future work flexibly

rasterising over the surface without prior knowledge or offline programming is a key consideration in terms of time optimality.

The CSFA presents a complete surface traversal and profiling method when the part is unknown, and can be applied to various situations involving autonomous exploration of unknown environments. For the application of robotic-arm NDT, there are significant short-falls. The work presented in Section: 4 seeks to address these challenges, and present an alternate autonomous scanning process that builds upon the progress made within this section.

Bibliography

[1] M. Callieri, A. Fasano, G. Impoco, Paolo Cignoni, R. Scopigno, G. Parrini, and G. Biagini. Roboscan: an automatic system for accurate and unattended 3d scanning. 2004.

[2] Simon Kriegel, C. Rink, T. Bodenmüller, and M. Suppa. Efficient next-best-scan planning for autonomous 3d surface reconstruction of unknown objects. *Journal of Real-Time Image Processing*, 10:611–631, 2013.

[3] Cihan Uyanik, Sezgin Secil, Metin Ozkan, Helin Dutagaci, Kaya Turgut, and Osman Parlaktuna. Spgs: A new method for autonomous 3d reconstruction of unknown objects by an industrial robot. In Manuel Giuliani, Tareq Assaf, and Maria Elena Giannaccini, editors, *Towards Autonomous Robotic Sys-*

tems, pages 15–27, Cham, 2018. Springer International Publishing. ISBN 978-3-319-96728-8.

[4] Randa Almadhoun, Abdullah Abduldayem, Tarek Taha, Lakmal Seneviratne, and Yahya Zweiri. Guided next best view for 3d reconstruction of large complex structures. *Remote Sensing*, 11(20), 2019. ISSN 2072-4292. doi: 10.3390/rs11202440. URL `https://www.mdpi.com/2072-4292/11/20/2440`.

[5] Aamir Khan, Carmelo Mineo, Gordon Dobie, Charles Macleod, and Gareth Pierce. Vision guided robotic inspection for parts in manufacturing and remanufacturing industry. *Journal of Remanufacturing*, 11(1):49–70, Apr 2021. ISSN 2210-4690. doi: 10.1007/s13243-020-00091-x. URL `https://doi.org/10.1007/s13243-020-00091-x`.

[6] Alojz Kopáčik, Ján Erdélyi, and Peter Kyrinovič. *Coordinate Measuring Systems and Machines*, pages 121–141. Springer International Publishing, Cham, 2020. ISBN 978-3-030-48309-8. doi: 10.1007/978-3-030-48309-8_7. URL `https://doi.org/10.1007/978-3-030-48309-8_7`.

[7] K. Lu, W. Wang, Yaofeng Wu, Yan ding Wei, and Zichen Chen. An adaptive sampling approach for digitizing unknown free-form surfaces based on advanced path detecting. *Procedia CIRP*, 10:216–223, 2013.

[8] Xue Ming He, Jun Fei He, Mei Ping Wu, Rong Zhang, and Xiao Gang Ji.

Reverse engineering of free-form surface based on the closed-loop theory. *The Scientific World Journal*, 2015, Mar 2015. ISSN 2356-6140. doi: 10.1155/2015/903624. URL https://doi.org/10.1155/2015/903624.

[9] Yang Zhang, Kai Chen, Peng Guo, Fan Li, Jiang Zhu, and Li-Min Zhu. Profile tracking for multi-axis ultrasonic inspection of model-unknown free-form surfaces based on energy concentration. *Measurement*, 172:108867, 2021. ISSN 0263-2241. doi: https://doi.org/10.1016/j.measurement.2020.108867. URL https://www.sciencedirect.com/science/article/pii/S0263224120313579.

[10] Zi Zhou, Yang Zhang, and Kai Tang. Sweep scan path planning for efficient freeform surface inspection on five-axis cmm. *Computer-Aided Design*, 77:1–17, 2016. ISSN 0010-4485. doi: https://doi.org/10.1016/j.cad.2016.03.003. URL https://www.sciencedirect.com/science/article/pii/S0010448516300045.

[11] D. Guo, Guojun Jiang, Yue Wu, and J. Cheng. Automatic ultrasonic testing for components with complex surfaces. *DEStech Transactions on Engineering and Technology Research*, 2017.

[12] M. Morozov, S.G. Pierce, C.N. MacLeod, C. Mineo, and R. Summan. Off-line scan path planning for robotic ndt. *Measurement*, 122:284–290, 2018. ISSN 0263-2241. doi: https://doi.org/10.1016/j.measurement.2018.

02.020. URL https://www.sciencedirect.com/science/article/pii/S0263224118301131.

[13] Bo Ye, Ming Li, and Fang Zeng. A novel technique for eliminating probe lift-off in eddy current nondestructive testing. In *Advances in Energy Science and Technology*, volume 291 of *Applied Mechanics and Materials*, pages 2474–2478. Trans Tech Publications Ltd, 4 2013. doi: 10.4028/www.scientific.net/AMM.291-294.2474.

[14] Mark Levoy. Area flooding algorithms: Two-dimensional computer animation course notes, 1981.

[15] MS Windows developer floodfill function. https://docs.microsoft.com/en-us/windows/win32/api/wingdi/nf-wingdi-floodfill, . Accessed: 19-03-2021.

[16] N. Bhargava, P. Trivedi, A. Toshniwal, and H. Swarnkar. Iterative region merging and object retrieval method using mean shift segmentation and flood fill algorithm. In *2013 Third International Conference on Advances in Computing and Communications*, pages 157–160, 2013. doi: 10.1109/ICACC.2013.100.

[17] P. Chu, Seoungjae Cho, Y. Park, and Kyungeun Cho. Fast point cloud segmentation based on flood-fill algorithm. *2017 IEEE International Conference*

on Multisensor Fusion and Integration for Intelligent Systems (MFI), pages 656–659, 2017.

[18] T. Lee, S. Lim, S. Lee, S. An, and S. Oh. Indoor mapping using planes extracted from noisy rgb-d sensors. In *2012 IEEE/RSJ International Conference on Intelligent Robots and Systems*, pages 1727–1733, 2012. doi: 10.1109/IROS.2012.6385909.

[19] Yixuan He, Tianyi Hu, and Delu Zeng. Scan-flood fill(scaff): an efficient automatic precise region filling algorithm for complicated regions, 2019.

[20] K. Chen, J. Xi, and Y. Yu. Fast quality-guided phase unwrapping algorithm for 3d profilometry based on object image edge detection. In *2012 IEEE Computer Society Conference on Computer Vision and Pattern Recognition Workshops*, pages 64–69, 2012. doi: 10.1109/CVPRW.2012.6239239.

[21] Yuanbo Li, Xiaoqian Cui, Hongbei Wang, Mengge Zhao, and Hongbin Ding. Comparison of phase unwrapping algorithms for topography reconstruction based on digital speckle pattern interferometry. In Jin Yu, Zhe Wang, Wei Hang, Bing Zhao, Xiandeng Hou, Mengxia Xie, and Tsutomu Shimura, editors, *AOPC 2017: Optical Spectroscopy and Imaging*, volume 10461 of *Society of Photo-Optical Instrumentation Engineers (SPIE) Conference Series*, pages 450–461, Oct 2017. doi: 10.1117/12.2285771.

[22] Qingliang Li, Chunyu Bao, Jiashi Zhao, and Zhengang Jiang. A new

fast quality-guided flood-fill phase unwrapping algorithm. 1069, aug 2018. doi: 10.1088/1742-6596/1069/1/012182. URL https://doi.org/10.1088/1742-6596/1069/1/012182.

[23] K. Chen, Jiangtao Xi, Yanguang Yu, and J. Chicharo. Fast quality-guided flood-fill phase unwrapping algorithm for three-dimensional fringe pattern profilometry. In *SPIE/COS Photonics Asia*, 2010.

[24] Lukasz Zmudzinski. Rough mereology based cfill algorithm for robotic path planning (short paper). In Krzysztof Ropiak, Lech Polkowski, and Piotr Artiemjew, editors, *Proceedings of the 28th International Workshop on Concurrency, Specification and Programming, Olsztyn, Poland, September 24-26th, 2019*, volume 2571 of *CEUR Workshop Proceedings*. CEUR-WS.org, 2019. URL http://ceur-ws.org/Vol-2571/CSP2019_paper_13.pdf.

[25] Ibrahim Elshamarka and Abu Saman. Design and implementation of a robot for maze-solving using flood-fill algorithm. *International Journal of Computer Applications*, 56:8–13, Oct 2012. doi: 10.5120/8885-2882.

[26] S. Kibler and D. Raskovic. Coordinated multi-robot exploration of a building for search and rescue situations. In *Proceedings of the 2012 44th Southeastern Symposium on System Theory (SSST)*, pages 159–163, 2012. doi: 10.1109/SSST.2012.6195147.

[27] S. Tjiharjadi and E. Setiawan. Design and implementation of a path

finding robot using flood fill algorithm. *International Journal of Mechanical Engineering and Robotics Research*, 5:180–185, Oct 2016. doi: 10.18178/ijmerr.5.3.180-185.

[28] S. Tjiharjadi, M. Wijaya, and E. Setiawan. Optimization maze robot using a* and flood fill algorithm. volume 6, pages 366–372, Sep 2017. doi: 10.18178/ijmerr.6.5.366-372.

[29] S. Ranade and P. V. Manivannan. Quadcopter obstacle avoidance and path planning using flood fill method. In *2019 2nd International Conference on Intelligent Autonomous Systems (ICoIAS)*, pages 166–170, 2019. doi: 10.1109/ICoIAS.2019.00036.

[30] M. Kalisiak and M. van de Panne. Rrt-blossom: Rrt with a local flood-fill behavior. In *Proceedings 2006 IEEE International Conference on Robotics and Automation, 2006. ICRA 2006.*, pages 1237–1242, 2006. doi: 10.1109/ROBOT.2006.1641878.

[31] J. Guo, Yung Lin, Kuo Su, and Bo Li. Motion planning of multiple pattern formation for mobile robots. *Applied Mechanics and Materials*, 284-287: 1877–1882, 01 2013. doi: 10.4028/www.scientific.net/AMM.284-287.1877.

[32] John M. Lee. *Riemannian Metrics*, pages 9–54. Springer International Publishing, Cham, 2018. ISBN 978-3-319-91755-9. doi:

10.1007/978-3-319-91755-9_2. URL https://doi.org/10.1007/978-3-319-91755-9_2.

[33] Rowe P. Kerr W, Pierce SG. Investigation of synthetic aperture methods in ultrasound surface imaging using elementary surface types. *Ultrasonics*, 72: 165–76, Dec 2016. doi: 10.1016/j.ultras.2016.08.007.

[34] *4. Migration*, pages 463–654. 2012. doi: 10.1190/1.9781560801580.ch4. URL https://library.seg.org/doi/abs/10.1190/1.9781560801580.ch4.

[35] H. Chase. Fundamental forms of surfaces and the gauss-bonnet theorem. https://math.uchicago.edu/~may/REU2012/REUPapers/Chase.pdf, Aug 2012. Accessed: 01-09-2021.

[36] Matthias Teschner, Bruno Heidelberger, Matthias Mueller, Danat Pomeranets, and Markus Gross. Optimized spatial hashing for collision detection of deformable objects. pages 47–54, 2003.

[37] Seonho Cho and Seung-Hyun Ha. Isogeometric shape design optimization: exact geometry and enhanced sensitivity. *Structural and Multidisciplinary Optimization*, 38(1):53, May 2008. ISSN 1615-1488. doi: 10.1007/s00158-008-0266-z. URL https://doi.org/10.1007/s00158-008-0266-z.

[38] Fengkui Cui, Yongxiang Su, Shaoke Xu, Fei Liu, and Guolin Yao. Optimization of the physical and mechanical properties of a spline surface fabri-

cated by high-speed cold roll beating based on taguchi theory. *Mathematical Problems in Engineering*, 2018:8068362, Feb 2018. ISSN 1024-123X. doi: 10.1155/2018/8068362. URL https://doi.org/10.1155/2018/8068362.

[39] Rajkumar Roy, Graham Jared, and Riaz Mussa. Curve and surface optimization within the cad/cam environment. *Journal of Engineering Design*, 13(2):121–139, 2002. doi: 10.1080/09544820210129797. URL https://doi.org/10.1080/09544820210129797.

[40] Pilseong Kang and Sung-Kie Youn. Isogeometric topology optimization of shell structures using trimmed nurbs surfaces. *Finite Elements in Analysis and Design*, 120:18–40, 2016. ISSN 0168-874X. doi: https://doi.org/10.1016/j.finel.2016.06.003. URL https://www.sciencedirect.com/science/article/pii/S0168874X16300798.

[41] Simon perreault's c++ octree implementation. https://nomis80.org/code/octree.html, . Accessed: 19-03-2021.

[42] *UR10e Product Fact Sheet*. Universal Robots, July 2021. URL https://www.universal-robots.com/media/1807466/ur10e-rgb-fact-sheet-landscape-a4-125-kg.pdf.

[43] Jonathan Malott. Calibrate a new tool, 2023. URL https://wikis.utexas.edu/display/SOAdigitech/Calibrate+a+New+Tool.

Chapter 4

Autonomous Collision Free Surface Profiling, Planning and Scanning using the Tool's, the Planar Projective, and the Robotic-Configuration Spaces

The algorithm introduced in the previous section has demonstrated an effective autonomous surface profiling methodology for limited aperture sensors. Despite defining coverage and closure conditions, collision with the part at unknown positions remains a possibility. The CSFA, and its single-element ultrasonic analogue

[1] enable the autonomous profiling of an entire surface given stand-off and curvature requirements. Both of these methods, however, utilise discrete positioning methods so that their speed is incomparable with digital-twin assisted methods. While the method presented in [1] allows efficient surface coverage, there is still an issue of collisions with unseen surface points. This is of particular importance for 6 DoF robotic arms, since their complex kinematic relations can admit 8 inverse kinematic solutions for each Cartesian position, some of which may collide with the part. For certain industrial robots such as KUKA KR16 arms, the limited angles of rotation for each joint complicate unknown-part scanning further. In Fig: 4.1 the limited angles for each joint of a KR6 are shown.

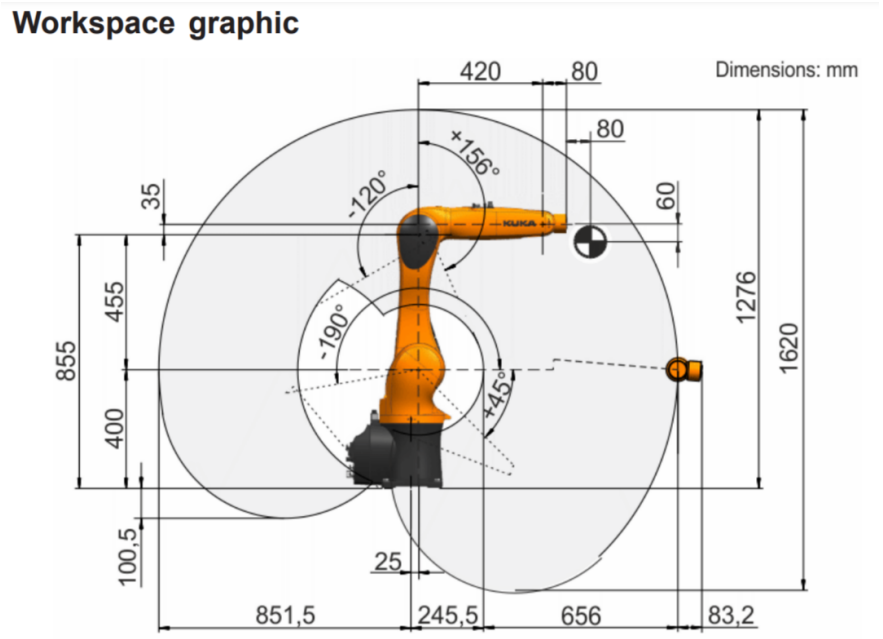

Figure 4.1: Cross section of the KR 6 R900 sixx's workspace [2]. The limited angles of each joint are graphically displayed, resulting in a limited work-space that is further restricted when considering specific poses well within the given work-volume.

While this thesis has chosen to use the Universal Robots series due to their maneuverability ensuring their applicability for on-site inspections, presented work within this thesis seeks to be applicable to static work-cells in industries such as remanufacturing.

The eight potential solutions are reduced depending on where in the Configuration space the part and arm are, requiring some positions to be either avoided or for complex re-arrangement procedures to enable the robot to reach additional positions. Prior knowledge of the part is required to enable the robot to fully traverse the surface in a way that avoids collisions and ensures full coverage.

This section seeks to address the issues of;

1. Efficient part localisation with a tool that enables further applications,
2. Collision detection using the surface location,
3. Efficient coverage of the part that has been seen,
4. Scanning speeds that can be commercially deployed,
5. Maximising overall maneuverability and minimising the costs of the above system to enable easy and risk minimised site deployment.

The outcome of this investigation is an algorithm that utilises potentially incomplete point cloud data with non-trivial depth estimation errors to autonomously plan paths over unknown geometries. The work-flow of this simple and fast

pipeline is shown in Fig: 4.2. Extending concepts from the previous section, the incomplete camera frame perspective is complemented with the tangent-plane perspective of the tool's frame of reference to provide full coverage with constant tool-part contact of the seen part.

Whereas the CSFA mainly utilised the tool's perspective to fully profile surfaces, this section explores further frames in order to efficiently cover the surface without collisions. Configuration space is utilised to find optimal starting positions to ensure full coverage of the part without collisions, enabled by additional environmental information. Environmental information collected flexibly requires additional sensing of the world frame, seen through the projective space of the tool.

The projective plane perspective is explored in Section: 4.1 as the perspective that enables the goal of flexibility in deployment mentioned in 5. Potential sensors and models are explored to find the optimal candidate sensor platform for gaining suitable environmental and part information with minimal accuracy, time, and data overheads. The robot's configuration perspective is applied to the collected noisy and incomplete environmental data in order to prevent collisions in Section: 4.2.1. The incomplete data collected is complemented by online control strategies in Section :4.2.2 that are taken from the tangent plane perspective, which was experimentally validated by the CSFA. The novel robotised CW probe method of deployment is then utilised to produce an additional and novel stream

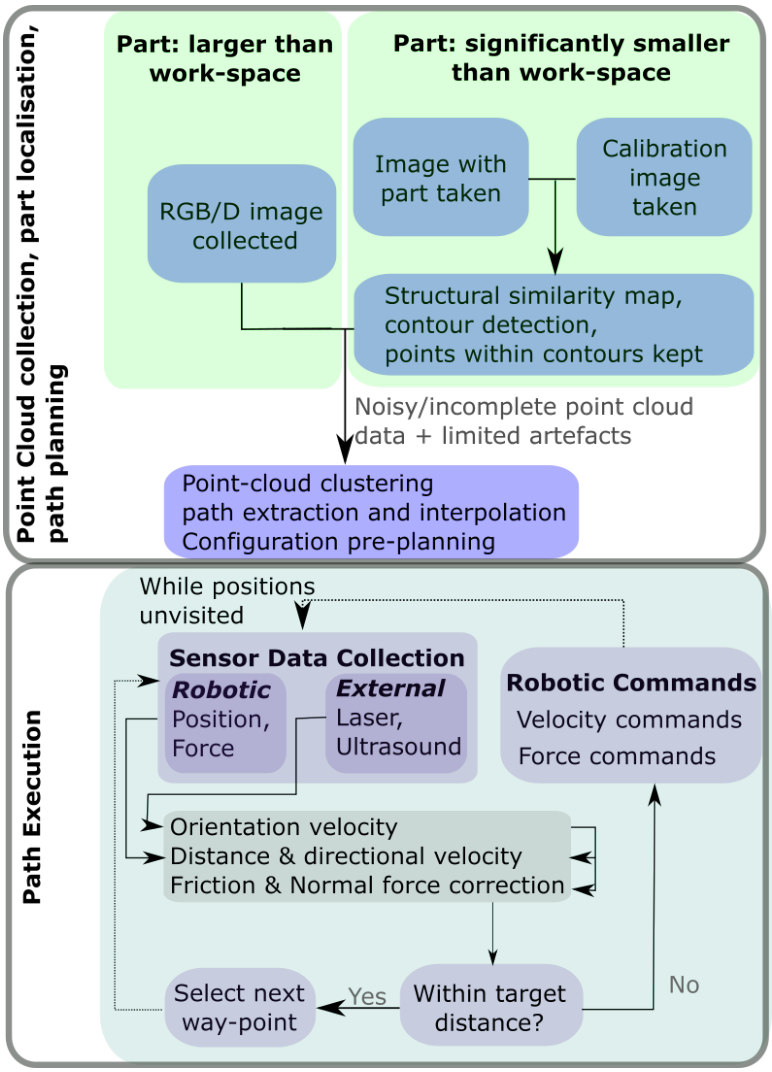

Figure 4.2: Part profiling, path planning, and path execution pipeline requiring minimal and noisy/incomplete visual information. The work-flows of path planning (top) and subsequent scanning (bottom) are presented in different containers. The top container illustrating the path planning work-flow highlights the individual image segmentation and planning processes for parts larger (left) and smaller (right) than the robot's work-space.

of NDT data in Section: 4.3, informing the operator of surface finish quality, an indicator of the scan's overall quality. Finally, experimental results are presented in Section: 5.5 demonstrating the efficacy of the individually developed

algorithms and pipeline as a whole on surfaces of selected geometries. Finally, the proof of concept CW probe tool introduced in Chapter: 3 is developed into a minimal-footprint modular sensor mount.

4.1 Path Planning from the Projected Plane Perspective

Traditional digital-representation applied path planning methods require accurate digital copies of the part available. In industrial applications [3], pre-scans involve high-quality reconstructions of parts using next-best-view methodologies such as in [4]. Point cloud representation quality can be assessed by metrics assessing deviations in curvature [5], as well as by area lost by the scanning processes' granularity imposed for example by voxelised data structures, highlighted as a quality metric in the 2D case in [6]. High quality models are not always necessary or time efficient. Power storage in remote applications is limited, reducing the time and motion the robot can scan, plan and then deploy in. While current models of scan, plan and deploy require precise robotic control and so an accurate map of the part, sub-optimal spatial maps of the part can be compensated for in the scan stage with online path corrections. By producing a noisy map that is then corrected for online, the overall time to deployment and energy cost of required motions is reduced. Further, for items of interest in remanufacturing a

full and accurate surface characterisation is not always a necessity for the rejection of a defective part on economic grounds [7]. Full surface reconstruction of large parts is considered in Chapter: 5.

Reducing the required time for path planning over traditional methods requiring accurate digital-representations, a sensor capable of capturing significant surface information within a single shot is preferable for speedy deployment. In order to minimise calibration time, tool interchange, and risk of collisions a compact, wide aperture profiling sensor that can be simultaneously mounted with the UT sensor is sought.

Allowing for a general method for path planning, the operator is assumed to position the probe to face the surface in a way that gains the most information about the area that needs to be scanned. The surface information gained from a single position is given by the maximum surface area captured when projected by line-of-sight to the tool's frame, an example in the context of a camera lens is displayed in Fig: 4.3.

The wider the frustum of the sensor, the greater the surface area captured. Similarly to the step-size moderation introduced in Chapter: 3, complex surfaces with greater local curvature require greater sampling rates in order to gain enough information to plan paths over the surface being imaged as mentioned in [5, 6]. The optimal sensor has a wide aperture, with a spatial sampling rate suitable for high surface curvatures.

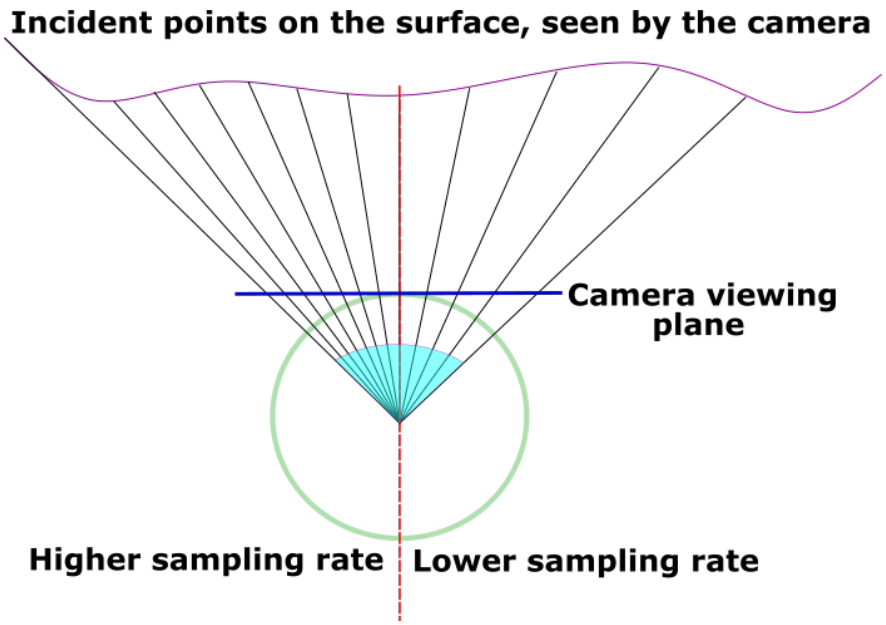

Figure 4.3: 3D data is projected to a 2D surface, given by the lines of sight of the camera's frustum. Projected to the viewing plane, the projected images can also be considered as projected to the sphere centred around the camera's focal point (in green). The wider the angle of the lens (highlighted in blue) around the circle's centre-line, the more information that is gained. Greater sampling on the left hand side captures more information about the surface's curvature.

Optical solutions such as LIDAR, structured light sensors, laser, and camera arrays provide dense point clouds of parts from static positions.

Static photogrammetric systems can provide accurate digital twins within a fixed work-volume [8]. However, they require a static work-environment making them unsuitable for on-site deployments in variable work-volumes. Laser sensors provide the highest accuracy solutions, with commercial lasers capable of positional accuracy in the region of tens of microns. Laser line scanners such as those listed in [9] can provide a sweep of the part from a single flange position. However, laser systems capable of high accuracy, wide aperture, and high spatial sampling

rate are comparatively bulky compared to visual alternatives, limiting collision free motion. Onsite deployment is further limited, high accuracy lasers of class II or above potentially harming human operators or limiting the work-spaces they may be deployed in. They may also require a tool-interchange process for low-payload robotic platforms such as the UR3e. Colour images complementary to collected point clouds place LIDAR and structured light cameras as the optimal candidates for a profiling sensor platform. Colour images are extensively used for surface defect detection in various industries [10, 11], a factor that is highly complementary to UT that has difficulties in finding surface defects. Mentioned in Section: 2 LIDAR cameras have seen extensive use within autonomous robotic localisation, mapping and navigation. However, their performance is optimised over medium to long range distances. The expected work-cell ranges are $0mm$ to $1500mm$ ($1300mm$ is the maximum range of the UR10e platform), with the most common data collection range $250mm$ to $750mm$. In this range, the D415 provides greater accuracy than the similar cost Intel Realsense L515 Lidar from $0mm$ to $500mm$, calibrating the radius of a spherical $25.4mm$ radius artifact with a $2.1mm$ radial calibration error compared to the L515's $6.23mm$ [12]. The performance of the D415 decreases over the range $500m$ to $1500m$ compared to the L515, with the D415 radial calibration error producing $5.62mm$ error compared to the L515's $3.48mm$ of error. Despite this, within the expected working ranges of the two instruments the error metrics are similar [13]. Since the robot must

take an image from an extended (and not the root) position, and since the robot can approach the surface to an almost arbitrary distance but not necessarily gain an arbitrary distance from the part, higher accuracy at closer ranges is deemed preferable for the application. Structured light cameras project patterned light, and at least two stereo cameras then interpolate the depth from the patterned light positions. Commercial platforms such as the Kinect are widely applied as motion and position sensors, and when coupled to advanced machine learning for object and motion tracking can be deployed in industrial environments [14]. Alternatively, comparing the latest models of the Intel Realsense RGB/D camera range, the D435 sensor has a wider field of view, it retains the same pixel-rate as the D415. While capturing more surface area, information on complex and curved surfaces is more accurately captured by the D415 [15]. Compact, weighing $72g$, and with a higher sampling rate per degree of field of view than the D435, the D415 camera was chosen. Shown in Fig: 4.4, the camera was mounted alongside the CW probe without causing a significant risk of collisions.

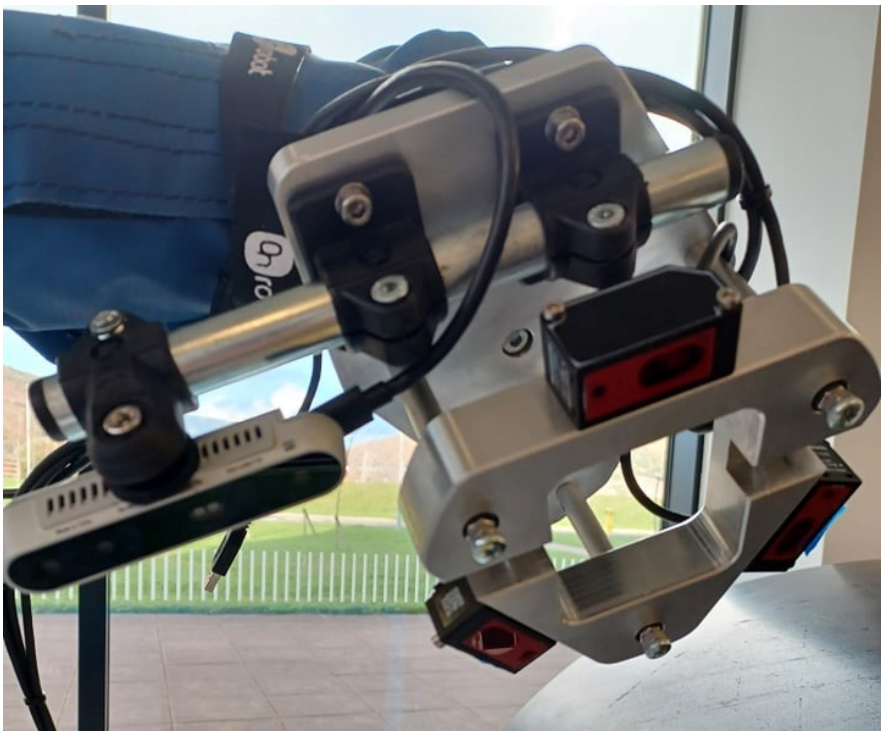

Figure 4.4: The camera dimensions of $99mm \times 20mm \times 23mm$ are non-restrictive to the robot's motion.

4.1.1 Computer Vision and Surface Profiling for NDT

An initial study of 2D Visual Odometry and part mosaicing [16] highlighted several drawbacks with visual imaging and NDT. The key block to wide-spread usage is that highly specular surfaces such as polished metal produce significant visual artefacts. For sectors such as remanufacturing and aerospace that rely on polished metal or highly reflective Carbon-Fibre Reinforced Polymer (CFRP) samples, this is a critical issue. A related work found that robotically applied Structure-from-Motion (SfM) reconstructions can reproduce parts with sub-millimetre accuracy, once the point clouds had been processed [17]. Key to this method is the presence

of significant visual artefacts on the part, allowing dense point-cloud extraction from subsequent 2D images taken at known positions. These studies have presented significant improvements in reverse engineering of parts for later NDT scanning. However, the scans taken for these parts are completed by two complex robotic procedures that are operator-specified. The operator must input a path that is known not to either collide with the part or meet kinematic singularities, and is entirely reachable by the robot. In order to construct a dense 3D map of the part, hundreds of images with up to 85% image to image overlap are required to ensure accurate part-reconstruction. This presents the significant disadvantage of requiring the part to be stationary within the cell while camera and UT probe tools are interchanged, since the derived CAD model is localised with respect to the robotic work-space.

A single one-shot RGB/D D415 does not require additional path planning processes for initial profiling of the part, or hundreds of images to reconstruct a dense model of the part as a monocular camera does. The depth camera using two stereoscopic cameras remove the need for triangulation from dense feature maps, imposing their own on the structure with a structured light projection. Several autonomous robotic arm [18, 19] and drone based [20] NDT scanning methods rely on the simultaneous depth and colour image approach. The key drawback of current depth-map camera deployments are their reliance on primitives such as cylinders and planes to provide path plans for NDT scans. These reduce the

flexibility of the system when faced with complex, warped, or unknown surfaces.

The strength of previous related works investigating RGB cameras is their use of established Computer Vision (CV) algorithms. Structured light cameras produce colour images and point clouds, empowering the use of a wide range of CV algorithms, coupling them with single-shot point cloud collection.

4.1.2 Path Planning from RGBD Images

CV and point cloud processing algorithms were used for point-cloud segmentation to seperate the part from the environment, generating two methods: for parts larger and smaller than the work-volume. A subsequent point cloud refinement process was then applied, creating a fully autonomous path selection program.

For parts larger than the work-cell, DB-scan clustering of the point cloud [21] is used, the closest point cloud cluster to the camera assumed to be the part. Spatial clustering in this way both highlights outliers in the case of reflections presenting as closer or father away from the camera than the rest of the part, and allows the user to set a distance threshold for cluster inliers. A disadvantage is that the operator needs to be aware of the proximity of objects closer to the part than this threshold, which is particularly problematic with specular surfaces causing dense reflections close to the part. This is solved with simple part re-positioning of refinement of the clustering parameters, however.

For parts smaller than the field of view of the camera, Structural SIMilarity

indices (SSIM) of an initial calibration image, and a subsequent image with the part seen. The pixel-by-pixel breakdown of the SSIM map converts the image to a binary-map, whose contours are extracted. The contours are then used as an image segmentation method, producing individual regions of structural dissimilarity between images. As opposed to methods such as the Hough line or circle transformations that only require single images for image segmentation, the SSIM is not limited to contour identification of a given geometric primitive shape. Additionally, unlike classical or probabilistic Hough methods the SSIM does not require thresholding by the operator for contour detection. While binary image conversion from the SSIM map does require a threshold, this investigation has found that this is a formality, as we can include all positive SSIM-indexed pixels as the 3D filtering process returns the correct region. Flexible alternatives such as Sobel or Laplacian edge detection also only require single images for contour extraction, however they may provide incomplete contours preventing proper image segmentation without further morphological operations reducing part mapping quality further, issues which the SSIM is less susceptible to. DB-scan clustering is then implemented, and either the largest or closest point cloud region chosen, depending on the perspective of the shot and geometry of the part.

Once the part's point cloud position is attained and normals are approximated, a rough path for the robot to follow is extracted from the camera's inherent rasterisation, shown in Figure 4.5, composed of path segments whose separation

is determined by the UT probe's aperture.

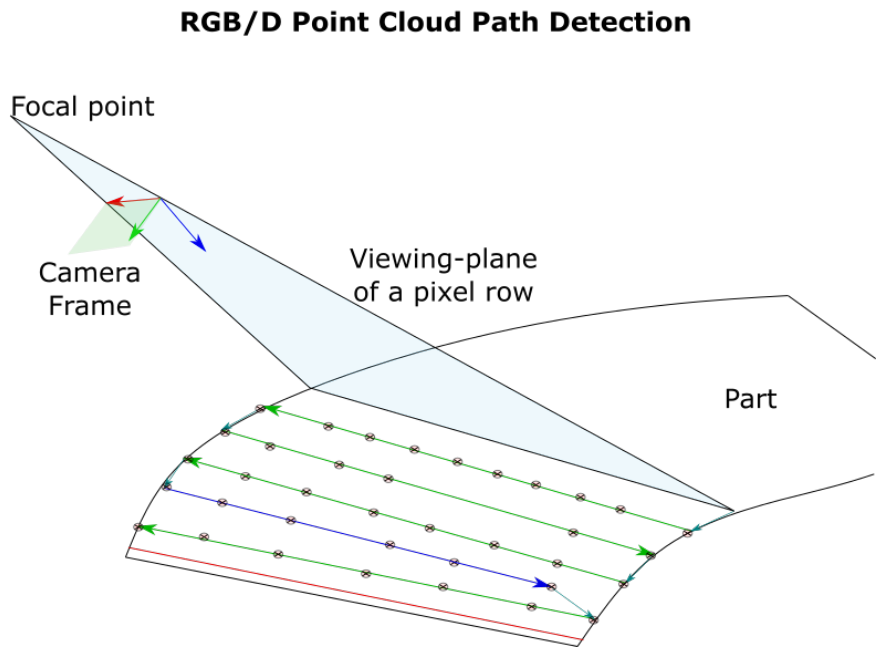

Figure 4.5: The viewing frustum of a camera intersects with the part along planes given by either each row or column of pixels. The planes of this chosen direction return points along the surface that form a raster-segments. These ordered raster segments can be reduced (red) if too close together, or regionally padded (blue) if the smallest distance from one raster-segment to another is larger than the sensor aperture. Key points (dots) can then be extracted directly from the point cloud and used as way-points. The overall path combining original (green) and inferred raster lines (blue) are denoted.

Since the structured light camera requires a coherent projected IR pattern to be seen by the two receiving lenses, reflections of ambient light result in unprocessed or 'dropped' pixels that result in non image-rasterised point clouds when using optimised third party software. This issue was present when using the python module for Open3D [22] for point cloud refinement in 3D. To solve this issue, re-projection and rasterisation of retained points utilised a proxy RGB image as a hash-map of the pixel's (x, y) positions. The hashing function that

returns a Red-Green-Blue vector, is applied to a well defined image size and so avoided hash-mapping collisions issues, the function is given in Eq: 4.1.

$$q(x, y) = x + y \times x_{\text{Max}}, \tag{4.1a}$$

$$H(x, y) = \left[\text{mod}\left(q(x, y), 255\right), \text{mod}\left(\left\lfloor \frac{q(x, y)}{255} \right\rfloor, 255 \right), \text{mod}\left(\left\lfloor \frac{q(x, y)}{255^2} \right\rfloor, 255 \right) \right]. \tag{4.1b}$$

This hashing method is limited to images of pixel count less than $255^3 \sim 1.7 \times 10^7$, due to the RGB values limited by the ceiling value of 255.

Though the RGB/D camera is composed of two cameras, their co-planarity allows the field to view to be merged and simplified to a single camera's. Excess information within the point cloud has then been utilised as environmental information to detect collisions.

For on-site and remote inspections, the operator may only need to scan a partial segment of a structure. An operator-guided region-of-interest based approach has also been introduced, so that the operator may select a region of the part on the colour image to scan, an example of which is shown in Figs:4.6. Areas such as port-holes can be clipped from these regions by excluding pixels covered by more than one bounding polygon. In this case, hole-covers and plugs may be produced to allow rasterisation and coverage over these areas even in the case of contact inspections. In cases such as remanufacturing where a digital twin is

sought from this process and a prior model does not exist, it may be preferable to simply scan the part without plugs covering surface discontinuities to retrieve an accurate representation of the part.

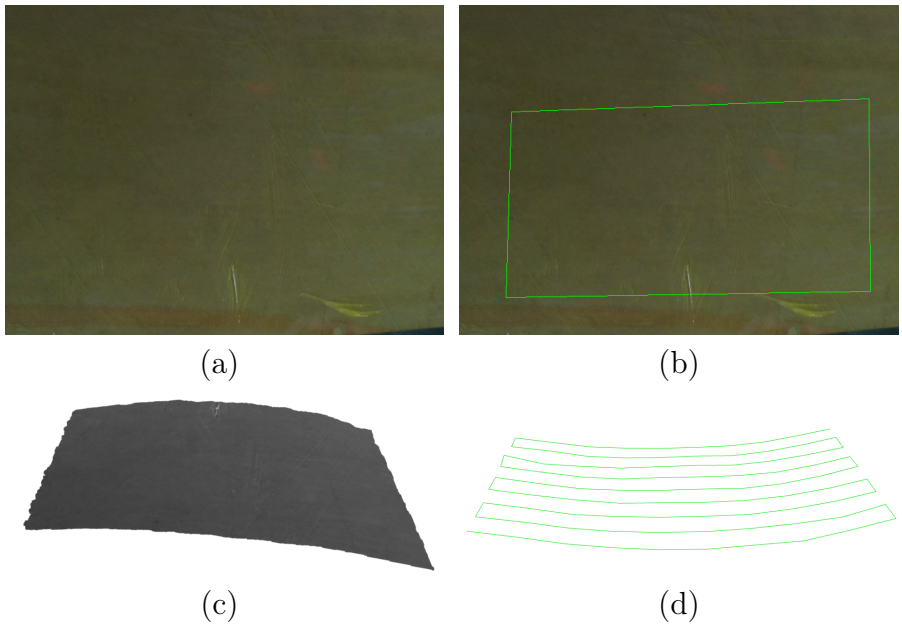

Figure 4.6: Image region selection to path creation. (**a**) The original colour image seen by the operator. (**b**) The region of interest is selected. (**c**) The selected region cropped and rendered as a point cloud. (**d**) The resultant robotic path.

The projective-map perspective is able to provide an efficient coverage pattern of the seen part which the tool's perspective alone was not able to within the CSFA. Use of a small low cost D415 camera meant the resulting map contains noise, particularly on specular surfaces. In order to couple the tool and part throughout the scan, online robotic control strategies are necessary to correct these positions. While there is noise throughout the full and unrefined map, collisions can be prevented by utilising the additional surface points. The next section discusses application of the tool's and robots perspectives in providing

online path corrections, and ensure optimal part-robot safety. Prior information from the RGB/D images is key to opening up the Configuration-space perspective to flexible and autonomous routines.

4.2 Configuration Space Pre-Planning and Robotic Control

To satisfy the system requirement 5, contact methodologies are preferred over jet-PAUT or immersion transmission methods. The contact method enables the use of force-control as a solution for in-path position corrections when traversing a map built from noisy data, ensuring the probe maintains contact with the part throughout the scan. Force data in the context of robotic UT-NDT have traditionally utilised roller probe technology, used to provide local corrections to the estimated position of a known part within the robot's frame of references [23, 24, 25]. These examples have, however, used known digital-twin models with limited positioning corrections required.

The main draw-back of roller probes are the uni-directional speed allowed along the tool's axis, due to their linear axis limiting their application to geometries curved in multiple directions. An alternative UT contact measurement device is the CW probe. Filled with water, the wedge's material has a near-identical UT wave-speed as water preventing reflection at the boundary. The CW probe

has a small conformable-planar aperture that allows application to geometries of greater omni-directional surface curvature, enabling a greater range of scan-able surfaces than a roller probe. Shear damage to the CW probe is prevented by using couplant on the surface. The main drawback of conformable wedges used within a force control schema is the potential for bursting. This method is not suitable for sharp surfaces or high forces, which is defined dependant on the probe material and thickness.

4.2.1 Configuration-Space Path Pre-Planning

Environmental information informs the path planning, and can also prevent collisions in pre-processing. As with digital-twin assisted models of path planning, the Cartesian poses at each path-position are extracted and in turn are converted to configuration-space coordinates. A path of length N, each admitting 8 configuration solutions, has 8^N potential traversing paths. Each of these paths may incur collisions, so the initial configuration space is refined to exclude collision inducing positions. The potential path number is reduced to 8 by considering starting from the initial position's configurations and iteratively finding the shortest-gap path within C-space for each. The process of this function is documented in Alg: 3.

Algorithm 3: Calculate possible collision-free paths, and the cost of each path from each potential initial configuration.

begin
  for $\overrightarrow{p} \in Path$ **do**
    $\overrightarrow{\Omega}_p = \{ \overrightarrow{\theta}^i_p = IK(p,i) : \text{notCollision}(\overrightarrow{\theta}^i_p)\}$;
  end
  for $k \in \{0 : MaxConfigs\}$, $\overrightarrow{p} \in Path$ **do**
    //For each configuration space path, iteratively choose the next best configuration pose;
    $\text{NextBestConfig}(k,p) = i : \min_{i \in \overrightarrow{\Omega}_{P+1}} | \overrightarrow{\theta}^k_p - \overrightarrow{\theta}^j_{p+1}|$;
    $\text{ConfigCost}(k,p) = | \overrightarrow{\theta}^k_p - \overrightarrow{\theta}^i_{p+1}|$;
  end
  for $k \in \{0 : MaxConfigs\}$ **do**
    $t = 0$;
    $GenCount = 0$;
    while $t + 1 \leq |Path|$ **do**
      //Calculate each path's cost, the total distance of the path in configuration space;
      if $ConfigCost(k,p) < L$ **then**
        $k_{+1} = \text{NextBestConfig}(t,k)$;
        $\text{Cost}(k) += \text{ConfigCost}(k,p)$;
        $GenCount += 1$;
        $t = t + 1$;
      else
        $t = |\text{Path}| + 1$
      end
    end
  end
end

Then either the closest initial configuration to the current one can then be used, the one which will lead to the longest collision-free path (given by 'Gen-Count' in Alg: 3), or the one that will lead to the shortest distance travelled in configuration-space depending on operator preference. The apriori point-cloud information provides utility through ensuring that large configuration changes

are not likely when scanning the entire surface, and that the platform will not collide with the part.

After the ideal starting configuration is decided, the approach towards it from the current position is calculated using linear motion in the configuration space. If a collision along this path is found, then a Rapidly-exploring Random Tree (RRT) framework calculates a collision free path.

Deployment on the Graphics Processing Unit (GPU) with CUDA software with a parallel architecture as displayed in Fig: 4.7 was enabled by the offline CSFA. Evenly space points along CAD models of the robot extracted by the CSFA removed bias due to long triangulations of the robotic model, such as on cylinders. GPU processing can be significantly slowed by memory transfer between the host and device memories [26]. Overheads were minimised through uploading the robotic and part point cloud data to the device memory directly. Collision detection sends configuration positions in batches to be then processed on the GPU, returning a boolean value. Memory allocation and transfer for each configuration check is minimised to 24 bytes to the host with 4 bytes returned. The collision detection package was developed and tested within CUDA, later converted to a dynamic-link-library (dll) for wider use within other programs.

The limitation of the pre-scan method is that the uncertainty in the point-cloud position and orientation may lead to positions being removed without causing a collision in process. However, the speed command control method requires

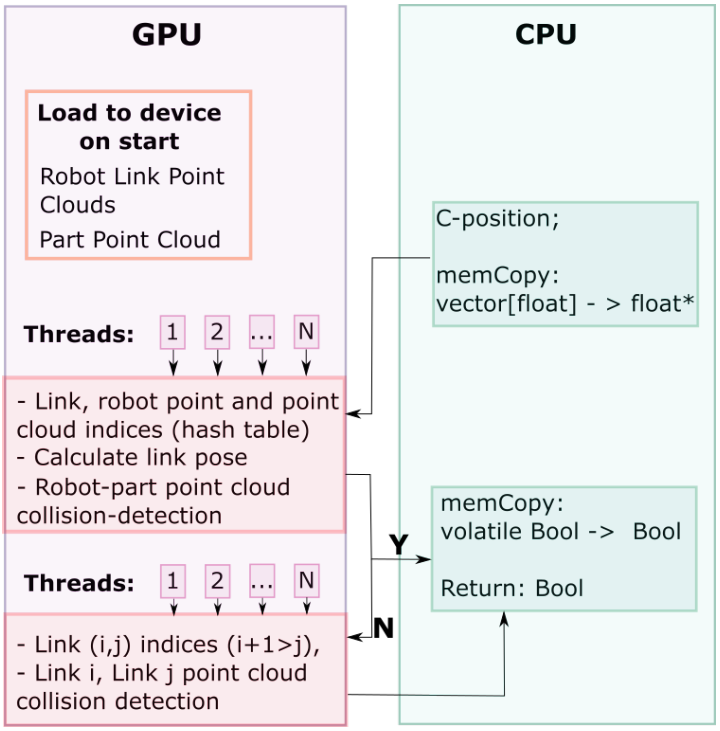

(**a**)

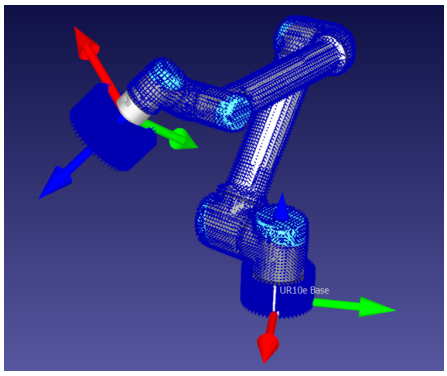

(**b**)

Figure 4.7: GPU parallelised collision detection process. In total, the running memory cost of the operation is: 6 floats sent to device, and one volatile bool returned. (**a**) Shows the process mentioned, displaying how the host and device topologies were optimised to minimise memory transfer costs, with (**b**) showing projected points for a given position over the RoboDK digital twin. The tool is simply modelled as a cylinder in this example due to its variable width modularity, shown attached to the flange.

regular updates, rendering an in-process collision detection method for an unknown surface unfeasible due to latency. The robotic platform has additional safety features, stopping its motion on collisions minimising risk to the robot and part.

4.2.2 Local Robotic Corrections

Once the rough surface has been profiled and localised and the optimal starting configuration and approach defined, the robot is ready to scan with the CW probe.

The point cloud's inaccuracies and coupling method of the conformable wedge probe require the conditions:

1. initial coupling to the surface from the erroneous point cloud;
2. a traversal method that keeps the sensor probe in contact with the surface;
3. direction commands for the robotic platform to visit each way-point in the path that also compensate for positioning errors;
4. stop conditions when visiting each way-point.

The Universal-Robot's UR10e platform deployed comes equipped with force-torque control, enabling the robot to move in a given direction until a force is felt. By utilising the first point's normal estimation, the robot is able to couple to the surface satisfying Condition: 1.

The Universal Robot's force control mode also allows users to set directed forces and admissible deviations while executing a path. By requiring the robot apply a set force in the tool's z-direction and allowing deviations in the workspace dimension that composes the majority of the current tool's z direction, the robot was able to maintain contact with the part. Allowing motion in all cardinal directions resulted in undesirable motion, requiring the restriction to the direction that gave the largest contribution.

While the CSFA planned paths with static configuration-steps, the goal 4 indicates that fast deployment is paramount to the industrial success of the presented method. The robotic paths were executed in Cartesian space with velocity control. Setting the position and rotational target velocities for the tool $\overrightarrow{v} = [\dot{p}_x, \dot{p}_y, \dot{p}_z, \hat{\omega}_x, \hat{\omega}_y, \hat{\omega}_z]$ within a control loop instead of by setting static target positions. While a directed point or planar force/torque sensor has the capability to correct for orientation deviations, the conformable wedge probe presented a non-planar surface that allowed the robot to slip into misalignment with the surface.

To aid in the high-accuracy reconstruction of the surface, three linear laser sensors were rigidly attached to the flange to collect surface positions during the scan. In addition to this the live measurements provided on-line orientation corrections, approximating the local tangent plane as was introduced in Section: 2.4.3. The laser-measurements provide the approximated surface orientation given by a 3×3

rotation matrix R_s within the world-frame, while the robot has current rotation R_r. Universal robots utilise the $\mathfrak{se}(3)$ convention, with the required orientation correction given by;

$$\overrightarrow{\omega} = R^{-1}\left(R_s R_r^T\right), \tag{4.2a}$$

where

$$R\left(\overrightarrow{\omega}\right) = \exp\begin{bmatrix} 0 & -\omega_z & \omega_y \\ \omega_z & 0 & -\omega_x \\ -\omega_y & \omega_x & 0 \end{bmatrix}, \tag{4.2b}$$

is the conversion between twist vectors and $\mathbb{SE}(3)$ group elements [27]. The angular difference is converted to angular velocity $\hat{\omega}$ using the average $\bar{t}$ and standard deviation σ_t of previous loop-durations, $\hat{\omega} = 0.5 \cdot \omega/(\bar{t} + \sigma_t)$. The damping factor is used to prevent over-corrections and loss of contact with the surface with variable loop speeds and unknown geometric factors.

While the force kept the tool coupled to the part, and the lasers kept the tool normal to the part satisfying Condition 2, data obtained by the RGB/D camera set the directional speed values $\dot{p}$.

Given a rough target position $\overrightarrow{P}_{t+1}$, current robotic position $\overrightarrow{P}_r$, current 3×3 flange orientation matrix $R_r = \left(\overrightarrow{dx}, \overrightarrow{dy}, \overrightarrow{dz}\right)$, and target tcp speed s, the values $\dot{\overrightarrow{p}}$ were calculated.

Taking the projection to the surface's tangent plane;

$$\overrightarrow{dP}_{\text{Proj}} = \left(\left(\overrightarrow{P}_{t+1} - \overrightarrow{P}_r\right) \cdot \overrightarrow{dx}\right) \overrightarrow{dx} + \left(\left(\overrightarrow{P}_{t+1} - \overrightarrow{P}_r\right) \cdot \overrightarrow{dy}\right) \overrightarrow{dy}, \tag{4.3}$$

and scaling this to the desired velocity; $\dot{\overrightarrow{p}} = s \cdot \overrightarrow{dP}_{\text{Proj}}/|\overrightarrow{dP}_{\text{Proj}}|$. When the remaining in-plane distance from the target is small enough that the robot would over-shoot in a control-loop cycle, the speed is reduced to the estimated value. This satisfies Condition: 3. The projection is necessary since point cloud errors along the surface normal result in jerky motion, with the velocity vector set away from the target surface while the robot tries to maintain a constant force against the surface.

Finally, the stop condition for the robot at each way-point is summarised by taking the current tool position $\overrightarrow{P}_r$, velocity vector $\overrightarrow{v}$, and way point $\overrightarrow{P}_{t+1}$. The distance q of the robot from the way-point in the plane is;

$$q = \left(\overrightarrow{P}_{t+1} - \overrightarrow{P}_t\right) \cdot \overrightarrow{v} \frac{1}{|\overrightarrow{v}|}. \tag{4.4}$$

Once q has reached a threshold value, the robot is considered to have reached the desired way-point, satisfying Condition: 4. This is represented graphically in Fig: 4.8.

This method is only suitable for point cloud representation of surfaces that fulfil the following condition: (a) there is a curve along the surface $\overrightarrow{\gamma}(t + \delta t)$

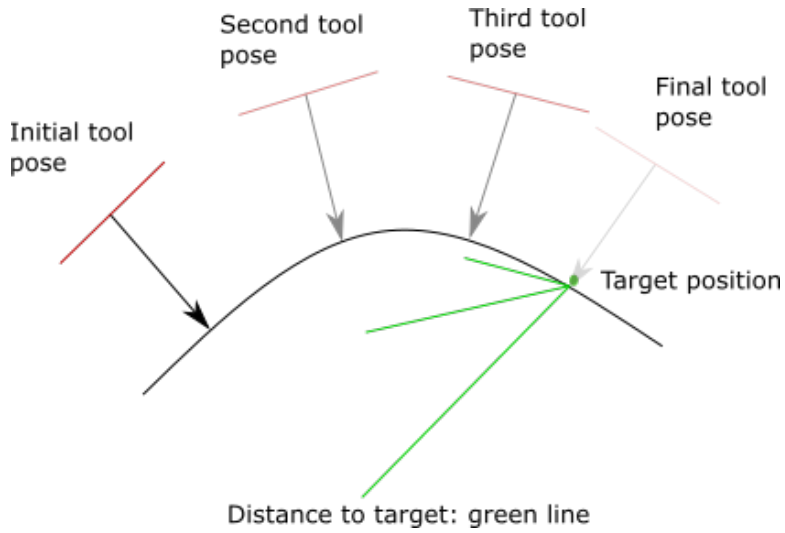

Figure 4.8: Tracking the tool's progress over the surface with local orientation corrections.

that intersects the current and next way-points $\overrightarrow{P}_t, \overrightarrow{P}_{t+1}$ such that $\dot{\overrightarrow{\gamma}}(\delta t) \sim Proj(\overrightarrow{P}_{t+1} - \overrightarrow{\gamma}(t))$, and (b) the global minima of the parameter q is attained at only one point along this curve. Point cloud representations of surfaces that do not follow this can only allow sub-optimal solutions to the path followed, or no solutions at all.

This process does assume that each point within the point cloud represents the closest position on the surface. This increases the accuracy threshold for suitable RGB/D sensors when applied to surfaces of high-curvature. For a surface with maximum normal curvature κ, the maximal inaccuracy can be δ with $\delta < 1/\kappa$.

The speed control for the robot is summarised in Algorithm: 4.

Algorithm 4: Speed control algorithm applied to reach each control point.

Data: Define acceptable stopping radius r and expected speed s.
begin
  for $\overrightarrow{p} \in Path$ **do**
    $\overrightarrow{P}_{TCP}$ = GetCurrentPose();
    $t = |\overrightarrow{P}_{TCP} - \overrightarrow{p}|$;
    $s_C = s$;
    while $t > r$ **do**
      $\overrightarrow{P}_{TCP}$ = GetCurrentPose();
      L = GetLaserData();
      //Constructing the local surface orientation matrix;
      if $|L|$==*3* **then**
        Extract surface orientation matrix: $f(L, \overrightarrow{P}_{TCP}) = R$;
      else
        Assert the current TCP orientation is the surface's:;
        $R = R_{TCP}$;
      end
      //Project vector difference to surface tangent;
      $\delta\overrightarrow{P}$ = Proj $\left(\overrightarrow{p} - \overrightarrow{P}_{TCP}\right)$;
      Update distance value;
      $t = |\delta\overrightarrow{P}|$;
      Moderate speed with average loop-time so far;
      $s_C = \min\left(t/\bar{dt}, s\right)$;
    end
  end
end

4.2.3 Force Control

Since the velocity control acts as a Position controller (P - controller), the force considered is only required to counter frictional forces felt, and ensure the coupling pressure is moderately consistent to assist automatic gating procedures by minimising corrections requisite in a varying-offset conformable wedge aperture.

Force control is determined by the Position-Integral (PI) errors experienced [28]. Determined by the given direction of motion, local roughness and errors in tool mass and centre-of-mass calibration, the frictional force is not consistent, with purely P-control used. Under the assumption that the tool is always aligned to the surface by laser-feedback, PI control is used for correcting the normal-force. PI controllers are more reliable than full Position-Integral-Derivative (PID) controllers from force-velocity/position control perspectives when applied to cobots such as the UR10e [29].

Fundamentally, the tangential velocity and force controls act as P controllers, set to follow the local values required to achieve the global target of attending each way-point. Meanwhile the normal force, with a desired global consistency, is a PI controller.

4.3 Friction as a Metric of Surface Finish Quality

While CW probes are more sensitive to sharp corners than roller probes, the nearly-flat aperture of the sensor presents the advantage of additional information in the form of surface friction. Corroded parts prevalent within sectors such as remanufacturing require surface pre-preparation to clean and level rusted patches in accordance with ISO standard 16809:2017 [30]. In certain regions, operators may have insufficiently prepared the surface, or the surface thickness may not allow levelling. In these cases, surface roughness data are advantageous to map

overlooked regions of the surface in the preparation stage. While laser data provides high-accuracy surface position feedback, the couplant fills pits on the surface, presenting it as smooth and preventing it from providing such a metric. For conformable and flat rigid surfaces separated by a thin film of fluid moving with a steady velocity [31], the frictional force is a sum of the hydrodynamic friction due to viscosity, and the asperity or contact force [32]. The hydrodynamic friction term τ, contact load P, area of the CW probe A, contact friction term f_c, and normal force F define the dimensionless coefficient of friction μ in a mixed-lubrication regime;

$$\mu = \frac{\int_A \tau \mathrm{dA} + \int_A f_C P \mathrm{dA}}{F}. \tag{4.5}$$

Contributions of hydrodynamic and contact friction are proportional to the surface area exposed to each regime. Along the Stribeck curve [33], the hydrodynamic coefficient of friction is related in a highly non-linear way with the average load P, wedge/couplant relative speed v, and fluid viscosity ν by the Hersey number $H = \nu v/P$. The Stribeck curve is shown in Figure 4.9.

Tribological studies in relation to robotics have historically studied gear friction in the field of precision robotics [34, 35]. The CW probe approach is the first such novel NDT deployment tool that enables the study of surface quality effects through Tribology. However, within a sprung and moving mechanical system such as the CW probe tool, multiple dynamic factors effect the actual frictional force felt. The tool shown in Fig: 4.4 is not always balanced between

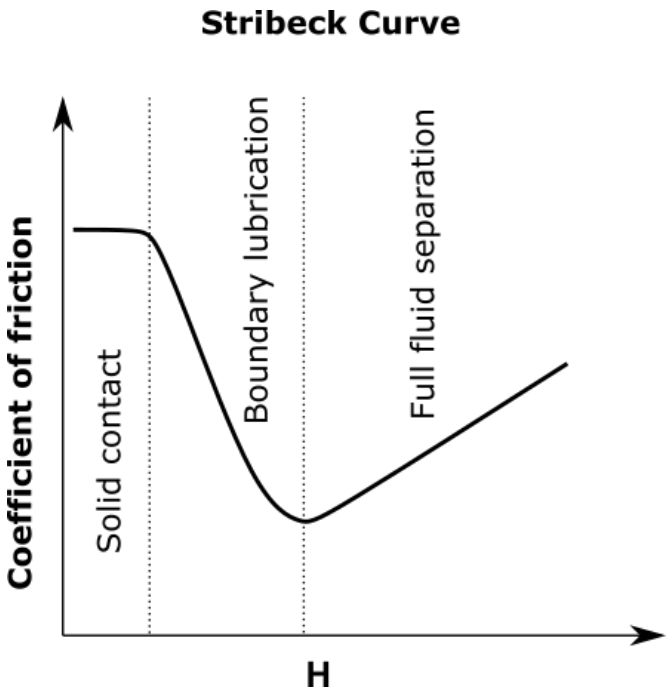

Figure 4.9: Stribeck curve; coefficient of friction against the Hersey number in the three lubrication regimes.

both springs. Either may be leveraged more than the other, resulting in variations in probe-surface friction. To prevent this undesirable effect the direction of motion of the tool, assumed to be the direction of maximal curvature variations along the tool's face, was directed perpendicular to the spring's axis. Variations in surface curvature transverse to the direction of motion still affect leverage on the individual springs, as well as mechanical effects of the tool itself.

Since surface preparation quality is not always available from colour images this novel approach provides an additional layer of information for operators on the overall scan-quality. For highly robotised processes such as remanufacturing is projected to be [36], this provides a key quality check on the automated pipeline

that may then indicate a need for re-finishing and re-scanning of a part.

4.4 Surface Reconstruction

The complete set of laser measurements are then used in post-processing to reconstruct a digital-twin of the part. The UT measurements provide a heat map from A-scan data, as is traditional in robotised NDT.

The TCP data at each UT measurement was used to project UT data onto the reconstructed surface, allowing a full 3D digital-twin representation of conventional C-scans. Variations in couplant thickness of up to a millimetre require the reconstructed surface to undergo a smoothing process. The chosen reconstruction method is the ball-pivoting algorithm [37], requiring a provided surface normal. The normal direction of the surface or robot at each discovered laser-point is provided to aid in this surface reconstruction. The surface is then passed through a single Laplace filter for smoothing. The advantage of using the laser data over the RGB/D point cloud is the inherent quality of the data resulting in fewer smoothing errors.

Once this is complete, the A-scan data are projected to the surface as a C-scan, as well as the surface friction data and re-made into C-scan and friction map digital twin models.

4.5 Experimental Results

An Intel D415 RGB/D camera was used to collect depth measurements, handled by the realsense2 Python package. The point cloud, colour and depth measurements were then processed using Open3D Python software [22]. A Universal Robots UR10e platform was deployed, controlled through the Real-Time-Data-Exchange (RTDE) package and supplemented by the On-Robot HEX E/H QC force-torque sensor, integrated through UR-Cap software. The tool setup is shown in Fig: 4.10.

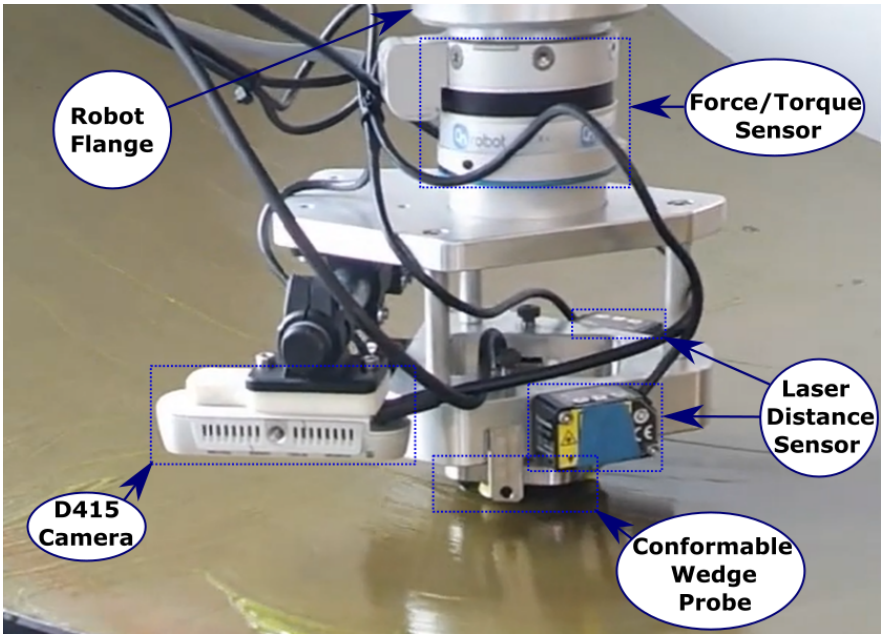

Figure 4.10: The experimental tool, mounting the laser-sensors, force/torque sensor, D415 camera, and CW probe to the robot's flange.

The CUDA library was imported into the Python environment and handled the pre-processing of the paths. For online orientation corrections, three Panasonic HG-C 24V class II laser distance sensors relayed data to the external con-

troller via an Arduino-uno at a power low enough to prevent surface ablations. Completed within a laboratory in direct proximity with a window, the the experiments show that the process is robust when exposed to a mixture of low and high intensity ambient lighting levels to be representative of site-inspection work. The robotic platform was statically mounted, with parts placed onto a table within the work-volume. A normal force of $50N$ was selected to maintain a high quality UT signal response, while also ensuring the CW probe was not damaged or split.

To test the collision detection pre-planning approach, a large non-planar surface was chosen, representing a wing-section from an aerospace component. A highly reflective CFRP section was also chosen to demonstrate resilience to holed and noisy point cloud data. A small metallic plate was chosen to demonstrate the use of the Structural Similarity Index to the location of small specular surfaces. Finally, a smooth and rough (0.1 mm ridged) CFRP components were chosen to test the applicability of surface friction measurements, and a friction stir weld plate used to validate friction-coefficient imaging.

The robot was capable of significant orientation and positional velocity control in the presence of a large curvature, as shown in Figure 4.11. In these experiments, the distance-metric used was not consistently monotonic in the case of inflection; however, the direction of motion was consistently correct. This agrees with the requirement made in Section4.2.2, as the surface inflects between points but the path taken passes local minima in the planar-distance parameter.

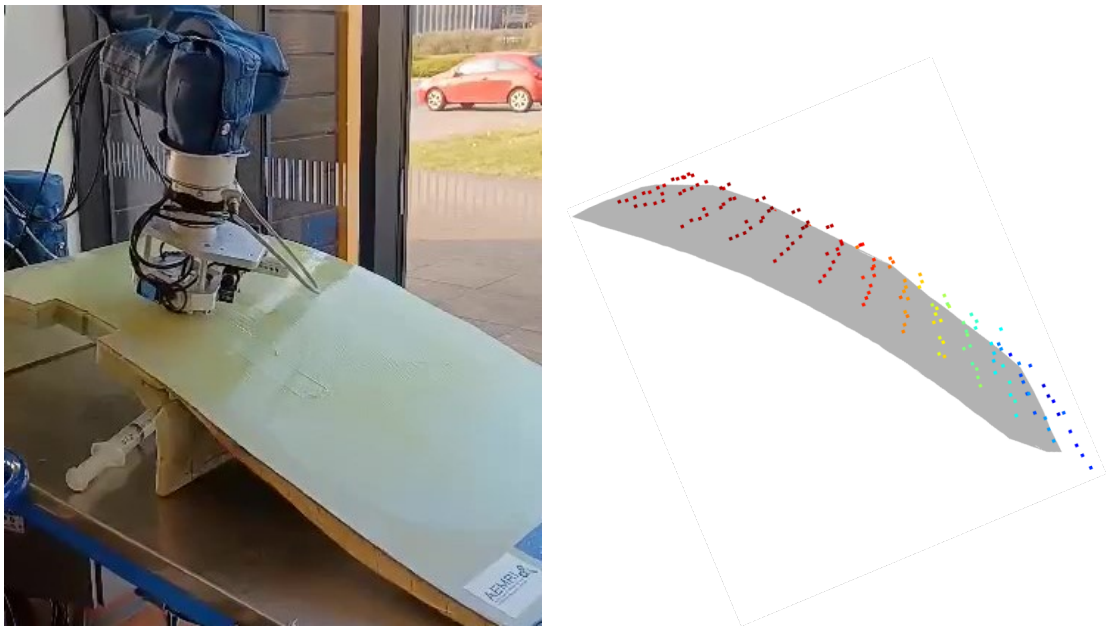

(a) (b)

Figure 4.11: Scanning of a mock-aerofoil sample. The original RGB/D data poorly represented the surface, with an offset of 5 mm. (**a**) Robotic -arm deployed to a mock aerofoil with large surface curvature. (**b**) Surface reconstructed using laser-data, waypoints from the RGB/D image embedded.

Principle to the path planning process is the initial collision detection procedure to remove points that potentially damage the part or robot. The same wing as used in Figure 4.11 was placed at an angle relative to the robot that would cause a collision. The result is a successful removal of points that would potentially cause a collision, as shown in Figure 4.12.

The ability to plan and scan over holed and noisy point cloud data is highlighted in Figure 4.13. Figure 4.13a shows the initial point cloud corrupted by light-interference. The resultant path executed by the robot is shown in Figure 4.13b, shown to cover the part despite the missing and noisy data.

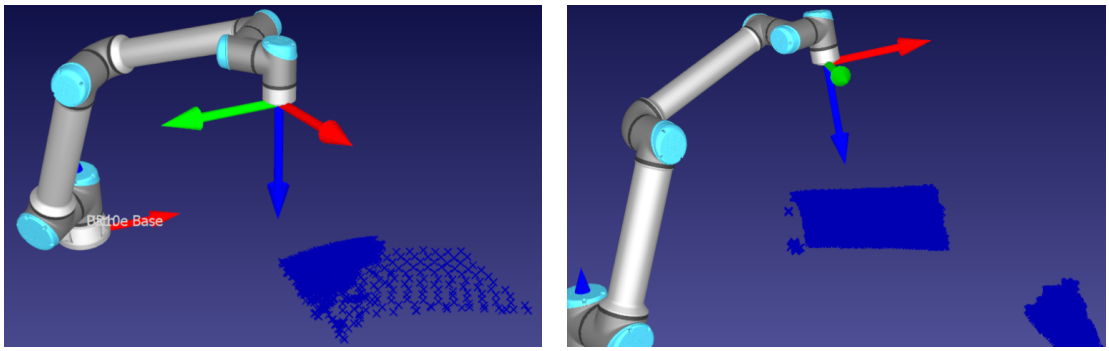

(a) (b)

Figure 4.12: Scanning of a mock-aerofoil sample. The original RGB/D data poorly represented the surface, with an offset of 5 mm. Imaged within RoboDK. (**a**) Path, and in high-frequency segments the laser-discovered positions on the part. (**b**) Original Point cloud of the part and environment.

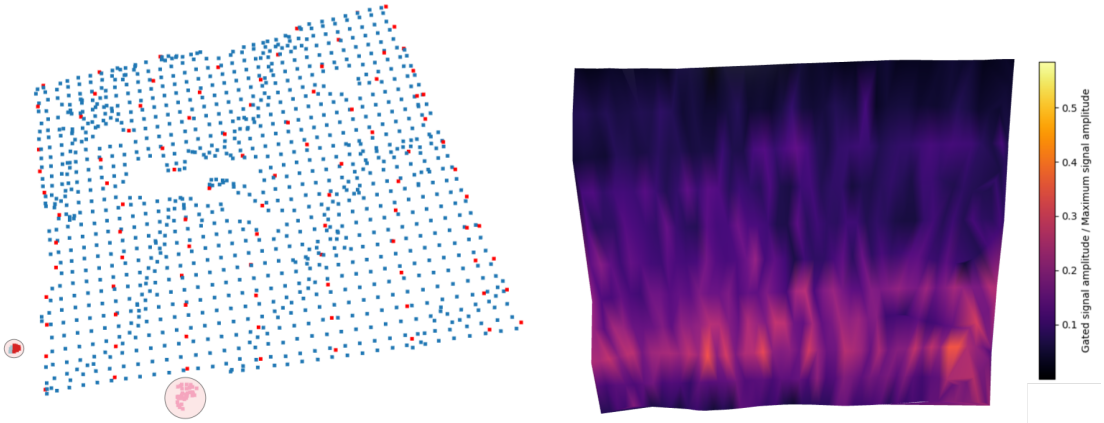

(**a**) (**b**)

Figure 4.13: Point cloud and C-scan of the part. The average error of RGB/D point cloud poses from the best fit plane of the collected laser data is 14.7 mm. (**a**) Point cloud map of a reflective CFRP component. Some sections of the point-cloud are missing, the surface data is considerably irregular. Visual artefacts incorrectly placed within the part are circled. (**b**) Heat-mapped C-scan of the part. The 5 mm thickness of the CFRP component placed the back-wall signal within the dead-zone of the 5 MHz probe. The support strut of the part can be seen within the gated region as higher-heat.

The images shown in Figure 4.14 demonstrates the structural similarity method of point-cloud selection prior to clustering and refinement. This is additionally re-

silient to variable lighting conditions, the main drawback of which is the potential for error when reflective regions are close to the surface of interest, resulting in artefacts seen in Figure 4.14c. The point cloud of the artefacts and the surface are then clustered, and the largest or closest to the camera is chosen, resulting in the surface alone being selected in Figure 4.14d. The operator should be aware of the placement of small parts so that the surface is not closer to reflective background regions than the clustering radius.

Both a smooth and a rough CFRP sample were used to test friction data at variable pressures and speeds. The results are presented as histogram values in Figure 4.15.

While the measured friction across the surface can differentiate between the differing surface roughness values, there is a significant change in the rough surface's measured friction value. Changes in the hydrodynamic friction of the UT couplant with TCP speed, combined with a mechanical locking of the spring-mechanism explain the shift in friction values across the observed data. The mechanical design of the tool allows for an angled locking of the UT's sprung support-struts due to the force acting along the strut's central axis. For rougher surfaces, the frictional force in this direction is great enough to lodge the probe and then on the return, dislodges the tool. The angled face of the tool then also creates a 'bow-wave' of UT couplant in one direction, allowing the tool to more smoothly pass over the surface with increased lubrication. The result is a split in

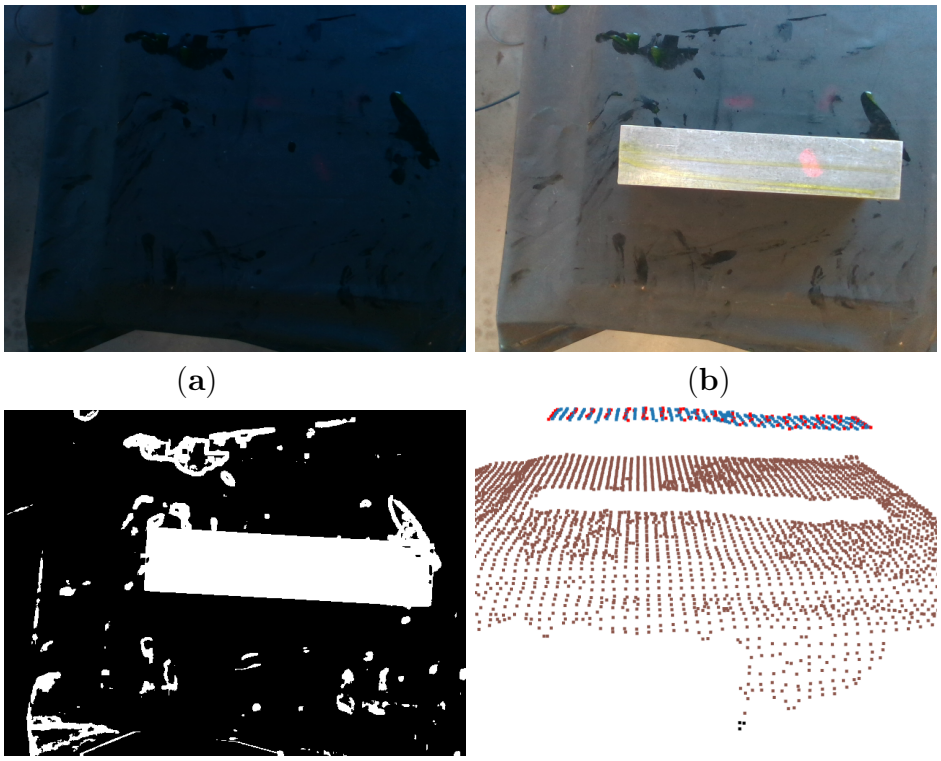

(**a**) (**b**)

(**c**) (**d**)

Figure 4.14: Structural-similarity based part localisation and path generation process for a small metallic block, demonstrating localisation and path generation on small objects. (**a**) Calibration image showing just the workcell. (**b**) Subsequent image with the part present. (**c**) Deducted image—kept pixels are shown in white, discarded pixels in black. (**d**) Resulting point cloud after remaining point clustering and selection. The identified part is in blue, extracted way-points in red.

the frequencies of observed friction values for plates of un-varying roughness, with principle modes becoming visible with greater speed as hydrodynamic friction increases. This is particularly noticeable on the smooth sample, as an increase in speed thereby furthers the split in friction values. Both samples see the peaks of friction inversely correlated with tool load. On the Stribeck curve seen in Figure 4.9, the majority of the tool's aperture is in the well-coupled region, ensuring

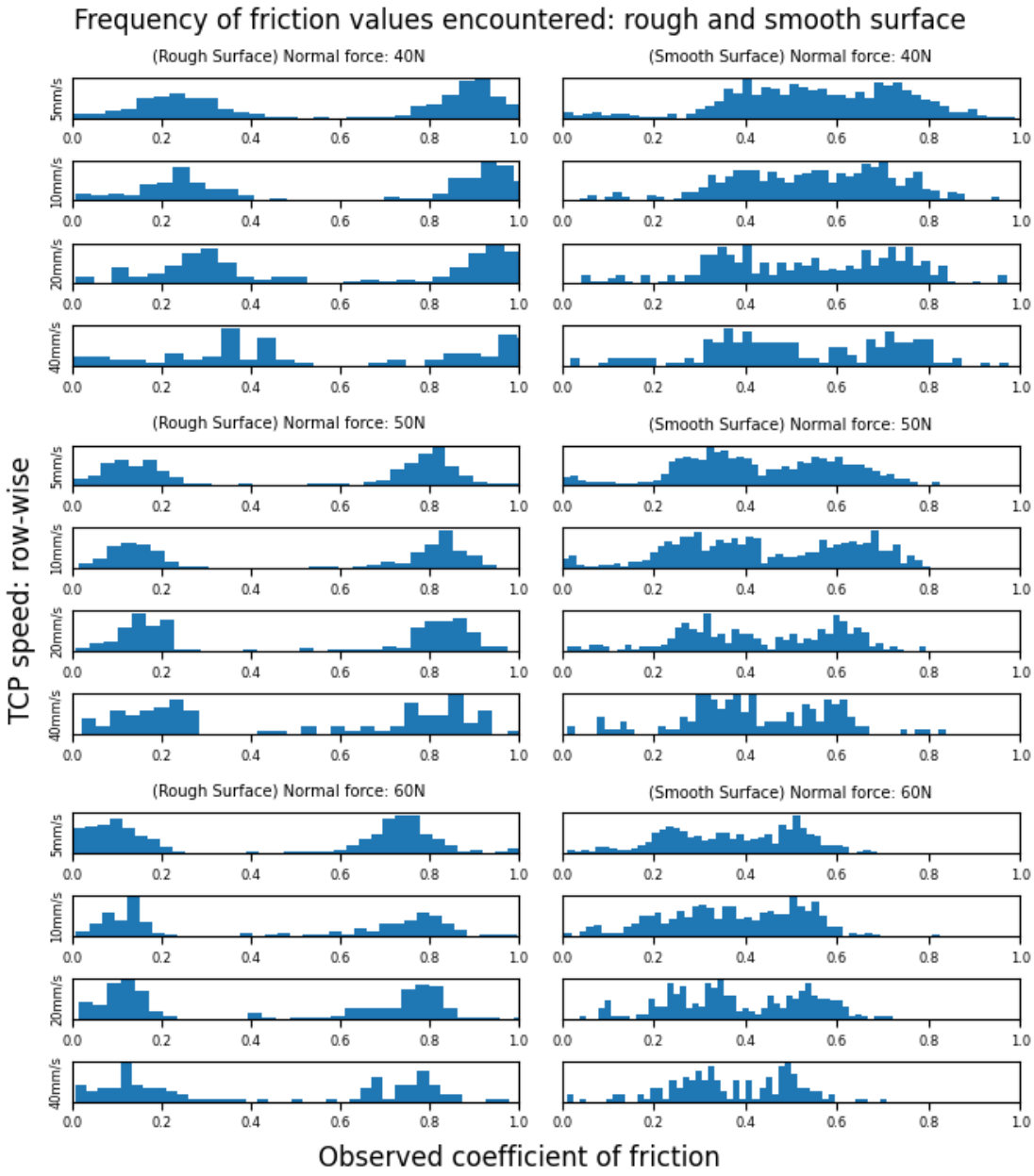

Figure 4.15: Histogram plot for two different raster paths over two plates of different roughness values. Results for rough and smooth CFRP surfaces show the effects of speed and applied force on the frequency of the observed friction values as a percentage of the total number of observations.

high quality UT data as there is a thick layer of couplant between the tool and part. This alternating bow-wave effect can also be seen in Figure 4.16.

At the raster end-points, the misalignment force is seen as spikes in the friction. The result is that along each raster-line, changes in the friction data can be accurately gathered. However, these data are not transferable across arbitrary raster line-paths. For the purpose of informing operators of changes in surface friction, this is sufficient to highlight potential issues such as significant surface corrosion within the region scanned.

Scanning of a friction-stir-weld is shown in Fig: 4.16. The ridges of a friction-stir welded plate, shown in Figure 4.16a with 0.5 mm ridges at the edge of the weld-line.

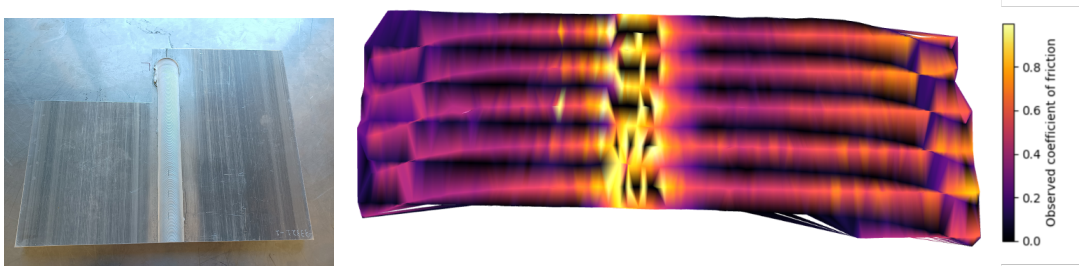

(**a**) (**b**)

Figure 4.16: Friction analysis of a friction-stir weld shows that measuring the surface-friction can indicate discontinuities in the surface. The upper section presented a sharpened lip, avoided for the safety of the wedge. (**a**) Colour image of the welding plate. The lower half of the plate was scanned as part of this analysis. (**b**) Friction coefficient encountered as a heat-map over the surface. The accuracy of the frictional values is determined by the size and shape of the wedge's surface—in this case, 25 × 25 mm.

In Figure 4.16b, the ridges can be seen as peaks in the observed coefficient of friction. The normal force control is to maintain consistent contact between the surface and probe, with surface to probe offset values for the curved sample scan

presented in Figure 4.17.

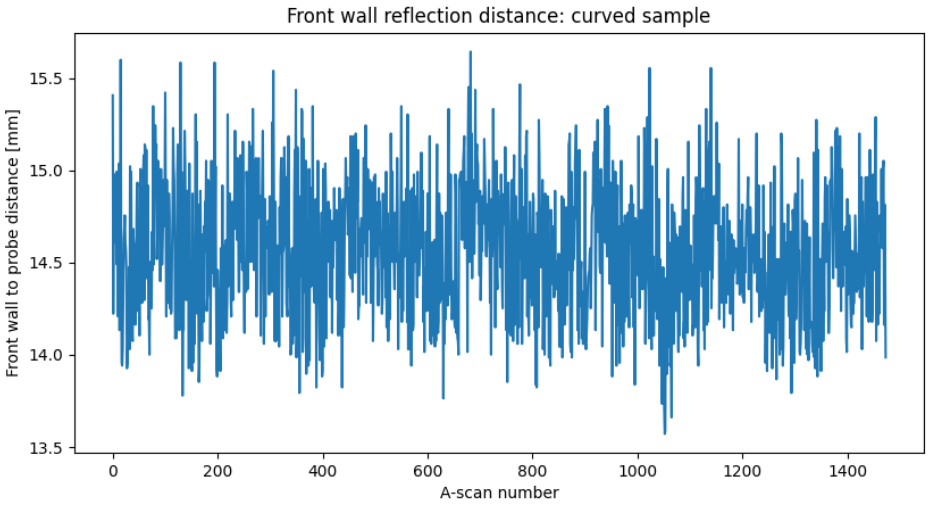

Figure 4.17: The maximum signal response for each A-scan used to calculate probe-surface offset.

The standard deviation of 0.36mm demonstrates the consistency of contact enabled by both the force-control implemented and the sprung tool deployed.

4.6 Discussion

The two-scale part localisation and path planning methods presented were shown to be robust to different parts with minimal requirements on the placement within the work-cell. However, the criticality of initial tool alignment to guarantee full surface traversal success may require either lasers with greater ranges or operator intervention to re-align the tool in cases of extreme curvature or point-cloud error.

The front-loading of collision avoidance in path planning stages allows the

positioning algorithm to react in real-time, correcting position and orientation deviations in a timely way. However, parallelised methods for simultaneous path correction and collision detection may require investigation for robotic platforms that have limited configuration spaces. The UR platform's joints, unlike many others, have the advantage of a $\pm 2\pi rad$ operating range allowing continuous motions over more complex shapes. Taking advantage of these data allows full collision-free coverage of surfaces whose point cloud representations cover all regions of extremal curvature. Future works will investigate integrating this process with the CSFA to capture positions outside of the initial point cloud but still within the robot's working-range.

While both of the part-localisation stages provided accurate surface positions to use as way-points, for smaller surfaces more appropriate tools such as roller probes or jet-phased array tools may be preferable to prevent wear and tear due to sharp corners.

The novel friction metric has demonstrated it is possible to differentiate regions of high and low friction within each raster-segment, providing useful information to the operator when a surface may be improperly prepared. However, a global friction-coefficient metric is not possible due to mechanical effects. The data collected on flat samples can be explained by the Stribeck-friction model used, the stick friction encountered at the end points being known and explicable [31].

Finally, the speed-control and correction mechanism has displayed effectiveness in path planning between inaccurate points using local data. The key drawback is the limitation to convex-shaped regions of parts. For the use-cases considered, the method was sufficient, however for use cases that present large holes in parts, the method may be modified so that the robot retracts within holed regions of a surface.

4.7 Conclusions

This section has presented a novel method of autonomous robotised UT deployment that locates the part, plans a path over its surface, approaches the surface without collisions, and scans the surface. In doing so, the proposed methodology frees up operator time and enables flexible collision-free UT sensor deployment to unseen surfaces without the need for a digital twin and without the need for a lengthy pre-scanning and path planning step - the side-by-side workflow comparison can be seen in Fig: 4.18.

The path planning methodology enables greater use of RGB/D cameras applied to robotised NDT, negating their relatively low accuracy without relying on limited-information primitives. Online sensor corrections of the robot's pose and directions of motion provide a significant bridge from local corrections to global coverage of parts using limited information. The approach further enables future part localisation methodologies that may use Artificial Intelligence approaches

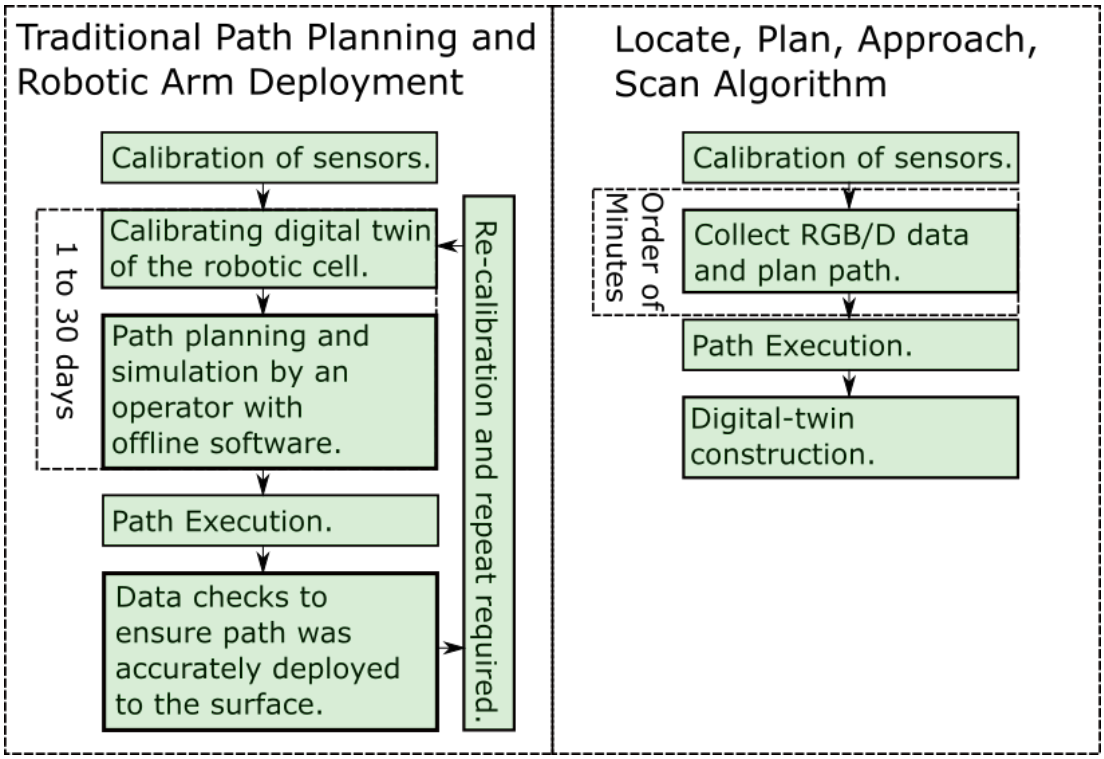

Figure 4.18: Side by side comparison of traditional and proposed work-flows. Saving time at the path planning stage, the proposed method also reduces the need for accurate virtual work-space calibration that may necessitate further scans for full and accurately placed data collection.

to segment work-spaces, potentially resulting in drop-out of surface point cloud positions due to mislabelling.

Local changes in friction can be mapped to an accuracy within that of the CW probe's planar aperture, informing operators of potential issues with surface preparation and signal gating which is of great interest to the automation of NDT processes.

Mentioned throughout the text are the process' limitations. Surfaces with inflections between way points may not result in scans that correctly identify way-

points. This can be solved by introducing multiple frames within a single path planning step. Small parts undergoing scan procedures in highly reflective work cells may require operator awareness for successful path planning using the Structural Similarity method. Path planning over parts smaller than the work-frame may also result in the probe partially overhanging the surface's lip. In processing UT data, the operator needs to be aware of any double reflections that may cause UT-signal gating issues. For online corrections the laser-distance measurements may be too widely spaced apart, preventing accurate surface normal alignment. To avoid this issue, the width of their spacing should be minimised. Finally, the success of the path planning method is reliant on the camera calibration quality. The operator is responsible for accurately calibrating the camera tool, so that the produced paths are accurately placed within the robotic work-cell.

One advantage of the CSFA over this method is its resilience to kinematic issues such as singularities, due to its iterative path-planning in Configuration-space. While operator intuition can place parts within the work-cell to avoid singularities, the goal of autonomous industrial use makes this requirement overly restrictive. Further, as mentioned in Section: 2.4.5, the configuration-space path over the part determines the energy and force-control efficiency of the Cartesian path. In this chapter, apriori Cartesian knowledge was used to inform the Configuration-space perspective, so far only used for collision avoidance, in order to optimise the developed flexible Robotic NDT deployment.

So far, this thesis has looked at parts for which an accurate digital twin is not available. Methods creating an STL then path planning over them are extensively mentioned as the nearest neighbours of the presented processes in the current and previous sections. In Chapter: 5, this thesis seeks to utilise the current work to introduce an iterative, portable, and low-risk process capable of simultaneous global profiling and scanning of parts larger than the work-volume by introducing further Cartesian perspectives.

Bibliography

[1] Carmelo Mineo, Donatella Cerniglia, and Alastair Poole. Autonomous robotic sensing for simultaneous geometric and volumetric inspection of free-form parts. *Journal of Intelligent & Robotic Systems*, 105(3):54, Jun 2022. ISSN 1573-0409. doi: 10.1007/s10846-022-01673-6. URL `https://doi.org/10.1007/s10846-022-01673-6`.

[2] *KR 6 R900 sixx*. KUKA. https://www.kuka.com/-/media/kuka-downloads/imported/6b77eecacfe542d3b736af377562ecaa/0000205456$_e$*n.pdf*.

[3] Visionic Fuzzy Logic. Fuzzy logic and visionic offer robotics for the nuclear industry. *BINDT*. URL `https://www.bindt.org/News/march-2022/fuzzy-logic-and-visionic-offer-robotics-for-the-nuclear-industry/`.

[4] Carmelo Mineo, Donatella Cerniglia, Vito Ricotta, and Bernhard Reitinger. Au-

tonomous 3d geometry reconstruction through robot-manipulated optical sensors. *The International Journal of Advanced Manufacturing Technology*, 116(5):1895–1911, Sep 2021. doi: 10.1007/s00170-021-07432-5. URL https://doi.org/10.1007/s00170-021-07432-5.

[5] Gabriel Meynet, Julie Digne, and Guillaume Lavoué. Pc-msdm: A quality metric for 3d point clouds. In *2019 Eleventh International Conference on Quality of Multimedia Experience (QoMEX)*, pages 1–3, 2019. doi: 10.1109/QoMEX.2019.8743313.

[6] M. Visvalingam and J. D. Whyatt. Line generalisation by repeated elimination of points. *The Cartographic Journal*, 30(1):46–51, 1993. doi: 10.1179/000870493786962263. URL https://www.tandfonline.com/doi/abs/10.1179/000870493786962263.

[7] Thomas A. Omwando. A fuzzy inference system approach for evaluating the feasibility of product remanufacture. *ProQuest Dissertations and Theses*, page 140, 2016. URL https://www.proquest.com/dissertations-theses/fuzzy-inference-system-approach-evaluating/docview/1857435877/se-2?accountid=14116.

[8] Silvano Galliani, Katrin Lasinger, and Konrad Schindler. Massively parallel multiview stereopsis by surface normal diffusion. In *2015 IEEE Interna-*

tional Conference on Computer Vision (ICCV), pages 873–881, 2015. doi: 10.1109/ICCV.2015.106.

[9] *3D Sesnors Catalogue*. Micro-Epsilon, 5 2022. https://www.micro-epsilon.co.uk/download/products/cat–3D-sensors–en.pdf.

[10] Sunil K. Sinha, Paul W. Fieguth, and Maria A. Polak. Computer vision techniques for automatic structural assessment of underground pipes. *Computer-Aided Civil and Infrastructure Engineering*, 18(2):95–112, 2003. doi: https://doi.org/10.1111/1467-8667.00302. URL `https://onlinelibrary.wiley.com/doi/abs/10.1111/1467-8667.00302`.

[11] Sanjay Kumar Ahuja and Manoj Kumar Shukla. A survey of computer vision based corrosion detection approaches. In Suresh Chandra Satapathy and Amit Joshi, editors, *Information and Communication Technology for Intelligent Systems (ICTIS 2017) - Volume 2*, pages 55–63, Cham, 2018. Springer International Publishing. ISBN 978-3-319-63645-0.

[12] Michaela Servi, Elisa Mussi, Andrea Profili, Rocco Furferi, Yary Volpe, Lapo Governi, and Francesco Buonamici. Metrological characterization and comparison of d415, d455, l515 realsense devices in the close range. *Sensors*, 21(22), 2021. ISSN 1424-8220. doi: 10.3390/s21227770. URL `https://www.mdpi.com/1424-8220/21/22/7770`.

[13] Francisco LourenÇo. and Helder Araujo. Intel realsense sr305, d415 and l515:

Experimental evaluation and comparison of depth estimation. In *Proceedings of the 16th International Joint Conference on Computer Vision, Imaging and Computer Graphics Theory and Applications - Volume 4: VISAPP,*, pages 362–369. INSTICC, SciTePress, 2021. ISBN 978-989-758-488-6. doi: 10.5220/0010254203620369.

[14] Chun-Chieh Chan and Ching-Chih Tsai. Collision-free path planning based on new navigation function for an industrial robotic manipulator in human-robot coexistence environments. *Journal of the Chinese Institute of Engineers*, 43(6): 508–518, 2020. doi: 10.1080/02533839.2020.1771210. URL `https://doi.org/10.1080/02533839.2020.1771210`.

[15] Intel Realsense. Which intel realsense device is right for you? *Intel*. URL `https://www.intelrealsense.com/which-device-is-right-for-you/`.

[16] Gordon Dobie, Rahul Summan, Charles Norman Macleod, and Stephen Gareth Pierce. Visual odometry and image mosaicing for nde. *Ndt & E International*, 57:17–25, 2013.

[17] Aamir Khan, Carmelo Mineo, Gordon Dobie, Charles Norman Macleod, and Gareth Pierce. Vision guided robotic inspection for parts in manufacturing and remanufacturing industry. *Journal of Remanufacturing*, 11:49–70, 2020.

[18] Vladimir Ivan, Arnau Garriga-Casanovas, Wolfgang Merkt, Frederic B. Cegla, and Sethu Vijayakumar. Autonomous non-destructive remote robotic inspection

of offshore assets. volume Day 1 Mon, May 04, 2020 of *OTC Offshore Technology Conference*, 05 2020. doi: 10.4043/30754-MS. URL `https://doi.org/10.4043/30754-MS`. D011S006R003.

[19] Changhong Chen, Shaofeng Wang, and Shunzhou Huang. A point cloud-based feature recognition and path planning method. *Shock and Vibration*, 2022:1050038, Feb 2022. ISSN 1070-9622. doi: 10.1155/2022/1050038. URL `https://doi.org/10.1155/2022/1050038`.

[20] Marko Car, Lovro Markovic, Antun Ivanovic, Matko Orsag, and Stjepan Bogdan. Autonomous wind-turbine blade inspection using lidar-equipped unmanned aerial vehicle. *IEEE Access*, 8:131380–131387, 2020. doi: 10.1109/ACCESS.2020.3009738.

[21] Martin Ester, Hans-Peter Kriegel, Jörg Sander, and Xiaowei Xu. A density-based algorithm for discovering clusters in large spatial databases with noise. In *Proceedings of the Second International Conference on Knowledge Discovery and Data Mining*, KDD'96, page 226–231. AAAI Press, 1996.

[22] Qian-Yi Zhou, Jaesik Park, and Vladlen Koltun. Open3D: A modern library for 3D data processing. *arXiv:1801.09847*, 2018.

[23] Carmelo Mineo, Charles MacLeod, Maxim Morozov, S. Gareth Pierce, Rahul Summan, Tony Rodden, Danial Kahani, Jonathan Powell, Paul McCubbin, Coreen McCubbin, Gavin Munro, Scott Paton, and David Watson. Flexible

integration of robotics, ultrasonics and metrology for the inspection of aerospace components. In *43rd Review of Progress in Quantitative Nondestructive Evaluation*, volume 1806 of *American Institute of Physics Conference Series*, page 020026, February 2017. doi: 10.1063/1.4974567.

[24] Robert Watson, Mina Kamel, Dayi Zhang, Gordon Dobie, Charles MacLeod, S. Gareth Pierce, and Juan Nieto. Dry coupled ultrasonic non-destructive evaluation using an over-actuated unmanned aerial vehicle. *IEEE Transactions on Automation Science and Engineering*, pages 1–16, 2021. doi: 10.1109/TASE.2021.3094966.

[25] Miguel Ángel Trujillo, José Ramiro Martínez-de Dios, Carlos Martín, Antidio Viguria, and Aníbal Ollero. Novel aerial manipulator for accurate and robust industrial ndt contact inspection: A new tool for the oil and gas inspection industry. *Sensors*, 19(6), 2019. ISSN 1424-8220. doi: 10.3390/s19061305. URL `https://www.mdpi.com/1424-8220/19/6/1305`.

[26] Chris Gregg and Kim Hazelwood. Where is the data? why you cannot debate cpu vs. gpu performance without the answer. In *(IEEE ISPASS) IEEE International Symposium on Performance Analysis of Systems and Software*, pages 134–144, 2011. doi: 10.1109/ISPASS.2011.5762730.

[27] Vladimir G. Ivancevic and Tijana T. Ivancevic. Lecture notes in lie groups, 2011.

[28] Rames C. Panda. *Introduction to PID Controllers*. IntechOpen, Rijeka, Feb 2012. doi: 10.5772/2422. URL https://doi.org/10.5772/2422.

[29] Rodrigo Pérez-Ubeda, Ranko Zotovic-Stanisic, and Santiago C. Gutiérrez. Force control improvement in collaborative robots through theory analysis and experimental endorsement. *Applied Sciences*, 10(12), 2020. ISSN 2076-3417. doi: 10.3390/app10124329. URL https://www.mdpi.com/2076-3417/10/12/4329.

[30] ISO Central Secretary. Non-destructive testing — ultrasonic thickness measurement. Standard ISO 16809:2017(E), International Organization for Standardization, Geneva, CH, 2017. URL https://www.iso.org/standard/62711.html.

[31] H. Olsson, K.J. Åström, C. Canudas de Wit, M. Gäfvert, and P. Lischinsky. Friction models and friction compensation. *European Journal of Control*, 4(3):176–195, 1998. ISSN 0947-3580. doi: https://doi.org/10.1016/S0947-3580(98)70113-X. URL https://www.sciencedirect.com/science/article/pii/S094735809870113X.

[32] Yansong Wang. Friction in conformal contact interface. In *Encyclopedia of Tribology*, pages 1311–1315. Springer US, Boston, MA, 2013. ISBN 978-0-387-92897-5. doi: 10.1007/978-0-387-92897-5_31. URL https://doi.org/10.1007/978-0-387-92897-5_31.

[33] Yansong Wang and Q. Jane Wang. *Stribeck Curves*, pages 3365–3370. Springer US, Boston, MA, 2013. ISBN 978-0-387-92897-5.

doi: 10.1007/978-0-387-92897-5_148. URL https://doi.org/10.1007/978-0-387-92897-5_148.

[34] B. Armstrong-Helouvry. Dynamic friction in the control of robots. In *Proceedings of the 1994 IEEE International Conference on Robotics and Automation*, pages 1202–1207 vol.2, 1994. doi: 10.1109/ROBOT.1994.351322.

[35] L.G. Garcia-Valdovinos and V. Parra-Vega. Experimental issues of finite time compensation of dynamic friction for robots. In *Proceedings of the 2003 American Control Conference, 2003.*, volume 4, pages 3275–3280 vol.4, 2003. doi: 10.1109/ACC.2003.1244036.

[36] Technology Agency for Science and Singapore Research. A new class of collaborative robots may be the future of industrial re-manufacturing. *Physics.org*. URL https://phys.org/news/2016-08-class-collaborative-robots-future-industrial.html.

[37] F. Bernardini, J. Mittleman, H. Rushmeier, C. Silva, and G. Taubin. The ball-pivoting algorithm for surface reconstruction. *IEEE Transactions on Visualization and Computer Graphics*, 5(4):349–359, 1999. doi: 10.1109/2945.817351.

Chapter 5

Extrinsic Planar Frames of Reference and Scalable NDT Data Stitching for full-structure Reconstuctions

Previous chapters investigated the perspectives of the tool and then Configuration and projective camera spaces in order to enable fully automated scanning within a limited work-volume. In order for the flexible system to be fully utilised, individual scans at different positions along a part require a method of relating the robot's base-poses for each individual scan to one another. The output of this chapter is a method using visual reference markers as additional, artifi-

cial frames of reference embedded within 3D space. Importantly, compared to other absolute relative positioning methods, in this novel perspective there is no definitive world-frame. Metrological equipment tracks the robot's pose within its frame of reference, defined as the world-frame. This method takes the novel perspective of obtaining the relative positioning of scans, as opposed to absolute positioning. The perspective allows expansion to an arbitrary number of linked frames, scanning arbitrarily large or small volumes, then reconstructing the data within a localised frame. Freedom from a world-frame allows easy re-localisation in the case of re-scanning or in long term health monitoring. Framing the problem as accurate relative positioning, it becomes a group-theory task where chosen branches are sought that; include all frames that are within connected components of the group, and minimise the estimated positioning error expressed as a cost. A graphical representation is in Fig: 5.1.

Related inertial and visual relative positioning techniques are explored in Sections: 5.1,5.2. Section 5.3.1 then presents alternatives to the chosen calculation process, and the chosen method presented in 5.3. The challenge of estimating the strength of individual relative transformations requires an accurate cost metric, investigated in Section: 5.5. Finally, the outcome of a multi-pose scan shows how it is both successful and complimentary to the methods developed for autonomous scanning in previous chapters.

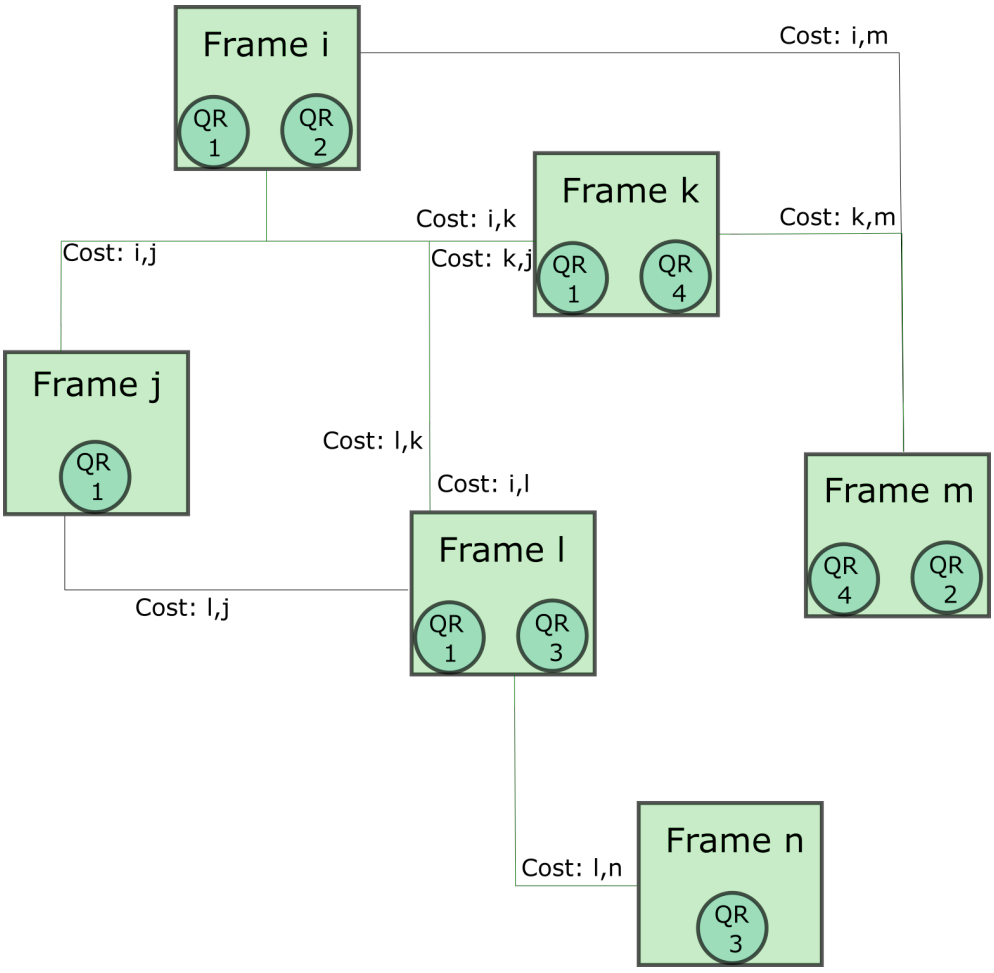

Figure 5.1: The problem of choosing the frame from which the others are stitched to is finding the frame such that minimises the total cost of all necessary minimal length sub-cycles of the graph. If we chose to minimise the maximal depth of the graph (equivalent to assuming each frame to frame cost is the same), frame k would be chosen with included links in green.

5.1 Related Works

While the arm's position relative to the base is accurately reported, full part reconstruction requires the base's position relative to a world-frame for each iterative scan.

Mobile platforms are often equipped with wheel encoders that provide Odom-

etry as to the current position. However, encoder calibration results in displacement errors to accumulate resulting in inaccurate estimates over long ranges, in addition to extrinsic factors such as water that can cause wheel-slippage [1]. In cases such as inspection in busy industrial environments that would demand a high TRL level for automotive base safety for deployment, Cobot platforms such as the UR10e can be mounted onto low-cost trolleys with no inertial data available as in Chapter: 7. In these situations, an accurate relative positioning method is necessary for large-structure scanning reconstructions. It is also desirable to ensure the positioning is robust in on-site environments to ensure industrial deployment.

Visual Odometry such as Visual Simultaneous Localisation And Mapping (V-SLAM) variants are commonly used to construct maps and provide a relative position of the mobile robot platform [2]. Visual Simultaneous V-SLAM applied to NDT data collection has been found to be limited to non-specular, visually isotropic materials from which consistent features can be extracted to provide sufficiently accurate positioning [3]. Further monocular camera positioning such as ego-motion [4, 5] provides high-quality position estimates, with greater reliability than wheel odometry in cluttered, steep, and slippery environments [1]. While VO provides greater certainty and accuracy in mapping than inertial based odometry, the requirement for feature dense static environments make their application unsuitable for robotic localisation relative to structures significantly larger than the

camera's field of view, in dynamic environments, or for featureless surfaces. The high data and computational quotient for part localisation with monocular VO methods provide additional disadvantages when deployed on-site with minimal operator intervention [6].

A low data alternative that does not rely on feature extraction for single-pose relative part-robot localisation are 3D Red-Green-Blue-Depth (RGB/D) structured light cameras. Robotic next-best-view planning using realsense RGB/D cameras have demonstrated high-quality reconstructions of whole parts within a static work-cell [7]. In that work, the reconstruction process is limited by the working envelope of the robot. Further, the time for reconstruction for these is added to the time for the scan creating a bottleneck, requiring an accurate digital twin for traditional NDT sensor deployment. The authors recently investigated streamlining the path planning process using noisy depth-camera data and live path corrections with force/laser feedback [8]. Accurate reconstructions were produced from supplementary data collected during the scanning process. The total visual data required is reduced from many shots to a single colour image coupled to a noisy depth image, with live path corrections removing the necessity for high reconstruction accuracy throughout the process, reducing computation and time bottlenecks. The low cost and volume of the RGB/D camera used minimises both risk and probability of collisions when mounted parallel to a UT sensor, allowing flexible deployment without changing tools.

To provide a global map of the part, multiple-pose localisation mirroring VO methods is necessary. Several methods for RGB/D image alignment are available, with global transformation estimates succeeding primarily due to the the fusion of traditional Computer-Vision techniques with depth data [9, 10]. Iterative-Closest-Point (ICP) is also a candidate alignment solution. However it is not a sufficient global alignment method, since ICP requires a relatively high initial alignment accuracy by virtue of its least squares approach applied to closest-points [11]. Relative positioning systems such as large-scale photogrammetry provide high accuracy solutions [12], however their work-space is still limited by their working volume. Further, when re-scanning of a particular area is necessary after the part or system has been moved, re-estimates of part-robot relative positioning are not possible.

5.2 Visual Reference Marker Reconstructions

Visual reference markers attached to parts offer a solution for scalable data stitching methods in the environments and with the parts of interest, and offer a method of localisation for subsequent scans. Quick-Response (QR) codes that are commonplace in every day environments are unique, orientable and contain an abundance of extractable features. The goal of the study is to find the relative transformation between scanning frames in order to reconstruct the part. The relations governing the multiple-scan reconstructions are represented graphically

in Fig: 5.2.

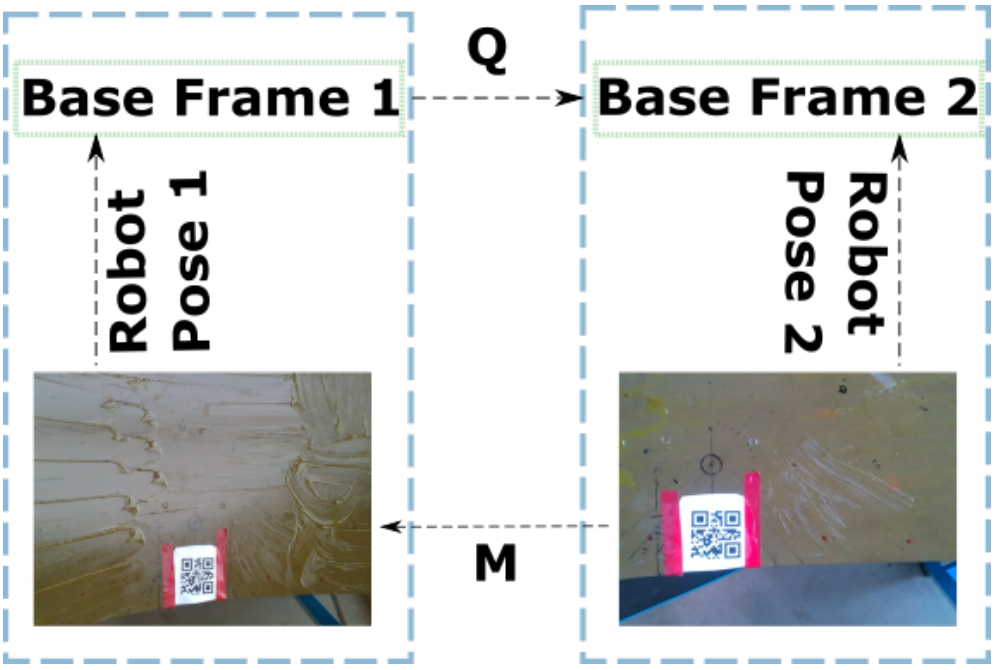

Figure 5.2: Matrix relations between images taken and the relative base frames of the robot relative to the part. The matrix Q is sought to reconstruct the part through iterative scans, when images of QR codes are taken at known robotic poses in each base frame. By finding the image to image transformation M, Q can be calculated when combined with the robot poses.

Alternative visual markers such as fiducial markers also provide orientable and unique markers. Image alignment correction using fiducial markers is well researched, proving a source of high-accuracy reconstructions [13, 14, 15]. QR codes are chosen in this thesis for the additional data they can be associated with, with the potential to provide easy reference to long term structural health information of the part. In instances where geometries are so complex the robotic paths and relative base positioning are severely restricted, such as automotive fuel tank inspections, using prior relative robot to part positioning and tool paths that

are associated with the QR code can reduce path planning costs from a running cost to an overhead. A complementary investigation in [16] demonstrates how futuristic NDT data visualisation on a phone or tablet with Virtual Reality is possible when visual markers can orient the data projection, and link the part to the digital twin. The introduced method may also be applied to other proprietary markers. Proof of concept studies have shown that in environments where feature symmetries are present such as in warehouse applications, QR codes can be used as navigation key-points and short-path planning aids with minimal data requirements [17]. For large-volume reconstructions, QR codes have enabled automatic key-frame extraction enabling accurate localisation [18, 19]. QR codes have seen further use in point cloud reconstruction, both in the case of small objects placed on a QR-calibrated rotating table [20], and as direct visual artefacts in large-scale point cloud merging for disaster-response robots [21]. They have even seen use in calibrating industrial robots with a monocular camera [22].

5.3 QR Code Stitching Algorithm

Complementary to the autonomous method presented by the authors in [8], after the scanning area was profiled with a commercial RGB/D camera a second image was taken of one or many QR codes. Once the whole part was scanned and QR codes decoded, the QR code images and their positions within each work-space are processed.

Key frames are selected using the individual QR code identifiers. QR codes are identified and a bounding polygon produced using the Pyzbar python package. selected through masking the image around the detected bounding polygon.

The Scale Invariant Feature Transform (SIFT) [23] estimates pixel to pixel correspondences between masked QR code images, producing a Homographic correspondence between the two images, a one-to-one correspondence due to the planarity of the QR code. The SIFT algorithm initially creates a 3D discrete manifold of intensity images convolved with a parameterised Gaussian intensity; $\tilde{I}(x, y, k) = I(x, y)G(k\sigma)$. A difference along the convolution scale dimension is taken to produce $L_{i,j} = \tilde{I}(x, y, k_i) - \tilde{I}(x, y, k_j)$, along which key points are selected by finding pixel values that are extrema. Key points are then refined within the regular 2D manifold $I(x, y)$ to reduce sensitivity to noise and minimise the effects of local translation invariance of image intensity. First, key points are compared with local pixels and those that differ by less than a theshold are removed. The remaining points that show a relatively high ratio of maximum to minimum principle curvatures within I are removed, as these points are indistinguishable under local distortions of the underlying manifold due to noise. Finally, image keys are defined as features identified with local gradients of I. The keys between two pictures are compared to form a distance bi-graph from which the most shortest distance pairings are taken and a probability measure is assumed by finding the ratio of the distances to first and second nearest potential matching

keys, that is then thresholded to remove low-likelihood matching candidates. Several other feature detection and matching algorithms exist with SIFT shown to be the most accurate under varying orientation and lighting conditions, though not necessarily the fastest [24]. While for real time applications other methods may be preferable, in this study the algorithm with the greatest accuracy is chosen.

Planar surfaces whose features are matched may then be used to produce probable distortion maps between the images. Homographic matrices H, pixel-wise affine maps between images $H : I_1 \rightarrow I_2$, are given by a 3×3 matrix;

$$\begin{bmatrix} x_1' \\ y_1' \\ \lambda \end{bmatrix} = \begin{bmatrix} h_{1,1} & h_{1,2} & h_{1,3} \\ h_{2,1} & h_{2,2} & h_{2,3} \\ h_{3,1} & h_{3,2} & h_{3,3} \end{bmatrix} \begin{bmatrix} x_2 \\ y_2 \\ 1 \end{bmatrix}. \tag{5.1}$$

The x_i, y_i coordinates referring to pixels of the i^{th} image, and x_i', y_i', λ referring to distorted coordinates of the i^{th} image. With at least four corresponding sets of coordinates the matrix H may be derived up to a scaling factor, resulting in non-zero values for $h_{3,1}$, $h_{3,2}$ and a non-singular value for $h_{3,3}$. The proper coordinates $(x_i, y_i) = (x_i'/\lambda, y_i'/\lambda)$ are obtained by re-projecting the space from $\mathbb{R}^3 \rightarrow \mathbb{R}^2$.

As feature dense and orientable, QR codes provide accurate Homography matrices as shown in Section: 5.5. Pixel matching between paired pixels is then used to match depth information shown graphically in Fig: 5.3, providing

linked 3D point sets between the camera frames. Singular value Decomposition

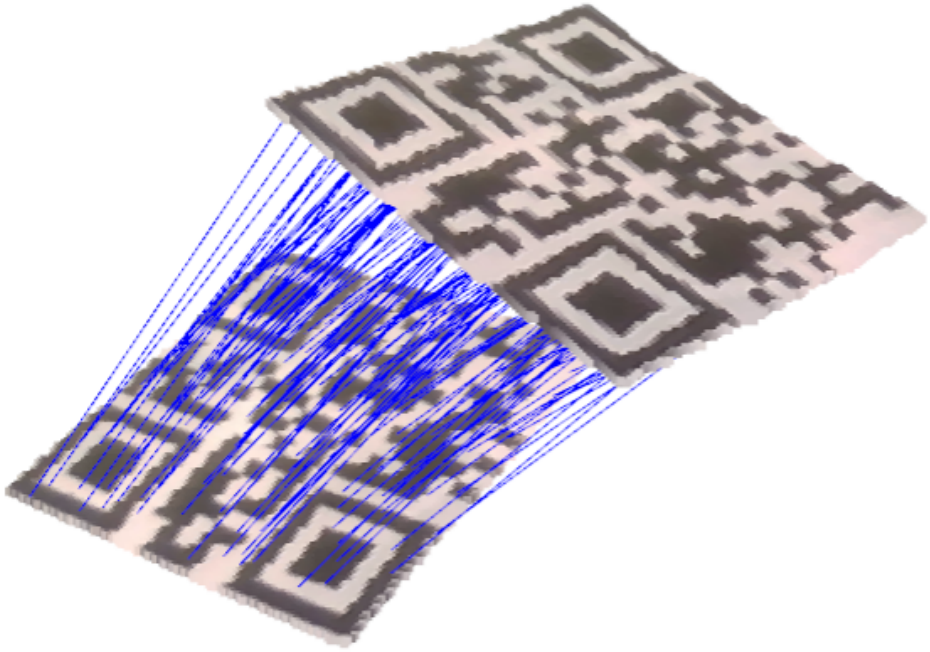

Figure 5.3: Down-sampled 3D representation of QR matches, containing 1% of the image-to image correspondences for visual clarity.

(SVD) method estimates the transformation from the robot to subsequent image frames. Assuming a Gaussian-error profile, a Maximum Likelihood Estimator (MLE) refines the transformation estimation between the two ordered point sets $\{Im_i, Im_j\}$ to the transformation $M_{j,i}Im_i = Im_j$. Shown to be highly linear with distance in ranges from $0.5m$ to $1m$ [25], point-wise probability of error of data P_i collected by the D415 was modelled as a Normal distribution;

$$\text{Error-Magnitude-Probability}(P_i) \sim \mathcal{N}\left(0, \sigma||P_i||\right), \tag{5.2}$$

from which the MLE is constructed. The errors for images i and j, ϵ_i and ϵ_j are assumed to have random magnitude with distribution given in Eq: 5.2. The best fit equation of $M_{i,j}$ is reduced to;

$$P_{i,\alpha} = M_{i,j}P_j + \epsilon, \tag{5.3}$$

where ϵ is modelled as the sum of error of P_i and error propagated from P_j through the rotation component of $M_{i,j}$. The variance of $|\epsilon|$, $\sigma_{|\epsilon|}$ is $\sigma_{|\epsilon|} = \sqrt{\sigma^2_{P_{i,\alpha}} + \sigma^2_{P_{j,\beta}}} = \sigma\sqrt{|P_{i,\alpha}|^2 + |P_{j,\beta}|^2}$. Due to the error distributions having random orientations, the covariance of error distribution ϵ is assumed to be randomly and independently distributed along cardinal directions;

$$\mathrm{Cov}_\epsilon = \sigma_\epsilon \begin{bmatrix} 1 & 0 & 0 \\ 0 & 1 & 0 \\ 0 & 0 & 1 \end{bmatrix}. \tag{5.4}$$

Since the magnitude of error is known, the variance along each cardinal direction can be calculated from the radial equation $r = \sqrt{x^2 + y^2 + z^2}$;

$$\sigma^2_{|\epsilon|} = \sigma^2_\epsilon \left(\left(\frac{\partial r}{\partial x}\right)^2 + \left(\frac{\partial r}{\partial y}\right)^2 + \left(\frac{\partial r}{\partial z}\right)^2 \right) = \sigma^2_\epsilon. \tag{5.5}$$

The log-likelihood of a transformation given the correspondence of $P_{i,\alpha}P_{j,\beta}$ is then

described by the exponent of a multivariate normal distribution, proportional to;

$$\log\left(\mathcal{L}(M_{i,j}|i,\alpha \leftrightarrow j,\beta)\right) \sim -\frac{1}{\sigma_\epsilon^2 2}\left(P_i - M_{i,j}P_j\right) I \left(P_i - M_{i,j}P_j\right). \tag{5.6}$$

The MLE of transform $M_{i,j}$ is then found by maximising;

$$G = -\sum_{\alpha\leftrightarrow\beta} \frac{1}{2\sigma^2\left(|P_{i,\alpha}|^2 + |P_{j,\beta}|^2\right)} |P_i - M_{i,j}P_j|^2, \tag{5.7}$$

that is independent of the scaling term σ.

Images $\{Im_i\}_{i=1}^N$ collected at corresponding positions $\{R_i\}_{i=1}^N$ with a tool T are related with respect to the world-frame transformation pair $Q_{i,j}$;

$$Q_{i,j}R_jTIm_j = R_iTIm_i, \tag{5.8a}$$

from which the world transformation is extracted;

$$Q_{i,j} = \left(R_iT\right) M_{j,i} \left(R_jT\right)^{-1}. \tag{5.8b}$$

Sources of error for point cloud transformations $M_{j,i}$ calculated in the image-frames are; the Homography matrix, uncertainty in depth measurement position within a pixel's width, and the depth measurement error.

Pixel to pixel alignment accuracy can either be thresholded, choosing pixel

matches that align within a given pixel-wise distance, chosen in this chapter to be 0.8 pixels, providing the best all round results. Finally, the depth image error is minimised with the MLE process, and further investigated in Section: 5.5. Robotic positioning and tool calibration errors can introduce uncertainty in the relative world-frame pose transformation $Q_{i,j}$. Robotic positioning errors can be reduced with joint calibration. The tool calibration procedure from [26] was used in order to minimise errors of the tool parameters.

A similar concept applied to mobile robotic platforms was applied to allow a world-frame calibration precision of $\pm 4mm$ using a 2D camera [27]. However, this method diverges from ours in two aspects; the use of 2D data requires large QR codes so that corner identification error is minimised which ours is immune to, and that our approach creates flexible relative-frame localisation within a free frame of reference, as opposed to robot localisation to one of multiple well known world-frames.

The combined group of QR codes after a full scan represent a weighted graph, where each node's weight is given by an accuracy maximisation heuristic. The central node in the graph to be taken as the world-frame is found by maximising the total of this heuristic over all nodes within the graph. The determinants of relative positioning accuracy are covered in the next section. Finally, after the QR code based alignment the combined point clouds for each scan undergo Coloured - Iterative Closest Point (C-ICP) optimisation [28] to further refine the

map. This is an additional benefit of using RGB/D cameras for world-frame calibration. The accuracy of C-ICP shall not be investigated in this chapter, since it is largely dependent on initial point cloud alignment, with poor initial alignment parameters requiring intensive operator intervention in setting inlier thresholds, iteration counts, and can produce misalignment with initially incorrect local correspondences.

The group structure shown in Fig: 5.1 can in some cases of lost inclusions or incomplete point clouds be fractured into sub-structures with un-viable cycles. In this case, while the key-frames and their links are determined by the QR code identification process, the transformations and related costs are unknown. For this reason, the final process engages in an expansionary graph approach, where the fully connected graph with the lowest optimal cost is chosen as the key-section. The unknown links between the disconnected components are then computed from the selection of QR and scan images, and feature transforms computed between each pair. A RANdom SAmple Consensus (RANSAC) process [29] is then applied, resulting in a bi-graph of images, from which the strongest link determined by inlier number is chosen.

The best link is then chosen and used as key-frame for the previously disconnected sub-graph, which is then locally optimised using C-ICP. In the case of a weak-link being retaken, the known existing link structures allow the combined key and newly added sections to be treated as the key section and optimal central

frame re-computed.

This process preserves the accuracy of the largest connected sub-graphs, allowing re-calculation of optimal frames and sections when more accurate data is collected at the cost of less-accurate sub-graphs. In the case of additional costs of re-taking information, such as distance, high traffic, or other exogenous factors in regions so that traversal to poorly defined frame transform regions is difficult, chosen key-sections can be weighted instead by these costs.

5.3.1 Alternate Alignment Method

Previous works such as [27] calibrate a relative pose with respect to the QR code using just the 2D image data. Prior knowledge of the QR's dimensions is coupled to the four observed edge points, allowing an extraction of the QR's relative pose.

However, QR code corner identification can be erroneous. Taking the reference image Fig: 5.4, the image is distorted with randomly generated homography matrices representing changes in planar perspective of up to $0.5m$ and rotations of up to $\pi/4$rad, showing a mean pixel identification error of 0.13 with a standard deviation of 0.47.

Solving the Perspective and Pose problem with OpenCV ('Solve PnP'), the 4 corners of the QR code can be identified and oriented as previously described, and the relative poses of the QR code to the camera P_1, P_2 extracted. The Transformation of data from frame of reference $2 \rightarrow 1$, when tool poses T_1, T_2

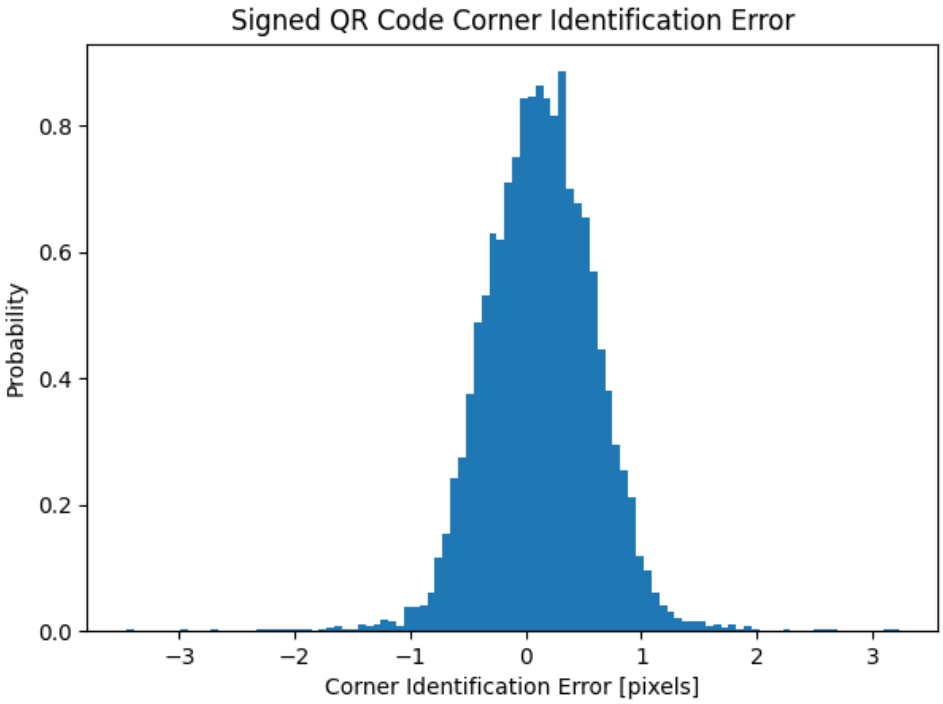

Figure 5.4: Histogram of pixel identification error. Using just corner points for pose estimation can suffer since the identified corner positions are only accurate to an order of a pixel. The pixel-wise error is pronounced for larger distances and small QR codes, necessitating the use of large visual artefacts by [27]. Further, this error distribution is generated within a virtual environment and not representative of real error taken within variable lighting conditions and an imperfectly calibrated camera intrinsic matrix.

within these frames are known is then;

$$M_{1,2} = (T_2 P_2)\,(T_1 P_1)^{-1} \tag{5.9}$$

Corner identification errors shown in Fig: 5.4 then result in position and orientation estimation errors, adding random noise to the pose estimations of P_i as shown in Section: 5.5.

The Solve PnP method implemented in this chapter can use the homographic decomposition method due to the co-planarity of the points. The 3D positions $\overrightarrow{X} = [x, y, z, 1]$ are projected to the $z = 0$ virtual image plane in 2D. The homography matrix H between the seen points $\overrightarrow{u} = [u, v, 1]$ and virtual plane is calculated, and with a given intrinsic matrix the 3×1 x and y axis orientation vectors $\overrightarrow{dx}, \overrightarrow{dy}$ and the translation vector $\overrightarrow{t}$ are extracted as;

$$\left[\overrightarrow{dx}, \quad \overrightarrow{dy}, \quad \overrightarrow{t}\right] = K^{-1}H, \tag{5.10}$$

from which the relative pose can be found.

5.4 NDT Data Reconstructions

Once the relative frame transformations are known, the NDT data can be projected to the chosen base frame. As in [8], laser data used for orientation corrections then is used to create a digital representation of the part that has been scanned. The laser data is collected as six-vectors, the position and approximated surface normal. The pivot-ball reconstruction algorithm [30] then reconstructed a digital representation of the seen part with the laser data as it is robust to non-convex parts. The UT data was collected with a 32 element 10MHz $0.3mm$ pitch sensor housed within a conformable wedge probe mounted in addition to the other sensors. The pose of the robot was simultaneously collected with each A-

scan, and the UT data projected from these known probes to the surface through a ray-tracing process.

While in [8] the authors projected data over each scanned section, it is now possible to create 3D NDT data reconstructions of the whole part at any stage.

5.5 Experimental Results

For the experiments, a Universal Robots UR10e platform deployed a Intel realsense D415 structured light depth camera. To process the data, a python application using Open3D, Universal Robot's Real Time Data Exchange, Intel Realsense' 2.0 SDK, and OpenCV was developed.

A sample set of 56 images were collected with the RGB/D camera, with varying distances and angles to a static QR code within the robot's work-frame. These were used to define determinants of alignment error, with the actual transformation $Q_{i,j}$ = Identity. A data-set of 1460 world frame transformations were generated from all image pairs.

In order to find the relative poses of QR codes, points within point clouds along the QR code are first matched with the Homographic correspondence between images, necessitating a high accuracy in Homographic correspondence between images. Homography matrix accuracy was quantified using the Structural Similarity Index (SSIM) between an image and another image after projection with the calculated Homography matrix. Robust in the present of shadows, the SSIM

indicates the quality of a match between images [31], where 1 is a full match. All Homography matrices between image pairs scored at least 0.97, demonstrating the accuracy of the projection method when considering relatively feature-dense QR code images. The results are shown in Fig: 5.5.

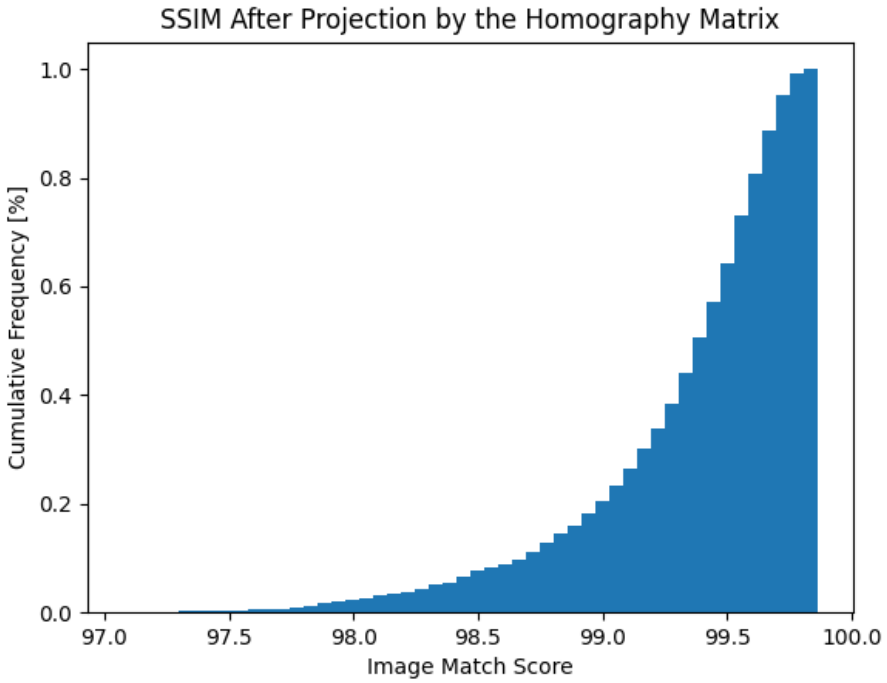

Figure 5.5: Homography matrix calibration accuracy scores. Taking Homography matrices with the QR code images, the second QR code is projected to the space of the first using the matrices. The SSIM then measures the similarity between the the first and projected second images. The scores for all image pairs are presented.

As the next source of image-frame transformation error, the depth image errors were then checked. For each image pair i, j, the positional error and orientation error in $\mathfrak{se}(3)$ coordinates [32] were collected. For all image pairs, the position and calibration accuracy are highly correlated, as highlighted in Fig: 5.6.

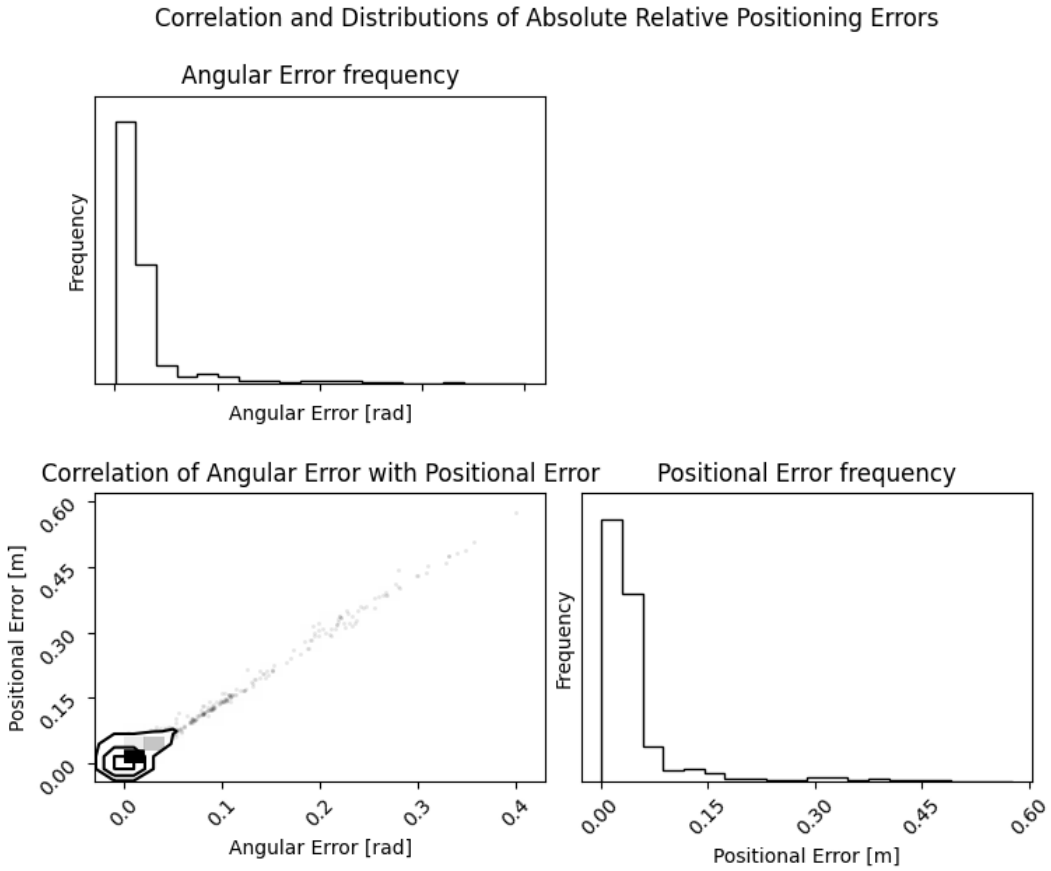

Figure 5.6: Corner plot of the position and orientation position errors for all 1460 image pairs. Corner plot made with the corner-python package [33].

Results from the Sove PnP method mentioned in Section: 5.3.1 are shown in Fig: 5.7.

In direct comparison, the position and orientation errors of the Solve PnP method are larger and less centred around zero than in the proposed method. Angular and positional error is significantly less correlated using the Solve PnP method than the point cloud method alluding to the random noise incurred in

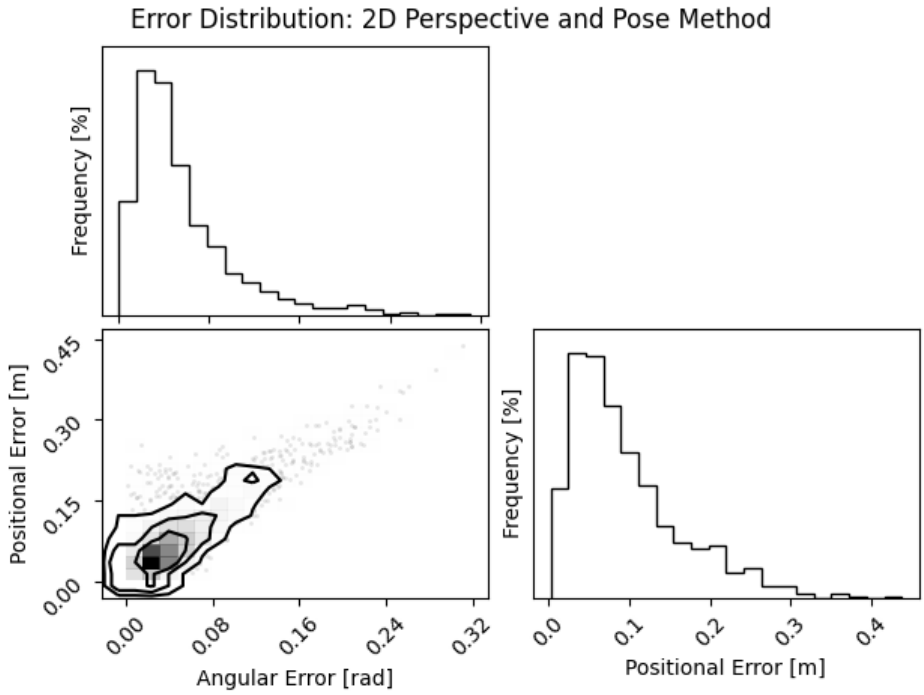

Figure 5.7: Position and orientation error distributions for frame of reference calibration using the Solve PnP method.

corner point identification that is shown in Section: 5.3.1. These results show the 3D alignment method has the dual benefits over the 2D method of; not requiring knowledge of the QR code dimensions, and a greater accuracy in position and orientation of relative frame of reference calibrations.

When compared to the nearest initial global RGB/D frame alignment method, RANSAC feature-based point cloud alignment [34], the Homographic method is significantly more accurate as seen in Fig: 5.8. Both were tested on the same data, and despite the significant information present in the QR codes, environmental data prevented the whole-image method from aligning the point clouds

consistently.

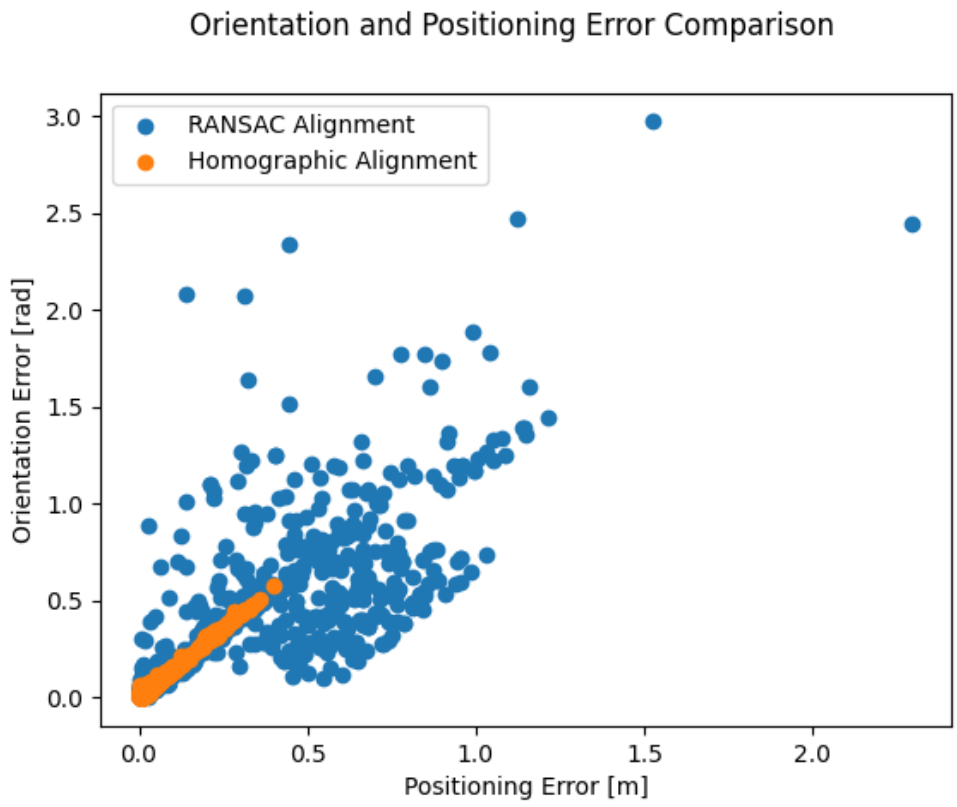

Figure 5.8: Despite both methods using SIFT feature extraction to align depth images with the same data-set, the Homographic QR alignment method proved to be significantly more accurate than the RANSAC based method, even within a static environment.

Since the position and orientation errors of the proposed method are highly correlated, as shown in Fig: 5.6, optimal calibration parameters were sought to minimise both. It was found that the inclusion of results closer than $0.5m$ reduced the average measurement accuracy. They were removed, and average world-frame transformation error was collected. In Fig: 5.9, frames containing the least number of points eliminated from the results on each iteration showing a

correlation between cumulative QR point cloud density and calibration accuracy. The optimal configuration for world-frame calibration is $0.5m$, from an angle that maximises the area of the QR code within the colour image. RGB/D images taken from this range reduce the linear positioning error to $2.5mm$ and angular positioning error to 0.005rad.

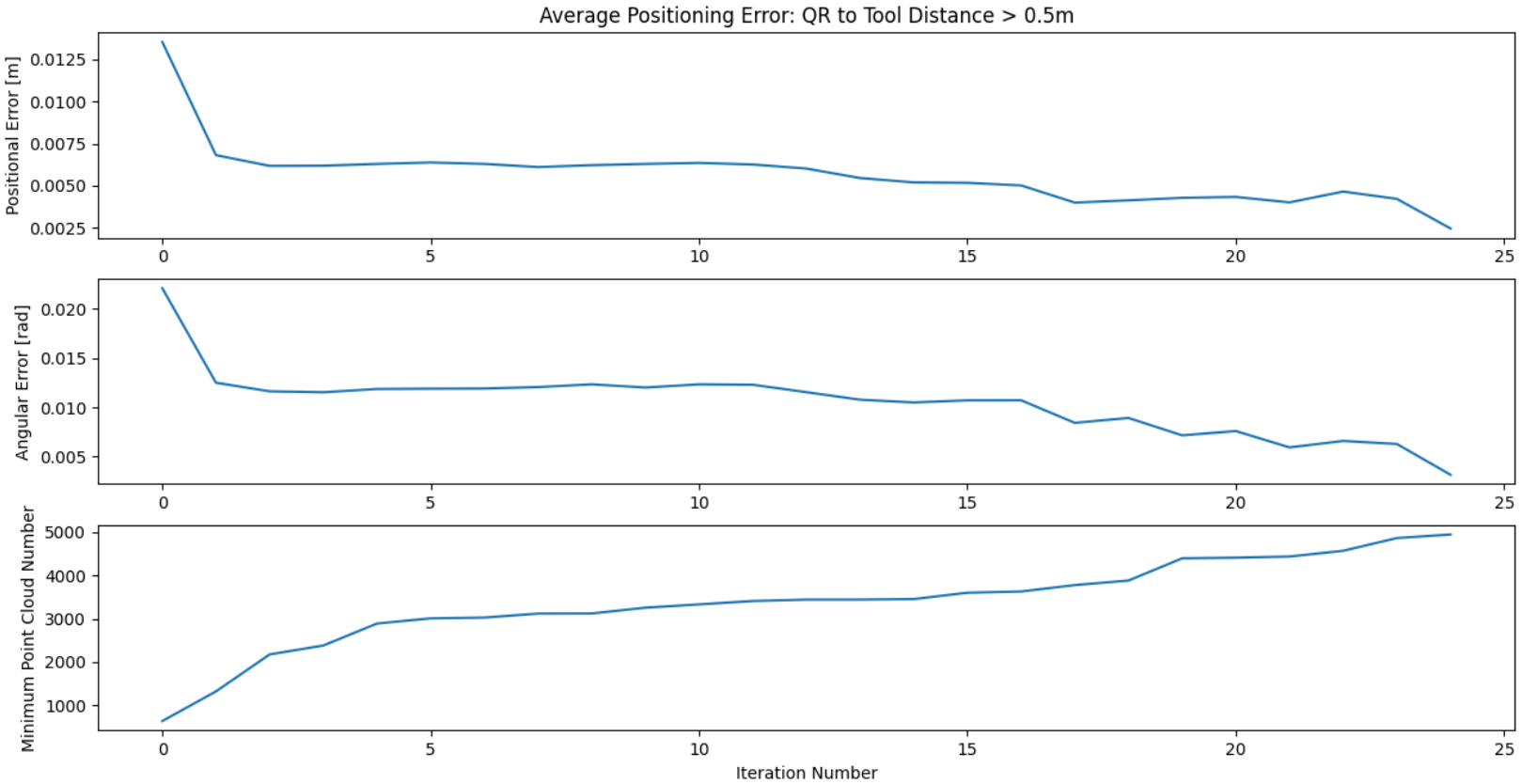

Figure 5.9: When the distance from the QR code is thresholded to be greater than $0.5m$, there is a clear relationship between QR point cloud number and world-frame calibration accuracy.

To demonstrate the method's performance, A-scans of a medium sized part shown in 5.10 were taken in iterative area segments of a part. The part is a $7mm$ thick CFRP section with 5 support struts, of which 4 were covered by scans. As a complementary method to the work developed in [8] three Panasonic HG-C1030 laser distance sensors of $30mm \pm 5mm$ range were used in addition to other sensors for data collection and digital twin construction.

Figure 5.10: Image of the part within the robot cell. The part had to be moved between scans to allow full coverage.

The fully aligned point clouds were stitched, with the resultant full point cloud in the presence of environmental and reflective noise presented in Fig: 5.11.

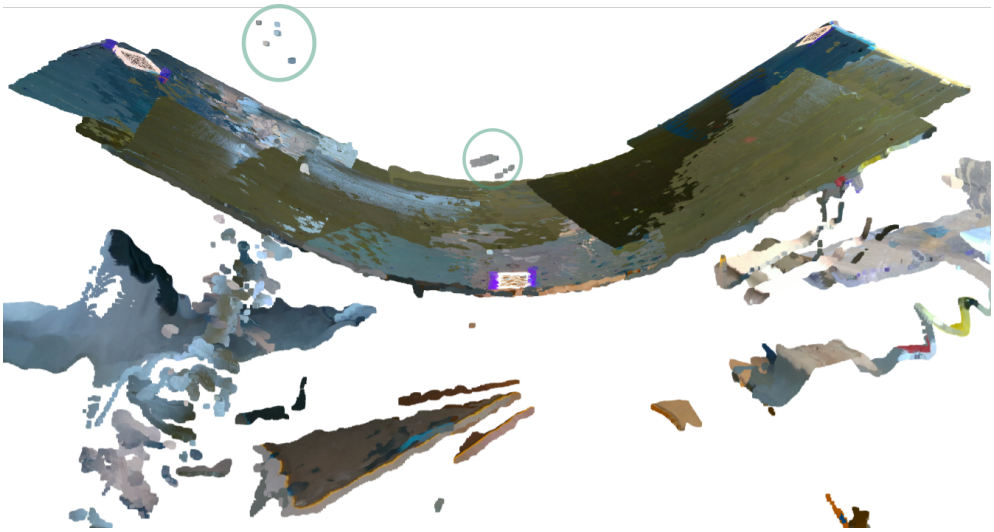

Figure 5.11: Point clouds of the part aligned to three QR code image artefacts. Artefacts caused by the reflective surface are highlighted, while the scattered background due to the part's movement is clearly seen. Differences in surface colouration are due to the changes in ambient light affecting image saturation in each pose.

A digital representation was later constructed from the collected laser data in Fig: 5.12. The A-scan data collected is then re-projected as described in Section: 5.4, and shown in Fig: 5.13.

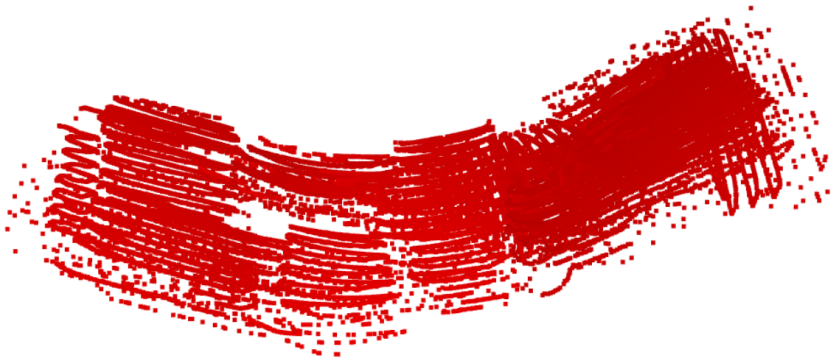

Figure 5.12: Point cloud of laser data collected in each frame, subsequently stitched with the calculated frame of reference transformations.

Figure 5.13: Ultrasonic data projected to the surface. The C-scan data has a point cloud representation, with the heat-map colour displaying gated signal intensity. The area which has not been scanned, highlighted in green, can be clearly seen for an operator or automated system to conduct subsequent scans, even once the part has been moved. Fuller coverage of the surface may be better achieved with full matrix data collection, but this is outside of the scope of this work. A conformable wedge UT probe was used to collect results, coupled to the surface with UT gel couplet.

The point cloud of UT data is then converted to an STereoLithography (STL) format, shown in Fig: 5.14. While missing data easily seen in Fig: 5.13 cannot be seen, the support struts of the structure shown in Fig: 5.10 can be more clearly viewed.

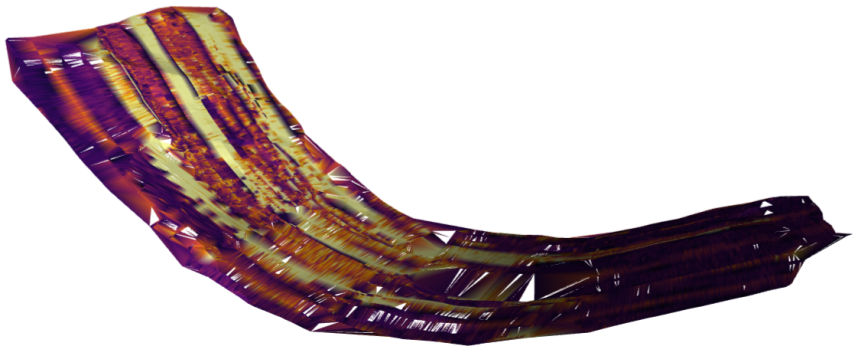

Figure 5.14: The point cloud representation of the UT data can be converted to a digital-twin using the pivot-ball algorithm. A full 3D reconstruction of the part with UT data allows the operator to interpret and assess the part.

5.6 Discussion and Conclusion

The novel use of QR codes for iterative world-frame calibrations allows operators to localise scans on large and visually isotropic parts, key to accurate and repeatable flexible robotic scanning processes. The use of orientable visual markers for data localisation enables both flexible iterative passes, and complements NDT - 4.0 data digitisation and positioning for the long term structural health monitoring of parts with embedded visual markers [16].

While the relative positioning of the camera to the QR code can cause up to 0.6m in positioning error, we have shown this can be reduced to 2.5mm with the optimal QR-robot stand off. This study has further determined a corresponding relationship between the point cloud capture number and world-frame calibra-

tion accuracy, providing the user with an easy to apply set of metrics for data collection in on-site settings. While other relative positioning methods would be preferable for low-tolerance scans in controlled or feature-dense settings, this method advances a previously developed autonomous UT scanning process to enable its accurate deployment on large-scale parts with few visual features in industrial environments. The method introduced allows an accuracy that is suitable for large-scale NDT applications and allows certain re-localisation, while also having minimal data requirements.

Directly complementing the already presented work of Chapter: 4, the implementation of this work within an industrial setting is applied to the industrial use case of this thesis, stitching C-scans to present a digital twin of large parts in the context of on-site deployments. Traditionally, this task has required static, cumbersome, but high accuracy metrological equipment with a calibration time-cost of hours. It is now possible to replace this equipment with low-cost, small profile equipment whose one-off calibration takes less than an hour, trading several orders of magnitude of cost and time for a minor cost in positional accuracy.

5.7 Corridor Reconstruction

The described process is aimed to aid the reconstruction accuracy of a mobile robotic manipulator scanning parts of varying scale, so its demonstration at scale is necessary for validation. To this end a corridor was reconstructed by mounting a D435 Intel Realsense sensor to a mobile KMR iiwa robotic platform. A series of QR codes were mounted on the walls, and the corridor profiled as set out in the proposed method by iteratively taking images of two QR codes at each static mobile-base position. An image of the final reconstruction can be seen in Fig: 5.15.

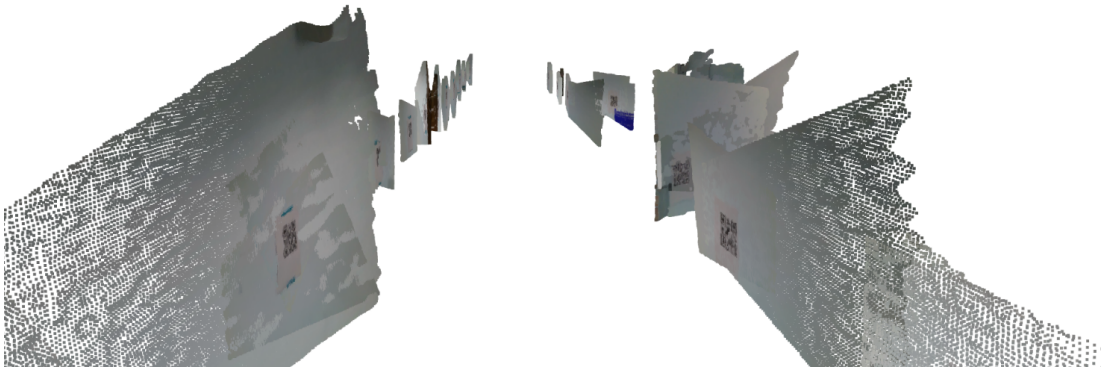

Figure 5.15: An image of the corridor point cloud map, the perspective taken from the end of the corridor. The unified point cloud is down-sampled to allow rendering.

This approach was deemed too inaccurate, since a D435 possesses a wider angle of view than a D415 used in the other experiments (85° vs 65°) with the same number of pixels, reducing the pixel-wise accuracy by up to half. This approach has shown that even with a reduced accuracy, a floor map can be created with

the proposed artificial visual artefact alignment algorithm to a degree that would be informative to a human operator, barring some surfaces such as those with specular reflections. This is confirmed by overlapping the corridor's schematic with the final corridor map as shown in Fig: 5.16.

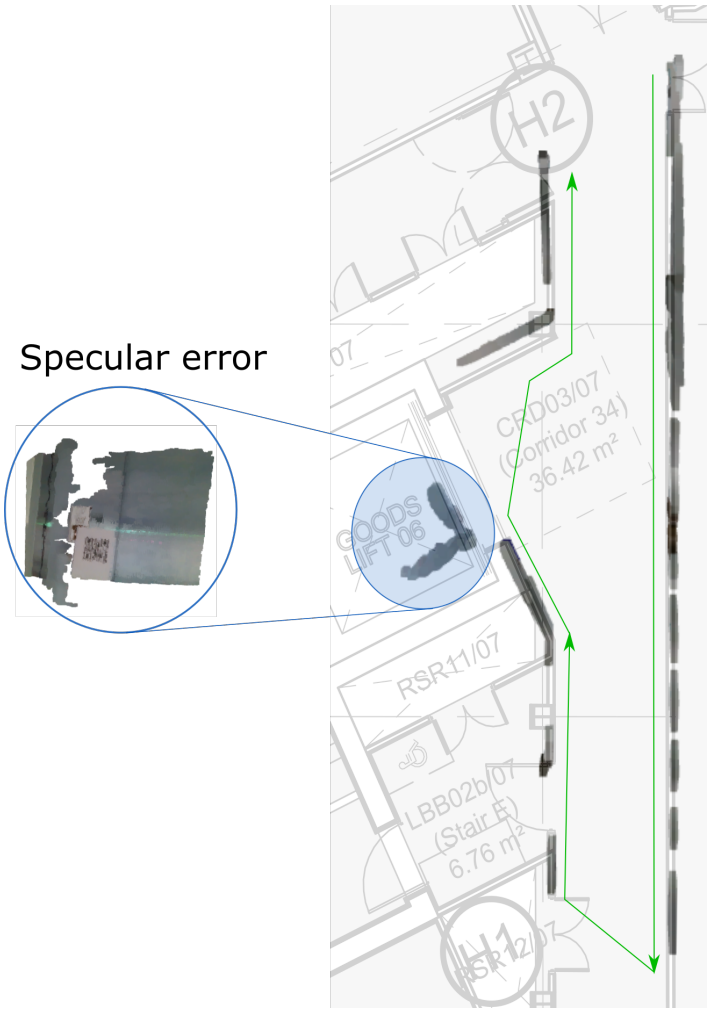

Figure 5.16: Corridor schematic overlayed with a QR code derived iterative map. The green arrows show the direction in which images were taken in. After the significant error caused by specular reflections, the map's accuracy is significantly reduced. Before this, the wall sections are clearly matched to the schematic, with the doorway inlet in the bottom left of the image clearly seen.

Bibliography

[1] Mark Maimone, Yang Cheng, and Larry Matthies. Two years of visual odometry on the mars exploration rovers. *Journal of Field Robotics*, 24 (3):169–186, 2007. doi: https://doi.org/10.1002/rob.20184. URL `https://onlinelibrary.wiley.com/doi/abs/10.1002/rob.20184`.

[2] Daniel T. Savaria and Ramprasad Balasubramanian. V-slam: Vision-based simultaneous localization and map building for an autonomous mobile robot. In *2010 IEEE Conference on Multisensor Fusion and Integration*, pages 1–6, 2010. doi: 10.1109/MFI.2010.5604466.

[3] Gordon Dobie, Rahul Summan, Charles MacLeod, and S. Gareth Pierce. Visual odometry and image mosaicing for nde. *NDT E International*, 57:17–25, 2013. ISSN 0963-8695. doi: https://doi.org/10.1016/j.ndteint.2013.03.002. URL `https://www.sciencedirect.com/science/article/pii/S0963869513000443`.

[4] Carlos Campos, Richard Elvira, Juan J. Gomez Rodriguez, Jose M. M. Montiel, and Juan D. Tardos. ORB-SLAM3: An accurate open-source library for visual, visual–inertial, and multimap SLAM. *IEEE Transactions on Robotics*, 37(6):1874–1890, dec 2021. doi: 10.1109/tro.2021.3075644. URL `https://doi.org/10.1109%2Ftro.2021.3075644`.

[5] Vladyslav Usenko, Nikolaus Demmel, David Schubert, Jorg Stuckler, and

Daniel Cremers. Visual-inertial mapping with non-linear factor recovery. *IEEE Robotics and Automation Letters*, 5(2):422–429, apr 2020. doi: 10.1109/lra.2019.2961227. URL https://doi.org/10.1109%2Flra.2019.2961227.

[6] Aamir Khan, Carmelo Mineo, Gordon Dobie, Charles Macleod, and Gareth Pierce. Vision guided robotic inspection for parts in manufacturing and remanufacturing industry. *Journal of Remanufacturing*, 11(1):49–70, Apr 2021. ISSN 2210-4690. doi: 10.1007/s13243-020-00091-x. URL https://doi.org/10.1007/s13243-020-00091-x.

[7] Carmelo Mineo, Donatella Cerniglia, Vito Ricotta, and Bernhard Reitinger. Autonomous 3d geometry reconstruction through robot-manipulated optical sensors. *The International Journal of Advanced Manufacturing Technology*, 116(5):1895–1911, Sep 2021. ISSN 1433-3015. doi: 10.1007/s00170-021-07432-5. URL https://doi.org/10.1007/s00170-021-07432-5.

[8] Alastair Poole, Mark Sutcliffe, Gareth Pierce, and Anthony Gachagan. Autonomous, digital-twin free path planning and deployment for robotic ndt : introducing lpas : Locate, plan, approach, scan using low cost vision sensors. *Applied Sciences*, 12(10), May 2022. ISSN 2076-3417. doi: 10.3390/app12105288. URL https://doi.org/10.3390/app12105288.

[9] Ilankaikone Senthooran, Manzur Murshed, Jan Carlo Barca, Joarder Kamruzzaman, and Hoam Chung. An efficient ransac hypothesis evaluation using sufficient statistics for rgb-d pose estimation. *Autonomous Robots*, 43 (5):1257–1270, Jun 2019. ISSN 1573-7527. doi: 10.1007/s10514-018-9801-y. URL `https://doi.org/10.1007/s10514-018-9801-y`.

[10] Eduardo E. Hitomi, Jorge V. L. Silva, and Guilherme C. S. Ruppert. *3D Scanning Using RGBD Imaging Devices: A Survey*, pages 379–395. Springer International Publishing, Cham, 2015. ISBN 978-3-319-13407-9. doi: 10.1007/978-3-319-13407-9_22. URL `https://doi.org/10.1007/978-3-319-13407-9_22`.

[11] K. S. Arun, T. S. Huang, and S. D. Blostein. Least-squares fitting of two 3-d point sets. *IEEE Transactions on Pattern Analysis and Machine Intelligence*, PAMI-9(5):698–700, 1987. doi: 10.1109/TPAMI.1987.4767965.

[12] Pierre Merriaux, Yohan Dupuis, Rémi Boutteau, Pascal Vasseur, and Xavier Savatier. A study of vicon system positioning performance. *Sensors*, 17(7), 2017. ISSN 1424-8220. doi: 10.3390/s17071591. URL `https://www.mdpi.com/1424-8220/17/7/1591`.

[13] David N. Mastronarde. *Fiducial Marker and Hybrid Alignment Methods for Single- and Double-axis Tomography*, pages 163–185. Springer New York, New York, NY, 2006. ISBN 978-0-387-69008-7.

doi: 10.1007/978-0-387-69008-7_6. URL https://doi.org/10.1007/978-0-387-69008-7_6.

[14] Fuxin Fan, Björn Kreher, Holger Keil, Andreas Maier, and Yixing Huang. Fiducial marker recovery and detection from severely truncated data in navigation-assisted spine surgery. *Medical Physics*, 49(5):2914–2930, 2022. doi: https://doi.org/10.1002/mp.15617. URL https://aapm.onlinelibrary.wiley.com/doi/abs/10.1002/mp.15617.

[15] C. Syben, B. Bier, M. Berger, A. Aichert, R. Fahrig, G. Gold, M. Levenston, and A. Maier. Joint calibration and motion estimation in weight-bearing cone-beam ct of the knee joint using fiducial markers. In *2017 IEEE 14th International Symposium on Biomedical Imaging (ISBI 2017)*, pages 494–497, 2017. doi: 10.1109/ISBI.2017.7950568.

[16] Martin Schickert, Christian Koch, and Frank Bonitz. Augmented-reality-visualisierung von abbildungsergebnissen an betonbauteilen – implementierung und ausblick. In *4. Fachseminar des FA MTHz, Mikrowellen- und Terahertz-Prüftechnik in der Praxis*, 2019.

[17] Bhusapalli Dhamodar Reddy and A. A. Nippun Kumaar. *Indoor Mobile Robot Path Planning Using QR Code*, pages 681–693. Springer Singapore, Singapore, 2020. ISBN 978-981-15-2612-1. doi: 10.1007/978-981-15-2612-1_65. URL https://doi.org/10.1007/978-981-15-2612-1_65.

[18] Grigori Goronzy, Mathias Pelka, and Horst Hellbrück. Qrpos: Indoor positioning system for self-balancing robots based on qr codes. In *2016 International Conference on Indoor Positioning and Indoor Navigation (IPIN)*, pages 1–8, 2016. doi: 10.1109/IPIN.2016.7743616.

[19] Roberto Quilez, Adriaan S. Zeeman, Nathalie Mitton, and Julien Vandaele. Docking autonomous robots in passive docks with infrared sensors and qr codes. *EAI Endorsed Trans. Self Adapt. Syst.*, 1:e2, 2015.

[20] Shidong Chen, Jianjun Yi, Hongkai Ding, Zhuoran Wang, Jinyang Min, Hailei Wu, Shuqing Cao, and Jinzhen Mu. 3d object reconstruction with kinect based on qr code calibration. In *2020 IEEE International Conference on Artificial Intelligence and Computer Applications (ICAICA)*, pages 459–463, 2020. doi: 10.1109/ICAICA50127.2020.9181884.

[21] Ogawa, Hiroaki, Shishiki, Keito, Manawadu, Udaka A., and Naruse, Keitaro. Large area inspection using 3d point cloud data in a disaster response robot. *SHS Web Conf.*, 102:04010, 2021. doi: 10.1051/shsconf/202110204010. URL `https://doi.org/10.1051/shsconf/202110204010`.

[22] Yizheng Zhang, Wangshu Zhu, and Andre Rosendo. Qr code-based self-calibration for a fault-tolerant industrial robot arm. *IEEE Access*, 7:73349–73356, 2019. doi: 10.1109/ACCESS.2019.2920429.

[23] D.G. Lowe. Object recognition from local scale-invariant features. In *Pro-*

ceedings of the Seventh IEEE International Conference on Computer Vision, volume 2, pages 1150–1157 vol.2, 1999. doi: 10.1109/ICCV.1999.790410.

[24] Ebrahim Karami, Siva Prasad, and Mohamed Shehata. Image matching using sift, surf, brief and orb: Performance comparison for distorted images, 2017. URL `https://arxiv.org/abs/1710.02726`.

[25] Michaela Servi, Elisa Mussi, Andrea Profili, Rocco Furferi, Yary Volpe, Lapo Governi, and Francesco Buonamici. Metrological characterization and comparison of d415, d455, l515 realsense devices in the close range. *Sensors*, 21(22), 2021. ISSN 1424-8220. doi: 10.3390/s21227770. URL `https://www.mdpi.com/1424-8220/21/22/7770`.

[26] Huy Nguyen and Quang-Cuong Pham. On the covariance of x in ax = xb, 2017. URL `https://arxiv.org/abs/1706.03498`.

[27] Rasmus S. Andersen, Jens S. Damgaard, Ole Madsen, and Thomas B. Moeslund. Fast calibration of industrial mobile robots to workstations using qr codes. In *IEEE ISR 2013*, pages 1–6, 2013. doi: 10.1109/ISR.2013.6695636.

[28] Jaesik Park, Qian-Yi Zhou, and Vladlen Koltun. Colored point cloud registration revisited. In *2017 IEEE International Conference on Computer Vision (ICCV)*, pages 143–152, 2017. doi: 10.1109/ICCV.2017.25.

[29] Martin A. Fischler and Robert C. Bolles. Random sample consensus: A

paradigm for model fitting with applications to image analysis and automated cartography. *Commun. ACM*, 24(6):381–395, jun 1981. ISSN 0001-0782. doi: 10.1145/358669.358692. URL `https://doi.org/10.1145/358669.358692`.

[30] F. Bernardini, J. Mittleman, H. Rushmeier, C. Silva, and G. Taubin. The ball-pivoting algorithm for surface reconstruction. *IEEE Transactions on Visualization and Computer Graphics*, 5(4):349–359, 1999. doi: 10.1109/2945.817351.

[31] Zhou Wang, A.C. Bovik, H.R. Sheikh, and E.P. Simoncelli. Image quality assessment: from error visibility to structural similarity. *IEEE Transactions on Image Processing*, 13(4):600–612, 2004. doi: 10.1109/TIP.2003.819861.

[32] Brian Hall. *Lie Algebras*, pages 49–76. Springer International Publishing, Cham, 2015. ISBN 978-3-319-13467-3. doi: 10.1007/978-3-319-13467-3_3. URL `https://doi.org/10.1007/978-3-319-13467-3_3`.

[33] Daniel Foreman-Mackey. corner.py: Scatterplot matrices in python. *The Journal of Open Source Software*, 1(2):24, jun 2016. doi: 10.21105/joss.00024. URL `https://doi.org/10.21105/joss.00024`.

[34] Jun Xie, Yu-Feng Hsu, Rogerio Schmidt Feris, and Ming-Ting Sun. Fine registration of 3d point clouds fusing structural and photometric information using an rgb-d camera. *Journal of Visual Communication and*

Image Representation, 32:194–204, 2015. ISSN 1047-3203. doi: https://doi.org/10.1016/j.jvcir.2015.08.007. URL `https://www.sciencedirect.com/science/article/pii/S1047320315001509`.

Chapter 6

Force and Sound Data Fusion for Enhanced Tap Testing Scanning of Composites

The industrial use case of this PhD thesis is centred on application to scanning RNLI Severn class lifeboat hulls. While the thesis has investigated workspace perspectives to produce algorithms that allow full boat hull scanning and reconstruction with a mobile robotic arm, the NDT sensing approach does not use UT sensors the thesis originally envisaged utilising. While previous sections investigate the relation of work-space representations to full surface coverage without apriori knowledge, this appendix investigates the relationship between force and sound data obtained during tap testing to enhance images for Tap Testing of

unknown or semi-known structures.

Several challenges are faced when inspecting the integrity of Glass Fibre Reinforced Plastics (GFRP) boat hulls of varying structure and age within a dry dock environment. Traditional techniques such as Ultrasound are often unable to penetrate the composite and its paint coating with an acceptable signal to noise ratio. Radiographic scans, though accurate, pose a health risk to others within the dry-dock, resulting in large down-times for other work. The author has turned to traditional Tap-Testing (TT) due to its success in other similar materials. Traditionally, TT requires a highly trained operator equipped with foreknowledge of the structure to discriminate changes in thickness from defects. Use of legacy hulls and hulls without detailed digital twins complicate the process, since variations in the hull's structure may be confused with defects, complex sub-structures have traditionally required other NDT techniques due to the relative inaccuracy of the TT method. Exterior damage can easily be assessed with visual inspection of the outer hull, and so only internal or sub-surface issues need to be considered.

Non-instrumented deployment of TT required a human operator to impact a surface with either a coin or hammer and resultant changes in the sound used to locate potential defects. The sonic response as a result of surface vibrations is also found to be recorded through the force-time history of the impact with near-surface defects. This was later developed into an instrumented tapping method, whereby a mass would strike a surface, and either a Piezo-electric piece in rigid

contact with the mass would monitor the impact force history, or a microphone would be used to listen to the resultant surface vibrations in order to detect defects, a graphical set-up of which is shown in Fig: 6.1. An example of the measured impact force and sound responses are shown in Fig: 6.2.

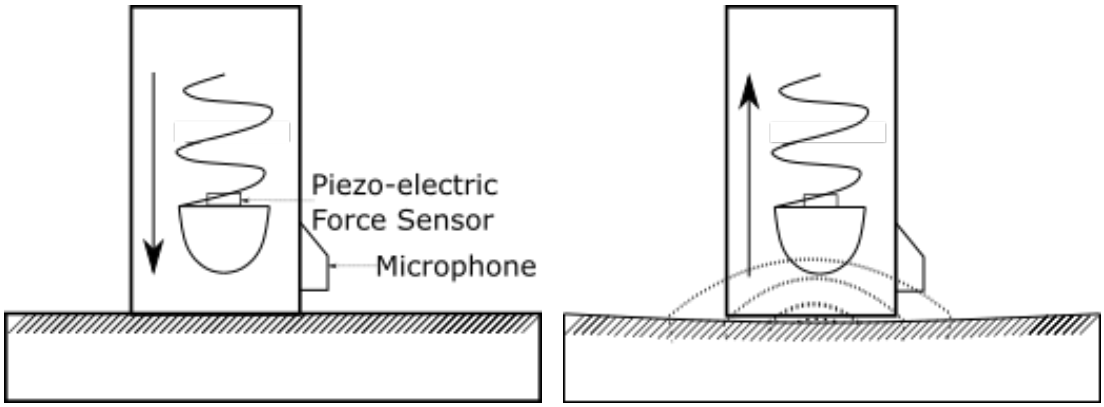

(a) (b)

Figure 6.1: Instrumented Tap-Testing equipment set-up. **(a)** depicts the Piezo-electric force sensor and microphone mounted to the instrumented tap testing housing, where the mass accelerates towards and strikes the surface. **(b)**, the resultant flexure of surface results in a pressure upon the mass while it is in contact with the part that is measured by the Piezo-electric sensor, and sound emitted by surface resonance that is collected by the microphone.

Building on previous impact modelling [1], the impact is modelled by [2] as a parallel two-spring system, of contact and defect stiffness. The natural harmonic frequency's dependence on defect stiffness value k and tapping-implement mass m correlates the time of impact τ to probable presence of a defect related to the stiffness;

$$\tau = \pi\sqrt{\frac{m}{k}}, \tag{6.1}$$

where thinner/defective surface regions have a reduced stiffness coefficient. Force-

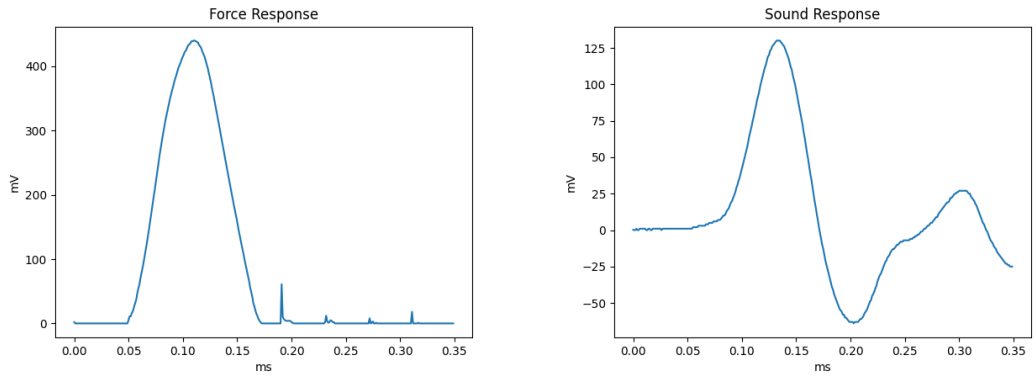

(a) (b)

Figure 6.2: Force and sound response examples taken with an EVOTIS tap testing device. Both Piezo force and microphone sound sensors collect in units of mV. (a) illustrates the force felt by the instrumented tap testing device during contact of the tapping element with the part, a semi-sinusoidal wave modelled as a dual-spring model introduced in Eq: 6.1. The force induces surface modes of oscillation that result in audible noise heard by the tap testing device's microphone, shown in (b).

time used as a proxy for audible acoustic frequency is applied to highly critical composite testing procedures due to its reliability and repeatability for certain materials [3, 4, 5], though only accurate to limited depths. The information within the force-time history has inspired Artificial-Intelligence (AI) approaches to defect classification as well as identification in aeronautical components [6]. Direct measurement of local stiffness effectively indicates near-surface defects such as voids but provides less accurate results for measurements within the material's bulk.

Audible measurements can provide greater information of defects at depth within a part. Utilising audible measurements, [7] applied previous work in membrane resonance NDT [8] to determine the detectability of defects using the in-

duced sound with respect to defect width and depth. This detectability index assumes the local membrane resonance directly around the defect is significant within the audible signal if the initial impact contains the defective regions' resonant frequencies, underpinning the theoretical aspects of: [8]. This work also produced a frequency-independent cost function for assessing structural integrity. The signal energy of the resultant sound is used to differentiate local structural depths. The energy E of the signal $s(t)$ heard by the microphone within a discrete time domain $t \in [0, T]$ is proportional to [9];

$$E = \sum_{t=0}^{T} |s(t)|^2. \tag{6.2}$$

Thicker surfaces are less deformed than thinner parts by equal forces, resulting in a duller, equivalently a less energetic tonal response enabling the detection of surface depth. Importantly, this analysis demonstrates that a low-mass striker induces a wide band of frequencies in the material, allowing imaging in structures of varying thicknesses. The results are however noisy, as can be seen in Section: 6.3, an issue when the structure is not well-known, potentially leading to an operator highlighting false-positives for defects within the hull.

Modelling for steel structures has demonstrated that defects' local resonance does dominate the signal [10]. Despite this, the key study of TT sonic/force analysis methods applied to thick composites by [11] shows that the vibrational

modes of the surface locally and globally need to be considered in order to build an accurate defect map for thick composites. The additional outcome of this study is the determination that force and sound combined can provide more information than either on their own, though without a suitable fusion method.

Several other approaches have sought to fuse or use both force and sound data to provide more information than either individually. The investigation of [12] found that the free-vibration sound (after the hammer's contact period) provides substantial information of bulk defects. Despite this, non-uniform response and propagation of surface vibration frequencies produces irregular results over the surface, highlighting machine learning methods as a necessary method to enhance signal interpretation. The Neural Network approach investigated by [13] found that the fusion of force/sound could provide a 100% true negative rate for non-defective regions, and a high true-positive rate for defects in fibreglass and Balsa wood samples. While this this is a demonstrably successful approach, there are two draw-backs of this approach for this use case. Firstly, the necessity for training data precludes use in this case on-site since a process would preferably be used on multiple boat-hull types with varying thicknesses due to differing specifications and manufacturing processes. Secondly and more significantly, machine learning processes require the defective and non-defective regions have unique depth signatures, which is not the case for the disbonding cases considered. This is illustrated in Fig: 6.3 where the defect's sonic signature is nearly identical to

a non-defective region, due to the part's varying thickness.

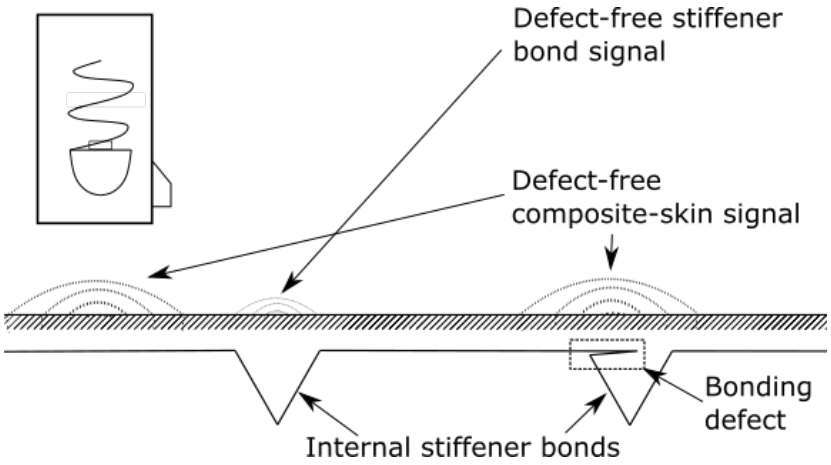

Figure 6.3: Cross-sectional schematic of depth measurement. An cross sectional image of a realistic hull sample is shown later in Fig: 6.5. While machine-learning methods applied to TT use prior information in order to detect unique outlier sonic or force response signatures to identify defects, for this case the varying depth can result in defect-free classification of defective positions. This issue is highlighted later with TT data in Section: 6.3

Meanwhile, a subsection of papers investigating Force Reconstruction (FR) also study the correlation of force and sound responses. Modelling or measuring the sound produced by an elastic wave within the surface allows the deduction of impact force and location from microphone data collected from multiple positions [14]. While in idealised scenarios such as circular or square plates, resonant modes are derived throughout the literature, for surfaces with either complex shapes or material characteristics, physical models are considered unreliable [15] while prior information approaches provide reliable results [16]. Even then, modal spread due to non-uniform surface features makes prior information incorporation difficult. However, errors in impact estimation caused by irregular mode propagation im-

plies that if the force and relative position of the impact to the microphone is constant, variations in the surface stiffness and depth can be mapped by cross-correlation variations within the frequency domain.

Applying this concept from a parallel field, this chapter seeks to introduce a novel approach to TT data processing resulting in smoother and more reliable maps for structural depth imaging than traditional techniques using only the audible response. The second output of this chapter is a novel metric function that quantifies and estimates surface non-uniformities as a result of cross correlation of data in the frequency domain. The process is described in Section: 6.1, then experimentally validated in Section: 6.3. Applicable to naive mapping of surfaces, this method is shown to enable an operator to accurately detect changes, anomalies and discontinuities in regular features of thick composite structures, which may be defects or irregular features such as sensor pockets, limber holes or internal bracketry. The combination of these maps results in a thickness variation map that more accurately represents the structure, and a defect recognition process that selects regions of concern.

6.1 Enhanced Resolution Imaging

Several papers have highlighted the effect of non-local modes on the frequency response of the audible sound, and also the need to separate the two sources of audible response in order to obtain high quality imaging of components. A

large portion of TT research has focused on the force-time response alone for this reason, as it is reflective of local modes of excitation only. While sound baffling could be used to shield the microphone from globally resonant modes, this would present significant challenges if robotically deployed as is the goal application of this technology. Rigid baffles would not conform well to parts of varying curvature, preventing isolation of the microphone from global resonant sound sources. Flexible baffles would present an issue for a robot in approaching the part and when covering the surface, causing snagging issues where a human operator would simply re-arrange the probe.

Separately, FR approaches such as [17] relate the sound heard at time t and position $\overrightarrow{x}$ due to an impact force $F(t)$ at the global origin by;

$$s(\overrightarrow{x}, t) = \int_0^t G(t-\tau, \overrightarrow{x}) F(\tau) d\tau. \tag{6.3}$$

Where G is the Greens function, propagating surface acceleration within the spatio-temporal domain, since this is directly related to the audible emissions. Analysing the sonic/force responses in the discrete frequency domain, the force/sound frequency kernel H takes a matrix form;

$$H_{i,j} = \frac{s(f_i)\bar{F}(f_j)}{|\bar{F}|^2}, \tag{6.4}$$

where $H_{i,j}$ is the convolution matrices i^{th} row and j^{th} column entry, and $\bar{F}$ is the

complex conjugation of the force-frequency spectrum. Taking a similar approach to [18], the total sound heard by the microphone is equated to a Rayleigh integral over the surface, introducing the new Green's function $\hat{G}$ that relates the initial impact force with the sound emitted from a surface position at a later time. Since, using the Rayleigh integral approach, the sound emitted from an infinitesimal position is proportional to surface acceleration that is in turn related to force propagation. This is an appropriate approach to take. Considering a wave of depth and frequency dependent on position, where $\overrightarrow{x} \in R$, the total measured sonic response $\hat{s}$ form the microphone's position $\overrightarrow{q}$ in the time domain is;

$$\hat{s}(t) = \int_R \int_0^t \hat{G}\left(t - \tau - \frac{|\overrightarrow{x} - \overrightarrow{q}|}{c}, \overrightarrow{x}\right) \frac{F(\tau)}{|\overrightarrow{x} - \overrightarrow{q}|} d^m x d\tau. \tag{6.5}$$

Applying the convolution kernel to the sound heard by a microphone;

$$\hat{s}(f) = \hat{H}F(f), \tag{6.6}$$

and transforming the components of Eq: 6.5 individually;

$$\hat{H} = \int_R \hat{H}_x \frac{d^m x}{|\overrightarrow{x} - \overrightarrow{q}|}. \tag{6.7}$$

Eq: 6.2 is modified to only reflect the local modal energies. The matrix $\hat{H}$ is decomposed into $\hat{H} = \hat{H}^{\parallel} + \hat{H}^{\perp}$, where $\hat{H}^{\parallel}$ and $\hat{H}^{\perp}$ are diagonal and off-diagonal

components respectively. The literature of impact response and TT stress the interaction and conversion of locally instrumented forces and their conversion to global and local modalities. Depth of the part is also a key determinant of the surface resonant frequency. Under an idealised system, the matrix $\hat{H}^{\parallel}$ represents the force directly exciting the local fundamental frequencies, that are also shown in the force history measurements. The matrix $\hat{H}^{\perp}$ represents modal conversions to global excitations that differ from local modes due to non-isotropic material properties and the varying depth of the part, converting the initial impact energy to sound energy within a broader set of audible frequency bands. Modelling the interaction of sound and force this way and taking the results of previous studies it is inferred that the local and global modes are excited by the initial impact, with the local modes representing an expanding elastic surface wave while surface stiffness diffuses the vibration energy towards the lower frequency global modes, seen in Fig: 6.4. As a result of this model, it is expected that that there will be a monotonic fractional increase in the dominance of off-diagonal elements as the impact energy is transferred to the global modes, given by Eq: 6.9.

Taking this perspective, the sound energy observed due to excitations of only the local modalities that reflect the local depth values E_{ϵ} is then reinterpreted from Eq: 6.2;

$$E_{\epsilon} = \sum_{f} |\hat{H}^{\parallel} F(f)|^2, \tag{6.8}$$

that is the first novel evaluation function introduced and named the matrix trace

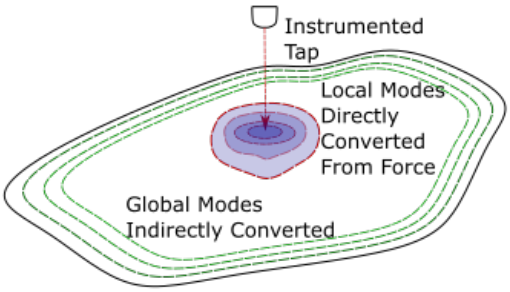

Figure 6.4: An instrumented tap causes material vibrations involving both local and non-local resonant modes. Interactions of the observed force and sound frequencies describes the conversion rate of energy from local to global resonances.

method. Where parts are of uniform or known thickness, methods such as simple frequency spectrum filtering would be an alternative to Eq: 6.2, since prior knowledge of local resonant frequencies could be ascertained. However in cases where the surface depth is unknown or a calibration model unavailable, prior knowledge cannot be incorporated. In consideration of the use case and future deployments with a robotic system, inclusion of prior knowledge and sound baffles is undesirable.

Accurate local depth measurement allows an operator to identify the hidden structure of thick composites. While other leading studies of TT utilise depth data to identify defects through machine learning methods, this is not applicable when the structure is unknown and of varying depth since a defect can be of the same depth and contain the same force and sonic response as a non-defective region, as exampled by the schematic in Fig: 6.3. In this case, the rate of change of depth information provides greater clarity of the presence of a defect.

Variations in structure can be measured as a function of the fraction of indirect force to sound conversion. A proportion of the initial resonant impact spectra produced by the tap and observed by the force undergoes modal conversions to non-local modes of vibration. Modal conversion's impact on the acoustic energy distribution through the observed frequency spectra reflects the similarity of the part's local and semi-local depths. Regions with consistent depth in the semi-locality will undergo little if any modal conversion, whereas regions with large depth variations will convert a larger portion of the acoustic energy to modes different to the local spectra. The second novel function is introduced;

$$q(\hat{H}) = \frac{|\hat{H}|_2^2 - |(\hat{H}^{\parallel})|_2^2}{|\hat{H}|_2^2} = \frac{|(\hat{H}^{\perp})|_2^2}{|\hat{H}|_2^2}, \tag{6.9}$$

where $|*|_2$ is the Frobenius norm. This metric q provides a metric for semi-local depth variations that highlights regions of rapid flux in depth. This is experimentally validated in Section: 6.3.2.

To provide accurate mapping of surface depth, this chapter has introduced the novel function: 6.8 that considers only local contributions to the sonic response of an instrumented tap, formally seen as exclusive benefit of the force response metric, but also containing the depth data available to the sonic response providing local structural information in greater clarity than the commonly used function Eq: 6.2. While this function is inspired by research within the domain of FR, it

introduces the novel concept of frequency domain separation using impact force information unavailable to FR analyses. This chapter has further introduced the novel metric q in Eq: 6.9, detecting the rate of change of surface depth. Whereas traditional TT methods rely on depth data alone for defect detection, in cases of varying depth or unknown structure the rate of change of depth provides a more informative mapping of defective regions as is shown later in Section: 6.4.

6.2 Lifeboat Hull Component

Critical defects in this analysis are delaminations of the outer GFRP skin from the internal stiffening members, in particular at the areas where these two components meet as highlighted in green in Fig: 6.5 to the hull, potentially leading to loss of rigidity and ultimately structural failure.

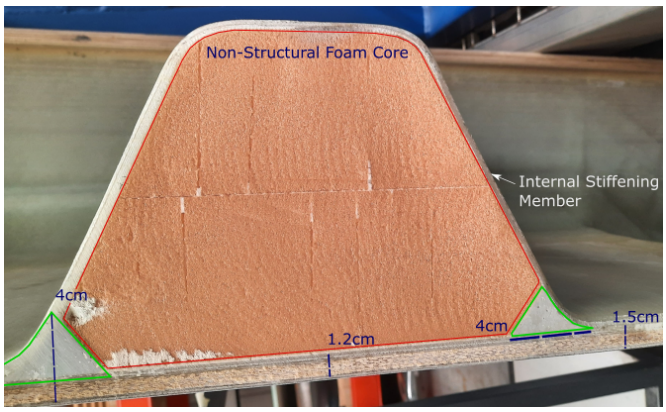

Figure 6.5: Cross sectional side-view of the part. Primary areas of interest in which disbonding may occur are highlighted in green, the secondary areas are in the outer (lower) composite material. The non-structural layer can be clearly seen.

Additional intra-composite delaminations in the outer layer are considered also, as wear and tear can lead to internal damage. Two artificial defects were created as back-drilled holes of $100mm \times 100mm$ representing these two defect types. These are shown from the back of the part in Fig: 6.6.

Figure 6.6: View of the part from behind showing the artificial defects embedded within the surface. Their dimensions are $100mm \times 100mm$ since defects below this threshold are not considered critical. Defect one represents a delamination of the stiffener member, cutting through the stiffener and intersecting the non-structural core with a depth of $2mm$ from the outside of the hull. A portion of the defect is present under the structural foam, represented by the dotted line. Defect two represents internal tear and wear to the hull's skin with a depth of $5mm$ from the outside of the hull. The image is reflected and rotated anti-clockwise by 90° relative to the images produced as a result of scanning later.

A frontal map showing both defects overlayed on the grid used for guiding scans is shown in Fig: 6.7.

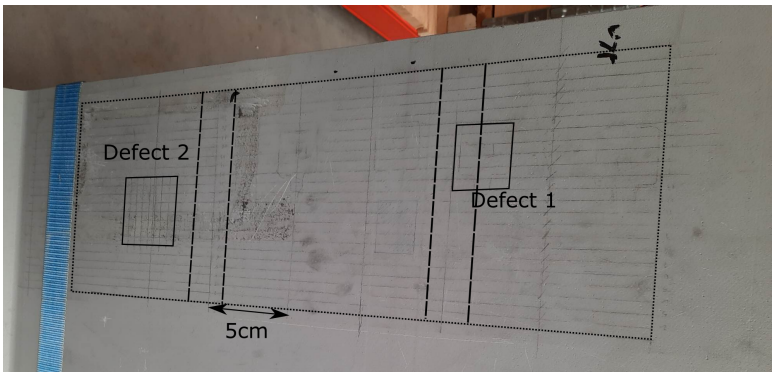

Figure 6.7: Frontal view of the part, the scanning region is highlighted. Two scale gradations were used of; $50mm \times 20mm$ for larger maps of the defect, and $10mm \times 10mm$ of each defect individually and the local area around them. The cross-cutting dotted guides indicate the approximate positions and boundaries of the internal stiffener bonds holding the non-structural foam core in-between as seen in Fig: 6.5 and Fig: 6.6.

The depth differentials between each defects and the surrounding hull vary significantly, with defect one's cut through the stiffener creating a depth differential of $35mm$, and for defect two, a depth differential of only $10mm$. Using sonic depth imaging metrics, defect one should be significantly easier to identify than defect two due to the greater difference in defect to surface depth values. The break in the stiffener member will still however have a similar signature to the surrounding composite material, reducing the efficacy of machine learning methods using raw depth information.

A cross sectional schematic of the defects with internal features are shown in Fig: 6.8.

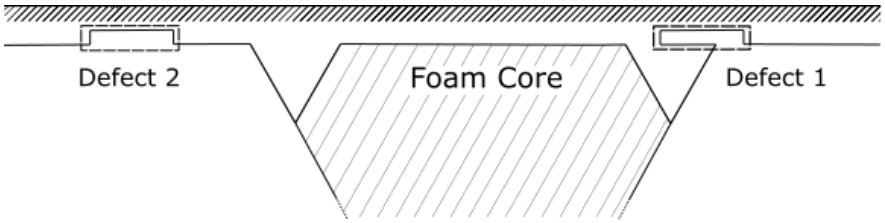

Figure 6.8: Cross section of the surface shown from the front in Fig: 6.7, outlining the structural features seen in Fig: 6.6.

6.3 Experimental Results

Several scans of a Class Severn hull boat were performed, collecting force and sound data with the hand-held EVOTIS device seen in Fig: 6.9, using stencilled guides to ensure repeatability and accurate relative positioning.

Figure 6.9: EVOTIS Instrumented Tap Testing device features a square faced contact aperture to ensure the strike is normal to the surface, consistent force application, and collects both force and sound time histories.

A C-scan representation is reconstructed by recording the position of each specific A-scan taken within the grid. The tool was held flat against the surface using the square aperture to prevent skewing of the striking hammer from the surface. Though tool-offset error is minimised so that the striking force is consistent, human positioning error is present as the operator misaligns the tool with

the provided stencil. The data was then visualised in Python, with a logarithmic energy scale as it better highlights changes in depth. All results in this section are plotted with x and y axes in units of cm.

The experimental set-up involved the EVOTIS TT device manually applied over a grid-stencilled part, and the data collected on an external computer, shown in Fig: 6.10.

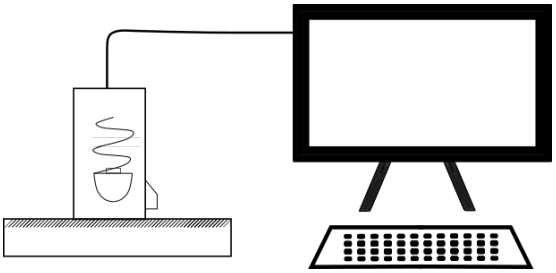

Figure 6.10: Experimental set-up of the TT device connected to an external computer. Data from the device was loaded into the EVOTIS software, then saved in csv format.

The logarithmic values of sonic response functions described in Eq: 6.2 and Eq: 6.8 were seen to provide greater imaging clarity. For these reasons, the units of sound are used for imaging are $\log(mV)$. While prior information analyses would indicate the local and global modes, the purpose of this chapter is to present application to an unknown part. The EVOTIS device is calibrated to ensure that it can identify the back-wall of the triangular wedge and the thinnest portion of GFRP skin only, providing a realistic scenario in which on-site access to the part is limited and defect depth unknown.

6.3.1 Force and Sound Responses

Though the defect-stiffness approach is validated for similar components to those considered here by [19], contact time results are experimentally found to be insufficient in this use-case, an example of which is shown in Fig: 6.11.

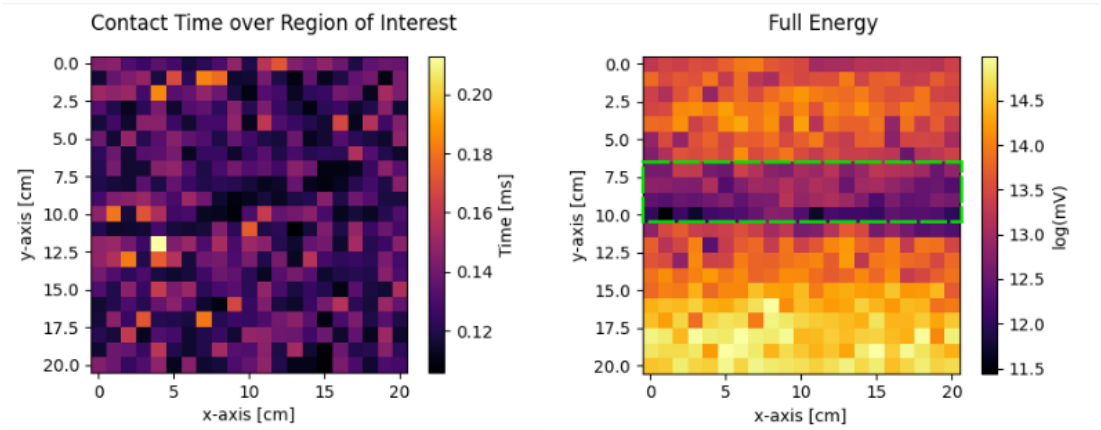

Figure 6.11: Contact time vs Full Energy imaging of a non-defective region. This scan is taken with the triangular stiffener bond section as seen in Fig: 6.5 and whose position is highlighted in Fig: 6.7 aligned to the x-axis, the variation in depth of the bond section shown in the variations of the sonic response, bounded by the green lines $40mm$ apart. Contact time undergoes little fluctuation, the results are constituted mainly of noise. The comparison imaging method shows depth fluctuations by using Eq: 6.2, highlighting the need for sonic rather than force based imaging methods.

The sonic response method is the primary candidate for defect detection. The prior full energy spectrum is compared with both matrix trace and metric function q in their ability to produce consistent, noise-free depth imaging of parts and in the identification of defects.

6.3.2 Modal Conversion

Conversion of energy from local to global modes can be seen in Fig: 6.12. This data is collected from the full sample region shown in Fig: 6.7, and varying time sampling windows are taken in order to confirm modal spread from the local to global. Since the metric value q is independent of total sonic energy, it measures the distribution of sonic energy in the binary bins of local and global modes. The observed half-sinusoidal contact period is $T = 0.14ms$, and time windows t are taken in proportion to this time period. The data shows that global modes absorb the majority of energy within one half-period of the contact motion. When the sampling window is increased to the full sinusoidal period of $0.28ms$ labeled as $t/T = 1$, the energy absorbed by global modes increases from 70% to 90% of the total sonic energy emitted by the surface, confirming the presence of modal spread while also confirming that there is significant initial resonance between the instrumented impact and global modes.

The effect on imaging for matrix trace and full energy methods is also investigated. The same region is imaged with both methods, presented in Fig: 6.13.

The traditional energy method shows the defects most clearly within one half-period of the sinusoidal motion, reflecting the local modalities most clearly. Meanwhile, the matrix trace method produces images better reflecting the underlying smooth depth variations with greater time sampling windows. However,

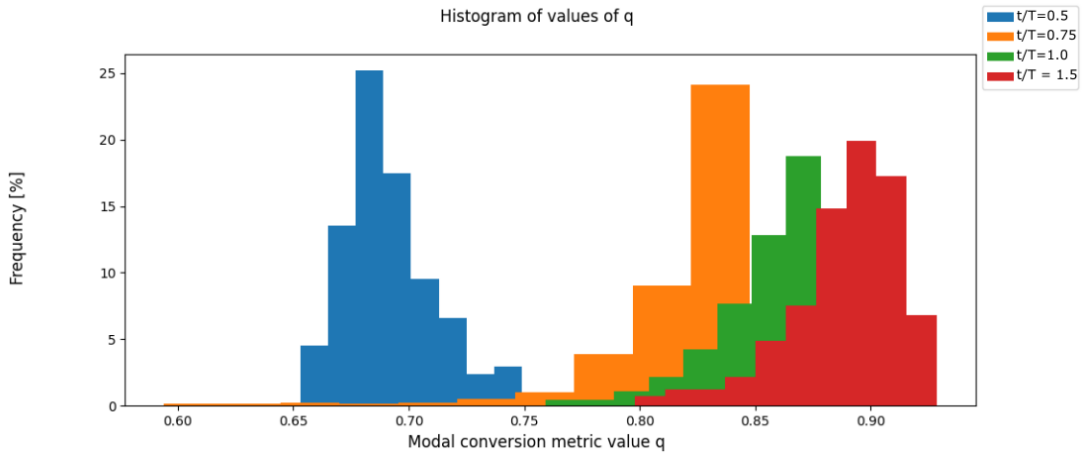

Figure 6.12: The metric value q describes the proportion of observed energy absorbed by global resonance modes. While after one half-period of the sinusoidal contact motion 70% of observed audible energy is absorbed by global modes, this increased to 85% within a full contact-period.

imaging with the full energy spread provides clearer indications of the defects. If the underlying structure is known, the full energy method would provide a clearer map of defects. However several false positives may be identified with variations in signal strength, mos clearly seen in-between triangular wedges where in lieu of a detailed part schematic, it is deduced that the composite skin is of marginally reduced thickness. Cost function q is used to identify depth variations with greater clarity using the energetic spread of modal energy, the mapped results of which can be seen in Fig: 6.14.

In all sampling regimes the defects can be clearly identified as peaks of the modal conversion metric. As observed in Fig: 6.12, modal spread increases with time, initially focused around the defective regions and later highlights regions of depth variation around the triangular wedges. These results imply that for

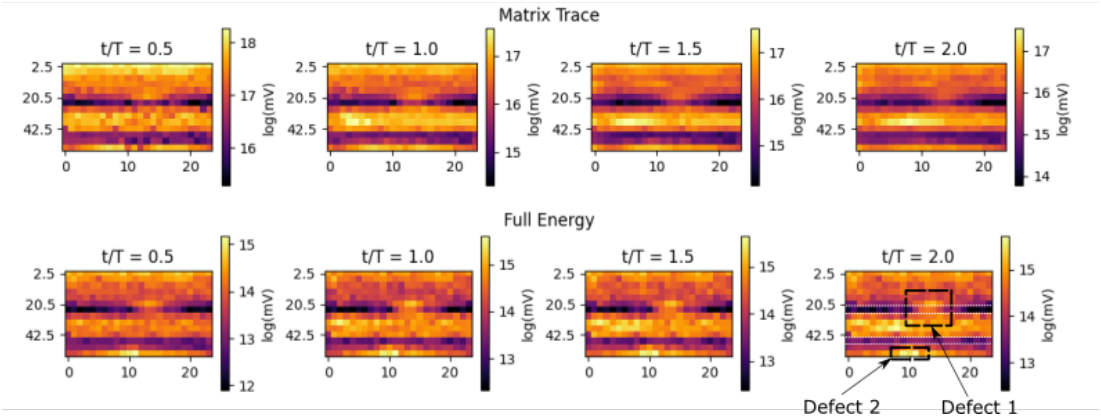

Figure 6.13: Comparison of the matrix trace and full energy methods of defect imaging within different time windows. The full energy method provides less consistent depth measurement results than the matrix trace method at higher sampling times. Axis values are in *cm*.

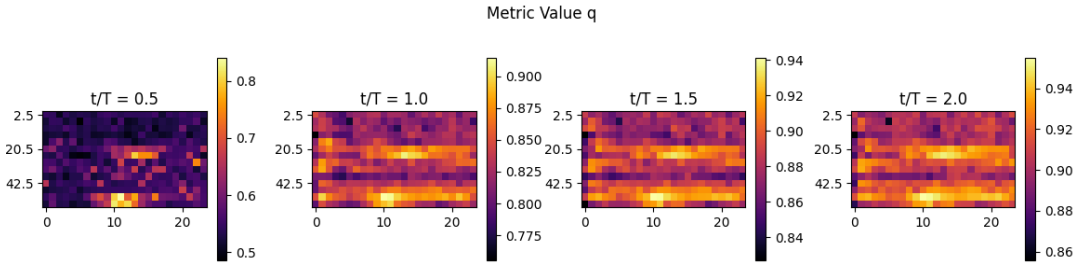

Figure 6.14: Metric function q highlights the divergence of surface excitations from local to global modes with an increased time window. Axis values are in *cm*, q is a dimensionless quantity.

defective regions where there is a sudden change in depth, the global modes resonate with the instrumented tap far more than the local modes, and that the energy induced in local modes of excitation is dispersed into global modes over the surface, particularly in regions where there is depth variation such as at the wedge boundary points.

The image quality for each metric differs in optimal sampling window. The traditional full energy metric is optimised for a sampling time over just the contact

period, highlighting the defective regions with fewer peaks elsewhere in the domain. Imaging in this domain results in granularity and identical signal response between the thinner non-defective region surrounding the bonding wedges, and the thinner defective region cutting through the wedge agreeing with the signal response schematic given in Fig: 6.8 that invalidates use of machine learning or spectral filtering techniques used elsewhere in the literature. The matrix trace method provides an optimal map of the structural features with a greater time sampling regime, allowing the operator to localise the scan with reference to features either with prior knowledge of the part or in accumulating an image of the part iteratively. In any sampling regime its utility in identification of defects is at best equal to the traditional full energy method, however, highlighting its utility in accurately identifying structural features only. However for the metric q, defects are best recognised in the half-period time sampling regime, with secondary features such as local wedge depth variation becoming pronounced with an increased sampling window.

6.4 Defect Identification

Utilising the results of the previous section, the defects and structural features are imaged in greater clarity with the use of optimal sampling conditions, and are compared with the full-energy method. Both defective regions are re-scanned with a spatial resolution of $10mm \times 10mm$. Defect one is imaged in Fig: 6.15

and defect two in Fig: 6.16. As seen in Fig: 6.15, the defective area cannot be clearly seen with either full energy or matrix trace imaging methods. However the structural features are seen with greater clarity using the matrix trace method. The metric q highlights the defect clearly in the half-period regime and the wedges edges, highlighted with vertical white lines, are present in the full period regime.

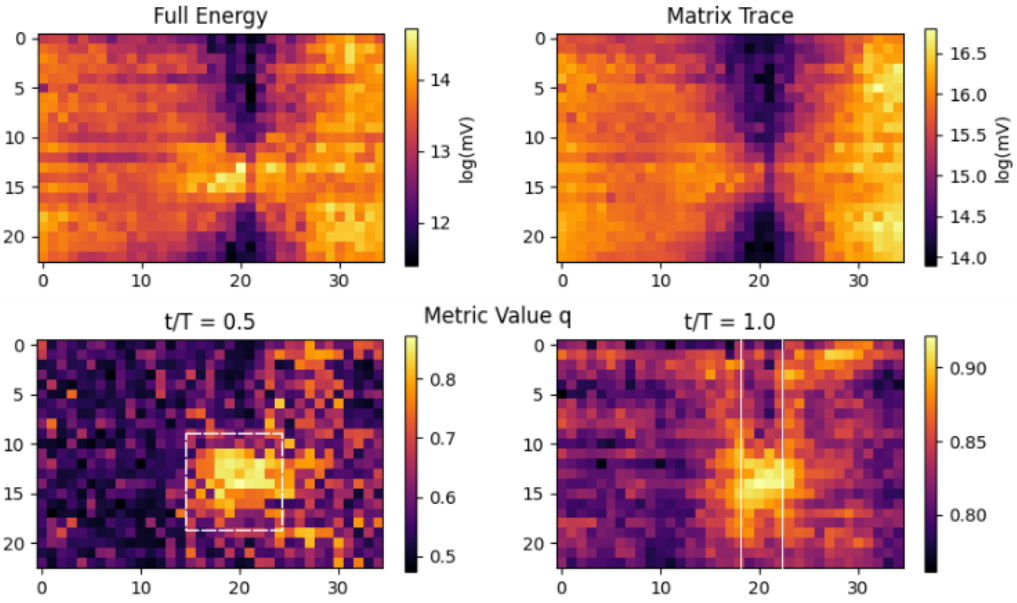

Figure 6.15: Imaging of defect one. Metric value q taken across two sampling regimes shows the defective region highlighted in the first sampling regime, the $100mm \times 100mm$ bounds of which are highlighted. The boundaries of the $40mm$ wide cross-cutting wedge bond are overlaid in white in the full period sampling regime, and are seen as positions of depth flux with the q metric. Axis values are in cm.

When a smoothing filter is applied over the half-period samples of the metric q, the defects become significantly clearer. The smoothing window reduces noise within the metric, highlighting the spatially significant distribution of higher values of q that correlate with the presence of defects. In this use-case defects

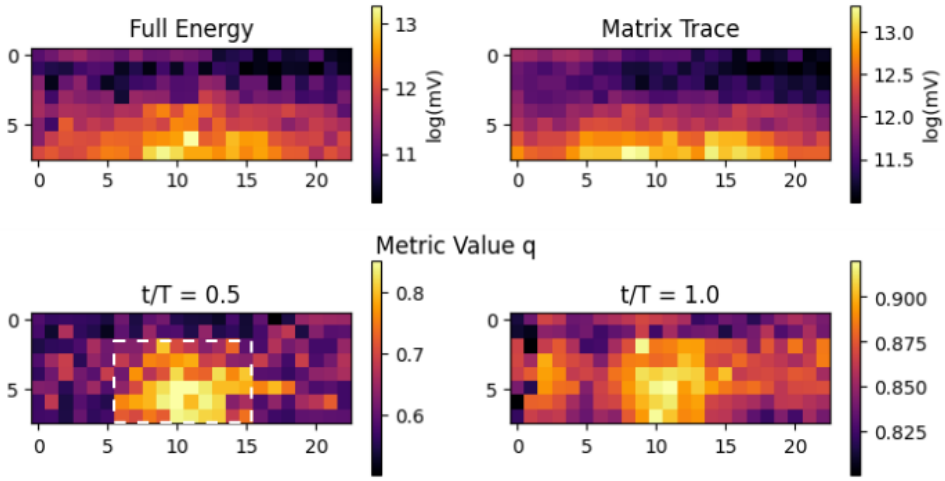

Figure 6.16: Imaging of the second defective region. There are no structural features surrounding the defect, resulting in a smoother map for the second sampling regime. The top 3/4 of the defect were imaged, since a strap holding the part in place seen in Fig: 6.7 prevented access to the remainder of the defect. Despite the smaller depth differential between the defect and its surroundings, the defect highlighted with a white box can still be clearly identified. Axis values are in cm. Both full energy imaging and matrix trace imaging were completed in the half-period time sampling regime, as the results earlier indicated this sampling period provided greater clarity in results.

larger than $100mm \times 100mm$ are considered critical, and so a $50mm \times 50mm$ average smoothing window provides accurate results for this aim. Applying such a window, it is shown with the novel metric introduced that an operator could easily identify defective regions where in the full-energy imaging method used for the sonic response, the operator would struggle to determine true positives when testing the sample for defects and also in not identifying false positives.

Images showing greater structural clarity with the matrix trace method, and the location of both defects with the metric q values is displayed in Fig: 6.17.

This process is also validated on the sampling regimes of $10mm \times 10mm$, shown

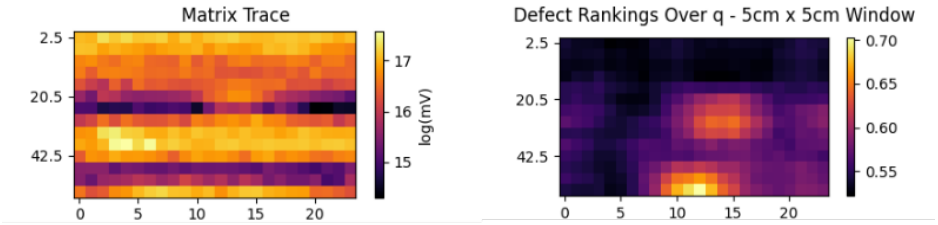

Figure 6.17: Both defects are clearly highlighted when the values of q are smoothed by a rolling averaging window when compared to the sonic method presented in Fig: 6.13, despite having difference depths and different depth differentials with the surrounding surface. Axis values are in *cm*. Both full energy imaging and matrix trace imaging were completed in the half-period time sampling regime.

in Fig: 6.18 where both the underlying structure and defects can be identified

with ease.

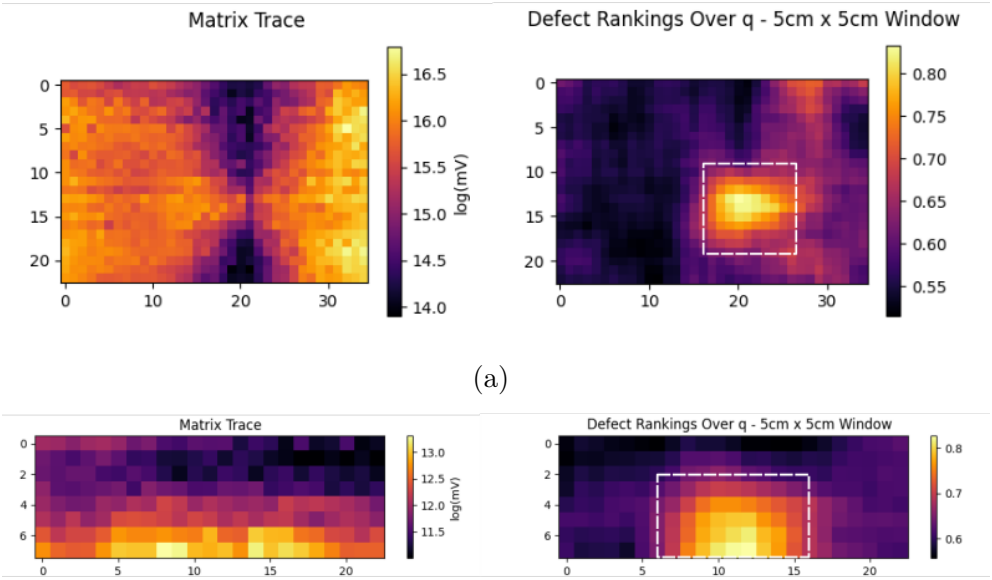

Figure 6.18: Matrix trace method is used to detect the underlying structure of the part, and metric q identifies defects. (a) The first defective region, with cross-cutting bond wedge is shown. (b) The second defective region is imaged. For both defects, the smoothing window applied to the half-period sampled data shows clearly where the defects are. Axis values are in *cm*. Matrix trace imaging was completed in the half-period time sampling regime.

6.5 Discussion

This chapter sought to identify an effective use of data in identifying defects within curved lifeboat hulls for which there is no digital twin of the structure containing thickness or precise material information. The method used is to be suitable for an automated robotised inspection system for future deployment, involving a robotic arm equipped with a mobile base.

The thickness of the sample part meant force data was unsuitable, while the traditional metric of measuring the sound response did not provide a map with great enough clarity for an operator to accurately identify defects with minimal prior knowledge of the structure of the part. This could in a realistic dock scenario result in time lost for the vessel to unnecessary maintenance of non-defective regions. The cause of this was found to be the interference of global modes of resonance being excited and exhibited in the scanning procedure, as is suggested by the advanced literature on Tap Testing. The robotised deployment aspect removed the possibility of using physical solutions such as sound baffles for audio isolation since these would present additional risks such as snagging negative their potential for automatic deployment.

Building upon results used in he area of Force Reconstructions, the matrix trace method was introduced to give the operator greater clarity of the underlying part structure. While the matrix trace method did not provide adequate indications of defects, the improved reliability of response to different surface

depths will allow future work to consider this data as a source of reconstruction algorithms. These future works will seek to produce accurate digital twins and data reconstructions in the case of mobile robotic deployment where the base's odometric readings have a relatively high margin of error, in a similar way to point cloud reconstructions.

To provide accurate defect identification the metric q was introduced, measuring surface depth variations through the relative spread of global and local energetic modes. This metric proved that the modal spread from local resonant modes of interest to global interference modes does occur. With a smoothing window applied, it was further shown the defects could be easily identified, even when the surface depth variation was modest and the depth of the defect differed little from surrounding non-defective regions in the case of defect one.

In cases where prior information can be incorporated, accurate calibration and filtering of signal response can be used as a way of identifying defective regions and so remove the need for force data entirely. Further, the device would need to be calibrated for thicker and stiffer materials to ensure the induction of resonant material modes, making prior material knowledge preferable in order to reduce scanning times. In instances of high through-put or parts equipped with digital twins, the presented methods may be sub-optimal to those using prior knowledge. Further, these methods are to be tested on a wider range of materials to validate them for components beyond thick GFRP sections.

Bibliography

[1] Werner Goldsmith and J. T. Frasier. Impact: The Theory and Physical Behavior of Colliding Solids. *Journal of Applied Mechanics*, 28(4):639–639, 12 1961. ISSN 0021-8936. doi: 10.1115/1.3641808. URL https://doi.org/10.1115/1.3641808.

[2] P. Cawley and R.D. Adams. The mechanics of the coin-tap method of non-destructive testing. *Journal of Sound and Vibration*, 122(2):299–316, 1988. ISSN 0022-460X. doi: https://doi.org/10.1016/S0022-460X(88)80356-0. URL https://www.sciencedirect.com/science/article/pii/S0022460X88803560.

[3] J. J. Peters, D. J. Barnard, N. A. Hudelson, T. S. Simpson, and D. K. Hsu. A prototype tap test imaging system: Initial field test results. *AIP Conference Proceedings*, 509(1):2053–2060, 2000. doi: 10.1063/1.1291323. URL https://aip.scitation.org/doi/abs/10.1063/1.1291323.

[4] R. Schroeer. The acoustic impact technique. *Non-Destructive Testing*, 3(3):194–196, 1970. ISSN 0029-1021. doi: https://doi.org/10.1016/0029-1021(70)90132-5. URL https://www.sciencedirect.com/science/article/pii/0029102170901325.

[5] Sensitivity of the coin-tap method of nondestructive testing: Cawley, p.; adams, r.d. materials evaluation, vol. 47, no. 5, pp. 558–563 (may 1989). *NDT*

E International, 27(3):164, 1994. ISSN 0963-8695. doi: https://doi.org/10.1016/0963-8695(94)90708-0. URL https://www.sciencedirect.com/science/article/pii/0963869594907080.

[6] Yanjun Li, Jian Zhang, Jing Zhao, and Jiandong Hu. Research on intelligent tap testing of aviation composite material. In *Proceedings of the 2016 International Conference on Advanced Materials Science and Environmental Engineering*, pages 44–47. Atlantis Press, 2016/04. ISBN 978-94-6252-209-1. doi: https://doi.org/10.2991/amsee-16.2016.13. URL https://doi.org/10.2991/amsee-16.2016.13.

[7] Peter Cawley. A high frequency coin-tap method of non-destructive testing. *Mechanical Systems and Signal Processing*, 5(1):1–11, 1991. ISSN 0888-3270. doi: https://doi.org/10.1016/0888-3270(91)90011-S. URL https://www.sciencedirect.com/science/article/pii/088832709190011S.

[8] P. Cawley and C. Theodorakopoulos. The membrane resonance method of non-destructive testing. *Journal of Sound and Vibration*, 130(2):299–311, 1989. ISSN 0022-460X. doi: https://doi.org/10.1016/0022-460X(89)90555-5. URL https://www.sciencedirect.com/science/article/pii/0022460X89905555.

[9] William M. Hartmann and James V. Candy. *Acoustic Signal Processing*, pages 519–563. Springer New York, New York, NY, 2014. ISBN 978-1-4939-

0755-7. doi: 10.1007/978-1-4939-0755-7_14. URL https://doi.org/10.1007/978-1-4939-0755-7_14.

[10] R.I. Mackie and A.E. Vardy. Applying the coin-tap test to adhesives in civil engineering: a numerical study. *International Journal of Adhesion and Adhesives*, 10(3):215–220, 1990. ISSN 0143-7496. doi: https://doi.org/10.1016/0143-7496(90)90106-8. URL https://www.sciencedirect.com/science/article/pii/0143749690901068.

[11] Shane Esola, Ivan Bartoli, Suzanne E. Horner, James Q. Zheng, and Antonios Kontsos. Defect detection via instrumented impact in thick-sectioned laminate composites. *Journal of Nondestructive Evaluation*, 36(3):47, Jun 2017. ISSN 1573-4862. doi: 10.1007/s10921-017-0422-8. URL https://doi.org/10.1007/s10921-017-0422-8.

[12] Huadong Wu and M. Siegel. Correlation of accelerometer and microphone data in the "coin tap test". *IEEE Transactions on Instrumentation and Measurement*, 49(3):493–497, 2000. doi: 10.1109/19.850382.

[13] João C. S. Queiroz, Ygor T. B. Santos, Ivan C. da Silva, and Cláudia T. T. Farias. Damage detection in composite materials using tap test technique and neural networks. *Journal of Nondestructive Evaluation*, 40(1):27, Feb 2021. ISSN 1573-4862. doi: 10.1007/s10921-021-00759-9. URL https://doi.org/10.1007/s10921-021-00759-9.

[14] E. Jacquelin, A. Bennani, and P. Hamelin. Force reconstruction: analysis and regularization of a deconvolution problem. *Journal of Sound and Vibration*, 265(1):81–107, 2003. ISSN 0022-460X. doi: https://doi.org/10.1016/S0022-460X(02)01441-4. URL `https://www.sciencedirect.com/science/article/pii/S0022460X02014414`.

[15] Mario Emanuele De Simone, Francesco Ciampa, and Michele Meo. A hierarchical method for the impact force reconstruction in composite structures. *Smart Materials and Structures*, 28(8):085022, jul 2019. doi: 10.1088/1361-665x/aae11c. URL `https://doi.org/10.1088/1361-665x/aae11c`.

[16] Marco Thiene, Z. Sharif-Khodaei, and M.H. Aliabadi. Comparison of artificial neural networks and the transfer function method for force reconstruction in curved composite plates. In *Advances in Fracture and Damage Mechanics XIII*, volume 627 of *Key Engineering Materials*, pages 301–304. Trans Tech Publications Ltd, 1 2015. doi: 10.4028/www.scientific.net/KEM.627.301.

[17] M. Thiene, M. Ghajari, U. Galvanetto, and M.H. Aliabadi. Effects of the transfer function evaluation on the impact force reconstruction with application to composite panels. *Composite Structures*, 114:1–9, 2014. ISSN 0263-8223. doi: https://doi.org/10.1016/j.compstruct.2014.03.055. URL `https://www.sciencedirect.com/science/article/pii/S0263822314001597`.

[18] Sung Joon Kim. Damage detection in composite under in-plane load using tap test. *Journal of Mechanical Science and Technology*, 29(1):199–207, Jan 2015. ISSN 1976-3824. doi: 10.1007/s12206-014-1103-5. URL https://doi.org/10.1007/s12206-014-1103-5.

[19] David K. Hsu, Daniel J. Barnard, John J. Peters, and Vinay Dayal. Physical basis of tap test as a quantitative imaging tool for composite structures on aircraft. *AIP Conference Proceedings*, 509(1):1857–1864, 2000. doi: 10.1063/1.1306256. URL https://aip.scitation.org/doi/abs/10.1063/1.1306256.

Chapter 7

Industrial Use Case: Dry Dock Scanning of a Lifeboat Hull

The industrial focus of this thesis is to enable fast, accurate scanning of an RNLI Severn-class lifeboat hull within a dry dock environment. A novel on-site process had been developed, which the author helped to conduct. The scanning context presented several challenges both in robotic deployment and path planning. An image of the dry dock can be seen in Fig: 7.1.

While some of the maintenance and repair items seen could be moved in order to manoeuvre the robot into position along the hull, support structures that held the boat in place could not be. The area that experienced the greatest damage during operations is the submerged portion closest to the bow, as these experience repeated impacts when navigating through choppy waters.

Figure 7.1: A Severn-class lifeboat hull mounted within a dry dock environment. Support structures limited the working volume and provided potential sources of collisions.

Mounting a UR10e Cobot onto a skeletal mobile frame a digital twin of which is shown in Fig: 7.2, motion around the structures was possible allowing the robot to align itself to the side of the boat.

Due to the limited penetrative depth of Ultrasound with the thick Glass-Fibre-Reinforced-Polymer (GFRP) composite material, data was collected with an EVOTIS Tap Testing device, explored previously in Chapter: 6.

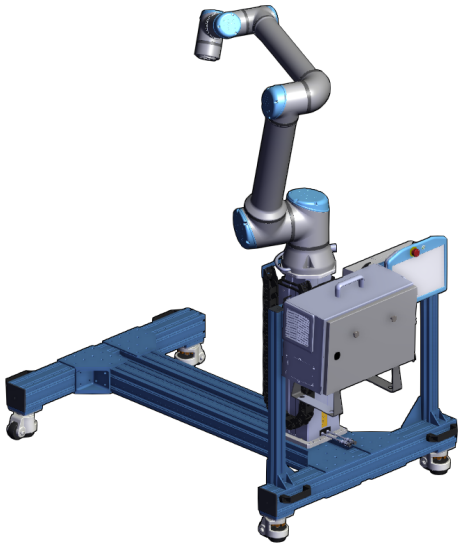

Figure 7.2: Digital representation of a UR10e and robotic controller unit upon a minimalist, mobile, and stabilised base.

7.1 Path Planning and Digital Twin Calibration

To avoid re-calibration of the relative pose of the boat's digital twin to the robot for each scan path, the pose of the boat and robot were calibrated to a fixed datum point. A linear laser distanceometer provided the relative displacement of the robot relative to the keel of the boat and its the bow. Calibration of the robot's pitch was achieved by measuring the displacement of bow and stern from the floor and linear distance of the bow from the stern, resulting the pitch angle. Since the floor was assumed to be flat and the robot's relative pose is given in 2 dimensions relative to the keel, the yaw was irrelevant. The roll could not be accounted for and caused issues later on in the process, since there is no linear datum along the boat orthogonal to the keel. Since these measurements were taken by hand, they allowed for a measure of human error that could not

be quantised or reduced with multiple multi-modal measurements due to time limitations.

The digital twin of the boat was then loaded into the RoboDK (robotic simulation and interaction software) plug-in for Solidworks for path planning [1]. Each path took from half an hour to an hour to plan, and were completed in batches while off-site to ensure minimal time to deployment. While the digital twin of the hull sections provided a good estimate of the hull parts of interest, they were provided from the manufacturing drawings and so differed from the actual boat due to warping due to load and fitting to the remains of the hull by several centimetres. While this is a non-critical deviation from the original part, a spring mounted tool was used to compensate for the deviation in the tool's linear z-axis that allowed up to $40mm$ of travel. Compounded with inaccuracies in the digital-twin calibration process, this proved too short a travel distance to allow accurate collections of data.

7.2 Data Collection

Using the process listed above during the first two days, several issues arose. While ideally off-site path planning was deemed optimal due to the time costs of each scan process, environmental issues such as the boat's support structures meant that initially the robot had to be aligned to each scanning section, then a path planned and subsequently deployed. By creating a digital twin including the

structures, some of these features could be negated but increased path planning time up to an hour, as the robot's position had to be optimised to maximise reachability and minimise singularities over the paths, while also ensuring obstacle avoidance. An example pose is shown in Fig: 7.3.

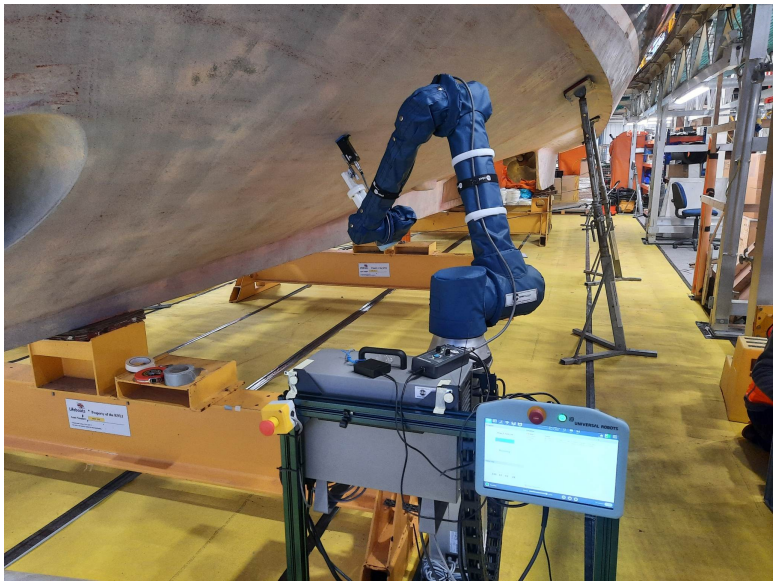

Figure 7.3: The mobile Cobot platform is tightly aligned to the yellow support, enabling maximal coverage and reach.

The digital twin - to - real world calibration process that allowed batch path planning incurred errors in reconstruction of the part. Errors in the calibration process, digital twin, and human error in measuring the robot's pose coupled to the limited tool travel distance meant some paths to had to be run several times with subsequent re-positioning of the robot relative to the boat to ensure full coverage, that ultimately led to deviations from the position used in path planning and reconstructions. The tool's design incorporated expected deviations by allowing up to $40mm$ of travel distance along a sprung metal extension, allowing

retraction and advancement along the tool's z-axis. Coupled to the relative unidirectional isotropy of the hull closer to the Stern meant that only cumulative errors within the surface's normal direction in the order of centimetres could be quantised, and further could not be assigned to stages of the process.

The listed scanning procedure proved to be too time intensive and produced too many reconstruction errors, taking 2 days to scan a quarter of the hull. The path planning process of the team took a different tack in response to the difficulties found. Since large portions of the hull were approximately planar, a linear relative motion rasterisation path planning program was produced on the controller that allowed repeated use of the code, and a flexibility enabling adaptation of the robot's pose and the raster pattern to the local surface shape. The data was then relatively positioned in reconstruction by adopting the traditional real world - to - digital twin calibration procedure, whereby the robot's pose relative to the datum was recorded for each scan and used for reconstructions, since path planning was no longer dependant on a well calibrated digital twin.

While this sped the process up and reduced the room for calibration and human error, the path planning process became a running cost that required the robot to be free, to check that at all points along the tool remained in contact with the hull. On average it took half an hour to produce each path. Over the next day and a half, the robot was able to scan half of a boat section. Due to the linear path planning, the curved sections provided a significant challenge that

took a large quantity of time to plan over and subsequently check. This can be seen in Fig: 7.4, where many scans were required for the bow section that had a greater curvature than the portion closer to the stern. The linear segments did not provide a regular and well fitted tiling of the surface, with some sections not overlapping fully instead extending out by up to $40mm$.

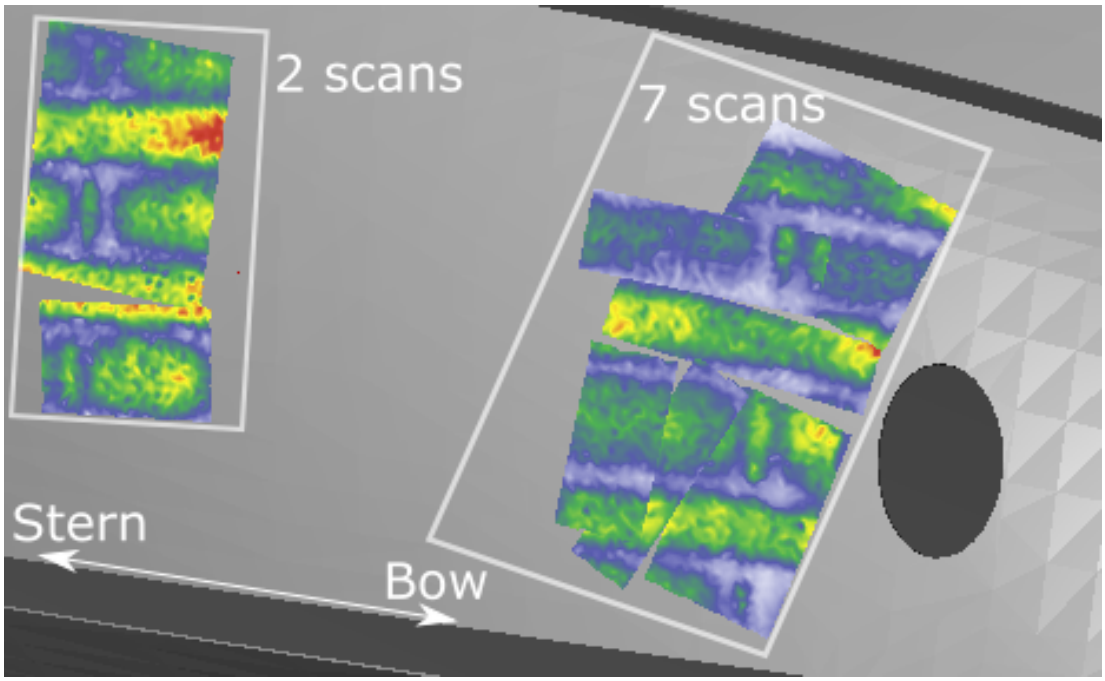

Figure 7.4: Comparison of the required number of scans to cover a hull section. Despite being of similar size, the curved bow-side sections required significantly more scans to ensure coverage than flatter stern-side portions.

A key issue with both data collection methods was the requirement for full part reconstruction to check for missed portions of data over the surface, displayed as gaps between the data shown in Fig: 7.5. The speed of the process could be refined if a display of previously covered portions was available at the time of path planning relative to the robot, reducing the overlap incurred by repeated

referencing to the reconstructed model.

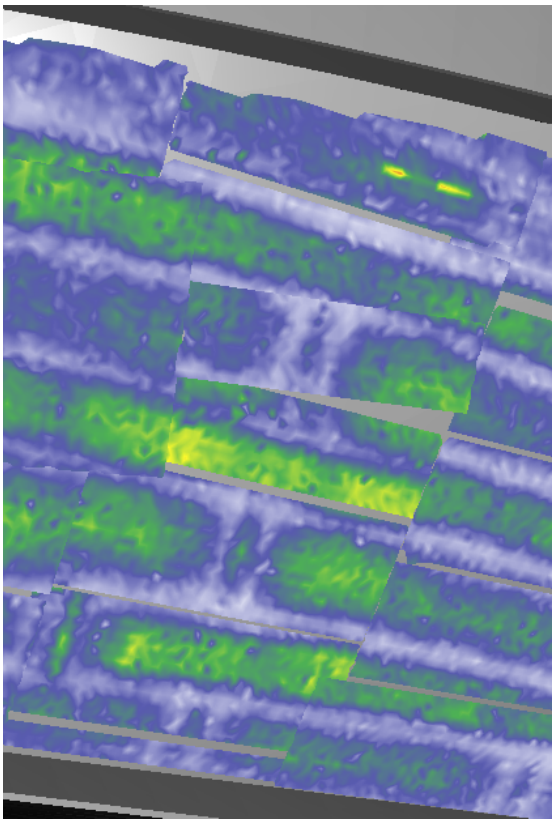

Figure 7.5: The operators have to judge where to place new paths to overlap with previously covered sections, resulting in small un-scanned portions, leading to additional path planning time costs.

7.3 Conclusions

The initial and novel application of a Cobot to an on-site environment for large structure scanning proved the concept and successfully surveyed the hull. Several areas of improvement were identified. These are broken down into enhancements of: speed of path planning, ease of use and deployment, and accuracy of reconstruction.

With either path planning process deployed, path planning contributed a significant time cost, either in manually configuring reachability or in aligning and re-aligning the robot in order to match the real-world pose of the hull. Particularly pronounced were the planning and alignment times required over curved sections of the hull, hampering deployments to more complex shapes found in other on-site inspection processes. After a covering path set is found during an initial scan and could be used for subsequent scans, however non-static extrinsic factors such as the yacht-supports and varying roll and pitch of the hull would require re-planning and path modifications on each subsequent deployment.

The path planning processes themselves were skill intensive, requiring an operator trained in either the robot's intrinsic planning process or in third party path planning software. Scalable deployment of this system to several parallel inspection routines would be limited by the availability of highly skilled robotic operators. A simpler planning process would reduce the required cost of retaining the necessary labour, and the time taken for path generation.

To accurately identify defective regions for repair, the method used of relying upon a fixed datum introduced several millimetres of error when matching scan positions. A combination of human error in measuring the datum's relative position, error in aligning the robot to the boat hull's axes, and offsets between the digital twin and real model all contributed to a model that did not align to the initial digital twin of the hull with the same accuracy as a track-mounted

industrial robot.

This thesis has sought to address these issues from the perspective of selecting the minimal number of work-space representations and embedded frames of reference.

In summary, enhance the approach so that it is flexible, scalable, and of minimal financial and time cost, this thesis has sought to provide developments in the following areas.

1. Autonomous path planning and simultaneous scanning, removing the path planning time cost and enabling a greater field of operators to profile surfaces with minimal intervention. This would further negate the need to calibrate a digital twin to the real-world model in cases a digital-twin is available. This thesis sought to address this issue with a novel, entirely autonomous process presented in Chapter: 3, requiring no operator intervention to simultaneously plan and scan unknown parts.

2. Aware path planning, able to consider and avoid collisions would reduce the need for lengthy simulations while considering and avoiding collisions, making it safe for on-site deployment. In lieu of myriad onsite challenges and obstacles, the minimalist tool-perspective from Chapter: 3 was built upon with a commercial, low-cost RGB/D camera environmentally-aware path planning incorporating collision avoidance, presented in Chapter: 4.

3. A relative coordinate referencing system that does not introduce human errors that relies on markers that are not in the way of other ongoing processes (repair, refitting) would enable accurate reconstructions of the NDT data, and if permanent would enable lifetime part integrity tracking. Such a relative positioning system would further enable location of uncovered sections of the surface. In order to provide a low-cost and scalable alternative to conventional metrological equipment that would be suitable for on-site inspections, Chapter: 5 built upon existing relative positioning methods using Computer Vision with commercial RGB/D cameras to provide an accurate iterative part reconstruction methodology suitable for on-site environments. This chapter further evaluated the optimal operating conditions of a D415 Intel Realsense camera for large part reconstructions.

Bibliography

[1] Universal Robots. Robodk add-in for solidworks, 2023. URL `https://robodk.com/doc/en/Plugin-SolidWorks.html`.

Chapter 8

Conclusions and Further Work

Manufacturing processes have undergone many cycles of innovation in recent years aiming to reduce waste of both energy and material. In the context of greenhouse emissions; remanufacturing, additive manufacturing, and novel light-weight composite production methods are all seen as complimentary routes towards a global net-zero target. These industries however demand more flexibility from robotised NDT than is possible within the traditional path planning methodologies. Issues in applying traditional robotic-arm NDT such as the presence of non-critical part defects disconnecting the correspondence between an idealised digital twin and real components could hamper the uptake of low-emissions procured vital components.

While surges in green electricity are leading to greater demand for novel means of production such as modular nuclear reactors and significant growth in tradi-

tional methods such as wind turbines globally, in several regions such as south-east Asia the labour market for NDT technicians remains a low-growth sector, highlighting the need for greater on-site automation and robotisation to deliver on energy needs globally.

Focus on answering the challenges of on-site and flexible inspections is rapidly gaining traction. The need for mobile, flexible systems capable of handling noisy environments with human operators working alongside inspection processes could reduce the down time and expense of a range of products, from dock-based aerospace inspections to intelligently inspecting critical components of a reactor in-service. Reliance on costly, fixed base robotic arm systems has presented a bottleneck in such situations, requiring disassembly of components to be scanned off-site, or on-site by human operators.

This thesis has sought to introduce algorithms that inflect the flexibility required of a mobile robotic system to scan structures of varying scales autonomously. Due to on-site demands and potential wear and tear of equipment, the minimal number of sensors for each aspect of the problem are desired, with the cost of each also minimised. To find the minimal number of sensors necessary for each task, different mathematical representations of the work-space were investigated.

The outcome of this thesis is a complete, easy to use process for autonomous or user-guided scanning of components without digital twins provided for offline

path planning. Whereas traditional offline path planning and the requisite real-world to digital-twin calibration stages could take up to a month of preparation for a skilled operator, the proposed algorithms reduce this to the order of minutes. Online path corrections utilising force and laser feedback ensure that even while using low-quality environmental sensors, the tool is kept in contact with and perpendicular to surfaces with curvature for tool speeds up to $30mm/s$.

By introducing a novel part stitching algorithm using RGB/D data, the process may be deployed on a mobile robotic arm scanning a large structure, reducing the costs of larger fixed cell industrial robot set-ups. While large-scale photogrammetric systems are used to stitch NDT data to within mm accuracy, they require extensive calibration routines that take in the order of hours for each set-up, and are further limited by working volumes of tens of cubic metres. The novel part stitching algorithm set out in this thesis requires sensor calibration only once, can be applied to arbitrary and unknown visual artefacts. The process further utilises the same RGB/D sensor as previous chapters, that is both un-encumbering and flange mounted. Experimentally determined optimal measurement conditions provides an accuracy of $\pm 2.5mm$ and ± 0.005rad for each frame of reference registration, within the same order of magnitude as photogrammetric equipment.

The industrially relevant portions of this thesis have shown proofs of concept for increasing the through-put of online flexible robotic systems. The by-product

of the mathematical investigations for full surface discovery is a novel algorithm that is applicable in areas beyond mobile robotic arms. The CSFA introduced is a powerful algorithm for hypothesised surface discovery in real-world environments, but is also a generalisation of the Flood Fill heuristic that may also be applied to fully mapping mathematical constructs such as unknown functionals in an arbitrary number of dimensions.

An industrial focus was placed on scanning a lifeboat hull, the challenges of which are shown to be met. Mounting a lifeboat within an off-site traditional large volume industrial-robotic cell would be impractical due to the necessarily large quantities of resources and time taken to move the boat, as well as considerably limiting robotic motion to account for the necessary boat-supports placed within the cell, being both costly and creating a large down-time of the boat as a life saving resource. The mobile base of the UR10e can instead be manoeuvred around obstacles and supports, up to the hull within a dry dock. Previous investigations had suggested on-site use of photogrammetric sensors for tool tracking to later reconstruct results. The cluttered, noisy environment would have been unsuitable, limiting the reconstruction effective range dramatically, would easily have suffered loss of accuracy with human operators accidentally moving equipment, extending the down-time of the hull significantly with multiple four-hour long calibration procedures. Instead the proposed reconstruction method can stitch the collected NDT data with a low-cost RGB/D camera, requiring one prior sen-

sor calibration and resulting in an accuracy of the same order of magnitude as a photogrammetric system costing £100,000.

To begin traditional offline path planning over the hull's surface the digital-twin would require calibration to the real-world placement of the robot, a process that is both time consuming and inaccurate due to the hull's large volume. Small angular errors of the roll pitch or yaw result in large offsets of executed paths from the surface, requiring lengthy re-calibration and subsequent re-placement of prior results. The demonstrated path planning and online path correction based deployment does not face these issues, deploying a real path within minutes, collecting data to sub-mm accuracy within the robot's frame of reference, later contextualised within the world frame during post processing. While each section of this thesis is demonstrated with use of an Ultrasonic sensor, for the lifeboat hulls UT was particularly inapt. Use of another sonic NDT method was shown to retain and enhance the benefits of CWP applied UT over jet-PAUT, though it provided challenges in terms of defect visualisation and accuracy. These issues were addressed in Chapter: 6.

8.1 Future Work

Progression of hardware, software, robotic, and sensor systems are rapidly opening avenues of innovation in this field. The algorithms developed in this thesis have produced several prospective topics of research.

Primarily, further development is necessary to not simply ensure safety of human operators and assets with use of Cobots. Methods of sensing dynamic components of an environment coupled to reactive algorithms capable of task re-planning are necessary to ensure the robotic platform can work with minimal down-time alongside human operators.

Obstacles found in on-site environments prevent simple application of the robot to the surface. In some circumstances, obstacles may be moved by a human operator requiring a communication method between human and robots. An algorithm that can detect obstacles to deployment, and that could then intelligently schedule scans and secondary tasks between multiple operators would increase scan through-put in large scale multi-day scans and improve the efficiency of other tasks such as re-fitting and repair.

Development of autonomous complete object mapping algorithms similar to or in extension of the CSFA using wide aperture sensors would assist in a variety of industries. Such mapping enhanced with object segmentation algorithms could produce accurate digital twins of unknown structures, vital to applications from industrial asset monitoring through to recording of archaeological finds.

Finally, this thesis has produced fast surface scanning algorithms for when accurate digital twins are not available. In cases where the part is known but not well reflected by the digital twin, such as in remanufacturing, the data collected by the algorithms presented may be used to improve manufacturing or

prognosis capabilities over the course of a product's lifetime. A natural extension of this thesis would be to compliment ongoing investigations such as Population based Structural Health Monitoring coupling visual, tribological, and UT data to a visual artefact such as QR code, that then either predicts the part's remanufacturing viability or optimises the manufacturing process of other similar parts. Similar work looking at the fields of computer vision and image segmentation will investigate enhancing the work developed throughout this thesis in application to unstructured environments and with parts where a prior digital twin is enabled.